

**International Journal on**

**Advances in Telecommunications**



The *International Journal on Advances in Telecommunications* is published by IARIA.

ISSN: 1942-2601

journals site: <http://www.ariajournals.org>

contact: [petre@aria.org](mailto:petre@aria.org)

Responsibility for the contents rests upon the authors and not upon IARIA, nor on IARIA volunteers, staff, or contractors.

IARIA is the owner of the publication and of editorial aspects. IARIA reserves the right to update the content for quality improvements.

Abstracting is permitted with credit to the source. Libraries are permitted to photocopy or print, providing the reference is mentioned and that the resulting material is made available at no cost.

Reference should mention:

*International Journal on Advances in Telecommunications, issn 1942-2601*  
vol. 14, no. 1 & 2, year 2021, <http://www.ariajournals.org/telecommunications/>

The copyright for each included paper belongs to the authors. Republishing of same material, by authors or persons or organizations, is not allowed. Reprint rights can be granted by IARIA or by the authors, and must include proper reference.

Reference to an article in the journal is as follows:

<Author list>, "<Article title>"  
*International Journal on Advances in Telecommunications, issn 1942-2601*  
vol. 14, no. 1 & 2, year 2021, <start page>:<end page> , <http://www.ariajournals.org/telecommunications/>

IARIA journals are made available for free, proving the appropriate references are made when their content is used.

Sponsored by IARIA

[www.aria.org](http://www.aria.org)

Copyright © 2021 IARIA

**Editors-in-Chief**

Tulin Atmaca, Institut Mines-Telecom/ Telecom SudParis, France  
Marko Jäntti, University of Eastern Finland, Finland

**Editorial Advisory Board**

Ioannis D. Moscholios, University of Peloponnese, Greece  
Ilija Basicovic, University of Novi Sad, Serbia  
Kevin Daimi, University of Detroit Mercy, USA  
György Kálmán, Gjøvik University College, Norway  
Michael Massoth, University of Applied Sciences - Darmstadt, Germany  
Mariusz Glabowski, Poznan University of Technology, Poland  
Dragana Krstic, Faculty of Electronic Engineering, University of Nis, Serbia  
Wolfgang Leister, Norsk Regnesentral, Norway  
Bernd E. Wolfinger, University of Hamburg, Germany  
Przemyslaw Pochec, University of New Brunswick, Canada  
Timothy Pham, Jet Propulsion Laboratory, California Institute of Technology, USA  
Kamal Harb, KFUPM, Saudi Arabia  
Eugen Borcoci, University "Politehnica" of Bucharest (UPB), Romania  
Richard Li, Huawei Technologies, USA

**Editorial Board**

Fatma Abdelkefi, High School of Communications of Tunis - SUPCOM, Tunisia  
Seyed Reza Abdollahi, Brunel University - London, UK  
Habtamu Abie, Norwegian Computing Center/Norsk Regnesentral-Blindern, Norway  
Rui L. Aguiar, Universidade de Aveiro, Portugal  
Javier M. Aguiar Pérez, Universidad de Valladolid, Spain  
Mahdi Aiash, Middlesex University, UK  
Akbar Sheikh Akbari, Staffordshire University, UK  
Ahmed Akl, Arab Academy for Science and Technology (AAST), Egypt  
Hakiri Akram, LAAS-CNRS, Toulouse University, France  
Anwer Al-Dulaimi, Brunel University, UK  
Muhammad Ali Imran, University of Surrey, UK  
Muayad Al-Janabi, University of Technology, Baghdad, Iraq  
Jose M. Alcaraz Calero, Hewlett-Packard Research Laboratories, UK / University of Murcia, Spain  
Erick Amador, Intel Mobile Communications, France  
Ermeson Andrade, Universidade Federal de Pernambuco (UFPE), Brazil  
Cristian Anghel, University Politehnica of Bucharest, Romania  
Regina B. Araujo, Federal University of Sao Carlos - SP, Brazil  
Pasquale Ardimento, University of Bari, Italy  
Ezendu Ariwa, London Metropolitan University, UK  
Miguel Arjona Ramirez, São Paulo University, Brasil

Radu Arsinte, Technical University of Cluj-Napoca, Romania  
Tulin Atmaca, Institut Mines-Telecom/ Telecom SudParis, France  
Mario Ezequiel Augusto, Santa Catarina State University, Brazil  
Marco Aurelio Spohn, Federal University of Fronteira Sul (UFFS), Brazil  
Philip L. Balcaen, University of British Columbia Okanagan - Kelowna, Canada  
Marco Baldi, Università Politecnica delle Marche, Italy  
Ilija Basicovic, University of Novi Sad, Serbia  
Carlos Becker Westphall, Federal University of Santa Catarina, Brazil  
Mark Bentum, University of Twente, The Netherlands  
David Bernstein, Huawei Technologies, Ltd., USA  
Eugen Borcoci, University "Politehnica" of Bucharest (UPB), Romania  
Fernando Boronat Seguí, Universidad Politecnica de Valencia, Spain  
Christos Bouras, University of Patras, Greece  
Martin Brandl, Danube University Krems, Austria  
Julien Broisin, IRIT, France  
Dumitru Burdescu, University of Craiova, Romania  
Andi Buzo, University "Politehnica" of Bucharest (UPB), Romania  
Shkelzen Cakaj, Telecom of Kosovo / Prishtina University, Kosovo  
Enzo Alberto Candrea, DEIS-University of Bologna, Italy  
Rodrigo Capobianco Guido, São Paulo State University, Brazil  
Hakima Chaouchi, Telecom SudParis, France  
Silviu Ciochina, Universitatea Politehnica din Bucuresti, Romania  
José Coimbra, Universidade do Algarve, Portugal  
Hugo Coll Ferri, Polytechnic University of Valencia, Spain  
Noel Crespi, Institut TELECOM SudParis-Evry, France  
Leonardo Dagui de Oliveira, Escola Politécnica da Universidade de São Paulo, Brazil  
Kevin Daimi, University of Detroit Mercy, USA  
Gerard Damm, Alcatel-Lucent, USA  
Francescantonio Della Rosa, Tampere University of Technology, Finland  
Chérif Diallo, Consultant Sécurité des Systèmes d'Information, France  
Klaus Drechsler, Fraunhofer Institute for Computer Graphics Research IGD, Germany  
Jawad Drissi, Cameron University, USA  
António Manuel Duarte Nogueira, University of Aveiro / Institute of Telecommunications, Portugal  
Alban Duverdier, CNES (French Space Agency) Paris, France  
Nicholas Evans, EURECOM, France  
Fabrizio Falchi, ISTI - CNR, Italy  
Mário F. S. Ferreira, University of Aveiro, Portugal  
Bruno Filipe Marques, Polytechnic Institute of Viseu, Portugal  
Robert Forster, Edgemount Solutions, USA  
John-Austen Francisco, Rutgers, the State University of New Jersey, USA  
Kaori Fujinami, Tokyo University of Agriculture and Technology, Japan  
Shauneen Furlong, University of Ottawa, Canada / Liverpool John Moores University, UK  
Emiliano Garcia-Palacios, ECIT Institute at Queens University Belfast - Belfast, UK  
Ana-Belén García-Hernando, Universidad Politécnica de Madrid, Spain  
Bezalel Gavish, Southern Methodist University, USA  
Christos K. Georgiadis, University of Macedonia, Greece

Mariusz Glabowski, Poznan University of Technology, Poland  
Katie Goeman, Hogeschool-Universiteit Brussel, Belgium  
Hock Guan Goh, Universiti Tunku Abdul Rahman, Malaysia  
Pedro Gonçalves, ESTGA - Universidade de Aveiro, Portugal  
Valerie Gouet-Brunet, Conservatoire National des Arts et Métiers (CNAM), Paris  
Christos Grecos, University of West of Scotland, UK  
Stefanos Gritzalis, University of the Aegean, Greece  
William I. Grosky, University of Michigan-Dearborn, USA  
Vic Grout, Glyndwr University, UK  
Xiang Gui, Massey University, New Zealand  
Huaqun Guo, Institute for Infocomm Research, A\*STAR, Singapore  
Song Guo, University of Aizu, Japan  
Kamal Harb, KFUPM, Saudi Arabia  
Ching-Hsien (Robert) Hsu, Chung Hua University, Taiwan  
Javier Ibanez-Guzman, Renault S.A., France  
Lamiaa Fattouh Ibrahim, King Abdul Aziz University, Saudi Arabia  
Theodoros Iliou, University of the Aegean, Greece  
Mohsen Jahanshahi, Islamic Azad University, Iran  
Antonio Jara, University of Murcia, Spain  
Carlos Juiz, Universitat de les Illes Balears, Spain  
Adrian Kacso, Universität Siegen, Germany  
György Kálmán, Gjøvik University College, Norway  
Eleni Kaplani, University of East Anglia-Norwich Research Park, UK  
Behrouz Khoshnevis, University of Toronto, Canada  
Ki Hong Kim, ETRI: Electronics and Telecommunications Research Institute, Korea  
Atsushi Koike, Seikei University, Japan  
Ousmane Kone, UPPA - University of Bordeaux, France  
Dragana Krstic, University of Nis, Serbia  
Archana Kumar, Delhi Institute of Technology & Management, Haryana, India  
Romain Laborde, University Paul Sabatier (Toulouse III), France  
Massimiliano Laddomada, Texas A&M University-Texarkana, USA  
Wen-Hsing Lai, National Kaohsiung First University of Science and Technology, Taiwan  
Zhihua Lai, Ranplan Wireless Network Design Ltd., UK  
Jong-Hyouk Lee, INRIA, France  
Wolfgang Leister, Norsk Regnesentral, Norway  
Elizabeth I. Leonard, Naval Research Laboratory - Washington DC, USA  
Richard Li, Huawei Technologies, USA  
Jia-Chin Lin, National Central University, Taiwan  
Chi (Harold) Liu, IBM Research - China, China  
Diogo Lobato Acatauassu Nunes, Federal University of Pará, Brazil  
Andreas Loeffler, Friedrich-Alexander-University of Erlangen-Nuremberg, Germany  
Michael D. Logothetis, University of Patras, Greece  
Renata Lopes Rosa, University of São Paulo, Brazil  
Hongli Luo, Indiana University Purdue University Fort Wayne, USA  
Christian Maciocco, Intel Corporation, USA  
Dario Maggiorini, University of Milano, Italy

Maryam Tayefeh Mahmoudi, Research Institute for ICT, Iran  
Krešimir Malarić, University of Zagreb, Croatia  
Zoubir Mammeri, IRIT - Paul Sabatier University - Toulouse, France  
Herwig Mannaert, University of Antwerp, Belgium  
Michael Massoth, University of Applied Sciences - Darmstadt, Germany  
Adrian Matei, Orange Romania S.A, part of France Telecom Group, Romania  
Natarajan Meghanathan, Jackson State University, USA  
Emmanouel T. Michailidis, University of Piraeus, Greece  
Ioannis D. Moscholios, University of Peloponnese, Greece  
Djafar Mynbaev, City University of New York, USA  
Pubudu N. Pathirana, Deakin University, Australia  
Christopher Nguyen, Intel Corp., USA  
Lim Nguyen, University of Nebraska-Lincoln, USA  
Brian Niehöfer, TU Dortmund University, Germany  
Serban Georgica Obreja, University Politehnica Bucharest, Romania  
Peter Orosz, University of Debrecen, Hungary  
Patrik Österberg, Mid Sweden University, Sweden  
Harald Øverby, ITEM/NTNU, Norway  
Tudor Palade, Technical University of Cluj-Napoca, Romania  
Constantin Paleologu, University Politehnica of Bucharest, Romania  
Stelios Papaharalabos, National Observatory of Athens, Greece  
Gerard Parr, University of Ulster Coleraine, UK  
Ling Pei, Finnish Geodetic Institute, Finland  
Jun Peng, University of Texas - Pan American, USA  
Cathryn Peoples, University of Ulster, UK  
Dionysia Petraki, National Technical University of Athens, Greece  
Dennis Pfisterer, University of Luebeck, Germany  
Timothy Pham, Jet Propulsion Laboratory, California Institute of Technology, USA  
Roger Pierre Fabris Hoefel, Federal University of Rio Grande do Sul (UFRGS), Brazil  
Przemyslaw Pochec, University of New Brunswick, Canada  
Anastasios Politis, Technological & Educational Institute of Serres, Greece  
Adrian Popescu, Blekinge Institute of Technology, Sweden  
Neeli R. Prasad, Aalborg University, Denmark  
Dušan Radović, TES Electronic Solutions, Stuttgart, Germany  
Victor Ramos, UAM Iztapalapa, Mexico  
Gianluca Reali, Università degli Studi di Perugia, Italy  
Eric Renault, Telecom SudParis, France  
Leon Reznik, Rochester Institute of Technology, USA  
Joel Rodrigues, Instituto de Telecomunicações / University of Beira Interior, Portugal  
David Sánchez Rodríguez, University of Las Palmas de Gran Canaria (ULPGC), Spain  
Panagiotis Sarigiannidis, University of Western Macedonia, Greece  
Michael Sauer, Corning Incorporated, USA  
Marialisa Scatà, University of Catania, Italy  
Zary Segall, Chair Professor, Royal Institute of Technology, Sweden  
Sergei Semenov, Broadcom, Finland  
Dimitrios Serpanos, University of Patras and ISI/RC Athena, Greece

Adão Silva, University of Aveiro / Institute of Telecommunications, Portugal  
Pushpendra Bahadur Singh, MindTree Ltd, India  
Mariusz Skrocki, Orange Labs Poland / Telekomunikacja Polska S.A., Poland  
Leonel Sousa, INESC-ID/IST, TU-Lisbon, Portugal  
Cristian Stanciu, University Politehnica of Bucharest, Romania  
Liana Stanescu, University of Craiova, Romania  
Cosmin Stoica Spahiu, University of Craiova, Romania  
Young-Joo Suh, POSTECH (Pohang University of Science and Technology), Korea  
Hailong Sun, Beihang University, China  
Jani Suomalainen, VTT Technical Research Centre of Finland, Finland  
Fatma Tansu, Eastern Mediterranean University, Cyprus  
Ioan Toma, STI Innsbruck/University Innsbruck, Austria  
Božo Tomas, HT Mostar, Bosnia and Herzegovina  
Piotr Tyczka, ITTI Sp. z o.o., Poland  
John Vardakas, University of Patras, Greece  
Andreas Veglis, Aristotle University of Thessaloniki, Greece  
Luís Veiga, Instituto Superior Técnico / INESC-ID Lisboa, Portugal  
Calin Vladeanu, "Politehnica" University of Bucharest, Romania  
Benno Volk, ETH Zurich, Switzerland  
Krzysztof Walczak, Poznan University of Economics, Poland  
Krzysztof Walkowiak, Wroclaw University of Technology, Poland  
Yang Wang, Georgia State University, USA  
Yean-Fu Wen, National Taipei University, Taiwan, R.O.C.  
Bernd E. Wolfinger, University of Hamburg, Germany  
Riaan Wolhuter, Universiteit Stellenbosch University, South Africa  
Yulei Wu, Chinese Academy of Sciences, China  
Mudasser F. Wyne, National University, USA  
Gaoxi Xiao, Nanyang Technological University, Singapore  
Bashir Yahya, University of Versailles, France  
Abdulrahman Yarali, Murray State University, USA  
Mehmet Erkan Yüksel, Istanbul University, Turkey  
Pooneh Bagheri Zadeh, Staffordshire University, UK  
Giannis Zaoudis, University of Patras, Greece  
Liaoyuan Zeng, University of Electronic Science and Technology of China, China  
Rong Zhao, Detecon International GmbH, Germany  
Zhiwen Zhu, Communications Research Centre, Canada  
Martin Zimmermann, University of Applied Sciences Offenburg, Germany  
Piotr Zwierzykowski, Poznan University of Technology, Poland

**CONTENTS**

*pages: 1 - 9*

**A Probabilistic Learning Reinforcement Model for the Performance Analysis of Multimedia Indexing and Packet Switching**

Clement Leung, Chinese University of Hong Kong, Shenzhen, China  
Yao Tong, Chinese University of Hong Kong, Shenzhen, China

*pages: 10 - 18*

**Software Environment for Performance Simulation of Three-hop Wireless Relay Channels under the Influence of Rician Fading**

Dragana Krstic, University of Nis, Faculty of Electronic Engineering, Serbia  
Petar Nikolic, TigarTyres, Pirot, Serbia  
Nenad Petrovic, University of Nis, Faculty of Electronic Engineering, Serbia  
Zoran Popovic, Higher Technical School of Professional Studies, Zvecan, Serbia  
Sinisa Minic, Faculty of Teacher Education in Prizren – Leposavic, University of Pristina- Kosovska Mitrovica, Serbia

*pages: 19 - 29*

**Next Generation IMPAQT Miniaturized Underwater Transmitter System Design**

Hamed Jafarzadeh, Tyndall National Institute, University College Cork, Ireland  
Marco Belcastro, Tyndall National Institute, University College Cork, Ireland  
Brendan O'Flynn, Tyndall National Institute, University College Cork, Ireland

*pages: 30 - 40*

**Requirements Identification for Vehicle-to-Everything and Internet of Vehicles dedicated 5G Slices**

Eugen Borcoci, University POLITEHNICA of Bucharest - UPB, Romania  
Marius-Constantin Vochin, University POLITEHNICA of Bucharest - UPB, Romania  
Serban Georgica Obreja, University POLITEHNICA of Bucharest - UPB, Romania  
Silvia Stanciu, University POLITEHNICA of Bucharest - UPB, Romania

*pages: 41 - 50*

**Improving the Design Performance of Field Programmable Gate Array Devices with Efficient Approach to Measure Power Consumption**

Esteve Hassan, Mohawk College, Canada  
Bilal Al Momani, Mohawk College, Canada

*pages: 51 - 69*

**Supervised Machine Learning in Inter-Level, Ultra-Low Frequency Power Line Communications**

Kushal Thapa, Texas State University, United States  
Stan McClellan, Texas State University, United States  
Damian Valles, Texas State University, United States

*pages: 70 - 99*

**Cloud Cost Optimization Based on Shifted N-policy M/M/M/K Queue Model**

Zsolt Saffer, Vienna University of Technology, Vienna, Austria

# A Probabilistic Learning Reinforcement Model for the Performance Analysis of Multimedia Indexing and Packet Switching

Clement H. C. Leung

School of Science and Engineering  
Chinese University of Hong Kong  
Shenzhen, China  
clementleung@cuhk.edu.cn

Yao Tong

School of Data Science  
Chinese University of Hong Kong  
Shenzhen, China  
yaotong@link.cuhk.edu.cn

**Abstract** — A stochastic model of binary classification in the presence of noise is considered where classification outcomes are non-deterministic. To ensure the correctness of a particular classification decision, repeated reinforcements need to be acquired. By accumulating sufficient reinforcements, one would learn to predict the class label. In this study, we develop a probabilistic learning reinforcement classification model and apply it to multimedia information indexing and to noisy network transmission. Three learning strategies are analyzed. The first one requires the accumulation of a total of a given number of pre-specified positive labels, while the second one builds from the first and requires additionally that such reinforcements occur consecutively in the observation sequence. The third strategy views the classification process from a multi-agent stochastic game perspective, with the labelling decision determined by which class label attaining a given threshold first. The model characteristics are studied for the three different strategies and key measures of performance are obtained. The model is applied to fault-tolerant network communications over a noisy channel, with learning success corresponding to error-free transmission of data packets, and to multimedia indexing where learning success correspond to the successful automatic installation of an index term to a particular data object. The present learning paradigm will be useful in allowing the effectiveness and performance of these systems and similar ones to be meaningfully quantified and evaluated.

**Keywords** – computer networks; packet switching; multimedia information indexing; reinforcement learning; multi-agent; naive Bayes classifiers; stochastic game

## I. INTRODUCTION AND RELATIONSHIP WITH OTHER WORK

Sequential classification problems are ubiquitous and many important decision problems can often be reduced to a classification problem. Among the variety of classification problems, binary classification problems consisting of two class labels are particularly common. However, classification verdicts returned by different classifiers over time are often non-deterministic, causing uncertainty in the classification decision. In such a situation, repeated reinforcements are necessary to ensure the reliability of the decision.

To be concrete, we shall use the multimedia indexing scenario [1] to explain the key concepts. Later we shall establish a correspondence between multimedia search and fault-tolerant network communications. In effective

information and document retrieval, it is often necessary to involve the users in the search process so as to improve the overall return results [18][19][22] [29]. In addition, affective indexing of multimedia content combines emotional responses generated by the users is sometimes employed, e.g., the psycho-physiological signals, galvanic skin response, face tracking [19][27].

In [20], it is proposed that a reinforcement learning approach is suitable for users exposing to raw and high-dimensional information, whereas instant rewards of the agents is generally able to impart significant improvements in the searching process [21]. In [23], it is shown that using Markov decision process improves the efficiency of locating video frames in a video, and in [24], the distribution of visual words of multimedia data is found to be probabilistic in relation to the concept relationship formed [24]. Users often allocate the results based on some form of scoring metrics; for example, a linear combination of posterior probability is employed to refine the search results [25]. In reinforcement learning, an agent learns through the interaction with the dynamic environment to maximize its long-term rewards, in order to act optimally. Most of the time, when modeling real-world problems, the environment involved is non-stationary and noisy [3][4][6]. More precisely, the next state results from taking the same action in a specific state may not necessarily be the same but appears to be stochastic [2][7][31][32][33][34][35]. And the exploration strategies adopted in different categories of reinforcement learning algorithms provide different levels of control to the exploration of unknown factors, which in turn give various possibilities to the learning outcomes. Hence, the observed rewards and punishments are often non-deterministic. For example, when one is trying to find a video for performing a particular task, a shortening of the searching time with respect to some anticipated norm may be regarded as a reward, while a lengthening of the same may be viewed as punishment. Likewise, when one is exploring a new advertising channel, a resultant significant increase in sales may be viewed as a reward, while failure to do so may be regarded as punishment. In situations like these, there are stochastic elements governing the underlying environment. In the new route to work example, whether one receives rewards or punishments depends on a variety of chance factors, such as weather condition, day of the week, and whether there happens to be traffic delays or road works.

The effect of noise in multimedia data is generally numerous and cannot be known or enumerated in a practical

sense, and these tend to mask the underlying pattern. Indeed, if stochastic elements are absent, the learning problems involved could be greatly simplified and their presence has motivated early research in the area. As early as 1990s, mainstream research in reinforcement learning, such as the survey assessing existing methods carried out by Kaelbling *et al.* [2], adopts the common assumption of a stationary environment within a reinforcement learning framework. Later on, with further advances in reinforcement learning, theoretical analyses addressing the concern of non-stationary environment attracted great interests. One of the works by Brafman and Tennenholtz introduces a model-based RL algorithm R-Max to deal with stochastic games [5]. Such stochastic elements can notably increase the complexity in multi-agent systems and multi-agent tasks, where agents learn to cooperate and compete simultaneously [6][10]. Autonomous agents are required to learn new behaviors online and predict the behaviors of other agents in multi-agent systems. As other agents adapt and actively adjust their policies, the best strategy for each agent would evolve dynamically, giving rise to non-stationarity [8][9].

For most of the aforementioned scenarios, the cost of a trial or observation to receive either a reward or punishment can be significant, and preferably, one would like to arrive at the correct conclusion by incurring minimum cost. In the case of the advertising example, the cost of advertising can be considerable and one would therefore like to minimize it while acquiring the knowledge whether such advertising channel is effective. Similarly, in reinforcement learning algorithms, we are always in the hope to rapidly converge to an optimal strategy with least volumes of data, calculations, learning iterations, and minimal degree of complexity [11][12]. To do so, one should explicitly define the stopping rules for specifying the conditions under which learning should terminate and a conclusion drawn as to whether the learning has been successful or not based on the observations so far.

The issue of finding termination conditions, or stopping rules, is an intensive research topic in reinforcement learning, which is closely linked to the problems of optimal policies and policy convergence [13]. Traditional reinforcement learning algorithms mainly aim for relatively small-scale problems with finite states and actions. The stopping rules involved are well-defined for each category of algorithms, such as utilizing Bellman Equation in  $Q$ -learning [14]. To deal with continuous action spaces or state spaces, new algorithms, such as the Cacla algorithm [15] and CMA-ES algorithm [16], are developed with specific stopping criteria. Still, most studies on stopping criteria are algorithm-oriented and do not have a unified measurement for comparison purposes.

In this study, we present an approach to reinforcement learning by using a naïve Bayes classification framework, which explicitly incorporates the stochastic aspects of the environment in multimedia information search and retrieval. Applying naïve Bayes methods for classification problems are often employed in a variety of contexts [26][36], such as crowdsourcing and police surveillance. Here, we shall also learn and estimate the underlying stochastic structure of the environment by making use of the random classification labels gathered in the course of the learning process.

The structure of this paper is organized as follows. Section II presents a unified framework in the probabilistic classification of binary outcomes, and key measures of performance are derived, while the estimation of parameters is described in Section III. Section IV views competing classification outcomes as a stochastic game involving multi-agents. Sections V and VI respectively apply the results to the performance analysis of network communications and multimedia search.

## II. A PROBABILISTIC FRAMEWORK AND FUNDAMENTAL STRATEGIES

We consider a binary classification problem with two class labels, 1 or 0, where for convenience the former is referred to as a success, and the latter, a failure. A success yields a positive outcome and may be referred to as a positive classification, while a failure may be referred to as a negative classification. We are interested in determining whether the sequential classifications indicate overall success or failure in the classification process. Evidently, if the number of 1-labels gathered is much greater than the number of 0-labels, then the conclusion drawn should be success, while if the opposite is true, then the corresponding conclusion should be failure. In order to proceed with the analysis, we first let  $p$  and  $q$  (with  $p + q = 1$ ) denote the probabilities of receiving a 1-label or 0-label respectively for a given classification. Furthermore, we shall make use of the naïve Bayes property that different classifications are independent of each other. Later on, we shall derive estimates for  $p$  and  $q$ , which capture the stochastic structure of the environment. For example, if  $p > q$ , then clearly the final conclusion should be success. An error often committed is that when the first few observations are all 0, one would terminate prematurely and return a verdict of failure. Let us consider the following termination strategy; such a strategy is also studied in [26][36] and is called majority voting.

**Strategy A:** *On accumulating a total of  $r$  labels all belonging to either 1 or 0, the process terminates and a decision is made in accordance with the accepted margin of the majority of voting of the classifiers.*

Here, we let the random variable  $X$  represent the number of classification labeling preceding the first positive classification; i.e.,  $X$  may be viewed as the waiting time to the first positive classification,

$$\Pr[X = k] = pq^k, \quad k = 0, 1, 2, 3, \dots \quad (1)$$

The probability generating function  $G(z)$  of  $X$  is given by

$$G(z) = \sum_{k=0}^{\infty} \Pr[X = k] z^k$$

$$= p \sum_{k=0}^{\infty} q^k z^k = \frac{p}{(1 - qz)}. \quad (2)$$

Note this is a regenerative process in that after the occurrence of the first positive classification, the process probabilistically repeats itself again, so that we have for the waiting time  $\mathbf{W}_r$  of the  $r$ th positive classification

$$\mathbf{W}_r = \sum_{k=1}^r \mathbf{X}_k, \quad (3)$$

where each  $\mathbf{X}_k$  has the same distributional characteristics as  $\mathbf{X}$ . From [17], the probability generating function of  $G_r(z)$  corresponding to  $\mathbf{W}_r$  may be obtained

$$\begin{aligned} G_r(z) &= G_1(z)^r \\ &= \left[ \frac{p}{(1 - qz)} \right]^r. \end{aligned} \quad (4)$$

To gain a better understanding of behavior specified above, it is useful to obtain the average waiting time  $\mathbf{W}_r$  and its variance when  $r$  positive labels are attained. From (4), the mean and variance of  $\mathbf{W}_r$  can be derived

$$E[\mathbf{W}_r] = G'_r(1) = \frac{rq}{p}, \quad (5)$$

$$\text{Var}[\mathbf{W}_r] = G''_r(1) + G'_r(1) - G'_r(1)^2 = \frac{rq}{p^2}. \quad (6)$$

Moreover, the probabilities  $\text{Pr}[\mathbf{W}_r = k]$  may be readily obtained from the expansion of (4) so as to study the probabilities for various waiting time,

$$\text{Pr}[\mathbf{W}_r = k] = \binom{-r}{k} p^r (-q)^k, \quad k = 0, 1, 2, 3, \dots \quad (7)$$

We note that, while  $-r$  appears as a negative integer in the binomial coefficient, the entire expression is actually non-negative [18]. Since  $\mathbf{W}_r$  is the sum of independent identically distributed random variables, when  $r$  is appreciable, it may be approximated by the normal distribution [17]

$$\mathbf{W}_r \sim N\left(\frac{rq}{p}, \frac{rq}{p^2}\right), \quad (8)$$

whence we have, denoting by  $\Phi$  the standard normal distribution,

$$\text{Pr}[\mathbf{W}_r > b] = \int_{\frac{bp - rq}{\sqrt{rq}}}^{\infty} \frac{1}{\sqrt{2\pi}} e^{-\frac{t^2}{2}}$$

$$= 1 - \Phi\left(\frac{bp - rq}{\sqrt{rq}}\right). \quad (9)$$

We next consider a more stringent strategy whereby consecutive occurrence of labels is required. As we shall see, it would take much longer to complete the process in Strategy B than in Strategy A.

**Strategy B:** *On the occurrence of  $m$  consecutive labels all belonging to either 1 or 0, the process terminates and a decision is made in accordance with the accepted margin of the majority of voting of the classifiers.*

To establish the results for this second case, we shall first derive the probability of occurrence of the event corresponding to Learning Strategy B *for the first time*. Let  $b_n$  be the probability that  $m$  consecutive positive rewards occurs at trial  $n$ , with  $n \geq m$ , not necessarily for the first time, and we denote by  $B(z)$  be the corresponding probability generating function. From [17], this probability generating function can be obtained as

$$B(z) = \frac{1 - z + qp^m z^{m+1}}{(1 - z)(1 - p^m z^m)}. \quad (10)$$

Since we need to obtain the corresponding generating function for the probability that the associated event occurs for the first time, we need to consider the relationship between the two events. We shall use the random variable  $\mathbf{V}_m$  to denote the number of plays preceding and including the receiving of the first set of  $m$  consecutive positive rewards, and we let  $a_n$  be the probability

$$a_n = \text{Pr}[\mathbf{V}_m = n], \quad n = m, m + 1, \dots \quad (11)$$

We denote by  $A(z)$  the probability generating function for the event that the accumulation of  $m$  positive rewards occurs for the first time. It can be shown in [17] that the generating function  $A(z)$  is related to  $B(z)$  by

$$A(z) = \frac{B(z) - 1}{B(z)}. \quad (12)$$

From this, we obtain, after simplification,

$$A(z) = \frac{p^m z^m}{1 - q^m \sum_{k=0}^{m-1} p^k z^k}. \quad (13)$$

From this, the mean and variance of  $\mathbf{V}_m$  can be readily obtained after simplification,

$$E[\mathbf{V}_m] = A'(1) = \frac{1 - p^m}{qp^m}, \quad (14)$$

$$\text{Var}[\mathbf{V}_m] = A''(1) + A'(1) - A'(1)^2$$

$$= \frac{1}{q^2 p^{2m}} - \frac{2m+1}{qp^m} - \frac{p}{q^2}, \quad (15)$$

It is interesting to compare Strategies A and B. It is evident that Strategy B is more stringent than Strategy A, since for  $m=r$ , obtaining  $m$  consecutive labels necessarily implies obtaining  $m$  total labels. Acquiring consecutive labels implies for example that, once a 1-label is acquired, no 0-label from that point is tolerated until all  $m$  1-labels are accumulated. Thus, when a 0-label arises, it may be interpreted as having the effect of cancelling out any previous 1-label, and the same applies to the commencement of the 0-label.

$$\rho(p) = \frac{E[W_r]}{r} = \frac{q}{p}. \quad (16)$$

From the above relationship, we can determine the inherent stochastic structure of the environment by estimating  $p$  from actual observed labels ratio  $W/r$ , where  $W$  is the sample mean of  $W_r$ . We can then form our estimator from the above just by solving for  $p$ . We shall estimate the probability  $P_b$  that the learning cost for this component exceeding this bound. From (7) above, this is given by

$$P_b = 1 - \sum_{k=0}^b \Pr[W_r = k] \\ = 1 - \sum_{k=0}^b \binom{-r}{k} p^r (-q)^k. \quad (17)$$

Here, the normal approximation can be invoked. In many reinforcement learning episodes,  $r$  tends to be under 100, as a lengthy iteration time is not feasible and most learning algorithms aim to converge in minimum time.

Clearly, the selection of the maximum cost weight  $b$  will have a significant impact on  $P_b$ . Very often, it is more meaningful to relate  $b$  to  $E[W_r]$  either additively or multiplicatively. Table I tabulates the values of  $P_b$  for different values of  $b$ . The first part of Table I considers  $b$  by adding a fixed value  $d$ , with  $d = 5$  and  $d = 10$ , while the second part considers  $b$  by multiplying by a fixed multiple  $\alpha$ , with  $\alpha = 1.2$  and  $\alpha = 1.5$ ; here,  $b$  is rounded to the nearest integer. In the first part of Table I, we see that for either value of  $r$ , when  $p$  is appreciably greater than  $q$ , the probability of exceeding cost bounds tends to be acceptably small, and this is especially so for  $r = 20$ . The reason is that, since  $d$  is a fixed value, its relative contribution to  $b$  increases as  $p$  increases, produces a relatively large cost bound weight compared to the average one, and accordingly lowers the probability of exceeding the bound. However, in the second part of Table I, the difference between  $E[W_r]$  and  $b$  decreases as  $E[W_r]$  decreases, so that  $P_b$  tends to be large for higher values of  $p$ .

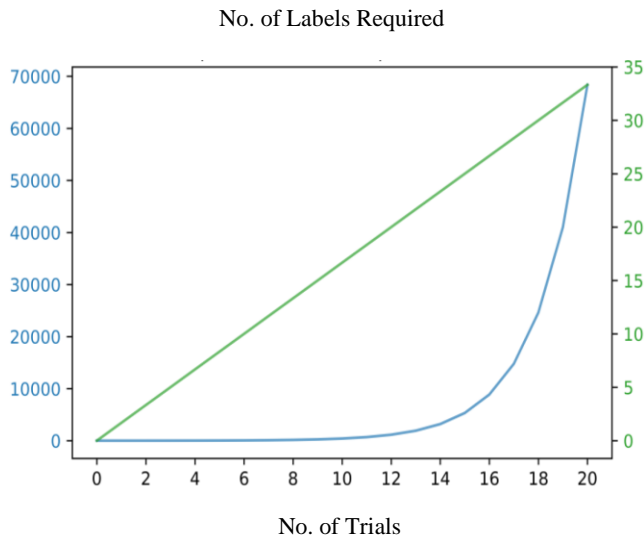


Fig. 1. Cost Comparison of Strategy A and Strategy B ( $p = 0.6$ ).

Figure 1 compares the average cost of play of Strategy A and Strategy B. Here, the left vertical axis is used for  $E(V_m)$  with an appropriate scale, while, the right vertical axis is used for  $E(W_r)$ . We see that the stringency of Strategy B is manifested in a steep climb in the number of trials as  $m$  increases, as opposed to a relatively moderate increase in Strategy A.

Depending on the outcomes of labelling, since Strategies A and B govern the time when the observation process terminates and accompanied by a decision being made, the underlying process may be regarded as a learning episode whereby a labelling is learned from the observations. Therefore, Strategies A and B may also be understood as learning strategies, and a resultant label of 1 would be referred to as learning success, whereas a resultant label of 0 would be referred to as learning failure.

### III. THE RATIO OF CLASS LABELS AND LEARNING SUCCESS

We denote by  $p$  the ratio of the average number of negative labels to the number of positive labels; thus

TABLE I. ANALYSIS OF PROBABILITIES OF EXCEEDING COST BOUNDS

$b$ Formula	$r$	$p$	$q$	$E[W_r]$	$b$	$P_b$	$P_b'$	$Err$
$b = E[W_r] + d$ ( $d = 5$ )	20	0.5	0.5	20.00	25	0.215	0.186	0.029
		0.8	0.2	5.00	10	0.023	0.026	0.003
		0.9	0.1	2.22	7	0.001	0.004	0.003
	50	0.5	0.5	50.00	55	0.309	0.279	0.030
		0.8	0.2	12.50	17	0.127	0.108	0.019
		0.9	0.1	05.56	11	0.014	0.017	0.003
$b =$	20	0.5	0.5	20.00	30	0.057	0.059	0.002

$b$ Formula	$r$	$p$	$q$	$E[W_r]$	$b$	$P_b$	$P_b'$	$Err$
$E[W_r] + d$ ( $d = 10$ )		0.8	0.2	5.00	15	0.000	0.001	0.001
		0.9	0.1	2.22	12	0.000	0.000	0.000
	50	0.5	0.5	50.00	60	0.159	0.147	0.012
		0.8	0.2	12.50	22	0.008	0.011	0.003
		0.9	0.1	05.56	16	0.000	0.000	0.000
$b = \alpha E[W_r]$ ( $\alpha = 1.2$ )	20	0.5	0.5	20.00	24	0.264	0.226	0.038
		0.8	0.2	5.00	6	0.345	0.253	0.092
		0.9	0.1	2.22	2	0.556	0.380	0.176
	50	0.5	0.5	50.00	50	0.159	0.147	0.012
		0.8	0.2	12.50	15	0.264	0.215	0.049
		0.9	0.1	05.56	7	0.280	0.207	0.073
$b = \alpha E[W_r]$ ( $\alpha = 1.5$ )	20	0.5	0.5	20.00	30	0.057	0.059	0.002
		0.8	0.2	5.00	7	0.212	0.156	0.056
		0.9	0.1	2.22	3	0.310	0.193	0.117
	50	0.5	0.5	50.00	75	0.006	0.010	0.004
		0.8	0.2	12.50	19	0.050	0.048	0.002
		0.9	0.1	05.56	8	0.163	0.121	0.042

In Table I, column  $P_b'$  gives the exact calculation using (17), while column  $P_b$  employs the normal approximation using (9). The absolute error between the exact calculation and the normal approximation is given by column  $Err$ . We see that the normal approximation is quite acceptable in most cases with absolute error less than 0.1. Note that no matter whether having  $b$  additively or multiplicatively related to  $E[W_r]$ , a higher value of  $d$  or  $\alpha$  always gives smaller absolute error. We therefore suggest that the approximation should only be used when  $r$ ,  $d$  and  $\alpha$  are sufficiently large.

#### IV. A LEARNING FRAMEWORK BASED ON COMPETING MULTI-AGENTS

In Learning Strategies A and B above, the termination of a learning episode is triggered whenever a fixed number of positive labels  $r$  is obtained, irrespective of the number of negative labels accumulated in the process of doing so. Sometimes, however, this may not be desirable, especially when an inordinate number of negative labels have been accumulated, in which case, termination should take place earlier along with the conclusion of learning failure. Therefore, one is comparing the number of positive labels gathered against the number of negative labels, and the learning is concluded as success or failure according to which of these achieve the majority.

More precisely, this may be viewed as a multi-agent tournament with two competing agents  $A_1$  and  $A_2$ , in which  $A_1$  is responsible for giving out the positive labels, while  $A_2$ , the negative labels (respectively the 1 and 0 labels). This framework is not unlike the game theoretic approach in statistical decision theory, where both the statistician and

nature are regarded as players in the game of estimation, and also this may be regarded as a kind of stochastic game involving agents [5][28][30]. While we shall focus on the agents  $A_1$  and  $A_2$ , we note that there is a further agent, the learner, so that three agents exist in this situation. Here, when a classification results in a positive labels, then  $A_1$  would gain a score of one, while when an observation results in a negative labels, then  $A_2$  would gain a score of one. When either 1 or 0 label first reaches a given threshold  $h$ , then this will trigger a termination and the learning episode is concluded as success or failure according to which agent attains the threshold score first. Therefore, we have the following Learning Strategy.

**Strategy C:** *The learning process terminates when either agent,  $A_1$  or  $A_2$ , first reach the threshold of either accumulating  $h$  labels of 1, or accumulating  $h$  labels of 0, which can then be concluded as a success or a failure according to which agent attains the threshold first.*

Here, without loss of generality, we shall let  $h = 2m+1$  be odd, where  $m$  is an integer, and similar to Section II, we let  $p$  and  $q$ , with  $p + q = 1$ , signify the probabilities of receiving a positive labels, and negative labels, respectively for a particular classification. In other words, for a given classification, agent  $A_1$  wins with probability  $p$ , while agent  $A_2$  wins with probability  $q$ . In order to attain  $h$  for either agent, the number of classifications  $\Omega$  will fall within the range

$$2m + 1 \leq \Omega \leq 4m + 1.$$

If  $f_k$  represents the probability that  $A_1$  wins at classifications number  $4m+1-k$ , which occurs if and only if  $A_1$  scored  $2m$  successes in the first  $4m-k$  observations, and subsequently score a final success, then  $f_k$  is given by

$$f_k = \binom{4m-k}{2m} p^{2m+1} q^{2m-k}.$$

The probability that  $A_1$  reaches the threshold first, irrespective of the classification number, is therefore given by

$$P_m = \sum_{k=0}^{2m} f_k = \sum_{k=0}^{2m} \binom{4m-k}{2m} p^{2m+1} q^{2m-k}.$$

That is,  $P_m$  gives the probability that the learning is successful (i.e., agent  $A_1$  wins) according to Learning Strategy C.

Table II computes  $P_m$  for different values of  $p$ ,  $q$ , and  $m$  for this tournament scenario. We see that, as expected, when  $p = q = 1/2$ ,  $P_m = 1/2$ , since neither  $A_1$  nor  $A_2$  has any advantage over its opponent. As  $p$  increases, however,  $P_m$  will increase, reaching almost certainty as  $p$  increases beyond 0.8. If we regard  $p$  as a measure of  $A_1$ 's winning ability per trial, then when  $p \gg q$ , most trials will be scored by  $A_1$ , so that winning the entire game (i.e., reaching  $h$  first) is almost a certainty, and this is especially so for higher values of  $h$ . It is interesting to see that when  $h$  or  $m$  is sufficiently high (e.g.,  $m=10$ ), a moderate advantage for  $A_1$  (e.g.,  $p = 0.6$ ) is enough to almost

guarantee success. On the other hand,  $1-P_m$  gives the probability that agent  $A_2$  wins, where the measure of  $A_2$ 's winning probability per trial is given by  $q$ . For instance, when  $q=0.4$ , then  $A_2$  stands a chance of around 27% of winning the game when  $m=2$ , and a chance of winning of around 10% when  $m=10$ .

TABLE II. PROBABILITIES OF LEARNING SUCCESS FOR THE TOURNAMENT SCENARIO

$m$	$p$	$q$	$P_m$	$m$	$p$	$q$	$P_m$
1	0.5	0.5	0.5000	5	0.5	0.5	0.5000
	0.6	0.4	0.6826		0.6	0.4	0.8256
	0.7	0.3	0.8369		0.7	0.3	0.9736
	0.8	0.2	0.9421		0.8	0.2	0.9990
	0.9	0.1	0.9914		0.9	0.1	1.0000
2	0.5	0.5	0.5000	10	0.5	0.5	0.5000
	0.6	0.4	0.7334		0.6	0.4	0.9035
	0.7	0.3	0.9012		0.7	0.3	0.9964
	0.8	0.2	0.9804		0.8	0.2	1.0000
	0.9	0.1	0.9991		0.9	0.1	1.0000

Returning to the estimation problem, by observing  $P_m$ , i.e., by computing the observed proportion of time that agent  $A$  wins, it is possible to infer the underlying probability  $p$ . While unlike in Section II, where an explicit formula exists linking directly the observations to the estimate, such explicit relationship is not available here. Nevertheless, as can be observed from Table II, useful estimation bounds can be drawn to determine whether  $p > 1/2$  or  $p < 1/2$ . We see that it is quite reasonable to estimate  $\hat{p} > 1/2$  whenever  $P_m > 1/2$ , and for most practical purposes, this would seem to be adequate.

In what follows, we shall apply the above analysis to network communications and the indexing of multimedia objects. While there are many situations that conform to the above framework such as those mentioned in the introduction, these particular applications are chosen partly because of their importance and partly because of their relevance to information processing in the present day big data era.

## V. APPLICATION TO PACKET SWITCHING

In packet switching, suppose we wish to transmit a number of data packets over a noisy channel, where a successful error-free transmission occurs with probability  $p$ , and an erroneous transmission occurs with probability  $q = 1 - p$ . An erroneous transmission may, for example, be detected from the error-detection mechanisms when a packet is corrupted by random noise. Where the error-correction mechanism is able to correct the error despite the noise, the packet is regarded as a success, and this is incorporated into the probability  $p$ . For a message  $D$  consisting of  $r$  packets, we measure communications performance by examining the total number of transmissions required to achieve successful transmission of the entire

message  $D$ . Let  $T_1$  be the time taken to successfully transmit a message consisting of  $r$  packets. An obvious analogy exists between the present situation and the multimedia information indexing situation above with respect to Learning Strategy A: we need a total of  $r$  classification of label 1 in order to achieve success. Consequently, we have the following results. Given a message consisting of  $r$  data packets, the total number of (error-free and erroneous) transmissions required in order to achieve a successful transmission of the entire message has mean and variance

$$E[T_1] = \frac{rq}{p}, \quad (18)$$

$$\text{Var}[T_1] = \frac{rq}{p^2}. \quad (19)$$

Moreover, the probabilities  $\Pr[T_1 = k]$  is given by,

$$\Pr[T_1 = k] = \binom{-r}{k} p^r (-q)^k, \quad k = 0, 1, 2, 3, \dots \quad (20)$$

This may be determined approximately by the normal distribution [17]

$$T_1 \sim N\left(\frac{rq}{p}, \frac{rq}{p^2}\right), \quad (21)$$

and,

$$\begin{aligned} \Pr[T_1 > t] &= \int_{\frac{tp-rq}{\sqrt{rq}}}^{\infty} \frac{1}{\sqrt{2\pi}} e^{-\frac{t^2}{2}} \\ &= 1 - \Phi\left(\frac{tp-rq}{\sqrt{rq}}\right). \end{aligned} \quad (22)$$

Next, suppose we have a message  $D$  broken up into  $m$  packets, and perhaps due to the error detection/correction or other requirements, it needs  $m$  consecutive successful transmissions to complete the entire transmission. In this situation, we again measure performance by examining the total number of transmissions required to achieve successful transmission of the entire message  $D$ . Let  $T_2$  be the time taken to successfully transmit the entire message consisting of  $m$  packets. Again, an analogy exists between the present situation and the multimedia information indexing situation above with respect to Learning Strategy B. Consequently, we have the following results.

$$E[T_2] = \frac{1-p^m}{qp^m}, \quad (23)$$

$$\text{Var}[T_2] = \frac{1}{q^2 p^{2m}} - \frac{2m+1}{qp^m} - \frac{p}{q^2}. \quad (24)$$

## VI. APPLICATION TO MULTIMEDIA SEARCH AND INDEXING

Many large enterprises rely on multimedia document repositories for their effective operation. However, unlike text-oriented objects, the retrieval of multimedia objects is often limited in their search and discovery mechanisms, since they do not readily lend themselves to automatic processing or indexing. The basic framework of the adaptive search mechanism is to capture human judgment in the course of normal usage from user queries in order to develop semantic indexes which link search terms to media objects semantics. This approach is particularly effective for the retrieval of such multimedia objects as images, sounds, and videos, where a direct analysis of the object features does not allow them to be linked to search terms, such as non-textual/icon-based search, deep semantic search, or when search terms are unknown at the time the media repository is built. The above model is able to represent such an adaptive search mechanism by making use of naïve Bayes classification approach based on the three learning strategies indicated. This approach allows for the efficient creation and updating of media indexes, which is able to instill and propagate deep knowledge relating to the enterprise functions into the media management system concerning the advanced search and usage of multimedia resources.

Thus, the above positive and negative classifications may be viewed as a learning sequence in multimedia indexing acquired from user interaction. Here, we are concerned with the status of the association of given search terms to particular multimedia objects. Through the interaction with users, positive and negative labels are handed out probabilistically. In the case of search terms to multimedia objects association, learning success would mean that the association in question is sound and should be incorporated as proper index, while failure would mean that the search term-object association cannot be established.

Similar to the previous application, the time to install an index term based on Strategy A would take a time of  $I_1$ , with mean and variance given by

$$E[I_1] = \frac{rq}{p}, \quad (25)$$

$$\text{Var}[I_1] = \frac{rq}{p^2}. \quad (26)$$

In addition, we have,

$$\Pr[I_1 = k] = \binom{-r}{k} p^r (-q)^k, \quad k = 0, 1, 2, 3, \dots \quad (27)$$

Similarly, the time  $I_2$  to install an index term based on Strategy B has mean and variance

$$E[I_2] = \frac{1-p^m}{qp^m}, \quad (28)$$

$$\text{Var}[I_2] = \frac{1}{q^2 p^{2m}} - \frac{2m+1}{qp^m} - \frac{p}{q^2}. \quad (29)$$

Furthermore, from Section IV, under Learning Strategy C with threshold  $h$ , the probability of successful installation of an index term is given by

$$\sum_{j=0}^{h-1} \binom{2h-j-2}{h-1} p^h q^{h-j-1}.$$

## VII. CONCLUSION AND FUTURE EXTENSION

We have presented a model of binary classification, operating in a stationary stochastic environment in the presence of noise. Stochastic methods are essential because various operating environments are often noisy and seldom static nor deterministic, and the use of probabilistic methods is therefore an unavoidable necessity. Indeed, if stochastic elements are absent, the same outcome will always occur, and repeated observations, and hence repeated reinforcements, are unnecessary. A unified probabilistic framework is developed for such a classification scenario. We first consider a situation where the cumulative number of classifications is pre-specified and fixed, which constitute the criterion for terminating the learning process. Two variations of this process are considered, one requires non-consecutive reinforcements and the other requires consecutive reinforcements. By observing the random positive to negative labels ratio, a meaningful estimation of either learning success or failure may be arrived at. In most practical situations, the cost of securing a classification can be significant, and this has been incorporated into our model, and we have obtained the probabilities of exceeding the classifications cost bounds.

A multi-agent framework where the handing out of positive and negative labels are viewed as being performed by agents have also been considered. Thus, the final learning outcome is determined by a kind of stochastic game with the agents competing against each other. The termination criterion here is determined by when and how the game is won. The respective probabilities of learning success and failure are also explicitly derived. Closed-form expressions of other relevant measures of interest are obtained. A procedure for estimating the underlying stochastic structure from the observed random agent winning frequencies is also developed.

The above results and algorithms have been applied to study the performance of human-assisted semi-automatic multimedia information indexing as well as to quantify communications network transmission performance operating in a noisy channel.

In this paper, we have employed the naïve Bayes assumption and assumed that positive labels and negative labels occur statistically independently. In the future, it may be more general to relax this assumption and incorporate different forms of dependencies into the model, such as single-step or multi-step Markov Chain conditional dependency.

## REFERENCES

- [1] C. H. C. Leung and Y. Tong, "Application of learning reinforcement classification to network communications and multimedia search", *Proc. International Conference on Advanced Engineering Computing and Applications in Sciences, ADVCOMP 2021*, Spain, 3-7 October, 2021.
- [2] M. Kearns and S. Singh, "Near-optimal reinforcement learning in polynomial time," *In Int. Conf. on Machine Learning*, 1998.
- [3] L. P. Kaelbling, M. L. Littman, and A. W. Moore, "Reinforcement learning: a survey" *Journal of artificial intelligence research*, vol. 4, pp. 237-285, 1996.
- [4] B. D. Ziebart, A. L. Maas, J. A. Bagnell, and A. K. Dey, "Maximum Entropy Inverse Reinforcement Learning," *Proc. Twenty-Third AAAI Conference on Artificial Intelligence (AAAI 08)*, vol. 8, pp. 1433-1438, 2008.
- [5] H. Santana, G. Ramalho, V. Corruble, and B. Ratitch, "Multi-agent patrolling with reinforcement learning," *Proc. Third International Joint Conference on Autonomous Agents and Multiagent Systems*, vol. 3, pp. 1122-1129, IEEE Computer Society, 2004.
- [6] R. I. Brafman and M. Tennenholtz, "R-max-a general polynomial time algorithm for near-optimal reinforcement learning," *Journal of Machine Learning Research*, vol.3, pp. 213-231, 2002.
- [7] L. Panait and S. Luke, "Cooperative multi-agent learning: The state of the art," *Autonomous agents and multi-agent systems*, vol. 11, no. 3, pp. 387-434, 2005.
- [8] E. Ipek, O. Mutlu, J. F. Martínez, and R. Caruana, "Self-optimizing memory controllers: A reinforcement learning approach," *ACM SIGARCH Computer Architecture News*, vol. 36, no. 3, IEEE Computer Society, 2008.
- [9] L. Busoniu, R. Babuska, and B. De Schutter, "A comprehensive survey of multiagent reinforcement learning," *IEEE Transactions on Systems, Man, And Cybernetics-Part C: Applications and Reviews*, vol. 38, no. 2, 2008.
- [10] S. V. Albrecht and P. Stone, "Autonomous agents modelling other agents: A comprehensive survey and open problems," *Artificial Intelligence* 258, pp. 66-95, 2018.
- [11] A. Tampuu, T. Matiisen, D. Kodelja, I. Kuzovkin, K. Korjus, J. Aru, and R. Vicente, "Multiagent cooperation and competition with deep reinforcement learning," *PLoS one*, vol. 12, no. 4: e0172395, 2017.
- [12] A.W. Moore and C.G. Atkeson, "Prioritized sweeping: Reinforcement learning with less data and less time," *Machine learning*, vol. 13, no.1, pp. 103-130, 1993.
- [13] E. Brochu, V. M. Cora, and N. De Freitas, "A tutorial on Bayesian optimization of expensive cost functions, with application to active user modeling and hierarchical reinforcement learning," unpublished.
- [14] Q. Wei, F. L. Lewis, Q. Sun, P. Yan, and R. Song, "Discrete-time deterministic Q-learning: A novel convergence analysis," *IEEE Transactions on Cybernetics*, vol. 47, no. 5, pp. 1224-1237, 2017.
- [15] C. J. Watkins and P. Dayan, "Q-learning," *Machine learning* 8.3-4 pp. 279-292, 1992.
- [16] H. Van Hasselt and M.A. Wiering, "Using continuous action spaces to solve discrete problems," *Proc. International Joint Conference on Neural Networks (IJCNN 09)*, pp. 1149-1156. IEEE, 2009.
- [17] N. Hansen, S. D. Müller, and P. Koumoutsakos, "Reducing the time complexity of the derandomized evolution strategy with covariance matrix adaptation (CMA-ES)," *Evolutionary computation*, vol. 11, no. 1 pp. 1-18, 2003.
- [18] W. Feller, *An Introduction to Probability Theory and its Applications*, Vol. 1, 3rd Edition, Wiley & Sons, 1968.
- [19] Q. Huang, A. Puri, and Z. Liu. "Multimedia search and retrieval: new concepts, system implementation, and application". *IEEE Transactions on circuits and systems for video technology*, 2000, 10.5: 679-692.
- [20] R.Gupta, M. Khomami Abadi, J. A.Cárdenes Cabré, F.Morreale, T. H. Falk, and N. Sebe, "A quality adaptive multimodal affect recognition system for user-centric multimedia indexing". *Proc. ACM International Conference on Multimedia Retrieval*. ACM, p. 317-320, 2016.
- [21] K. Arulkumaran, M. P. Deisenroth, M. Brundage, and A. Bharath, "Deep reinforcement learning: A brief survey," *IEEE Signal Processing Magazine*, 34(6), 26-38, 2017.
- [22] X. Yao, J. Du, N. Zhou, and C. Chen, "Microblog Search Based on Deep Reinforcement Learning," *In Proceedings of 2018 Chinese Intelligent Systems Conference* (pp. 23-32). Springer, Singapore, 2019.
- [23] Y.C. Wu, T. H.Lin, Y. D. Chen, H. Y Lee, and L. S. Lee, "Interactive spoken content retrieval by deep reinforcement learning". arXiv preprint arXiv:1609.05234, 2016.
- [24] S. Lan, R. Panda, Q. Zhu, and A. K. Roy-Chowdhury, "FFNet: Video fast-forwarding via reinforcement learning", *In Proceedings of the IEEE Conference on Computer Vision and Pattern Recognition*, pp. 6771-6780, 2018.
- [25] R. Hong, Y. Yang, M. Wang, and X. S. Hua, "Learning visual semantic relationships for efficient visual retrieval", *IEEE Transactions on Big Data*, 1(4), 152-161, 2015.
- [26] R. Yan, A. Hauptmann, and R.Jin, "Multimedia search with pseudo-relevance feedback. In International Conference on Image and Video Retrieval" (pp. 238-247). Springer, Berlin, Heidelberg, 2003.
- [27] E. Manino, L. Tran-Thanh, and N. R. Jennings. "On the Efficiency of Data Collection for Multiple Naïve Bayes Classifiers," *Artificial Intelligence*, 275: 356-378, 2019.
- [28] J. Deng and C. H. C. Leung, "Dynamic Time Warping for Music Retrieval Using Time Series Modeling of Musical Emotions," *IEEE Transactions on Affective Computing*, Vol. 6, No. 2, pp. 137-151, 2015.
- [29] H. L. Zhang, C. H. C. Leung, G. K. Raikundalia, "Topological analysis of AOCD-based agent networks and experimental results." *Journal of Computer and System Sciences*, pp. 255-278, 2008.
- [30] I. Azzam, C. H. C. Leung, J. Horwood, "Implicit concept-based image indexing and retrieval." *In Proceedings of the IEEE International Conference on Multi-media Modeling*, pp. 354-359, Brisbane, Australia 2004.
- [31] H. Zhang, C. H. C. Leung and G. K. Raikundalia, "Classification of intelligent agent network topologies and a new topological description language for agent networks." *In Proceedings of the 4th International Conference on Intelligent Information Processing*, Adelaide, Australia, pp. 21-31 2006.
- [32] N. L. J. Kuang, C. H. C. Leung, and V. Sung, "Stochastic Reinforcement Learning." *In Proc. IEEE International Conference on Artificial Intelligence and Knowledge Engineering*, pp. 244-248, California, USA 2018.
- [33] N. L. J. Kuang and C. H. C. Leung, "Performance Dynamics and Termination Errors in Reinforcement Learning - A Unifying Perspective," *In Proc. IEEE International Conference on Artificial Intelligence and Knowledge Engineering*, pp. 129-133, California, USA 2018.
- [34] V. Sutton *et.al.*, "Multi-armed bandit algorithms and empirical evaluation," *In Proc. 16th European Conference on Machine Learning*, Springer, Porto, Portugal, pp. 437-448, 2005.

- [35] N. L. J. Kuang and C. H. C. Leung, "Analysis of Evolutionary Behavior in Self-Learning Media Search Engines," in *Proceedings of the 2019 IEEE International Conference on Big Data*, Los Angeles, USA, 2019.
- [36] N. L. J. Kuang and C. H. C. Leung, "Performance Effectiveness of Multimedia Information Search Using the Epsilon-Greedy Algorithm," in *Proceedings of the 2019 IEEE International Conference on Machine Learning and Applications*, pp. 929-936, Florida, USA 2019.
- [37] E. Manino, L. Tran-Thanh, and N. R. Jennings. "On the Efficiency of Data Collection for Crowdsourced Classification." In *Proceedings of the Twenty-Seventh International Joint Conference on Artificial Intelligence*, 1568-1575, 2018.

## Software Environment for Performance Simulation of Three-hop Wireless Relay Channels under the Influence of Rician Fading

Dragana Krstic

University of Niš,

Faculty of Electronic Engineering

Niš, Serbia

e-mail: dragana.krstic@elfak.ni.ac.rs

Petar Nikolic

TigarTyres

Pirot, Serbia

e-mail: nikipetar@gmail.com

Nenad Petrovic

University of Niš,

Faculty of Electronic Engineering

Niš, Serbia

e-mail: nenad.petrovic@elfak.ni.ac.rs

Zoran Popovic

Higher Technical School of Professional Studies,

Zvečan, Serbia

e-mail: z.popovix@live.com

Sinisa Minic

Faculty of Teacher Education in Prizren – Leposavic,

University of Pristina- Kosovska Mitrovica,

Serbia

e-mail: sinisa.minic@pr.ac.rs

**Abstract—** In this work, a three-hop wireless relay channels under the influence of Rician fading will be observed. Three-hop wireless relay system model is made as the product of three independent, but not necessarily identically distributed, Rician random variables. Some important wireless relay system performance of the first and second order, as cumulative distribution function, outage probability, level crossing rate and average fade duration will be determined and graphically presented. The impact of fading parameters will be highlighted based on presented graphs. Then, simulation software environment for modelling and planning the wireless three-hop relay systems performance under the influence of Rician fading will be described. The goal of this method is to minimize the transmission costs and provide the best possible Quality of Service for defined wireless transmission scenario.

**Keywords-** Graphics Processing Unit (GPU); linear optimization; random variables; Rician fading; system performance, three-hop relaying system.

### I. INTRODUCTION

Performance of three-hop wireless relay channels under the influence of fading have not yet been analyzed enough in available literature [1] - [5]. Different authors mainly analyze multi-hop relay systems with the application on dual-hop channels [6] - [8].

The multi-hop communication in relay systems is introduced for improving the quality of transmission in cellular and ad hoc networks because of transmit power limitations. The benefits of multi-hop relays are visible in rural areas with small population and low level of traffic density.

Multi-hop routing is the way of communication in radio networks where network coverage area is larger than radio range of single nodes [9]. So, to get to a destination, node can utilize other nodes as relays. This is also very justified for energy efficiency reasons. After the transceiver is the

major source of power consumption in a node, and transmission to long distance needs high power, in many cases multi-hop routing is more energy efficient than single-hop transmission [10], [11]. Hence, relay technologies have the potential to offer extended cell coverage, better energy efficiency and improved capacity over the next generation wireless networks.

In wireless environments, properties of communications systems are disturbed notably due to the signal envelope fluctuations based of the presence of multipath fading [12] [13]. Because of that, it is of substantial importance to characterize these random fluctuations in terms of the fading characteristics and derive the first and second order system performance [14], [15].

Although the existence of a direct path between the transmitter and the receiver, called line of sight (LOS), is not a prerequisite for wireless communication, in many modern applications, with the reduction of the coverage area there is a LOS between the transmitter and receiver. The Rician distribution is used to mathematically describe these propagation conditions with LOS. This is the reason we use this fading model in our paper.

Namely, we consider here a three-hop relay channel, as a special case of multi-hop relay channel, under the presence of Rician fading. This case is important for the environment where an optical LOS is present. By our opinion, there are not enough reported papers in available literature on this topic.

This paper consists of seven sections. In introduction, the main terms are defined. The literature review is presented in the second section. In the third section, the system model is shown. The first order characteristics of the product of three Rician random variables (RVs) are defined in the fourth section, but the second order characteristics of this product are presented the fifth one. The graphs for all performance are plotted and parameters analysis is done. In the sixth section, software environment for smart city mobile network

planning is introduced. The last section consists of concluding remarks.

## II. RELATED WORK

The closed-form expressions for the outage probability ( $P_{out}$ ), the channel capacity (CC), and also the average symbol error probability (ASEP) were calculated in [6] for amplify-and-forward (AF) multi-hop relay network in the presence of Rayleigh fading. The analytical expressions are obtained for some scenarios of dual-hop relay systems.

The output signal from multi-hop relay system is product of random variables at hops outputs. In [16], multi-hop system in the presence of Nakagami fading is analyzed through  $N$ \*Nakagami distribution as suitable for modeling of realistic wireless fading channels. Statistical analysis of cascaded Rician fading channels is given in [17]. Different performance is derived for both fading channels in terms of the Meijer G-function.

Our group of authors analyzed different products of RVs and obtained some system performance for dual and three-hop relay systems in closed forms in [3], [4], [18], [19]. Wireless dual-hop relay system in  $\kappa$ - $\mu$  short term fading environment is presented in [18]. An analytical approach for evaluating performance of dual-hop cooperative link over shadowed Ricean fading channels is shown in [19]. All performance of product of three Rayleigh RVs are presented in [3]. The product of three Nakagami- $m$  RVs is observed in [4] and some statistical characteristics are derived.

Three-hop system is also observed in [2]. The second order characteristics for such three-hop relay system were derived. The knowing of second-order statistics (level crossing rate (LCR) and average fade duration (AFD)) of multipath fading channels help in better understanding the effects of fading and then easier mitigation. As example, the AFD determines the average length of error bursts in fading channels [20]. So, in fading channels with relatively large AFD, long data blocks will be significantly affected by the channel fades than short blocks [21].

A knowledge of this fact is necessary for better choose of the frame length for coded packetized systems, designing interleaved or non-interleaved concatenated coding methods [22], optimizing the interleaver size, choosing the buffer depth for adaptive modulation schemes [23] [24], throughput (efficiency) estimation of communication protocols, and so on. Empirically-verified formulas for the LCR and AFD of common multipath fading models are necessary for all observed applications.

## III. SYSTEM MODEL

The observed three-hop communication system is illustrated in Fig. 1 [7]. It consists of a source node, marked by (S), sending the information signal to the destination, marked by (D), using two consecutive relays, signed by R1 and R2.

All nodes are equipped with a single antenna operating in half-duplex mode. The contiguous relays help delivering the information to the destination. This is valid when the network nodes are under heavy shadowing, or when the distance between terminals is large, and also when the nodes suffer limited power resources [7].

## IV. THE FIRST ORDER PERFORMANCE OF PRODUCT OF THREE RICIAN RANDOM VARIABLES

For description of three-hop wireless relay system it is necessary to derive the first-order characteristics of the product of three Rician RVs. In this context, PDF, CDF and  $P_{out}$  will be analyzed.

### A. PDF of Product of Three Rician RVs

Rician fading is a stochastic model for radio propagation where the signal arrives at the receiver by several different paths when one of the paths, typically a line of sight signal or some strong reflection signals, is much stronger than the others.

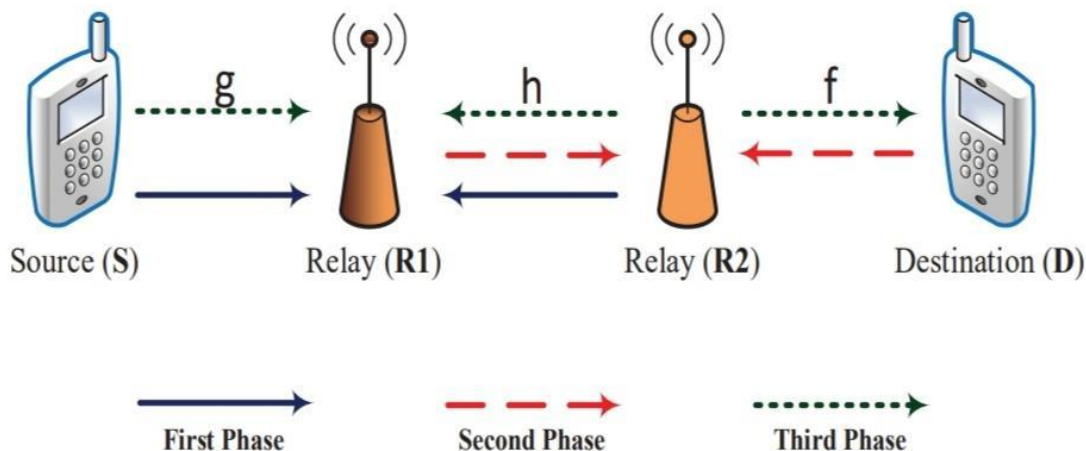


Figure 1. System model of a three-hop wireless relay [7].

In Rician fading, the amplitude gain is characterized by Rician distribution. It was named after Stephen O. Rice [25]. Rician RVs  $x_i$  have Rician distribution [25]:

$$p_{x_i}(x_i) = \frac{2(\kappa_i + 1)}{\Omega_i e^{\kappa_i}} \sum_{j_i=0}^{\infty} \left( \frac{(\kappa_i + 1)\kappa_i}{\Omega_i} \right)^{j_i} \frac{1}{(j_i!)^2} \cdot x_i^{2j_i+1} e^{-\frac{\kappa_i+1}{\Omega_i} x_i^2}, \quad x_i \geq 0, \quad (1)$$

where  $\Omega_i$  are mean powers of RVs  $x_i$ , and  $\kappa_i$  are Rician factors. Rician factor is defined as a ratio of signal power of dominant component and power of scattered components. It can have values from  $[0, \infty]$ .

A random variable  $x$  is product of three Rician RVs [3, eq. (2)]:

$$x = \prod_{i=1}^3 x_i, \quad (2)$$

which implies:  $x_j = x / x_2 x_3$ .

Probability density function of product of three Rician RVs  $x$  is [26, eq. (7)]:

$$p_x(x) = \frac{2(\kappa_1 + 1)}{\Omega_1 e^{\kappa_1}} \sum_{j_1=0}^{\infty} \left( \frac{(\kappa_1 + 1)\kappa_1}{\Omega_1} \right)^{j_1} \frac{1}{(j_1!)^2} \cdot \frac{2(\kappa_2 + 1)}{\Omega_2 e^{\kappa_2}} \sum_{j_2=0}^{\infty} \left( \frac{(\kappa_2 + 1)\kappa_2}{\Omega_2} \right)^{j_2} \frac{1}{(j_2!)^2} \cdot \frac{2(\kappa_3 + 1)}{\Omega_3 e^{\kappa_3}} \sum_{j_3=0}^{\infty} \left( \frac{(\kappa_3 + 1)\kappa_3}{\Omega_3} \right)^{j_3} \frac{1}{(j_3!)^2} \cdot \int_0^{\infty} dx_2 \int_0^{\infty} dx_3 x_2^{-1-2j_1+2j_2} x_3^{-1-2j_1+2j_3} \cdot x^{2j_1+1} e^{-\frac{\kappa_1+1}{\Omega_1} \left(\frac{x}{x_2 x_3}\right)^2 - \frac{\kappa_2+1}{\Omega_2} x_2^2 - \frac{\kappa_3+1}{\Omega_3} x_3^2}. \quad (3)$$

### B. CDF of Product of Three Rician RVs

Cumulative distribution function (CDF) of product of three Rician RVs is [1]:

$$F_x(x) = \int_0^{\infty} dt p_x(t) = \frac{2(\kappa_1 + 1)}{\Omega_1 e^{\kappa_1}} \sum_{j_1=0}^{\infty} \left( \frac{(\kappa_1 + 1)\kappa_1}{\Omega_1} \right)^{j_1} \frac{1}{(j_1!)^2} \cdot \frac{2(\kappa_2 + 1)}{\Omega_2 e^{\kappa_2}} \sum_{j_2=0}^{\infty} \left( \frac{(\kappa_2 + 1)\kappa_2}{\Omega_2} \right)^{j_2} \frac{1}{(j_2!)^2} \cdot \dots$$

$$\begin{aligned} & \cdot \frac{2(\kappa_3 + 1)}{\Omega_3 e^{\kappa_3}} \sum_{j_3=0}^{\infty} \left( \frac{(\kappa_3 + 1)\kappa_3}{\Omega_3} \right)^{j_3} \frac{1}{(j_3!)^2} \cdot \int_0^{\infty} dx_2 \int_0^{\infty} dx_3 x_2^{-1-2j_1+2j_2} x_3^{-1-2j_1+2j_3} e^{-\frac{\kappa_2+1}{\Omega_2} x_2^2 - \frac{\kappa_3+1}{\Omega_3} x_3^2} \\ & \int_0^x dt t^{2j_1+1} e^{-\frac{\kappa_1+1}{\Omega_1} \frac{t^2}{x_2^2 x_3^2}} = \\ & = \frac{2(\kappa_1 + 1)}{\Omega_1 e^{\kappa_1}} \sum_{j_1=0}^{\infty} \left( \frac{(\kappa_1 + 1)\kappa_1}{\Omega_1} \right)^{j_1} \frac{1}{(j_1!)^2} \cdot \frac{2(\kappa_2 + 1)}{\Omega_2 e^{\kappa_2}} \sum_{j_2=0}^{\infty} \left( \frac{(\kappa_2 + 1)\kappa_2}{\Omega_2} \right)^{j_2} \frac{1}{(j_2!)^2} \cdot \frac{2(\kappa_3 + 1)}{\Omega_3 e^{\kappa_3}} \sum_{j_3=0}^{\infty} \left( \frac{(\kappa_3 + 1)\kappa_3}{\Omega_3} \right)^{j_3} \frac{1}{(j_3!)^2} \cdot \int_0^{\infty} dx_2 \int_0^{\infty} dx_3 x_2^{-1-2j_1+2j_2+2j_1+2} x_3^{-1-2j_1+2j_3+2j_1+2} \cdot e^{-\frac{\kappa_2+1}{\Omega_2} x_2^2 - \frac{\kappa_3+1}{\Omega_3} x_3^2} \cdot \frac{1}{2} \left( \frac{\Omega_1}{\kappa_1 + 1} \right)^{j_1+1} \gamma \left( j_1 + 1, \frac{\kappa_1 + 1}{\Omega_1} \frac{x^2}{x_2^2 x_3^2} \right). \quad (4) \end{aligned}$$

In contrast to Rician, Rayleigh fading is a model for stochastic fading when there is no LOS signal. Since that it is considered as a special case of Rician fading. Rayleigh fading is obtained for Rician factor putting Rician factor  $\kappa=0$ . Because of that, derived expressions for CDF of product of three Rician RVs can be used for obtaining a CDF of product of three Rayleigh RVs, also for CDF of product of two Rayleigh RVs and Rician RV, and CDF of product of two Rician RVs and Rayleigh RV. The obtained results can be used in performance analysis of wireless three-hop relay radio system in the presence of multipath fading. This means that derived CDFs are used for the next cases: 1) when Rician fading is present in all three sections ( $\kappa_i \neq 0, i = 1, 2, 3$ ), then 2) when Rayleigh fading is present in all three sections ( $\kappa_1 = \kappa_2 = \kappa_3 = 0$ ), the next 3) when Rayleigh fading is present in two sections and Rician in one ( $\kappa_1 = \kappa_2 = 0, \kappa_3 \neq 0$ ), and 4) when Rayleigh fading is present in one and Rician fading in two sections ( $\kappa_1 = 0, \kappa_2 \neq 0, \kappa_3 \neq 0$ ). A case with  $\kappa \rightarrow \infty$  presents the scenario without fading.

### C. Outage probability of Product of Three Rician RVs

The outage probability is an important performance measure of quality of fading channels.  $P_{out}$  is defined as the probability that information rate is less than previously defined threshold information rate  $\Gamma_{th}$ . Actually,  $P_{out}$  is the probability that an outage occurs within a specified time period [14]:

$$P_{out} = \int_0^{\Gamma_{th}} p_x(t) dt, \quad (5)$$

where  $p_x(x)$  is the PDF of the signal and  $\Gamma_{th}$  is the system protection ratio depending on the type of used modulation and the receivers' characteristics [27].

Using (4),  $P_{out}$  is expressed as [14]:

$$P_{out} = F_x(\Gamma_{th}). \quad (6)$$

Some graphs of the  $P_{out}$  are presented in Figs. 2 and 3 for different values of parameters.

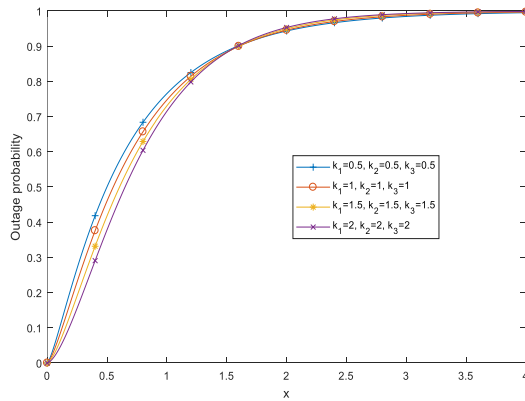


Figure 2. Outage probability of product of three Rician RVs versus signal envelope  $x$  for different values of Rician factor  $\kappa_i$  and signal power  $\Omega_i=1$ .

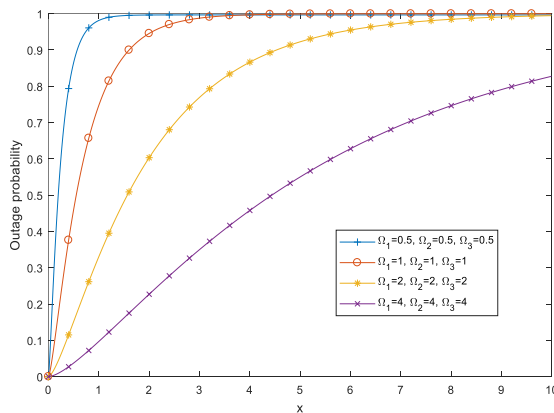


Figure 3. Outage probability of product of three Rician RVs depending on signal envelope for different values of signal power  $\Omega_i$  and Rician factor  $\kappa_i=1$ .

The choice of parameters illustrates the broad range of shapes that the curves of the resulting distribution can have. It is evident that performance is improved with an increase in Rician factors  $\kappa_i$ . Also, higher values of fading powers  $\Omega_i$  tend to reduce the  $P_{out}$  and improve system performance, as it is expected.

### V. THE SECOND ORDER PERFORMANCE OF THE PRODUCT OF THREE RICIAN RANDOM VARIABLES

Level crossing rate and average fade duration of the signal envelope are very important second-order statistics of wireless channel. They enable useful information about the dynamic temporal behavior of multipath wireless fading channels.

#### A. LCR of Product of Three Rician RVs

Level crossing rate is one of the most important second-order performance measures of wireless communication system. LCR has application in modelling and designing of communication systems, but also in the design of error correcting codes, optimization of interleave size and throughput analysis.

LCR is defined as the expected rate at which a fading signal envelope crosses the given level in the downward direction, expressed in crossings per second [15]. The LCR of RV shows how often the envelope crosses a predetermined threshold  $x$  [28]. Let us first determine  $p_{x\dot{x}}(x\dot{x})$  (the joint probability density function (JPDF) between  $x$  and  $\dot{x}$ ), then apply the Rice's formula [25, Eq. (2.106)] to finally calculate the LCR [13]:

$$N_x = \int_0^{\infty} dx \dot{x} p_{x\dot{x}}(x\dot{x}). \quad (7)$$

LCR of product of three Rician RVs is derived in [5, eq. (20)]:

$$\begin{aligned} N_x = & \frac{1}{\sqrt{2\pi}} \pi f_m \frac{\Omega_1^{1/2}}{(\kappa_1 + 1)^{1/2}} \cdot \frac{2(\kappa_1 + 1)}{\Omega_1} \cdot \frac{2(\kappa_2 + 1)}{\Omega_2} \cdot \frac{2(\kappa_3 + 1)}{\Omega_3} \cdot \\ & \sum_{i_1=0}^{\infty} \sum_{i_2=0}^{\infty} \sum_{i_3=0}^{\infty} \left( \frac{\kappa_1(\kappa_1 + 1)}{\Omega_1} \right)^{i_1} \frac{1}{(i_1!)^2} \left( \frac{\kappa_2(\kappa_2 + 1)}{\Omega_2} \right)^{i_2} \frac{1}{(i_2!)^2} \cdot \\ & \left( \frac{\kappa_3(\kappa_3 + 1)}{\Omega_3} \right)^{i_3} \frac{1}{(i_3!)^2} x^{2i_1+1} \\ & \cdot \int_0^{\infty} dx_2 \int_0^{\infty} dx_3 \left( 1 + \frac{x^2}{x_2^4 x_3^2} \frac{\Omega_2}{\kappa_2 + 1} \frac{\kappa_1 + 1}{\Omega_1} + \frac{x^2}{x_2^2 x_3^4} \frac{\Omega_3}{\kappa_3 + 1} \frac{\kappa_1 + 1}{\Omega_1} \right)^{1/2} \cdot \\ & \cdot x_2^{-2i_1-1+2i_2+1} x_3^{-2i_1-1+2i_3+1} e^{-\frac{\kappa_1+1}{\Omega_1} \frac{x^2}{x_2^2 x_3^2} - \frac{\kappa_2+1}{\Omega_2} x_2^2 - \frac{\kappa_3+1}{\Omega_3} x_3^2}. \quad (8) \end{aligned}$$

Last integral can be solved by using Laplace approximation theorem for solution the two-fold integrals [29]. It was solved in [5, Eqs. (22) - (29)] in the form:

$$\int_0^\infty dx_2 \int_0^\infty dx_3 g(x_2, x_3) e^{\lambda f(x_2, x_3)} = \frac{\pi}{\lambda} g(x_{20}, x_{30}) e^{\lambda f(x_{20}, x_{30})} \frac{1}{(B(x_{20}, x_{30}))^{1/2}} \quad (9)$$

Some graphs for normalized LCR of product of three Rician RVs versus this product  $x$  are plotted in Figs. 4 and 5 [1] for different values of Rician factor  $\kappa_i$  and average power  $\Omega_i$ .

It is visible that LCR increases when Rician signal power increases. The impact of signal envelope power on the LCR is higher for bigger values of Rician factor  $\kappa_i$ . Also, LCR increases with increasing of  $\Omega_i$  for all values of signal envelope.

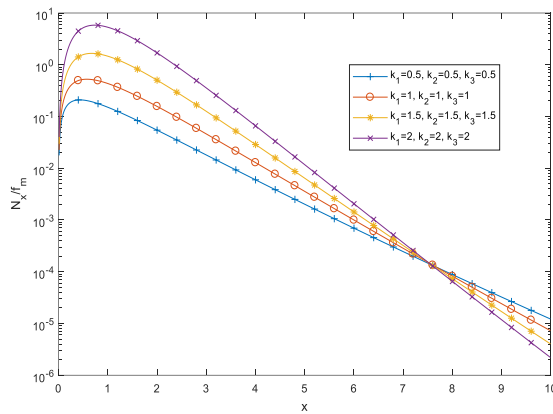


Figure 4. LCR normalized by  $f_m$  depending on signal envelope  $x$  for various values of Rician factor  $\kappa_i$  and signal power  $\Omega_i=1$ .

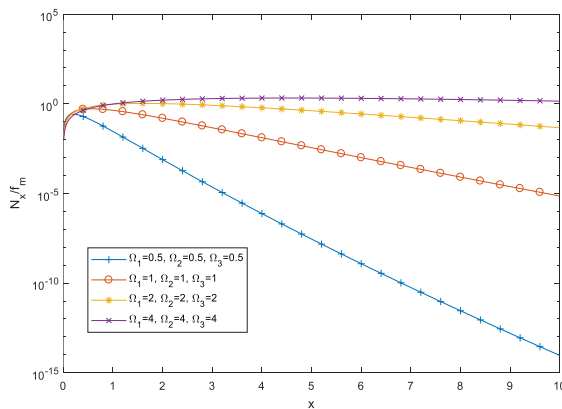


Figure 5. LCR normalized by  $f_m$  versus signal envelope  $x$  for various values of signal powers  $\Omega_i$ .

The impact of signal envelope on the LCR is larger for higher values of the signal envelope, when  $\Omega_i$  changes. It is known from theory that system has better performance for lower values of the LCR.

### B. AFD of Product of Three Rician RVs

Average fade duration measures how long a signal's envelope or power stays below a given threshold, i.e., how long the user is in continuous outage. This is important for coding design.

AFD is derived from the LCR [4]. According to that, AFD is [30, eq. (9)]:

$$T_x(x) = \frac{P(x \leq X)}{N_x(x)} = \frac{\int_0^x p_x(x) dx}{N_x(x)} \quad (10)$$

In numerator is actually the CDF of  $x$  from (4), and  $N_x(x)$  is LCR given presented by (8) [31].

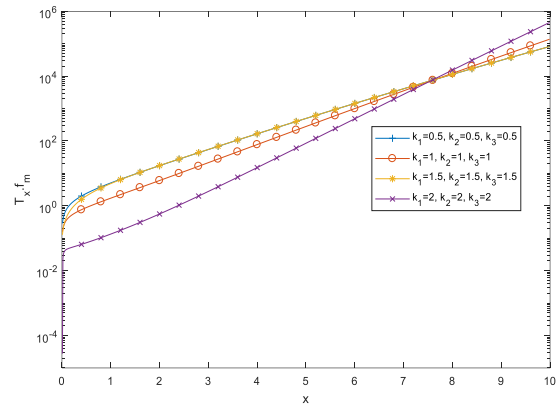


Figure 6. AFD normalized by  $f_m$  versus signal envelope  $x$  for different values of Rician factor  $\kappa_i$  and signal powers  $\Omega_i=1$ .

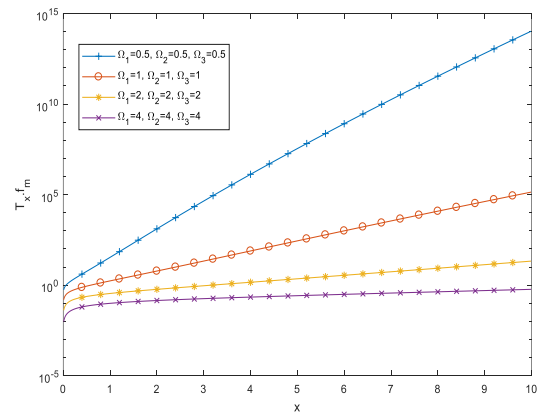


Figure 7. AFD normalized by  $f_m$  depending on signal envelope  $x$  for  $\kappa=1$  and different values of signal powers  $\Omega_i$ .

The normalized AFD ( $T_{i,f_m}$ ) of product of three Rician RVs is shown in Figs. 6 and 7 [1] depending on signal envelope  $x$ . One can observe from these figures that AFD has smaller values for higher parameter  $\kappa_i$  and lower signal envelope  $x$ . Also, it is possible to see from Fig. 7 that AFD increases for whole range of envelopes and lower  $\Omega_i$ . The impact of  $\Omega_i$  is bigger at higher envelopes' values.

## VI. SOFTWARE ENVIRONMENT FOR SMART CITY MOBILE NETWORK PLANNING

Moreover, we make use of the previously derived expressions within software simulation environment that aims optimal mobile network planning in order to support state-of-the-art services within smart cities. The tools are accessible using web browser and build upon the software engine presented in [8], [32], [33]. In Fig. 8, the workflow of this software environment is depicted.

The first step in this workflow represents creation of user-drawn smart city mobile network model relying on 3D graphical environment implemented using Three.js. When it comes to modelling, the following factors are taken into account: network provider's infrastructure (represented as base stations); terrain configuration (represented as different forms of obstacles, such as buildings and trees); end-users of provided network service (represented as autonomous cars, drones, surveillance cameras); smart city locations of interest, referred to as places.

Once user completes a network model, fading effect-related values are calculated:  $P_{out}$ , LCR and AFD relying on NVIDIA CUDA [34] which makes use of Graphics Processing Unit (GPU). This approach is beneficial, as the time required for these calculations is reduced due to impact of loop-level parallelization. Considering the fact that loop-based calculations represent the constituent part

of fading expressions [35], significant acceleration was noticed in comparison with equivalent program written in Mathematica and executed entirely on CPU – 59 times for  $P_{out}$ , 61 times for LCR and 69 times for AFD. The structure generalized structure of CUDA C kernel is illustrated in Fig. 9, where *FadingMeasure* is changed with one of the fading-related measures – either  $P_{out}$ , LCR or AFD.

On the other side, we also make use of GPU hardware for prediction of service demand regarding the number of service consumers at given place within smart city. This prediction problem is treated as regression.

The input (independent) variables are the following: place id, day of the week, daily average temperature and daily number of COVID-19 cases, as each of them is assumed to be affecting how crowded certain place would be. The output is number of mobile network users. For this purpose, we use deep neural network with three hidden layers, 30 nodes per layer and ReLU activation function, while there is one linear node in the output layer.

Furthermore, Adam optimizer and Mean Squared Error cost function was used, with learning rate 0.01. The mean relative error of this model was around 6%. In Fig. 10, an excerpt of Python code relying on PyTorch [36] framework for deep learning, defining the proposed neural network is given. The approach to service demand prediction builds upon our previous work done in [37].

In the last step, once we have both the fading effect measures and service demand predictions calculated, the procedure of linear optimization can be executed in order to find the best possible selection of base stations, suitable for the selected smart city places. In this context, linear optimization model is written using AMPL 9 [38] and optimization problem solved relying on CPLEX [39] that implements simplex method.

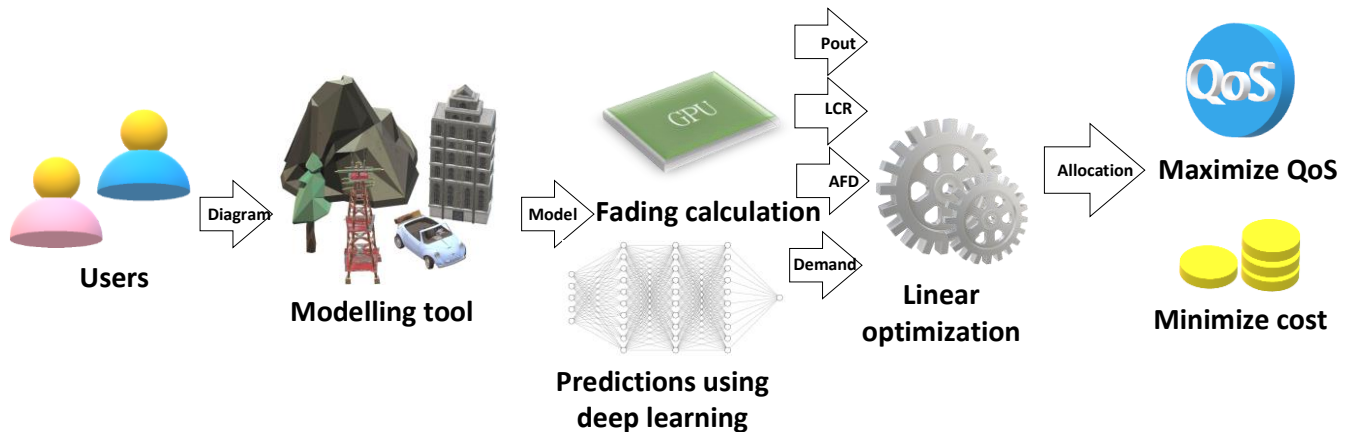


Figure 8. Smart city mobile network planning workflow.

```

__global__ void fading_kernel(Place* p, BStation* bs, float* fading)
{
    int k = threadIdx.x + blockIdx.x * blockDim.x;
    while (k < N)
    {
        out[k] = FadingMeasure(bs, p[k]);
        k += blockDim.x * gridDim.x;
    }
}

```

Figure 9. Generalized CUDA C kernel illustrating GPU-enabled fading effect calculation.

```

class ServiceDemandModel(torch.nn.Module):
    def __init__(self, input_length):
        super(ServiceDemandModel, self).__init__()
        self.input_num = input_length

        self.layer1 = torch.nn.Linear(input_length, 35)
        self.layer2 = torch.nn.Linear(35, 35)
        self.layer3 = torch.nn.Linear(35, 35)
        self.layer4 = torch.nn.Linear(35, 1)

    def forward(self, x):
        output = F.relu(self.layer1(x))
        output = F.relu(self.layer2(output))
        output = F.relu(self.layer3(output))
        nu = self.layer4(output)
        return nu

predictor=ServiceDemandModel(4)

```

Figure 10. Excerpt from Python code showing deep neural network definition using PyTorch for service demand prediction treated as regression.

In this case, the optimization model's objective function has goal to minimize the overall mobile network maintenance costs  $dmc[bs, p]$  for placing base station  $bs$  at place  $p$ . On the other side, it aims to maximize the network performance by keeping  $P_{out}$  and AFD as low as possible:

$$\underset{bs \in BS, p \in P}{\text{minimize}} \sum AFD[p, bs] P_{out}[p, bs] dmc[p, bs] x[p, bs]. \quad (11)$$

**Table I**  
Results for varying network model size.

Base stations [num]	Places [num]	$P_{out}$ [s]	LCR [s]	AFD [s]	Pred [s]	Opt. [min]	Cost red. [%]
3	2	0.61	0.72	0.94	0.33	0.29	36
5	3	0.94	1.07	1.21	0.36	0.73	42
9	4	1.33	1.69	1.88	0.41	1.04	78
12	5	1.92	2.13	2.76	0.47	3.04	61

In this equation,  $x[p, bs]$  is decision variable that will take value 1 in case when base station  $bs$  is about to be allocated to place  $p$ , while it is 0 otherwise. Moreover, for each place  $p$ , the channel capacity [40] of a base station  $cap[p, bs]$  should be enough to handle the predicted number of users  $nu[p]$ :

$$\sum_{bs \in BS} x[p, bs] cap[p, bs] \geq nu[p], p \in P. \quad (12)$$

Finally, when it comes to evaluation of the proposed approach making use the synergy of GPGPU calculations, deep learning and linear optimization, the cost reduction percentage and execution times for different sizes of network models (number of base stations and places) are presented in Table I. According to these results, it can be seen that it takes more processing time for larger models, while the cost reduction depends on the specific model instance.

## VII. CONCLUSION

In this paper, we analyzed the influence of Rician fading to the three-hop wireless relay system. The output signal from such system was obtained as the product of three Rician RVs. For this scenario, we presented previously determined formulas for the next performance: PDF, CDF, Pout, LCR and AFD. Based on the presented results it is possible to anticipate the behavior of the real wireless relay system in the presence of Rician fading. The parameters influence is analyzed based on plotted graphics.

Finally, in the last part of this paper, the previously derived expressions for performance of wireless system in the presence of fading were incorporated into GPU-enabled network planning environment. Considering the achieved results, it can also be concluded that the proposed approach leveraging synergy of GPGPU calculations, deep learning and linear optimization, enables more efficient network planning. This approach provides the highest possible Quality of Service (QoS), keeping at the same time the costs as lowest as possible. The procedure depends also on the specific fading conditions in smart city.

## ACKNOWLEDGMENT

This article was realized under the projects of the Ministry of Education, Science and Technological Development of the Republic of Serbia.

## REFERENCES

- [1] D. Krstic, P. Nikolic, S. Minic, and Z. Popovic, "Some Performance of Three-hop Wireless Relay Channels in the Presence of Rician Fading", The Sixteenth International Conference on Wireless and Mobile Communications ICWMC 2020, October 18, 2020 to October 22, 2020 - Porto, Portugal, pp. 18-23.
- [2] D.-H. Kim, Y.-C. Ko, and S. Park, "Three-hop MIMO relaying systems in Gaussian broadcast channels", 2nd International Conference on Signal Processing and Communication Systems, ICSPCS, Australia, Gold

- Coast. 15-17 December 2008. doi:10.1109/icspcs.2008.4813661
- [3] D. Krstic, P. Nikolic, Z. Popovic, and M. Stefanovic, "First and second order characteristics of wireless three-hop relay channel with presence of Rayleigh fading", *Journal of Telecommunications and Information Technology (JTIT)*, no. 2/2020, pp. 36-44, <https://doi.org/10.26636/jtit.2019.130018>
- [4] D. Krstic, P. Nikolic, I. Vulic, S. Minic, and M. Stefanovic, "Performance of the product of three Nakagami-m random variables". *Journal of Communications Software and Systems (JCOMSS)*, vol. 16, no. 2, June 2020, pp. 122-130, <http://dx.doi.org/10.24138/jcomss.v16i2.989>
- [5] D. Krstic, M. Stefanovic, M.M.B. Yaseen, S. Aljawarneh, and P. Nikolić, "Statistics of the product of three Rician random processes with application", *International Conference on Data Science, E-learning and Information Systems 2018 (Data'18)*, Madrid, Spain, October 1-2, 2018. DOI: 10.1145/3279996.3280015
- [6] A. Panajotovic, N. Sekulovic, A. Cvetkovic, and D. Milovic, "System performance analysis of cooperative multihop relaying network applying approximation to dual-hop relaying network", *Int. J. Commun Syst.* 2020; e4476, p. 1-10, <https://doi.org/10.1002/dac.4476>
- [7] A. Kuhistani, M. T. Mamaghani, and H. Behroozi, "A new secure multi-hop untrusted relaying scheme", *ArXiv*, Corpus ID: 162184290, May 2019.
- [8] D. Milić, S. Suljović, N. Petrović, S. Koničanin, and S. Panić, "Software environment for performance of relay signal by DF technique influenced by  $k-\mu$  fading", *INFOTEH* 2020, pp. 1-4, 2020. <https://doi.org/10.1109/INFOTEH48170.2020.9066304>
- [9] N. Athanasopoulos, P. Tsiakas, K. Voudouris, I. Georgas, and I. Agapiou, Multi-hop Relay in Next Generation Wireless Broadband Access Networks: An Overview. In: Chatzimisios P., Verikoukis C., Santamaría I., Laddomada M., Hoffmann O. (eds) *Mobile Lightweight Wireless Systems. Mobilight 2010. Lecture Notes of the Institute for Computer Sciences, Social Informatics and Telecommunications Engineering*, vol 45. Springer, Berlin, Heidelberg, 2010. [https://doi.org/10.1007/978-3-642-16644-0\\_47](https://doi.org/10.1007/978-3-642-16644-0_47)
- [10] U. M. Pešović, J. J. Mohorko, K. Benkič, and Ž. F. Čučej, "Single-hop vs. Multi-hop – Energy efficiency analysis in wireless sensor networks", *Telekomunikation forum TELFOR*, Serbia, Belgrade 23–25 November 2010, pp. 471–474.
- [11] S. Fedor and M. Collier, "On the problem of energy efficiency of multi-hop vs one-hop routing in Wireless Sensor Networks", 21st International Conference on Advanced Information Networking and Applications Workshops (AINAW'07)
- [12] P. M. Shankar, *Fading and shadowing in wireless systems*, Springer, New York Dordrecht Heidelberg London. 2012, DOI 10.1007/978-1-4614-0367-8.
- [13] G. L. Stüber, *Principles of Mobile Communications*, 2nd ed., MA, USA, Springer, 2001. ISBN 978-1-4614-0364-7
- [14] M. K. Simon and M. S. Alouini, *Digital communication over fading channels*, (2nd ed.), New York, Wiley-IEEE Press. ISBN: 978-0-471-64953-3, 2004.
- [15] A. Goldsmith, *Wireless Communications*, Cambridge University Press, 2005, DOI: <https://doi.org/10.1017/CBO9780511841224>
- [16] G. K. Karagiannidis, N. C. Sagias, and T. Mathiopoulos, "The N\*Nakagami fading channel model", 2005 2nd International Symposium on Wireless Communication Systems, Siena, Italy, 5-7 Sept. 2005, pp. 185-189, DOI: 10.1109/ISWCS.2005.1547683
- [17] I. Ghareeb and D. Tashman, "Statistical analysis of cascaded Rician fading channels", *International Journal of Electronics Letters*, November 2018. doi:10.1080/21681724.2018.1545925
- [18] D. Krstic, M. Stefanovic, R. Gerov, and Z. Popovic, "Wireless relay system with two sections in  $\kappa-\mu$  short term fading channel", *The Twelfth International Conference on Wireless and Mobile Communications, ICWMC 2016*, Barcelona, Spain, Nov. 13 - 17, 2016, pp. 110 - 114.
- [19] A. Cvetković, J. Anastasov, S. Panić, M. Stefanović, and D. Milić, "Performance of dual-hop relaying over shadowed Rician fading channels", *Journal of Electrical Engineering*, 2011, 62(4), pp. 244–248. doi:10.2478/v10187-011-0039-6
- [20] C. Wang and D. Xu, "A study on burst error statistics and error modelling for MB-OFDM UWB systems", *IET Seminar on Ultra Wideband Systems, Technologies and Applications*, 2006, p. 244-248, DOI: 10.1049/ic:20060518
- [21] A. Abdi, K. Wills, H. A. Barger, M.-S. Alouini, and M. Kaveh, "Comparison of the level crossing rate and average fade duration of Rayleigh, Rice, and Nakagami fading models with mobile channel", *52nd Vehicular Technology Conference IEEE VTS Fall VTC2000*, Boston, MA, USA, pp. 1850-1857, DOI: 10.1109/VETECF.2000.886139
- [22] J. M. Morris and J. L. Chang, "Burst error statistics of simulated Viterbi decoded BFSK and high-rate punctured codes on fading and scintillating channels," *IEEE Trans. Commun.*, vol. 43, pp. 695-700, 1995.
- [23] A. J. Goldsmith and S. G. Chua, "Variable-rate coded M-QAM for fading channels", *IEEE Trans. Commun.*, vol. 45, pp. 1218-1230, 1997.
- [24] G. N. Onoh, T. L. Alumona, and C. O. Ezeagwu, "Adaptive modulation techniques for capacity improvement of BER in WCDMA", *International Journal of Advanced Research in Computer Engineering & Technology (IJARCET)*, Vol. 4, Issue 9, September 2015, pp. 3537-3542.
- [25] S. O. Rice, "Mathematical analysis of random noise". *Bell System Technical Journal*. 23(3). 1944, pp. 282–332. doi:10.1002/j.1538-7305.1944.tb00874.x
- [26] D. Krstic, P. Nikolic, Z. Popovic, S. Minic, and M. Stefanovic, "Moments of signals over wireless relay fading environment with line-of-sight", *SoftCom 2020*, Hvar, Croatia, September 17-19, 2020. DOI: 10.23919/SoftCOM50211.2020.9238347
- [27] I. Trigui, A. Laourine, S. Affes, and A. Stephenne, "Outage analysis of wireless systems over composite fading/shadowing channels with co-channel interference", *IEEE Wireless Communications and Networking Conference*, 5-8 April 2009, Budapest, Hungary
- [28] W. C. Jakes, *Microwave Mobile Communications*. Piscataway, NJ: IEEE Press, 1994.
- [29] J. L. Lopez and P. J. Pagola, "A simplification of the laplace method for double integrals. Application to the second appell function", *Electronic Transactions on Numerical Analysis*, vol. 30, 2008.
- [30] T. T. Tjhung and C. C. Chai, "Fade statistics in Nakagami-lognormal channels". *IEEE Transactions on Communications*, 1999, 47(12), pp. 1769–1772. doi:10.1109/26.809692

- [31] X. Dong and N. C. Beaulieu. "Average level crossing rate and average fade duration of selection diversity". *IEEE Communications Letters*, 5(10), 2001, pp. 396–398, doi:10.1109/4234.957373
- [32] N. Petrović, S. Koničanin, D. Milić, S. Suljović, and S. Panić, "GPU-enabled framework for modelling, simulation and planning of mobile networks in smart cities", *ZINC 2020*, pp. 1-6, 2020, <https://doi.org/10.1109/ZINC50678.2020.9161773>
- [33] N. Petrović, S. Vasić, D. Milić, S. Suljović, S. Koničanin, "GPU-Supported Simulation for ABEP and QoS analysis of a Combined Macro Diversity System in a Gamma-Shadowed  $k-\mu$  fading channel", *Facta Universitatis: Electronics and Energetics* Vol. 34, No 1, March 2021, pp. 89-104. <https://doi.org/10.2298/FUEE2101089P>
- [34] J. Sanders, E. Kandort, *CUDA By Example: An Introduction to General-Purpose GPU Programming*, Addison-Wesley, 2011.
- [35] A. F. Abdelrazek, M. Kaschub, C. Blankenhorn, M. C. Necker, "A Novel Architecture using NVIDIA CUDA to speed up Simulation of Multi-Path Fast Fading Channels", pp. 1-5, 2009.
- [36] E. Stevens, L. Antiga, T. Viehmann, *Deep Learning with PyTorch*, Manning Publications, 2020.
- [37] D. Krstić, S. Suljović, N. Petrović, S. Minić, "Effects of Weibull fading and co-channel interference shape and scale parameters and number of branches on multi-branch SC receiver outage performance", *15th International Online Conference on Applied Electromagnetics - PIEC 2021*, pp. 141-144, 2021.
- [38] R. Fourer, D. Gay, B. Kernighan, *AMPL: A Modeling Language for Mathematical Programming*, Duxbury Press, 2003.
- [39] IBM CPLEX Optimizer [online]. Available on: <https://www.ibm.com/analytics/cplex-optimizer>, last accessed: 01/03/2021.
- [40] D. Krstić, S. Suljović, N. Petrović, Z. Popović, S. Minić, "Channel Capacity of Macrodiversity System in Gamma Shadowed  $k-\mu$  Fading Environment", *AIIT 2020 International conference on Applied Internet and Information Technologies*, pp. 125-130, 2020.

## Next Generation IMPAQT Miniaturized Underwater Transmitter System Design

Hamed Jafarzadeh

Tyndall National Institute  
University College Cork  
Cork, Ireland

e-mail: hamed.jafarzadeh@tyndall.ie

Marco Belcastro

Tyndall National Institute  
University College Cork  
Cork, Ireland

e-mail: marco.belcastro@tyndall.ie

Brendan O'Flynn

Tyndall National Institute  
University College Cork  
Cork, Ireland

e-mail: brendan.oflynn@tyndall.ie

**Abstract** - In recent years, terrestrial wireless sensor networks and Internet of Things (IoT) technologies have developed rapidly. However, due to the limitations of Electromagnetic (EM) signal propagation in water, there is less development and advancement in the underwater wireless sensor networks domain. As part of the IMPAQT project, a novel wireless underwater telemetry platform using acoustics has been proposed. This telemetry platform has the potential to replace the underwater sensors cables and provide a wireless method to collect and transmit a variety of environmental sensor data under water. The proposed platform system architecture consists of several ultrasonic transmitter nodes and a gateway buoy as a data aggregator node to transmit the data from the sensors to the cloud for analytics to be carried out. Transmitter nodes will read the attached sensor data and transmit it to the gateway buoy. The gateway buoy will send the collected data to a data management system using a Long Range (LoRa) communication link. The next generation IMPAQT Transmitter node developed is a compact, low-cost, low-power acoustic transmitter node that has an external sensor interface to receive data from attached sensors is described in detail in this paper. In addition, the potential for short-range EM-based underwater LoRa communication is evaluated and described.

**Keywords**- *Biotelemetry; Underwater communication; Underwater sensors network; Acoustic communications, underwater sensor node.*

### I. INTRODUCTION

This paper is an extension of a previous conference submission [1]. According to the latest United Nations world population estimation, by the year 2050, the population of the earth will reach approximately 10 billion people [2], and this increase will result in a higher demand for food and consequently seafood as it is one of the primary sources of protein and nutrition for many people. In the past, capture fisheries productions were the primary source of seafood, but this has changed in 2012, where aquaculture production volumes exceeded that of the traditional capture fisheries, and it is seen to be increasing rapidly in recent years to meet demand [3].

To provide more sustainability, reduce environmental impacts, and promote economic gains, integrated multi-trophic aquaculture (IMTA) is gaining popularity among marine farmers. In IMTA, farmers combine fed species (e.g., fish, shrimp, oysters) with extractive species (e.g., seaweed,

mussels), and the extractive species will use the by-products of the fed species, reducing the environmental impact of the sites and also providing commercial profit to farmers.

IMPAQT [4] is a European project aimed at promoting and supporting the development of IMTA sites by providing a multi-purpose (Inland, coastal, offshore), multi-sensing (heterogeneous sensors, biosensors, smart systems), and multi-functional (Monitoring, data analytics, decision making) data management platform [5]. The IMPAQT project also aims at providing training based on the obtained data to the farmers and improving farming sector performance [6]. In Figure 1, an overview of the IMPAQT project has been proposed by Michalek et al. [7].

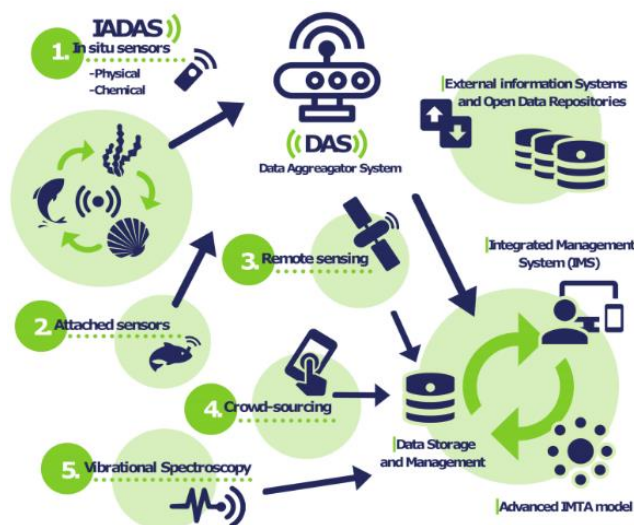


Figure 1. IMPAQT Project overview [7].

As part of the IMPAQT Data acquisition system, a communications device was required to collect information from the underwater sensors and transmit it to the data aggregator system (DAS) to provide accurate, real-time, and relevant information about the underwater environment.

As a result, a novel miniaturized low-power and low-cost underwater acoustic transmitter node and a gateway buoy receiver have been proposed as a telemetry system and evaluated to collect data from sensors and transmit it to the inland data aggregators.

The transmitter node has an optional extension sensor board, and the transmitter node is capable of interfacing with external commercially off-the-shelf sensor modules using an external sensor connector. Due to its small size and lightweight design, it has little impact on the working environment and the artefacts to which the sensors are attached.

In Section II, the related research projects, and specifically underwater monitoring systems, is summarised. Section III describes the LoRa underwater EM communications experiments that were carried out as part of this work to clarify the reasons that electromagnetics cannot be used for underwater communications except for very short-range applications. Section III continues by describing the methodology and development of the acoustic transmitter node circuit, design parameters and also describes the power analysis of the circuit to maximize system lifetime underwater. Section IV discusses the obtained results, and Section V addresses the result of the project and future work.

## II. BACKGROUND AND RELATED WORK

With the rapidly increasing and evolving aquaculture market sector, it is essential to monitor and analyze the effects of the methods that have been used in aquaculture to reduce the costs and improve the stability and sustainability of sea farms. Experimental monitoring in labs and tanks can help in establishing optimal best practices. However, due to the differences between the experimental environment and real aquaculture environments, it is hard to compare the findings accurately, especially when it comes to the biasing caused by the handling of marine animals [8]. In [9], M. Føre et al. proposed the concept of Precision Fish Farming intending to use scientific methods to manage fish production by enabling farmers to monitor, control and document the biological processes in fish farms. With the advancement of chemical and electrical sensing technologies, it is now possible to develop miniaturized attached sensor devices to track and study the natural behaviour of marine animals and plants in their natural environment. This section includes an overview of the current marine monitoring platforms and also acoustic telemetry platforms and modems.

### A. State-of-art marine monitoring platforms

To achieve the goal of precision aquaculture and fish farming, in [10], J. A. Martos-Sitcha et al. describe the development of the AE-FishBIT, shown in Figure 2A, an ultra-low-power sensor device, for monitoring physical activities and respiratory frequency of the farmed fish, using the on-board accelerometer sensor. AE-FishBIT is a small non-invasive monitoring sensor with a footprint of 14mm x 7mm x 7mm and a total mass of 600mg. AE-FishBIT is not able to transmit the data, and the fish is required to be captured to download the sensors data.

Almeida et al. [11] monitored the behaviour of the Lusitanian toadfish using accelerometry data provided by the externally attached AccelTag, which was able to recognize

and log behaviour activities of the fish. It is capable of continuously recording tilt, roll, forward acceleration, lateral acceleration, vertical acceleration of fish for more than 7 hours. To download the recorded data, the tag needs to be extracted and connected to a computer to download its data.

There are also devices for tracking the movement of the fish in dams, fisheries, and cages. In [12][13], authors have developed the Juvenile Salmon Acoustic Telemetry System (*JSATS*), shown in Figure 2B, to identify and track the movement of juvenile salmon in dams and rivers. *JSATS* tags are incredibly compact that can be injected using a needle into the fish's body. They can transmit ultrasonic pings for a year with a 15-second ping interval. But *JSATS* tags are only capable of transmitting a pre-programmed unique identification code and temperature data, and as they are sealed, they cannot provide any other sensor data. According to the report published in the journal of "review of scientific instruments" [14], the latest version of the *JSATS* tags can last up to 285 days with the ping rate of 15 seconds and 98 days with the ping rate of 5 seconds at 163dB sound level, and each ping can travel up to 500m.

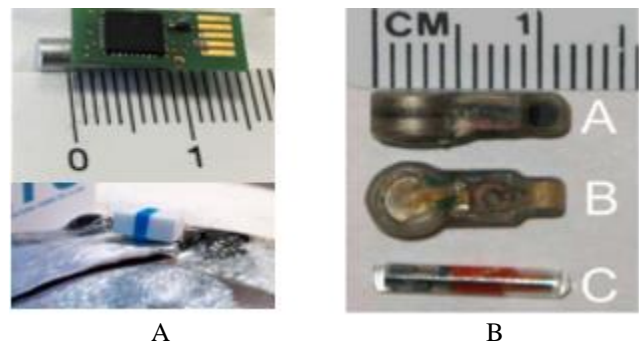


Figure 2. (A) AE-FishBIT Tags [10] (B) JSATS Tags [12]

In [15], C. Brockmann et al. implemented an energy-efficient system for monitoring fish in freshwater using high-frequency RF transceivers, capable of operating for one month using a single coin cell battery, with a measurement and transmission duty cycle of once every second. They utilized a low-power sub-GHz RF transceiver, CC1101 [16], which transmits at 866 MHz. They implemented an EMG sensor and a temperature sensor inside the module. They reported that the device was able to transmit data out of the fish cage, and they measured -70.52 dBm as the Received Signal Strength Indicator (RSSI) outside of the fish cage. They also reported that the module was able to cover one cubic meter of signal traveling distance in the water, which is not suitable for open-water communication requiring a more significant range.

Monitoring the marine environment parameters such as wave motion and light intensity, which are known to impact plant growth and harvest levels, is important in IMTA aquaculture scenarios. In a recent research, Peres et al. [17] developed a seaweed monitoring tag named AquaBit, shown

in Figure 3, to record the accelerometry data of seaweed movement alongside recording the temperature, light intensity, and water pressure of the marine environment that it is deployed in. This novel miniature low-power NFC-enabled tag records the relevant seaweed growth parameters for roughly two weeks at a 52 Hz sampling rate, and the recorded data can be downloaded using the on-board NFC transceiver and a mobile phone or using a USB cable and provided Python-based host application.

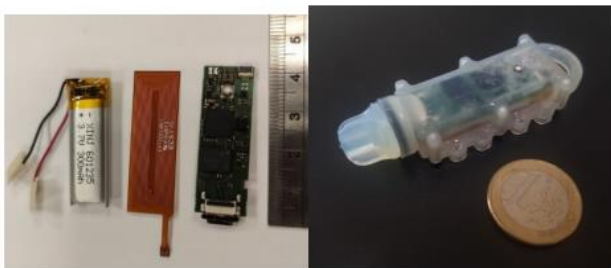


Figure 3. AquaBit seaweed monitoring tag [17].

Another method to monitor the marine environment is to use unmanned underwater vehicles. SeaSmart has introduced three patented wireless drones to collect environmental data, such as oxygen, salinity, biomass, and temperature, by travelling through the cage to collect data and returning to the surface to transmit the collected information to the cloud. It can also measure where the fish are in the cage, which can help farmers in their production and also feeding procedures. The SeaSmart Sensor Drone, depicted in Figure 4, can run 24/7 for six months on a single battery charge [18].



Figure 4. SeaSmart drone [18].

The Waterlinked company also has a solution for sensing aquaculture cages, called CageSense, shown in Figure 5. It is a network of various sensors and gateways that provide real-time underwater sensing [19]. They provide a wireless sensor that can be attached to cages using zip ties, and they can report the oxygen, salinity level, and cage's tilt and depth. There is a limited amount of information regarding these sensors at the time of writing this paper.

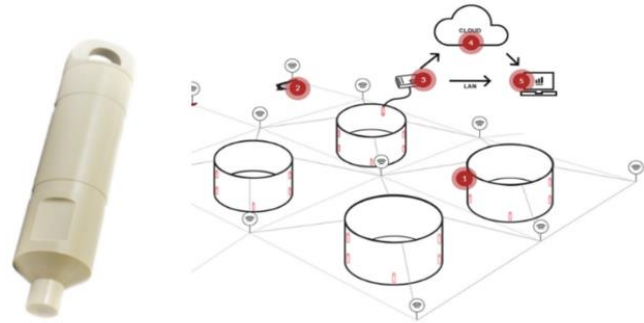


Figure 5. Waterlinked Cage Sense monitoring system [19].

There are also efforts on monitoring IMTA and aquaculture sites using remote sensing technologies; in [20], C. C. Krueger et al. have used multi-sensor (satellite, unmanned aerial vehicle, and ground spectroradiometer) remote sensing techniques to monitor seaweed aquaculture in the Yellow Sea.

There are also underwater modems that are of large size, bulky and designed for specific purposes, i.e., Underwater Robotics, etc. [21][22], and these are not designed for general-purpose marine environmental monitoring and are not reported in this paper.

In summary, various sensors can be used underwater for monitoring applications, but in order to extract their datasets, many of these need to be retrieved for data download at regular intervals. Wired sensors also exist, but there are limited numbers of sensors with underwater wireless communications capability for data download and analysis in real time.

### III. MATERIALS AND METHOD

As it can be inferred from the state-of-the-art monitoring systems, there is a lack of a general-purpose miniaturized, low-power, wireless underwater transmitter that can be integrated with other commercial and research sensors to provide a telemetry system to collect sensors' information wirelessly.

The focus of the IMPAQT telemetry platform is on providing a communication link for monitoring IMTA sites, where all sensors will be deployed in a bounded area, and it is considered that the gateway buoy will be located at a maximum distance 100m from each sensor tag. Although an ultrasonic platform would be the optimum telemetry platform, there is also the possibility to use an ElectroMagnetic (EM) based solution at the shorter range, where the gateway is installed at the water surface of a cage right above the sensor, where a range of few meters would be required.

The transmitter needs to be miniaturized to enable integration with a wide range of sensors without requiring special mounting, and it should run on its own battery, to be able to communicate with the gateway node even in the case that the external sensor's battery is depleted. Having an internal battery and a battery management system also makes

it easier to manage the battery health and estimate the charging status.

Considering the IMPAQT deployment requirements, there is a possibility of using electromagnetic waves communication at ultra-short range and ultrasonic waves communications at longer ranges. In the next section, the possibility of underwater electromagnetic communication is discussed, and a practical experiment carried out to confirm the results is explained.

#### A. Underwater electromagnetic communication

In various publications, researchers have studied electromagnetic waves propagation underwater [15][23]–[25]. In underwater communications, the transmission range is dependent on all the power gains and losses that a communication signal experiences during the transmission process. The most significant factor in establishing underwater communication is path loss. Path loss is the amount of wave signal degradation that occurs when a wave propagates in a medium, and it degrades as it moves in the medium channel. The amount of degradation depends on the conductivity and distance that the signal has travelled, and it is usually called path loss attenuation.

There are two primary path loss ( $PL$ ) types that could happen in underwater RF communication. Attenuation loss and complex permittivity are shown as  $L_{\alpha,\epsilon}$  in an underwater environment, and reflection loss ( $L_R$ ) at the surface, as shown in equation (1) below.

$$PL = L_{\alpha,\epsilon} + L_R \quad (1)$$

The path loss model for an underwater environment is extensively discussed in [24][25] for far-field electromagnetic communication and in [26] for near-field communications (i.e. NFC, RFID). Although there are various theoretical models available, there are limited numbers of publications describing practical experiments. To evaluate the potential for short-range (all that is possible according to theory and modelling) EM underwater communication, a series of practical experiments were carried out in a freshwater river using off-the-shelf LoRa transceivers to validate the theoretical models. According to the theoretical studies, lower frequency EM signals should attenuate less in the water, maximizing the range as much as possible. However, lower frequency EM transceivers require a longer antenna, which is not optimal for IMPAQT project context. For the evaluation of EM waves underwater, it has been decided to use a general purpose LoRa transceivers. Current state-of-the-art LoRa transceivers by Semtech, SX127x series, offer a receiver sensitivity of -133 dBm with the most optimal configuration [40] and they are working in a range of 169MHz to 868MHz, According to Maxwell equation and experimental models such as Lioyd [19] and Hattab et al. [33] models, at the frequency of 169MHz the maximum travelling distance for the SX127x series should be around 2.3 meter in freshwater and less than 20cm in

Seawater. Similarly, at 868MHz frequency, the travelling distance is limited to less than 110cm in freshwater and less than 13cm in seawater.

For the experiment, a LoPy4 radio node has been selected as the controller and RF module. LoPy4 [27] is a compact MicroPython enabled radio node based on SX1276 transceivers, designed to work at 868 MHz frequency. A transmitter and a receiver with identical setups have been prepared to communicate at 868 MHz frequency range, The diagram of the setup is shown in Figure 6, and the prepared setup is shown in Figure 7. An STM32F4-Disco board [28] has been used to control custom made SX1276RFIIAS modules, which have not been used in this test. It also monitors the external start switch to initiate the test procedure and synchronise the transmitter and receiver's timings for logging purposes.

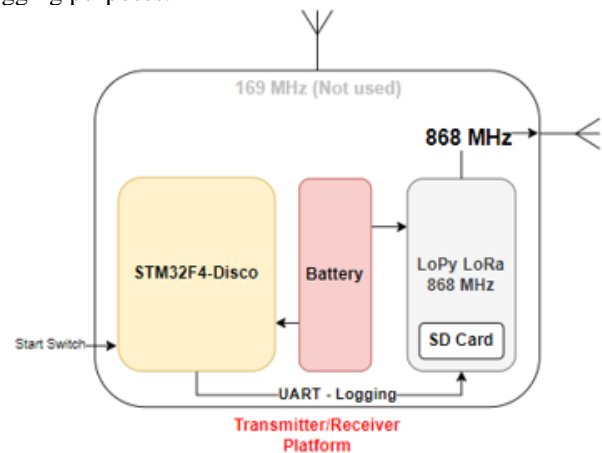


Figure 6. Underwater RF evaluation board diagram.

An SD Card is used for logging the communication packets statistics and network quality of service. As these evaluation setups are intended to be immersed underwater, two IP68 plastic containers [29] were used as system enclosures, and a silicon sealant material was used to seal the antenna connectors and control switches. Airtight plastic bags are also used to cover the enclosure and antenna to provide an extra level of water protection. Using a 70 micrometer airtight plastic bag adds an extra layer of plastic between the antenna and water, which is inevitable. However, based on the practical experiments by Donmez [30] on 1mm plastic material and another experiment demonstration at 10 GHz frequency on a range of plastic materials [31], the effect of a thin plastic layer can be considered to be negligible.

Initially, an urban environment communication range test in free space was performed to confirm that the modules were correctly configured. The non-line-of-sight urban communication test was carried out near *Tyndall National Institute* [32] in *Cork* [51.898736, -8.483184]. In these tests, the transmitter characterisation node was installed on the second floor of a four-level building in the urban area and received signal strength was recorded while increasing the distance of transmission.

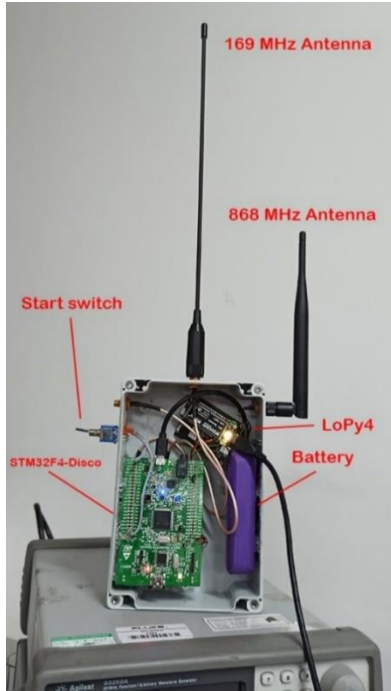


Figure 7. Underwater RF Evaluation platform.

In Figure 8, an aerial image of the test and average RSSI is shown. The red line shows the path taken with the transmitter board. The LoPy4 868 MHz receiver node managed to receive the transmitter signals up to 240 meters away from the starting point, with no line-of-sight, with the presence of dense and high buildings in between the transmitter and receiver and the transmitter located inside a four-level building. This indicates that the setup was working as expected, and there were no loose connections or deficiencies in the RF transceiver setup.

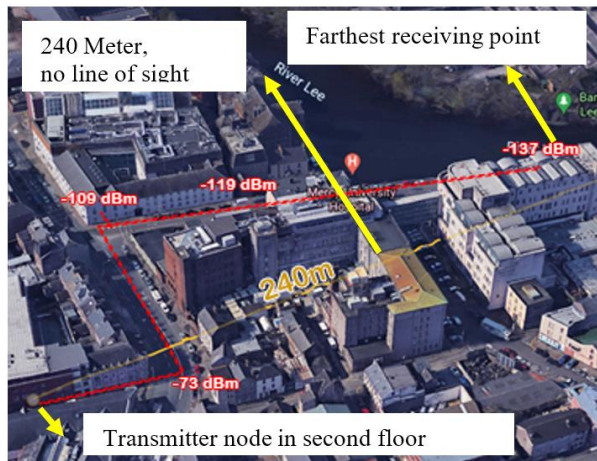


Figure 8. RF Evaluation platform air communication test.

After testing the EM waves communication in the air, River Lee in Cork [51.898757, -8.483163] was selected for performing the EM waves underwater communication test. First, the salinity of the water was measured using a salinity refractometer. “Refractometers measure the degree to which the light changes direction, called the angle of refraction. A refractometer takes the refraction angles and correlates them to refractive index (nD) values that have been established. Using these values, you can determine the concentrations of solutions” [33]. The salinity of the River Lee water was measured, and it was approximately 0%, which means that it is a freshwater river.

In the test scenario, the 868MHz transceivers were kept underwater while the receiver was recording the RSSI values. Then the distance between transmitter and receiver increased from 50cm to 120cm, as shown Figure 9. At 50cm, the average RSSI was -112 dBm, decreased to -120dBm at 100cm, however at 100cm, the percentage of packet drops increased significantly, and at approximately 120cm, the communications were significantly degraded, and the average RSSI of the limited received packets were -130dbm approximately.

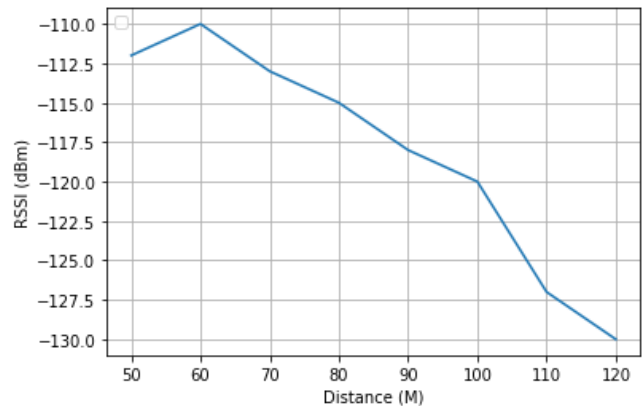


Figure 9. EM RSSI vs Distance Underwater at 868MHz.

The experiment proved that communication underwater using high-frequency, high-power radio frequencies is not an optimal solution even at a range of a few metres, as a consequence, starting from 100cm, the signals are seen to be significantly attenuated, and a stable communication link was not possible. The result is generally in line with the theoretical background, however, the signals got more attenuated possibly due to the transceivers antenna misalignment, refraction, and diffraction caused by the environmental factors in a non-ideal environment.

By validating the theoretical results for underwater electromagnetic communication, it is concluded that the solution for IMPAQT sites would be using acoustic communication rather than electromagnetic communication. In the next section, underwater acoustic communication is discussed, and the relevant telemetry platform is proposed.

**B. Underwater acoustic communication**

As in most Aquaculture sites, a long-range communications system is required to get data from the deployment site to the mainland, an ultrasonic underwater telemetry platform was developed as an alternative to the short-range EM transceiver system described in the previous section. In Figure 10, the proposed IMPAQT telemetry platform concept is shown, and this is described in the rest of this paper, and also the design method of the ultrasonic transmitter node is described. The goal of the transmitter is to transmit sensors data provided by an externally connected sensor to the gateway buoy using acoustic waves. The IMPAQT telemetry platform has been previously discussed in [34]. In comparison with the previous publication about the IMPAQT transmitter node design [34], in this publication, a simpler design with fewer components and smaller size is proposed. The on-board sensors were removed to lower the transmitter node cost, size and increase the battery life.

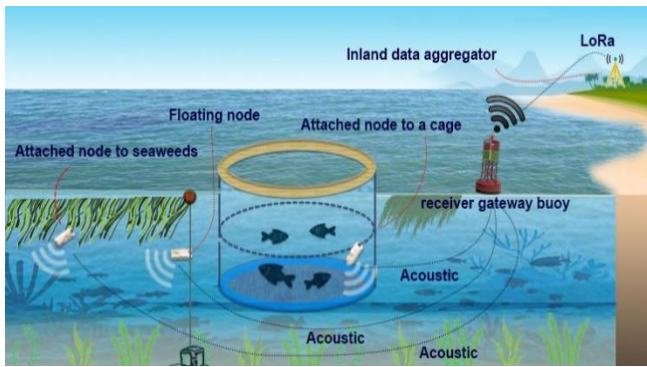


Figure 10. IMPAQT telemetry platform.

The transmitter node needs to be miniaturized to minimize its impact on the deployment environment, and the system block diagram design is shown in Figure 11.

The focus of this publication is on the detail associated with the ultrasonic transmitter design. It is anticipated that the complete transceiver platform (gateway and transmitter) and its deployment will be described in full in a follow on publication when the system as a whole is fully characterised.

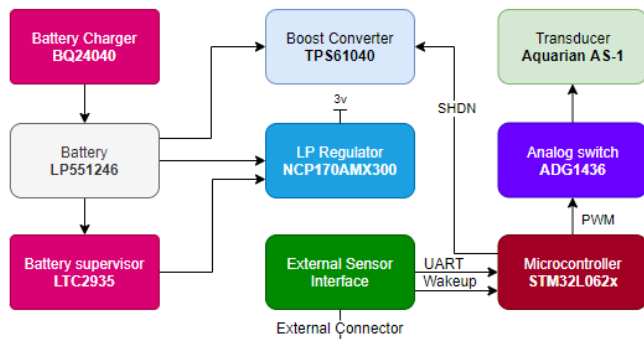


Figure 11. IMPAQT Ultrasonic Transmitter.

An ultrasonic transmitter, in the simplest form, generally consists of a transducer (usually piezoelectric) to produce acoustic waves, a transducer driver to apply the voltage and current to the transducer terminals, a controller to modulate the data, and a boost converter to step-up the battery voltage to provide adequate ultrasonic vibration wave amplitude level for the acoustic transmission. In the rest of this section, each of these elements is discussed for the IMPAQT transmitter node.

**1) Transducer Element**

Acoustic waves are the result of variations of pressure in a medium. The variation of pressure can be made by acoustic transducers. Piezoelectric materials are one the materials that are being used to convert electrical energy to mechanical displacement and vice versa. PZT (lead zirconate titanate (Pb[Zr(x)Ti(1-x)]O<sub>3</sub>)) materials are one of the widely used piezoelectric materials, and they have been used in different applications, in particular as fish tags [11][12][35]. In [36], four types of PZT materials' (Customized Type VI, Type VI, Type I, and Type II) energy consumption, source-level, and frequency response have been compared in operation. From the energy consumption aspect, PZT Type I and II consume the least amount of energy per transmission compared to other types, but they provide a lower source level and lower frequency response compared to others. However, in source level and frequency response, the difference between the four types is about 6dB, for short-range applications such as those in the IMPAQT project is not a primary factor.

As a result of the above comparison and also the availability of the commercial transducers, three commercial hydrophones have been short-listed, shown in Table I. From the provided list, for the receiver side, BII-7003 has been selected as it covers a wide range of frequencies, virtually enabling us to research various miniaturized transducers. It also has reasonable sensitivity and working depth.

TABLE I AVAILABLE COMMERCIAL HYDROPHONES

Manufacturer Part number	Frequency range	Receiver Sensitivity (dB re 1 V/ $\mu$ Pa)	Working depth (m)	Type
BII-7003 [37]	1 Hz to 560 kHz	-211	400	Type I
AS-1 [38]	1 Hz to 100 kHz	-208	200	Type II
H3 [39]	10 Hz to 100 kHz	-192	80	Type II

For the transmitter, AS-1 from Aquarian scientific was selected since it has a wide frequency range of 1Hz to 100kHz, and it is compact in size with a good working depth appropriate for the IMPAQT application. It is encapsulated in a polyurethane material, and its dimension is 12mm D x 40mm L; it can operate up to 200m depth. It is important to note that AS-1 can act as a transmitter and also receiver. In transmitter mode, the transmitting sensitivity is 140dB SPL re 1 $\mu$ Pa, 1 Vrms input at 1 meter, at 90kHz frequency [38].

## 2) Acoustic path loss and transducer driver

The pressure of the acoustic waves produced by a transducer has a direct relationship with the voltage applied to the transducer's terminal. To estimate the required driving voltage for the piezo transducer, to provide sufficient detection range in any application, it is necessary to understand underwater acoustic models and associated signal path loss. The ultrasonic wave emitted by the piezo transducers is attenuated by two main factors in an aquatic environment, spherical spreading loss and absorption loss [40]. The absorption loss coefficient ( $\alpha$ ) depends on two variables, viscous absorption [41], and chemical relaxation effect [42]. Viscous absorption is significant at high frequency (above 100 kHz). At the low-frequency range (up to a few kHz), boric acid chemical relaxation is the primary source of absorption and for intermediate range (up to few 100 kHz) magnesium sulphate is the main source of absorption [43]. In the IMPAQT Project, the ultrasonic frequency range will be used to communicate, and in the ultrasonic frequency range, viscous absorption and the magnesium sulphate relaxation effect is seen to be significant. The absorption loss coefficient ( $\alpha$ ) can be estimated by the following simplified equation [43] :

$$\alpha = 0.106 \frac{f_1 f^2}{f^2 + f_1^2} e^{(pH-8)/0.56} + 0.52 \left( 1 + \frac{T}{43} \right) \left( \frac{S}{35} \right) \frac{f_2 f^2}{f^2 + f_2^2} e^{-z/6} + 0.00049 f^2 e^{-\left(\frac{T}{27} + \frac{z}{17}\right)} \quad (2)$$

Where in the proposed design and operating environment,  $f=42\text{KHz}$  (Piezo resonance frequency),  $T = 8^\circ\text{C}$  (water temperature),  $S = 35\text{ppt}$  (seawater salinity),  $pH = 8.1$  (current ocean pH level [44]),  $z = 50\text{m}$  (estimated working depth), and relevant relaxation frequencies are:

$$f_1 = 0.78 \left( \frac{S}{35} \right)^{\frac{1}{2}} e^{\frac{T}{26}} \quad (\text{for boron}), \quad (3)$$

$$f_2 = 42 e^{\frac{T}{17}} \quad (\text{for magnesium}). \quad (4)$$

Using (2) by substituting the parameters, an absorption loss of 12.3 dB per kilometer has been estimated for an infinitely narrow acoustic beam; however, in practice, beams spread as they propagate through the water, and as their area increase, they lose more power. If a transducer radiates waves equally in all directions, the waves will spread spherically from it. Thus, the transmission loss due to the spherical loss can be estimated using the following equation:

$$TL_1 = 20 \log R \quad (5)$$

Where  $TL_1$  is the transmission loss due to the spherical loss, and  $R$  represents the distance from the source in metre. It is important to note that  $R$  is the horizontal distance in water

rather than depth. Using the equation (2) and (5), the transmission loss (TL) at the distance of  $R$  can be estimated using equation (6) [40]:

$$TL = TL_1 + \alpha R \quad (6)$$

In the IMPAQT project, a maximum distance of 100m is considered between the transmitter and receiver nodes, which leads to an overall transmission loss of 41.2 dB at 100m. There is an online absorption loss calculator provided by *National Physical Laboratory of United Kingdom*, that can be useful to estimate the absorption loss coefficient [45]. The transmission loss as a function of distance for 42 KHz frequency (for the IMPAQT project) is shown in Figure 12.

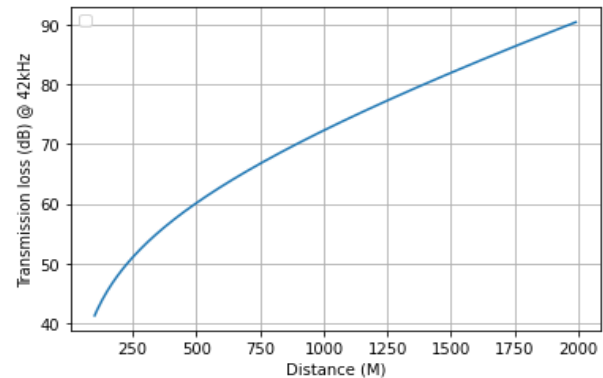


Figure 12. Acoustic transmission loss vs. Distance at 42kHz.

To provide an adequate ultrasonics level, a voltage booster circuit has been implemented using the TPS61040 controller, which can boost the 2.5-3.7v (LiPo cell voltage) up to 28v. In the proposed transmitter design, a voltage booster is configured to boost the voltage to 20v. Having a voltage over 25V requires capacitors in the voltage range of 50V, which are bulky and not suitable for a miniaturized system. Hence, it has been decided to use 20V as the driving voltage level. It is 5V less than the maximum voltage of the capacitors, but it provides a safe margin in case of a high-voltage ripple when driving the transducer. The average current of the piezo transducer can be estimated by (7) [46] :

$$I_{Avg} = \frac{2Q}{T} = 2CVf \quad (7)$$

Where  $Q$  = Charge in the piezoelectric transducer,  $T$ =Period of the driving signal,  $C= 5\text{nF}$  (Static capacitance),  $V = 20\text{v}$  (Maximum Driving voltage),  $F = 42\text{KHz}$  (Resonance frequency). Using the parameters of the selected hydrophone, the average current would be about 8.4mA while transmitting at the highest sound level. At  $F=100\text{KHz}$ , the average current of AS-1 transducer would 24.72mA. It is important to note that these current consumptions are from 20v (boosted voltage) supply. If needed, these values can be converted to the equivalent current drawn from the battery using the Electrical Power (P) equations [76] and booster efficiency value.

As the on-board microcontroller cannot handle the boosted voltage level and also cannot handle the required current directly, a driver is needed to supply the voltage and current to the ultrasonic transducer. The driver should be able to perform driving at the designated frequency (42KHz), and it needs to be low power and small size. Hence, an ADG1436 analog switch IC has been used to drive the piezo terminals at the boosted voltage using PWM modulation provided by the microcontroller. ADG1436 has a 4mm x 4mm footprint, with 125ns transition period; theoretically, it can reach up to 8MHz input frequency, which is significantly above 42kHz.

### 3) Sensors and external interface

In the previous publication regarding the first design of the tag, an accelerometer sensor (LIS3DH), and a pressure and temperature sensor (MS5837-30BA) were included in the IMPAQT transmitter tag design to monitor the aquaculture environment and tag's movement. In the latest version of the transmitter, these embedded sensors were considered surplus to requirements for the use case in question and that the transmitter would be used in conjunction with external environmental sensors. The external infrared sensor interface, TFBS4650, was also removed, as it required a specific external sensor design with infrared interface capabilities to be able to communicate with the tag. The infrared communications interface was replaced with a wired serial UART connector, which simplifies the integration of the tags with other commercial-off-the-shelf sensors. Removing the internal sensors and also the infrared interface not only reduced the transmitter's cost significantly but also improved the expected battery life. It also simplifies the transmitter's integration so that other researchers may be able to use it with few modifications in their own systems and sensors in the future.

In the latest version of the node, external sensors can trigger the IMPAQT transmitter node to wake up from sleep mode to read the external sensor's data using the wake-up pin fitted on the external connector. Also, there is an option to schedule a program for the node to wake up and read the external sensor data and transmit the collected data.

### 4) Power consumption and battery management

The transmitter tag runs on a 1200mAh LiPo battery with the Part number LP503562 [47]. There is a compact battery charger and a battery supervisor circuit on the board to charge and cut off the battery in the case of a full discharge. The transmitter consumes 10.5 $\mu$ A in the sleep mode, 62545 $\mu$ A in the transmitting logic-one, and 1290 $\mu$ A in transmitting logic-zero (refer to Table II, which is based on data available on individual product datasheets) and considering the 1200mA battery, based on user configuration and desired transmission cycle, the battery can last from two weeks to six months. The current consumption for the STM32 microcontroller is estimated using STM32CubeMX microcontroller power profile estimator.

TABLE II COMPONENTS POWER CONSUMPTION

Component	Sleep current ( $\mu$ A)	Max Supply Current ( $\mu$ A) when transmitting logic-one	Max Supply Current ( $\mu$ A)- when transmitting logic-zero
BQ24040	1	1	1
LTC2935	0.5	0.5	0.5
TPS6104	1	25	25
NCP170AMX300	0.5	0.9	0.9
ADG1436	1	170	170
STM32L062x	0.41	1150	1093
AS-1 [38] + 10m Cable	0	61200	0
<b>Total</b>	<b>4.41</b>	<b>62547.4</b>	<b>1290.4</b>

To maximize the battery life, the tag can be programmed via an external interface to wake up and read the sensor's data at regular intervals, while also an external sensor or module can force the tag to wake up using the wake-up pin.

## IV. COMMUNICATIONS TEST RESULTS

The transceiver system prototype boards, shown in Figure 13, have been developed and evaluated in seawater, and 100 bits per second achieved using on-off-keying at 42KHz modulation frequency at the range of 92m.

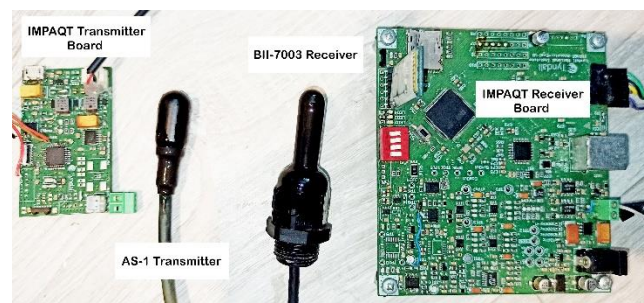


Figure 13. IMPAQT telemetry platform evaluation board.

Regarding the communication range test, the system was evaluated in the Cork Harbour Marina pier (51.845202, -8.332210), shown in Figure 14.

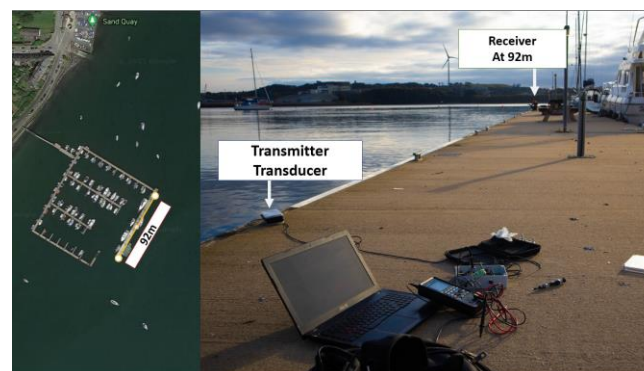


Figure 14. Range test in Cork Harbour Marina.

During the test, the signal to noise ratio (SNR) value has been recorded while increasing the distance between the transmitter and receiver up to the range of 92m. The same test was carried out at two different depths to study the effect of depth on the SNR value. The SNR values are shown in Figure 15, and it can be seen that by increasing the depth, the SNR improved. This was concluded to be as a result of noise affecting the signal from the water surface and terrestrial environment, and also less sound reflection from the water surface. The G percentage shows the receiver gain, which was adjusted based on the distance. The 100% gain in the receiver board is equivalent to 52dB, and 6% is 3.12 dB.

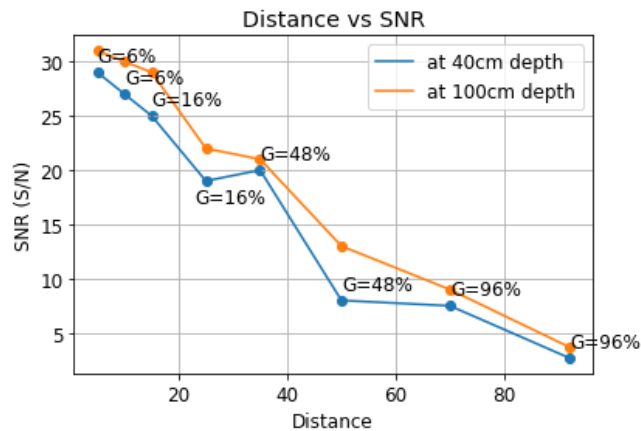


Figure 15. Distance vs Acoustic SNR in seawater.

In addition to the deployment tests in a real marine environment, a collection of analog datasets has been captured in a tank environment, which is accessible in a GitHub repository for further studies and analysis [48]. The dataset contains the captured signal by the receiver board where the transmitter was transmitting a fixed batch of data in on-off-keying modulation and binary-phase-shift-keying modulation. A sample captured dataset is shown in Figure 16, where (B) is the ground-truth data that transmitted, (A) is the binary-phase-shift modulation received on the receiver side, and (C) is the On-Off-Keying modulation received on the receiver side.

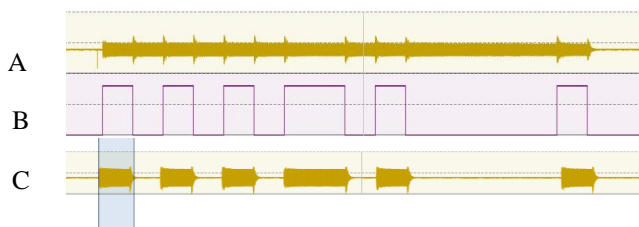


Figure 16. A sample dataset visualization in PulseView Software.

- A) Captured BPSK signal    B) Ground truth binary data  
C) Received OOK signal

The datasets for each modulation are provided independently, and in the above figure, they merged for demonstration purposes only.

## V. CONCLUSION AND FUTURE WORK

By evaluating electromagnetic communications underwater, it is concluded that it is not suitable for far-field communications other than for extremely short-range applications, as the communication got blocked at approximately 100cm range at 868MHz transmission frequency, using high-power LoRa modules. An alternative longer-range communications mechanism was investigated by evaluating the effective parameters in acoustic communication underwater, and finally, the IMPAQT next-generation ultrasonic transmitter has been proposed. This ultrasonic transmitter using an acoustic transmitter and a gateway buoy can help farmers and researchers to monitor and analyze the underwater environment wirelessly. It also enables the researchers to develop sensors and deploy them in the water without the need for a cable to be connected. The main novelty of this work is its size, the novel low-cost transmitter design, and that it is designed to be attachable to other sensors and modules with multiple sensor interface options.

In the future, more studies can be done on the optimization of the battery consumption, bitrate improvement, and a more miniaturized design. Also, there would be an opportunity to connect the tag to the sensors developed by other colleagues in the IMPAQT project to provide a better understanding of underwater environments.

Based on the components that have been selected, it is estimated that the final dimension of the tag would be less than 4 cm x 2 cm x 2 cm. This system will be tested in an aquatic environment alongside other sensors developed by the partners in the IMPAQT project and will report on in a subsequent publication.

This project is a work in progress, and it is considered to improve aquaculture sites monitoring as a part of the IMPAQT project, which is ongoing, and deployment in the marine environment are planned for the coming period.

## ACKNOWLEDGMENTS

This work is part of IMPAQT project (<https://impaqtproject.eu/>) – and it has received funding from the European Union's Horizon 2020 research and innovation programme under Grant Agreement No 774109. Aspects of this publication have been funded in part by a research grant from Science Foundation Ireland (SFI) - co-funded under the European Regional Development Fund under Grant Number 16/RC/3835 – VISTAMILK and 13/RC/2077 - CONNECT.

## REFERENCES

- [1] H. Jafarzadeh, M. Belcastro, and B. O'Flynn, "IMPAQT Miniaturized Underwater Acoustic Telemetry Platform: Transmitter Node System Design," in *Proc. SENSORCOMM*, Nov. 2020, pp. 34–37. 2021.05.14. [Online]. Available: [http://www.thinkmind.org/index.php?view=article&articleid=sensorcomm\\_2020\\_1\\_60\\_10031](http://www.thinkmind.org/index.php?view=article&articleid=sensorcomm_2020_1_60_10031)
- [2] "World Population Prospects - Population Division - United Nations." <https://population.un.org/wpp/Graphs/DemographicProfiles/Line/900> 2020.09.16.
- [3] "Seafood production: wild fish catch vs aquaculture," *Our World in Data*. <https://ourworldindata.org/grapher/capture-fisheries-vs-aquaculture-farmed-fish-production> 2020.09.16.
- [4] "IMPAQT – Intelligent Management Systems for Integrated Multi-Trophic Aquaculture." <https://impaqtproject.eu/> 2021.05.18.
- [5] U. Acar *et al.*, *Designing An IoT Cloud Solution for Aquaculture*. 2019, p. 6. doi: 10.1109/GIOTS.2019.8766428.
- [6] "OLCreate: PUB\_4560\_1.0 Integrated Multi-Trophic Aquaculture and Precision Aquaculture." <https://www.open.edu/openlearncreate/course/view.php?id=7116> 2021.08.08.
- [7] K. Michalek, A. MacLeod, A. Ditchfield, and M. Stanley, *Towards an Intelligent Management System for Integrated Multi-Trophic Aquaculture*. 2019.
- [8] E. Baras and J.-P. Lagardère, "Fish telemetry in aquaculture: review and perspectives," *Aquac. Int.*, vol. 3, no. 2, pp. 77–102, Jun. 1995, doi: 10.1007/BF00117876.
- [9] M. Føre *et al.*, "Precision fish farming: A new framework to improve production in aquaculture," *Biosyst. Eng.*, vol. 173, pp. 176–193, Sep. 2018, doi: 10.1016/j.biosystemseng.2017.10.014.
- [10] J. A. Martos-Sitcha *et al.*, "Ultra-Low Power Sensor Devices for Monitoring Physical Activity and Respiratory Frequency in Farmed Fish," *Front. Physiol.*, vol. 10, 2019, doi: 10.3389/fphys.2019.00667.
- [11] P. R. de Almeida, T. J. Pereira, B. R. Quintella, A. Gronningsaeter, M. J. Costa, and J. L. Costa, "Testing a 3-axis accelerometer acoustic transmitter (AccelTag) on the Lusitanian toadfish," *J. Exp. Mar. Biol. Ecol.*, vol. 449, pp. 230–238, Nov. 2013, doi: 10.1016/j.jembe.2013.09.015.
- [12] T. N. Pearsons, "The Juvenile Salmon acoustic telemetry system : a new tool," *Fisheries*, vol. 35, no. 1, pp. 23–31, Jan. 2010, doi: 10.1577/1548-8446-35.1.23.
- [13] M. A. Weiland *et al.*, "A Cabled Acoustic Telemetry System for Detecting and Tracking Juvenile Salmon: Part 1. Engineering Design and Instrumentation," *Sensors*, vol. 11, no. 6, pp. 5645–5660, May 2011, doi: 10.3390/s110605645.
- [14] J. Lu *et al.*, "A small long-life acoustic transmitter for studying the behavior of aquatic animals," *Rev. Sci. Instrum.*, vol. 87, no. 11, p. 114902, Nov. 2016, doi: 10.1063/1.4967941.
- [15] C. Brockmann, V. Großer, J. Hefer, S. Guttowski, and H. Reichl, "Miniaturized Implantable Wireless Sensor System for Realtime Measurement of Well-Being of Fishes," in *2010 Fourth International Conference on Sensor Technologies and Applications*, Jul. 2010, pp. 453–457. doi: 10.1109/SENSORCOMM.2010.72.
- [16] "CC1101 data sheet, product information and support | TI.com." <https://www.ti.com/product/CC1101> 2021.11.29.
- [17] C. Peres, M. Emam, H. Jafarzadeh, M. Belcastro, and B. O'Flynn, "Development of a Low-Power Underwater NFC-Enabled Sensor Device for Seaweed Monitoring," *Sensors*, vol. 21, no. 14, Art. no. 14, Jan. 2021, doi: 10.3390/s21144649.
- [18] "SeaSmart AS (EN)." <https://www.seasmart.no/english.html> 2020.10.19.
- [19] "CageSense Wireless Sensors – Water Linked AS." <https://waterlinked.com/cagesense/> 2021.07.09.
- [20] C. C. Krueger *et al.*, "Acoustic telemetry observation systems: challenges encountered and overcome in the Laurentian Great Lakes," *Can. J. Fish. Aquat. Sci.*, vol. 75, no. 10, pp. 1755–1763, Dec. 2017, doi: 10.1139/cjfas-2017-0406.
- [21] B.-C. Renner, J. Heitmann, and F. Steinmetz, "ahoi: Inexpensive, Low-power Communication and Localization for Underwater Sensor Networks and AUVs," *ACM Trans. Sens. Netw.*, vol. 16, no. 2, p. 18:1–18:46, Jan. 2020, doi: 10.1145/3376921.
- [22] L. Freitag, M. Grund, S. Singh, J. Partan, P. Koski, and K. Ball, "The WHOI micro-modem: an acoustic communications and navigation system for multiple platforms," in *Proceedings of OCEANS 2005 MTS/IEEE*, Sep. 2005, pp. 1086–1092 Vol. 2. doi: 10.1109/OCEANS.2005.1639901.
- [23] I. F. Akyildiz, D. Pompili, and T. Melodia, "Underwater acoustic sensor networks: research challenges," *Ad Hoc Netw.*, vol. 3, no. 3, pp. 257–279, May 2005, doi: 10.1016/j.adhoc.2005.01.004.
- [24] L. B. Vkr, "Underwater Radio Communication," *Amateur Radio*, pp. 1–8, 1987.
- [25] G. Hattab, M. El-Tarhuni, M. Al-Ali, T. Joudeh, and N. Qaddoumi, "An Underwater Wireless Sensor Network with Realistic Radio Frequency Path Loss Model," *Int. J. Distrib. Sens. Netw.*, vol. 9, no. 3, p. 508708, Mar. 2013, doi: 10.1155/2013/508708.
- [26] C. Peres *et al.*, "Theoretical models for underwater RFID and the impact of water salinity on the design of wireless systems," *Int. J. Adv. Netw. Serv.*, vol. 13, no. 34, pp. 45–59, Dec. 2020.
- [27] "The LoPy4 is a quadruple bearer MicroPython enabled development board including LoRa, Sigfox, WiFi and Bluetooth," *Pycom*. <https://pycom.io/product/lopy4/> 2021.08.25.
- [28] "STM32F4DISCOVERY - Discovery kit with STM32F407VG MCU \* New order code STM32F407G-DISC1 (replaces STM32F4DISCOVERY) - STMicroelectronics." <https://www.st.com/en/evaluation-tools/stm32f4discovery.html> 2021.08.25.
- [29] "1554H2GYCL - Plastic Enclosure, Small, Polycarbonate, 61 mm, 119 mm, 180 mm, IP68." <https://ie.farnell.com/hammond/1554h2gycl/small-enclosure-small-pc-grey/dp/2988671> 2020.10.31.
- [30] R. G. Donmez, "A STUDY ON PATH LOSS FOR INDOOR WIRELESS COMMUNICATION NETWORKS," p. 70.
- [31] w8bya, *RF Attenuation of Common Plastics at 10 GHz*, (Jun. 28, 2020). 2021.11.03. [Online Video]. Available: [https://www.youtube.com/watch?v=-oIT\\_qjKwFw](https://www.youtube.com/watch?v=-oIT_qjKwFw)
- [32] "Tyndall National Institute - Excellence in ICT Research." <https://www.tyndall.ie/> 2021.08.25.

- [33] “What is a Refractometer & How Does it Work - Cole-Parmer.” <https://www.coleparmer.com/tech-article/refractometers> 2020.10.31.
- [34] H. Jafarzadeh, M. Belcastro, and B. O’Flynn, “IMPAQT miniaturized underwater acoustic sensors network platform,” vol. 2020, pp. A216-0010, Dec. 2020.
- [35] R. B. Mitson and T. J. Storeton-west, “A transponding acoustic fish tag,” *Radio Electron. Eng.*, vol. 41, no. 11, pp. 483–489, Nov. 1971, doi: 10.1049/ree.1971.0147.
- [36] H. Li, Z. D. Deng, Y. Yuan, and T. J. Carlson, “Design Parameters of a Miniaturized Piezoelectric Underwater Acoustic Transmitter,” *Sensors*, vol. 12, no. 7, Art. no. 7, Jul. 2012, doi: 10.3390/s120709098.
- [37] “BII-7003 Datasheet Technical document.” 2020.11.01. [Online]. Available: <https://www.benthowave.com/products/Specs/BII-7003Datasheet.pdf>
- [38] “AS-1 Hydrophone.” <https://www.aquarianaudio.com/as-1-hydrophone.html> 2020.11.01.
- [39] “H3 Technical document.” 2020.11.01. [Online]. Available: [https://www.aquarianaudio.com/AqAudDocs/H3\\_manual.pdf](https://www.aquarianaudio.com/AqAudDocs/H3_manual.pdf)
- [40] “4. FORMING THE ACOUSTIC EQUATIONS.” <http://www.fao.org/3/X5818E/x5818e05.htm> 2020.09.24.
- [41] “Calculation of absorption of sound in seawater - Underlying Physics.” <http://resource.npl.co.uk/acoustics/techguides/seaabsorption/physics.html> 2021.11.12.
- [42] “relaxation phenomenon | physics and chemistry | Britannica.” <https://www.britannica.com/science/relaxation-phenomenon> 2021.11.12.
- [43] M. A. Ainslie and J. G. McColm, “A simplified formula for viscous and chemical absorption in sea water,” *J. Acoust. Soc. Am.*, vol. 103, no. 3, pp. 1671–1672, Mar. 1998, doi: 10.1121/1.421258.
- [44] “Ocean Acidification | Smithsonian Ocean.” <http://ocean.si.edu/ocean-life/invertebrates/ocean-acidification> 2020.09.25.
- [45] “Calculation of absorption of sound in seawater.” <http://resource.npl.co.uk/acoustics/techguides/seaabsorption/2020.09.25>.
- [46] “Please tell me a current consumption by a Piezoelectric Sounder (External Drive Type). | Murata Manufacturing Co., Ltd.” <https://www.murata.com/en-us/support/faqs/products/sound/sounder/char/sch0003> 2020.09.27.
- [47] “503562 Battery document.” 2021.10.28. [Online]. Available: <https://cdn-shop.adafruit.com/datasheets/503562+1200mah.pdf>
- [48] HamedJafarzadeh, *HamedJafarzadeh/IMPAQT-Telemetry-Platform*. 2021. 2021.08.10. [Online]. Available: <https://github.com/HamedJafarzadeh/IMPAQT-Telemetry-Platform>

## Requirements Identification for Vehicle-to-Everything and Internet of Vehicles dedicated 5G Slices

Eugen Borcoci, Marius Vochin, Serban Georgica Obreja, Silvia Stanciu

University POLITEHNICA of Bucharest - UPB

Bucharest, Romania

Emails: eugen.borcoci@elcom.pub.ro, serban@radio.pub.ro, marius.vochin@elcom.pub.ro ,

silvia.stanciu@elcom.pub.ro

**Abstract** — Vehicle-to-Everything (V2X) communications, Internet of Vehicles (IoV) based on V2X and their services have been intensively studied and developed in the last decade. The V2X supports a large range of applications, such as safety oriented, vehicular traffic optimization, autonomous driving, infotainment and auxiliary operations in vehicular area. Various stakeholders/actors are playing roles in such a complex system, e.g., regulators, authorities, service or network providers, operators, manufacturers, tenants and end users. Therefore, to specify and design a specific V2X/IoV system, one should first identify the ecosystem actors and then derive in a structured way the system requirements, while harmonizing needs coming from different entities. The 5G slicing technology is seen as a strong candidate to support V2X communications, in multi-tenant, multi-domain, multi-operator and end-to-end contexts. The 5G slicing allows construction of dedicated slices, to meet particular V2X requirements. Given the large variety of environments and actors involved in a planned V2X system, the identification of the system requirements is a complex process that could benefit from a structured approach. This paper is an extension of the work presented at IARIA Mobility 2020 Conference. It contributes to develop a methodology to perform a top-down systematic identification of requirements for a V2X system supported by 5G dedicated slices. Examples from a recent research project in 5G area are given.

**Keywords** — *Vehicle-to-Everything; V2X; Internet of Vehicles (IoV); 5G slicing; Ecosystem; Business model; Stakeholders; Requirements, Software Defined Networking; Network Function Virtualization; Service management.*

### I. INTRODUCTION

This paper is an extension of a previous paper [1] published in the proceeding of the IARIA Mobility 2020 Conference.

The Vehicle-to-Everything (V2X) communications and services include several types, where X can be: vehicle (V2V), road/infrastructure (V2R/V2I), pedestrian (V2P), vulnerable road user (VRU), network (V2N) - including cellular networks and Internet, sensors (V2S), power grid (V2G) and home (V2H) [1]. The V2X systems can be deployed in single or multi-tenancy, multi-operator and multi-domain contexts. V2X support a large range of services/applications: road safety (warnings, notifications, assistance); road traffic optimization and management;

autonomous driving; infotainment. Recently, V2X has been extended to *Internet of Vehicles (IoV)* aiming to create a global network of vehicles – enabled by various *Wireless Access Technologies* (WAT) [1][2].

The V2X/IoV systems are complex, involving several technical and organizational entities, which cooperate in a business *ecosystem V2X-ES* (or, equivalently, business model *V2X-BM*). The participating entities/actors can be organizations/ stakeholders such as technology suppliers, distributors, road authorities, customers/users, municipalities, regulators, vehicle manufacturers *Original Equipment Manufacturers* (OEM), government agencies, etc. The above entities interact with each other, in order to achieve together the general goals of the system. A large variety of use cases and deployments can exist, each one having different functional and performance-related requirements. Apart from general V2X requirements, a specific set should be identified and adapted to the particular V2X-ES selected (including the use cases targeted), and also to some technological solutions and constraints.

Initially, defined as LTE V2X in 3GPP Release 14, C-V2X has been defined as a platform for an evolution track that further enables enhancements in Releases 15, 16, etc. for LTE-Advanced Pro and for the 5G New Radio (NR) [3-5].

Advanced solutions - 5G [6-8] and especially the slicing technology (based on virtualization and softwarization) - can successfully support V2X. 5G can provide dedicated types of services to satisfy various (vertical) customer/tenant demands in a multi-x fashion (the notation -x stands for: tenant, domain, operator and provider) [9-12]. A *Network Slice* (NSL) is a virtual dedicated managed network, isolated from other slices (w.r.t. performance and security), but they share the same infrastructure.

The functional components of a network slice are Physical/Virtual Network Functions (PNFs/VNFs). They are chained in graphs, in order to compose services dedicated to different sets of users. The slices are programmable and expose their capabilities to the users. The actual run-time entities are instantiated slices (NSLIs), whose life cycles are controlled by the management and control entities belonging to the *Management, Orchestration and Control* architectural Plane (MO&C).

The *Network Function Virtualization* (NFV) [13-15] and *Software Defined Networks* (SDN) technologies can cooperate [16] to manage, orchestrate and control the 5G sliced environment. The 3GPP [7][8] has defined three fundamental categories of 5G slices: *Massive machine type communication (mMTC)*; *Ultra reliability low latency communication (URLLC)*; *Enhanced mobile broadband (eMBB)*.

Several proposals of V2X systems based on 5G slicing exist, e.g., [17-21]. The V2X dedicated 5G slices can provide the required capabilities for multiple tenants, while working mono or multi-domain infrastructure. However, the basic reference slice types – like eMBB, URLLC and mMTC cannot fully solve the needs of the heterogeneous features of V2X services [20]; additional customization of V2X oriented slice is necessary.

The definition of BMs/ESs, essentially determines the entities, their roles and responsibilities in a system; out of these, one can derive the system requirements and functional architecture. In V2X area, the 5G PPP Automotive Working Group, Business Feasibility Study for 5G V2X Deployment [22]) outlined the BM picture; however, they shows a lack of a complete vision on different stakeholders roles, necessary investments, required rollout conditions, and expected profit from *Connected and Automated Mobility* (CAM) services.

This paper contributes to develop a methodology to perform a top-down and complete identification of requirements for a V2X system supported by 5G dedicated slices. The paper structure is described below. To make the paper more self-contained, the first two sections introduce the elements of the ecosystem/business model. Specifically, Section II offers a summary of ES/BMs in a 5G sliced system, while Section III completes the general ES/BMs and adapt them to 5G V2X environment. Section IV proposes our methodology for systematic requirements identification. Section V details V2X- 5G general requirements. Finally, Section VI develops the requirements identification for a V2X- 5G slice in a structured and top-down way. Section VII summarizes conclusions and future work.

## II. 5G SLICING ECOSYSTEM

This section will shortly present a few relevant ES/BMs proposed for 5G sliced systems, which will be further extended for V2X environment in Section III.

The work [10] (A. Galis), introduces a basic ES/BM for 5G slicing, including several actors:

*Infrastructure Provider (InP)* - owns and manages the physical infrastructure (network/cloud/data centre). It could lease its infrastructure (as it is) to a slice provider, or it can itself construct slices (the BM is flexible) and then can lease the infrastructure in network slicing fashion.

*Network Slice Provider (NSLP)* - is typically a telecommunication service provider (owner or tenant of the infrastructures from which network slices are constructed). The NSLP can construct multi-tenant, multi-domain slices, on top of infrastructures offered by one or several InPs.

*Slice Tenant (SLT)* - is a generic user of a specific slice,

including network/cloud/data centers, which can host customized services. A SLT can request from a *Network Slice Provider (NSLP)* to create a new slice instance dedicated to support some SLT specific services or subscribe to a convenient existing one. The SLT can also lease virtual resources from one or more NSLPs in the form of a virtual network, where the tenant can realize, manage and then provide *Network Services (NS)* (composed of *Network Functions (NFs)*) to its individual end users. A single tenant may define and run one or several slices in its domain.

*End User (EU)*: consumes (part of) the services supplied by the slice tenant, without offering them to other business actors.

The above model is operational only, i.e., it does not detail all external entities, which may influence the system architecture and functionalities, e.g., Standards Developing Organizations (SDOs), policy makers, etc. The above BM is its recursive (see Ordonez et al., [11]); a tenant can at its turn offer parts of its sliced resources to other tenants, and so on.

The 5G-PPP Architecture Working Group [7] introduces a BM in which the main entities are: *Service Customer (SC)*, *Service Provider (SP)* and *Network Operator (NOP)*. The SP role is actually an umbrella, comprising three possible sub-roles, depending on the service offered to the SC: *Communication SP*, *Digital SP* and *Network Slice as a Service (NSLaaS) Provider*. The SPs must design, build and operate high-level services, using aggregated network services. The NOP orchestrates resources, potentially offered by multiple *virtualized infrastructure providers (VISPs)* and uses aggregated virtualized infrastructure services to design, build, and operate network services that are offered to SPs. Another actor could be *Data Center SP (DCSP)*, which designs, builds, operates and offers data center services. A DCSP differs from a VISP by offering “raw” resources (i.e., host servers) in rather centralized locations and simple services for consumption of these raw resources. In practice, a single organization can play one or more roles of the above list.

Other similar models have been proposed [23-27], some of them being more refined than the basic previous one. Several recent Public Private Partnership (PPP) Phase I/II research projects have as objectives 5G technologies [10]. Some of them extended the list of role definitions, to allow various possible customer-provider relationships between verticals, operators, and other stakeholders.

## III. 5G V2X ECOSYSTEM

This section provides an extended example of ES/BM for 5G V2X. It is forecasted that advanced CAM services (e.g., high-definition (HD) maps support, highway chauffeur, tele-operated driving, platooning, fully autonomous driving, extended sensors, etc.) will be enabled through next-generation 5G V2X defined in 3GPP Release 16 specifications [4-5][24].

The 5G PPP Automotive Working Group [22] has defined a general 5G V2X-ES, capturing operational features and business relationships. One can distinguish

among *operational* BM including: *5G industry* (network operators, network and devices vendors), *automotive industry*, *road infrastructure operators*, *users* and *external entities* such as *Standards Developing Organizations* (SDOs), and *policy makers* - the latter providing input requirements for the *operational* BM (Figure 1).

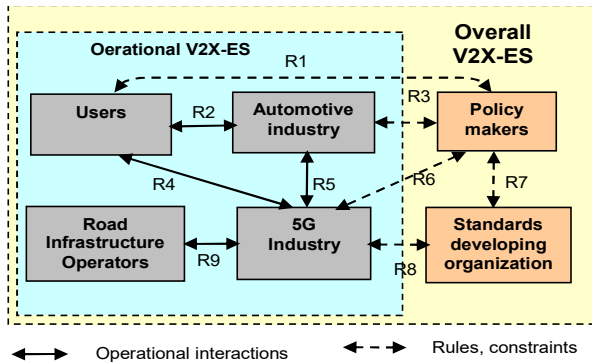


Figure 1. The main stakeholders and interactions in 5G V2X-ES (adapted from [22])

*5G industry* - includes any business entity developing or using/providing 5G-related services, e.g., *Mobile Network Operators (MNOs)*, *Telecom vendors*, *Cloud providers*, *device providers*, *software developers*, etc.

*Automotive Industry (AutoIn)* - includes car *Original Equipment Manufacturer (OEMs)* (e.g., car/component manufacturers), Tier 1 suppliers, CAM SPs HD map providers and other automotive-specific technology providers. This category brings the automotive expertise and services (including mobility services) to customers (business and consumers).

*Road Infrastructure Operators (RIO)* are national or regional entities performing deployment, operation, and maintenance of physical road infrastructure. They may also manage road traffic operations, own or operate the toll system, etc. *Users can be* drivers, vehicle owners, passengers or pedestrians.

The *external* entities are providing significant inputs to the operational V2X-ES actors, strongly influencing the requirements to be met by the overall system.

The set of SDO is large: 3rd Generation Partnership Project (3GPP), European Tele-communications Standards Institute (ETSI), Internet Engineering Task Force (IETF), Internet Research Task Force (IRTF), Institute of Electrical and Electronics Engineers (IEEE) and 5G-related alliances such as Next Generation Mobile Networks (NGMN), Industrial Internet Consortium (IIC), 5G Automotive Association (5GAA) and Automotive Edge Computing Consortium (AECC). For safety-related 5G applications (e.g., *Advanced Driver Assistance Systems - ADAS* and autonomous driving), pertinent standards developing organizations such as International Organization for Standardization (ISO) may be also relevant players.

*Policy Makers (PM)* are the highest authorities that regulate the relationships within the V2X-ES. They are international or national government authorities or

organizations defining the legal framework and policies, such as road and transport authorities or telecom regulators. The ITU as well as national spectrum regulators belong to this category.

The detailed description of the interactions between the stakeholders is given in [23]. They will influence the system requirements addressed to different functional blocks. The interactions are shortly described below.

The policy makers and SDOs provide sets of rules to the operational entities and get feedback from the latter. The interactions are: *R1 (Users - PMs)*, *R3 (PMs - AutoIn)*, *R6 (PMs - 5G Industry)*, *R8 (SDO - 5G Industry)*. The *R7 (PMs - SDO)* represents cooperation between SDOs and policy makers in order to harmonize their specifications. The interactions inside the V2X-ES operational part are: *R2 (Users - AutoIn)*, *R4 (Users - 5G Industry)*, *R5 (AutoIn - 5G Industry)*, *R9 (5G Industry - RIO)*.

Usually, the 5G network providers will own and operate most or parts of the network infrastructure. However, RIOs may participate in the deployment of 5G V2X and provide or facilitate licenses or other infrastructure requirements that are under their responsibility (PMs are also involved here). The 5G Industry shall offer communication services to the RIO based on commercial agreements.

The 5G part can be split into Radio Access Network (RAN) infrastructure provider and cloud infrastructure provider (central data centers providing virtual resources, such as computing, storage, and networking). In practice, the roles of 5G network providers can be taken by the Mobile Network Operators (MNOs), but is possible that RIOs deploys or operate (parts of) the 5G V2X network, directly providing the necessary coverage for CAM services to the users. The model in Figure 1 is general; potentially, any actor (e.g., a road operator) could invest in network deployment.

Another similar V2X-ES/BM is adopted in the research projects 5GCAR [25][26].

Actually, the variety of involved (directly or indirectly) actors and also generating requirements for a V2X-ES/BM, is still larger than that described in Figure 1. Actors providing key services for the automotive sector can be split in two major categories:

- service providers of enabling platforms, which manage the data and allow services to be built on top of the data;
- connectivity providers, which construct and manage connectivity facilities over cellular networks. Inside each category several types of actors can be included.

A non-exhaustive list of actors comprises: *Connectivity Players* (MNOs, Transport Services Providers, (TSPs), ICT Solution & Cloud Platform Providers, Intelligent Transportation System (ITS)); *Automotive OEMs* (Cars, Trucks); *Suppliers* (Tier 1 & 2 (System Integrators), Wireless Module Vendors, Chipset Vendors, Software/Solutions, Middleware, Over the Top Services Providers (OTT), Connectivity/ Bluetooth, Databases, etc.); *Application platforms* (Software - based, Fleet/ Commercial, Autonomous Driving, Smartphone Platforms); *Business Users* (Public Transport, Company Fleets, Freight, Car Rental, Taxi Fleets, Delivery systems, Emergency Response

systems); *Consumers* (End user consumers, Families, Small Office Home Office (SoHo); *Application types* (Mobility as a Service, Maps & Navigation Telematics / Tracking, Communications Safety & Maintenance, Media & Entertainment, Productivity). More than these, *additional stakeholders* can play specific roles: Insurance, Dealers, Auto Repair, Regulatory Bodies, Local Authorities (Government, Law Enforcement, Smart City, Road Operators), Location-based commerce players, Security infrastructure and services providers.

The above large picture clearly shows that the process of collecting and aggregating system requirements for a V2X system is really a challenging one and a methodology for this would be useful.

#### IV. REQUIREMENTS IDENTIFICATION METHODOLOGY

This section will outline a methodology to structure the process of system requirements identification with example of a use case - V2X system 5G-sliced based. This will be shortly named "SYSTEM".

##### A. The Business Model Impact on Requirements

The V2X-ES/BM (Section III) will be considered and particularly the operational part of the BM. The target is to identify the system requirements for a V2X-5G sliced system. The factors outside the operational BM itself will be called "external". The influence of them can be captured by some *Assumptions, Dependencies and Constraints (ADC)*.

The ADCs are expressed as *initial - general (predefined) statements* derived from both the environment in which the SYSTEM will work and from its main objectives. They can also represent *predefined restrictions* obtained from SYSTEM scope. So, the ADCs also establish the limits of the SYSTEM related to services offered, technologies used and the scope and its relationship with its environment.

The *assumptions* are factors considered to be true during the SYSTEM life cycle. If changed, they may affect negatively the system outcomes. They include, but are not limited to, End-User characteristics, technology used, resource availability, and funding availability. Some external *dependencies* may exist, that can affect the system requirements specification (SRS). They are outside of the system scope of control and must remain true for the SYSTEM life, to succeed. (e.g., an application relies on a different application, outside the SYSTEM, to get specific data).

The *constraints* are factors to be obeyed by the SYSTEM; they can impose rules, can limit the system scope and functionality, etc. Here, one can include (but not limited) regulatory policies, e.g., coming from SDOs and policy makers (see Section III, V2X-ES/BM). Also, one may have limitations related to infrastructure, technologies, resources and licensing. Constraints are imposed on the solution by circumstance, force, or compulsion. They limit the options available to the system design by imposing immovable boundaries and limits.

The ADCs may be expressed at two levels: *Business (High) level* – resulted from business or regulation

considerations; *Technical (Low) level* – usually derived from the former (expressed as technical sets or can be directly expressed in technical form.

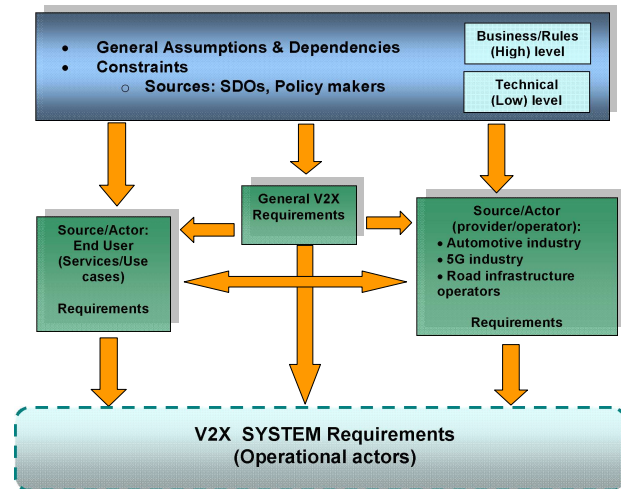


Figure 2. Requirements identification methodology for a V2X system

The *ADCs scope* is *global* to a multi-domain environment if they are related to the SYSTEM as a whole. However, the ADCs can also be applied recursively to subsystems. There can be a mapping *1-to-1* or *1-to-many* between an ADC statement and a requirement in the sense that a given ADC can induce a single system requirement or several ones.

The Figure 2 shows the relationships between entities. The general ADCs can influence directly the *General, User and Provider Requirements*. The *End-User Requirements* and *Provider Requirements* specify refinements of the assumptions from their point of view and introduce additional specific requirements, which will be finally mapped on system requirements. Two generic sources/actors issuing requirements are defined: *End-User (usage scenarios)* – defining requirements to be met by the SYSTEM in order to satisfy the high-level services scenarios and user needs; *Provider/Operator* – defining requirements to be met by the SYSTEM to satisfy the provider/operator needs (can be specific to the development, exploitation and maintenance).

A bi-directional interaction arrow between *End-User (usage scenarios)* and *Provider/Operator* may exist because: a. Some *End-User* needs will influence the *Provider/Operator* choices if wanting to satisfy the user needs; b. Some *Provider/Operator* business or technical decisions may affect or limit the range of requirements asked from the system by the *End-User*.

##### B. Requirements Taxonomy

In a simplified view, two generic actors/business entities are generating requirements: *customer* and *provider*. The customer asks services from a *provider* and therefore this induces some requirements on provider side. In a V2X system one can consider as generic customers the entities providing applications and services to real end users. The

providers could be *5G industry* (network operators, network and devices vendors), *automotive industry*, *road infrastructure operators*, etc. They may also impose a set of requirements upon the system, which is managed by it as a consequence of: some ADCs that have been already generally defined and/or some own business and technical considerations.

The requirements categories can be: *Functional* - related to the correctness, which the functions of the system should fulfil; *Non-functional* - related to flexibility, reliability, availability, scalability, security, traffic capacity, performance metrics, etc. Note that, generally, depending on the system role, some non-functional requirements can be included in the functional category (e.g., security).

One can distinguish two levels of expressing requirements: *Business/Rules (high) level* - they are resulted from business considerations or regulations; *Technical (low) level* - usually translated from the former in a set of technical ones, or can be directly expressed in technical form.

The requirements may have one of the three scopes: *Global* to a multi-domain environment, i.e., referring to a larger environment than SYSTEM scope. Such requirements will characterise the environment in which the SYSTEM will act. They are actually needed and should be fulfilled in order that SYSTEM can smoothly cooperate in end-to-end environment with other systems. Actually, these global requirements are expressed as general ADCs or derived from them; *Local* to "SYSTEM" (Local\_SYSTEM); *Local* to a subsystem of the SYSTEM (*Local subsystem*).

One can define as a *class*, a "dimension" or a "point of view" on a given requirement. Therefore, the same particular requirement may belong to several classes. We may have:

*Specific function class* - defining the specific requirements of a functionality or subsystem. On the vertical architectural vision, it is not strictly related/ limited to a given architectural layer.

*Architectural class* - related to one or more architectural layers set seen as a whole.

The degree in which some requirements have to be met are: *Mandatory: must be met* (during system validation the decision on their fulfillment is *yes* or *no*); *Trade-offs*: they are more or less quantitatively met; note that mandatory requirements could be seen in some cases as lowest limits of the trade-offs requirements.

## V. 5G V2X GENERAL REQUIREMENTS

This section will shortly present the general 5G V2X requirements, which are coming from SDOs, Policy makers, V2X application scenarios (serving the users) and 5G industry actors. Then, for different use cases, specific refined requirements should be derived.

Support of the CV2X requirements has been introduced for Long Term Evolution (LTE) in 3GPP Release 14, 15 [3], and then, with regards to 5G, Release 16 has been completed in 2019 [4-5][24].

The document 3GPP TS 22.186 V16.2.0 (2019-06) "Enhancement of 3GPP support for extended eV2X scenarios", Stage 1 (Rel.16) [4] specifies the general

requirements for eV2X based on 5G. The generic SYSTEM considered in the Section IV will be here a 3GPP System.

The service requirements to enhance 3GPP support for V2X are grouped in six areas: General aspects (interworking, communication-related requirements valid for all V2X scenarios); Vehicles platooning; Advanced driving; Extended sensors; Remote driving; Vehicle quality of service support. In a slicing solution one can design a specific slice to serve a given scenario/use case, e.g., platooning, advanced driving, extended sensors, etc., or a more complex slice could offer several services. Of course, the system requirements will strongly depend on such a choice.

As an example, advanced driving enables semi-automated or fully automated driving. Longer inter-vehicle distance is assumed. Each vehicle and/or Roadside Unit (RSU) should share data obtained from its local sensors with vehicles in proximity, thus allowing vehicles to coordinate their trajectories or manoeuvres. In addition, each vehicle should share its driving intention with vehicles in proximity. The benefits of this use case group are safer travelling, collision avoidance, and improved traffic efficiency.

A relevant aspect of eV2X applications is the *Level of Automation (LoA)*, which reflects the functional aspects of the technology and affects the system performance requirements. In accordance with the levels from SAE Int'l. Std. J3016", US Homeland Security Digital Library, "Self-Driving Cars: Levels of Automation", March 2017, the LoA are: 0 - No Automation, 1 - Driver Assistance, 2 - Partial Automation, 3 - Conditional Automation, 4 - High Automation, 5 - Full Automation. A general 3GPP system should be able to be customized for all levels of automation.

The document 3GPP [4] defines general requirements for a 3GPP system supporting V2X, to be met by any particular V2X system, irrespective if slicing technology is used or not. Considering the taxonomy developed in Section IV, these requirements are applied for the overall system and belong to the architectural class, i.e., they can affect several layers of the functional layered architecture. Given the importance of security, confidentiality and reliability capabilities in V2X systems, those specific requirements have been included in the functional categories. Note: when "User Equipment" (UE) appears in a requirement text, actually it means "UE supporting V2X applications".

### A. Functional 5G-V2X requirements-3GPP

The 3GPP system shall support

- a defined communication range for a message transmitted by a UE;
- the message transfer for group management operations as requested by the application layer;
- message transfer among a group of UEs;
- message transfer between two UEs belonging to the same group of UEs;
- confidentiality and integrity of message transfer among a group of UEs;
- relative lateral position accuracy of 0.1 m between UEs;
- high connection density for congested traffic;
- control the UL and DL reliability of transport of V2X

communications, depending on the requirement of V2X application;

- message transfer of type UE-UE and UE-[UE-type RSU] (UEs could be or not subscribers of the same PLMN);
- discovery and communication between UEs supporting the same V2X application;
- the operators to select which 3GPP RAT to use for a V2X application;
- a UE to obtain network access via another UE supporting V2X application;
- a UE to discover another UE supporting V2X application that can offer access to the network;
- switching between direct 3GPP connection and indirect 3GPP connection via a UE;
- confidentiality and integrity of message transfer between a UE and network, when the UE is using an indirect 3GPP connection;
- a UEs to use *New Radio (NR)* direct communication when the UEs are not served by a RAN using NR;
- UEs to use *E-Universal Terrestrial Radio Access (E-UTRA)* for direct communication when the UEs are not served by a RAN using E-UTRA;
- an RSU to be able to communicate with up to 200 UEs;
- confidentiality and integrity of message transfer between a UE and a V2X application server;
- provision of addressing information (e.g., IP address) of V2X application server(s) to the UEs;
- the UE to use multiple 3GPP RATs (i.e., NR & E-UTRA) simultaneously for direct communication.

#### B. Non-functional 5G-V2X requirements

The 3GPP system shall

- optimize the communication between UEs belonging to the same group and in proximity;
- support efficient coordination of radio resources used (spectrum utilization and reliability);
- minimize the impact to E-UTRA(N) by UE supporting only New Radio (NR) based V2X communication;
- minimize the impact to NR by UE supporting only E-UTRA based V2X communication;
- in case the UEs are subscribers to different PLMNs, there shall be no service degradation of the message transfer.

#### C. Other 5G V2X General Requirements

Apart from requirements defined in Subsection A, still more general requirements can be identified, for 5G V2X systems and also specific ones, in order to support V2V, V2I, V2N, V2P, V2S, V2H scenarios in multi-domain, multi-operator/provider, multi-tenant contexts.

Let us consider for instance, the Mobile Network Operator (MNO) as a principal actor belonging to the 5G Industry category, in a general 5G-V2X-ES/BM environment. Usually, the MNO owns and manages the physical and logical (virtualized) infrastructure, to support the above services. Specific sets of requirements can be identified for 5G dedicated slices, provided by MNO, for

V2V, V2I, V2N, etc. However, more general aspects are still open issues in V2X area.

For critical vehicle functions and improved safety, connectivity is demanded from MNO but also for the delivery of audio, video, social media access and location-based services, among others, in daily driving. However, there is still lack of flexibility for vehicle owners to choose the MNO to serve their vehicles. Currently, the connected service packages integrated in vehicles are limited to a single designated provider. From a business perspective it is a future requirement that vehicle owners may select their MNO, as they do for their smart phones today. So, interoperability of vehicles among available cellular networks will ensure redundancy for critical safety features and will result in better value and service for consumers. Such a multi-MNO model is proposed in the work [28][29] as an extended business model including several MNOs, while sharing the same infrastructure. Also, some other entities are defined in the BM, e.g., location-based services providers, cloud providers, intermediate bodies, etc.

The mobile system should provide “predictive QoS”, i.e., inform the vehicle of connectivity quality changes to be provided in the future so that the vehicle could decide to switch from autonomous driving mode to manual driving mode (factors: weather conditions, road situation, network availability at the vehicle position/location, etc.).

#### D. General requirements for applications

The large range of V2X applications generates a lot of requirements. Here we only give some examples of general requirements [31]. We denote with VAE, a *V2X Application Enabler*. Considering the taxonomy of the Section IV the requirements below belong to the architectural class and are focused mainly on the functional application layer.

- The VAE client and the VAE server shall support
  - o one or more V2X applications;
  - o obtaining information of the available V2X services (e.g., identified by V2X service ID) from the V2X application;
  - o obtaining information of the associated geographical area from the V2X application;
- The VAE client shall be able to communicate to multiple VAE servers
- The VAE capabilities should be offered as APIs to the V2X applications;
- the VAE capabilities shall enable V2X UEs to obtain
  - o the address of available V2X application servers associated with served geographical area information;
  - o the information of available V2X services (e.g., identified by V2X service ID).

Specific requirements are defined for V2X group communication, V2X dynamic groups, File distribution capability, V2X application message distribution, Service continuity.

TABLE I. PERFORMANCE REQUIREMENTS FOR ADVANCED DRIVING (simplified, adapted from [4])

Note 1: The reliability required for all scenarios is higher than 99.9%

Note 2: All UEs are supposed to support V2X applications.

Communication scenario description		Payload (Bytes)	Tx rate (Message/Sec)	Max E2E latency (ms)	Data rate (Mbps)	Min required Communication range (meters) (NOTE 4)
Scenario	Automation Degree					
Cooperative collision avoidance between UEs		2000 (NOTE 5)	100 (NOTE 5)	10	10 (NOTE 1)	
Information sharing for automated driving between UEs	Lower	6500 (NOTE 1)	10	100		700
	Higher			100	53 (NOTE 1)	360
Information sharing for automated driving between UE and RSU	Lower	6000 (NOTE 1)	10	100		700
	Higher			100	50 (NOTE 1)	360
Emergency trajectory alignment between UEs		2000 (NOTE 5)		3	30	500
Intersection safety information between an RSU and UEs		UL: 450	UL: 50		UL: 0.25 DL: 50 (NOTE 2)	
Cooperative lane change between UEs	Lower	300-400		25		
	Higher	12000		10		
Video sharing between a UE and a V2X application server					UL: 10	

NOTE 1: This includes both cooperative maneuvers and perception data exchanged using two separate messages within the same period of time (e.g., required latency 100ms).

NOTE 2: This value is referring to a maximum number of 200 UEs. The value of 50 Mbps DL is applicable to broadcast or is the maximum aggregated bitrate of all the UEs for unicast.

NOTE 3: Sufficient reliability should be provided even for cells having no values in this table

NOTE 4: This is obtained considering UE speed of 130km/h. Vehicles may move in different directions.

NOTE 5: These values are based on calculations for cooperative maneuvers only.

### E. Example of 5G V2X Requirements for Specific Scenarios : Advanced Driving

Specific scenarios have different requirements; therefore, a slicing approach is attractive. As an example, the TABLE I shows the performance requirements for a 5G-V2X system, dedicated to advanced driving adapted from [4]. The requirements are coming from the use cases scenarios. Their level is *Technical (low)*, specifying quantitative ranges for different parameters. Their scope is system-wide, i.e., addressed to the system as a whole. However, after defining the system architecture and subsystems, these requirements should be mapped on those specific subsystems mainly involved to contribute to achieving the required ranges.

Similar examples of technical requirements are identified in [4] for other scenarios like Vehicles platooning, Extended sensors, Remote driving and Vehicle quality of service support.

## VI. 5G V2X SLICING REQUIREMENTS

The slicing solution to realize 5G V2X systems should of course take into account the general requirements issued by different participating actors in the 5G V2X ES/BM. However, it has been shown (C. Campolo, [20]) that V2X services require complex features, which do not map exactly on the basic reference slice types: eMBB, URLLC and mMTC. Therefore, dedicated V2X slicing solutions have

been proposed [17][20][30]. This paper space does not allow to detail and structure all the aspects of 5G V2X slices requirements in the manner presented in Section IV. So, an outline of more relevant challenges will be presented here.

*Traffic safety and efficiency* oriented slices (use cases - V2V, V2P, V2I) should be able to: transport and process periodic and event-driven messages (carrying position and kinematics information of vehicle); allow vehicles to broadcast messages to surrounding environment; assure low latency and high reliability requirements.

*Autonomous driving* oriented slices (use cases - V2V, V2I, V2N) should: enable ultra low-latency V2V RAT connection mode; support additional RAN/Core Network (CN) functions (e.g., for network-controlled resource allocation over the interface PC5 - in eNBs); support mobility, authentication, authorization and subscription management (in Mobility Management Entity – MME and Home Subscribers System – HSS ); support low-latency and reliable video/data exchange needs by the V2X Application servers (AS), deployed at the network edge.

*Tele-operated driving* slices should: assure ultra-low latency and highly-reliable E2E connectivity between the controlled vehicle and the remote operator (typically hosted outside the CN; data flows passes through a Packet Gateway P-GW); identify the special circumstances in which such services should be activated.

*Vehicular Internet and Infotainment* slices should be able

to use multiple RATs to get a high throughput; the contents can be located in the remote/edge cloud (e.g., server co-located in eNodeBs via *Multi-Access Edge Computing technology* - MEC); multiple MME instances may be required depending on the users mobility degree.

Vehicle management and remote diagnostics slices should support the exchange of low-frequency small amounts of data between vehicles and remote servers outside the core network; the architectural Data Plane and Control Plane should handle multiple interactions.

The general approach of V2X 5G slicing involve multi-tenant, multi-domain multi-operator and E2E capabilities. E2E V2X slices need dynamic composition of different slice instances in the RAN and in the CN segments; e.g., some functions in CN can be shared by several specific slices (authentication/ authorization), while each slice in RAN domain could be differently customized.

3GPP proposed for slices creation a multi-dimensional slice descriptor. It contains among others: *Tenant ID* (e.g., the car manufacturer, the road authority), *Slice Type* (e.g., vehicular infotainment, remote diagnostic), but also some additional specific parameters like: position/kinematics parameters.

A vehicle can be a multi-slice device, able to simultaneously attach to multiple slices.

Multi-tenancy and multi-operator capabilities raise several new requirements given that different providers can offer different services mapped onto different slices, over the infrastructure owned by different network operators. Optimal Resource allocation between domain-scoped slices composing a general E2E slice generates a rich set of functional and security performance requirements.

## VII. EXAMPLE OF A 5G V2X SLICED SYSTEM

This section will present a 5G system oriented towards

IoV/V2X services and maritime applications, “A Massive MIMO Enabled IoT Platform with Networking Slicing for Beyond 5G IoV/V2X and Maritime Services” - SOLID-B5G [31] (<https://solid-b5g.upb.ro/>). (see Figure 3). Requirements identification (after defining the target use cases) is an important activity, supporting further the architecture definition and then the system design.

The objectives of the SOLID-B5G project are the following:

- O1: To develop ultra-low latency massive MIMO based concurrent transmission mechanisms for data collection in massive IoT;
- O2: To develop advanced B5G slicing methods, algorithms, and protocols with a focus on Orchestration Management and Control (OMC) of resources and dedicated services for IoV/V2X and maritime services;
- O3: To develop decentralized decision-making mechanisms by introducing data processing capacity and intelligence to the edge (based on Multi-access (Mobile) Edge Computing (MEC) and machine learning (ML)-to-the-edge);
- O4: To implement a proof-of-concept *standalone* B5G testbed to demonstrate the orchestration of RAN and CN based on 5G network slicing and MEC procedures. Two main categories of use cases, i.e., IoV/V2X and satellite based maritime low-latency will be considered.

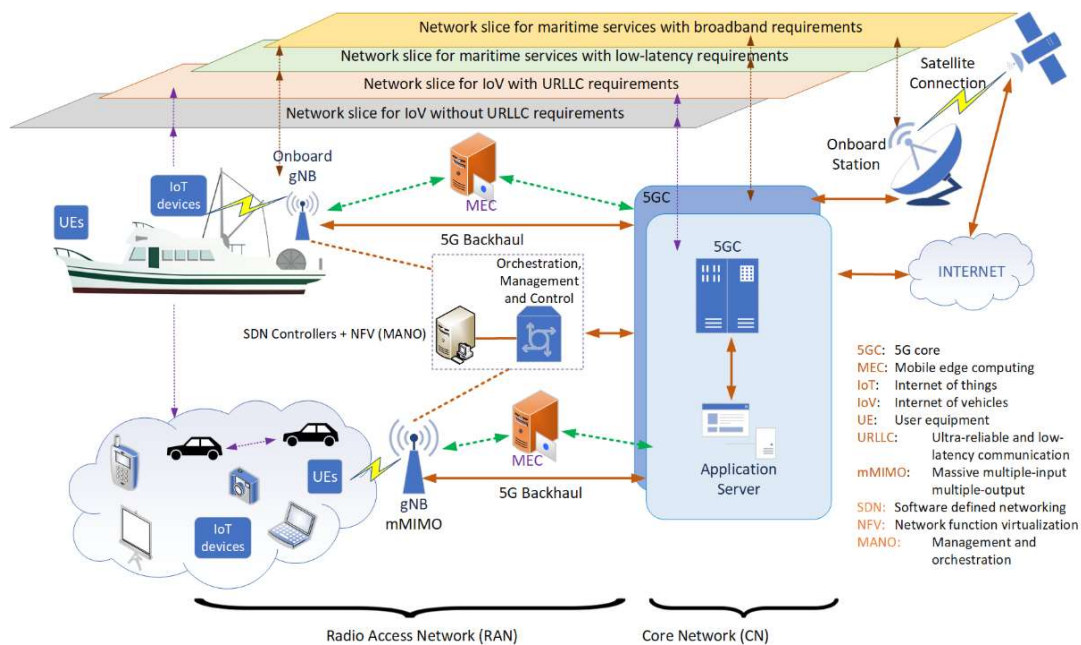


Figure 3. SOLID-B5G system architecture - high level view

One goal of the the SOLID-B5G project is develop a study and contributions in the domain of V2X/IoV systems based on 5G slicing solutions. The basic three types of 3GPP-defined slices, i.e., ultra- reliable low-latency communications (URLLC), enhanced mobile broadband (eMBB) and massive machine type communications (mMTC), will be investigated.

*5G URLLC-type slices* are appropriate to support e.g., *automated driving, road safety and traffic efficiency* services, etc., given that many such V2X use cases and associated scenarios can be considered as latency sensitive applications. The cars can be fully connected and can react to complex road situations by cooperating with each other. The information is disseminated among vehicles reliably within short time duration. On top of an URLLC slice, vehicles can perform V2V or V2I communications. The typical UCs supported are automated overtake, cooperative collision avoidance and highdensity platooning, which require an end-to-end latency of 5–10ms and a BLER down to  $10^{-5}$  [32].

URLLC is supported by 5G New Radio (NR), as specified in 3GPP Release 15 and Release 16. Typical requirements are  $\sim 1$  ms for latency, end-to-end security, small data packet loss of  $10^{-5}$  and high reliability  $\sim 99.999\%$ . [33]. The URLLC is useful when events occur and warning, alarm, etc. are necessary to be triggered, with very small delay and high reliability. Usually, the URLLC transmissions are aperiodic and are supported by appropriate scheduling (grant-based, grant-free/configured grant scheduling) to guarantee high reliability and efficient resource usage. The requirements for such sporadic communication still ask for predictability of available resources, diversity using multiple frequencies or spatial resources in addition to random access.

UCs like *platooning, remote driving, advanced driving, and extended sensors* require low latency  $\sim 1$  ms and reliability of up to 99.999%. Open research issues in V2X supported by URLLC are related to resource allocation, energy savings, etc. Given the specific needs of V2X/IoV and also IoT for maritime systems the project will also apply decentralized solutions like Multi-access Edge Computing (MEC), in a sliced environment. Therefore, an important challenge is MEC-URLLC integration, to improve latency, throughput and computation -intensive processing. Additional system requirements appear in this solution.

*eMBB- type slices* are supported by 5G new radio (NR) and to increase the data rate in data-driven UCs that require high data rates across the coverage area, and to ensure reliability with a packet error rate in the range of  $10^{-3}$ . The services that can be supported by eMBB are virtual reality, augmented reality and direct video transmission in UltraHD or 360 degrees while respecting the latency and reliability requirements; such services can be also useful in IoV/V2X

domain [33]. The advanced V2X use cases need high data rate requirements. eMBB with 10 Gbps for uplink and 20 Gbps for downlink channel are important solutions for various multimedia services (e.g., in-car video conferences/games, HD map downloading). eMBB Slices can serve vehicles on the highway with heterogeneous traffic requirements. Slices for autonomous driving safety messages and infotainment and video streaming can also be constructed. eMBB are important for V2X applications, e.g., when high data rates requirements exist for the extended sensors group or sharing high-precision video as in the case of remote driving. eMBB even has non-safety applications such as infotainment and multimedia services.

*mMTC-type slices* are appropriate for sporadic and data is transmitted randomly, but for a high number of connected machines/objects. The geographical area is wider and the objectives are low-power, low-cost, low complexity, and low transmission rate communications with a packet error rate of  $10^{-1}$  [34]. The number of active devices using radio resources is variable, so it is necessary to have random access to resources. Narrowband IoT (NB-IoT) and enhanced MTC(eMTC) are specified by 3GPP to support long and medium range IoT applications respectively and can meet 5G mMTC needs. With mMTC slices, vehicles can sense and learn environmental changes from built-in sensors deployed in cars or within infrastructure. mMTC is also important within a dense connected environment to support non-delay-sensitive V2X applications (e.g., dynamic ride sharing, software update) or even to provide more data for safety-related applications [33].

Generally, two types of dedicated slices URLLC and non-URLLC will be considered in the project, for two categories of applications:

*Safety and traffic efficiency slice-* for V2V and vehicle-to-pedestrian (V2P). Such slices will transport and process *event-driven* and *periodic* messages containing position and kinematics parameters and support applications such as: forward collision warning; cooperative adaptive cruise control that allows a group of vehicles in proximity to share the same path (a.k.a. platooning); vulnerable road users (VRU) safety to alert a vehicle of the presence of a VRU;

*Autonomous driving slice* – having more powerful characteristics than those for safety applications, the reason being higher speed, more complex environment- including geographical and road-related aspects, cooperative needs, etc. Such slices can offer ultra-low-latency V2V communications via RAT connection mode and additional RAN/CN functions.

## VIII. CONCLUSIONS AND FUTURE WORK

This paper had as objective to develop a systematic procedure for V2X system requirements collection and apply it on examples of implementation solutions based on a

5G sliced infrastructure. First, the paper introduced the ecosystems/ business models (ES/BM), given that the system requirements are issued by the participating actors.

It has been shown that business models/ecosystems for 5G V2X systems are considerably richer than those for basic 5G slicing. The reason consists in large set of V2X applications and variety of commercial services offered.

A general methodology is proposed to structure the process of system requirements identification. Considering the above, examples of V2X system requirements have been exposed.

Several steps should be followed to identify the system requirements. First, the V2X set of high level of services (seen from the end user perspectives) to be implemented should be defined among the rich possible ones. Then, the identification of the set of involved actors and a first assignment of their roles (especially from business/services point of view) is the next step. Here, some actors would provide only indirect actions (Policy Makers, SDOs, local regulators, etc.). Other actors will participate at operational phases (MNOs, OEMs, Service providers - e.g., OTT, Infrastructure providers, etc.) at run-time.

Some general characteristics of the overall system should be defined such as multi-domain, multi-tenant, multi-operator characteristics. Definition of interactions between the actors will complete the high-level description of the 5G V2X BM/ecosystem. The regulations, standards, etc., to be enforced have to be identified; they will define but also limit the system capabilities and scope.

The following steps will refine the BM and go to the requirement identification, where inputs coming from all actors involved in ES/BM should be considered.

To refine the requirements for a 5G V2X slicing solution, it is necessary to select technologies for RAN, core and transport part of the network) should be selected. Then, the system architecture (general and layered - functional) has to be defined, allowing further technical refinement of the system design.

An example is given of a system based on 5G slicing in a research project SOLID-B5G, aiming V2X/IoV and maritime applications.

Future work can go further to consider more deeply depending on use cases targeted, and the multi-x aspects, system capabilities.

#### ACKNOWLEDGEMENT

The research leading to these results has received funding from the NO Grants 2014-2021, under Project contract no. 42/2021, RO-NO-2019-0499 - "A Massive MIMO Enabled IoT Platform with Networking Slicing for Beyond 5G IoV/V2X and Maritime Services" - SOLID-B5G.

#### REFERENCES

[1] E.Borcoci, M. Vochin, and S. G.Obreja, "On Systematic Identification of Requirements for Vehicle-to-Everything 5G Slices", The Tenth International Conference on Mobile Services, Resources, and Users MOBILITY 2020,

- September 27, 2020 to October 01, 2020 - Lisbon, Portugal, <https://www.iaria.org/conferences2020/MOBILITY20.html>
- [2] C. Renato Storck and F. Duarte-Figueiredo, "A 5G V2X Ecosystem Providing Internet of Vehicles", *Sensors* 2019, 19,550, doi: 10.3390/s19030550, [www.mdpi.com/journal/sensors](http://www.mdpi.com/journal/sensors), [retrieved January, 2020].
- [3] 3GPP TS 22.185 V15.0.0 (2018-06) "Service requirements for V2X services" Stage 1, Release 15.
- [4] 3GPP TS 22.186 V16.2.0 (2019-06) "Enhancement of 3GPP support for V2X scenarios", Stage 1, Release 16.
- [5] 3GPP TS 23.286 V16.3.0 (2020-03), "Application layer support for Vehicle-to-Everything (V2X) services; Functional architecture and information flows", Release 16.
- [6] N. Panwar, S. Sharma, and A. K. Singh 'A Survey on 5G: The Next Generation of Mobile Communication' Elsevier Physical Communication, 4 Nov 2015, <http://arxiv.org/pdf/1511.01643v1.pdf>
- [7] 5G-PPP Architecture Working Group, "View on 5G Architecture", Version 3.0, June, 2019, [https://5g-ppp.eu/wp-content/uploads/2019/07/5G-PPP-5G-Architecture-White-Paper\\_v3.0\\_PublicConsultation.pdf](https://5g-ppp.eu/wp-content/uploads/2019/07/5G-PPP-5G-Architecture-White-Paper_v3.0_PublicConsultation.pdf), [retrieved June, 2019].
- [8] 3GPP TS 23.501 V15.2.0 (2018-06), System Architecture for the 5G System; Stage 2, (Release 15)
- [9] X. Foukas, G. Patounas, A. Elmokashfi, and M. K. Marina, "Network Slicing in 5G: Survey and Challenges", *IEEE Communications Magazine*, May 2017, pp. 94-100.
- [10] A. Galis, "Network Slicing- A holistic architectural approach, orchestration and management with applicability in mobile and fixed networks and clouds", <http://discovery.ucl.ac.uk/10051374/>, [retrieved July, 2019].
- [11] J. Ordonez-Lucena et al., "Network Slicing for 5G with SDN/NFV: Concepts, Architectures and Challenges", *IEEE Communications Magazine*, 2017, pp. 80-87, Citation information: DOI 10.1109/MCOM.2017.1600935.
- [12] I. Afolabi, T. Taleb, K. Samdanis, A. Ksentini, and H. Flink, "Network Slicing & Softwarization: A Survey on Principles, Enabling Technologies & Solutions", *IEEE Communications Surveys & Tutorials*, March 2018, pp. 2429-2453.
- [13] ETSI GS NFV 002, "NFV Architectural Framework", V1.2.1, December 2014.
- [14] ETSI GR NFV-IFA 028, "Network Functions Virtualisation (NFV) Release 3; Management and Orchestration; Report on architecture options to support multiple administrative domains", Technical Report, V3.1.1, January, 2018.
- [15] ETSI GR NFV-EVE 012, Release 3 "NFV Evolution and Ecosystem; Report on Network Slicing Support with ETSI NFV Architecture Framework", Technical Report, V3.1.1, December, 2017.
- [16] ONF TR-526, "Applying SDN Architecture to 5G Slicing", April 2016, [https://www.opennetworking.org/wp-content/uploads/2014/10/Applying\\_SDN\\_Architecture\\_to\\_5G\\_Slicing\\_TR-526.pdf](https://www.opennetworking.org/wp-content/uploads/2014/10/Applying_SDN_Architecture_to_5G_Slicing_TR-526.pdf), [retrieved December, 2019].
- [17] A. Molinaro and C. Campolo, "5G for V2X Communications", <https://www.5gitaly.eu/2018/wp-content/uploads/2019/01/5G-Italy-White-eBook-5G-for-V2X-Communications.pdf>, [retrieved December, 2019].
- [18] S. A. Ali Shah, E. Ahmed, M. Imran, and S. Zeadally, "5G for Vehicular Communications", *IEEE Communications Magazine*, January 2018, pp.111-117.

- [19] K. Katsaros and M. Dianati, "A Conceptual 5G Vehicular Networking Architecture", October 2017, <https://www.researchgate.net/publication/309149571>, DOI: 10.1007/978-3-319-34208-5\_22, [retrieved December 2019].
- [20] C. Campolo, A. Molinaro, A. Iera, and F. Menichella, "5G Network Slicing for Vehicle-to-Everything Services", IEEE Wireless Communications, Volume: 24 Issue: 6, DOI: 10.1109/MWC.2017.160040, [retrieved December, 2019].
- [21] Friedhelm Ramme, ITS, Transport & Automotive, Ericsson 5G: "From Concepts to Reality" Technology Roadmaps <https://5gaa.org/wp-content/uploads/2019/02/Final-Presentation-MWC19-Friedhelm-Ramme-ERICSSON.pdf>, [retrieved January, 2020].
- [22] 5G PPP Automotive Working Group, "Business Feasibility Study for 5G V2X Deployment", [https://bscw.5g-ppp.eu/pub/bscw.cgi/d293672/5G%20PPP%20Automotive%20WG\\_White%20Paper\\_Feb2019.pdf](https://bscw.5g-ppp.eu/pub/bscw.cgi/d293672/5G%20PPP%20Automotive%20WG_White%20Paper_Feb2019.pdf), [retrieved, January, 2020].
- [23] H2020-ICT-2016-2, Monarch Project, 5G Mobile Network Architecture for diverse services, use cases and applications in 5G and beyond, Deliverable D2.2, "Initial overall architecture and concepts for enabling innovations", <https://5g-monarch.eu/deliverables/> 2018, [retrieved June, 2019].
- [24] 3GPP TR 22.830 V16.1.0, TS Group Services and System Aspects, "Feasibility Study on Business Role Models for Network Slicing", (Release 16), 2018 <https://itectec.com/archive/3gpp-specification-tr-22-830/> [retrieved May, 2020].
- [25] 5GCAR White Paper : Executive Summary, Version: v1.0, 2019-12-10, <https://5gcar.eu/wp-content/uploads/2019/12/5GCAR-Executive-Summary-White-Paper.pdf>, [retrieved, January 2020].
- [26] 5GCAR, Fifth Generation Communication Automotive Research and innovation Deliverable D2.2 "Intermediate Report on V2X Business Models and Spectrum", v2.0, 2019-02-28, [https://5gcar.eu/wp-content/uploads/2018/08/5GCAR\\_D2.2\\_v1.0.pdf](https://5gcar.eu/wp-content/uploads/2018/08/5GCAR_D2.2_v1.0.pdf), [retrieved, January, 2020].
- [27] B. Martínez de Aragón, J. Alonso-Zarate and, and A. Laya, "How connectivity is transforming the automotive ecosystem". Internet Technology Letters. 2018; 1:e14. <https://doi.org/10.1001/itl2.14> [retrieved, January, 2020].
- [28] Katsalis, N. Nikaein, and A. Edmonds, "Multi-Domain Orchestration for NFV: Challenges and Research Directions", 2016 15th Int'l Conf. on Ubiquitous Computing and Communications and International Symposium on Cyberspace and Security (IUCC-CSS), pp. 189–195, DOI: 10.1109/IUCC-CSS.2016.034, <https://ieeexplore.ieee.org/document/7828601>, [retrieved July, 2019].
- [29] M. Usman et al., "A Business and Legislative Perspective of V2X and Mobility Applications in 5G Networks", IEEE Access, 2020, <https://ieeexplore.ieee.org/abstract/document/9057672>, [retrieved June, 2020].
- [30] J. Mei, X. Wang, and K. Zheng, "Intelligent Network Slicing for V2X Services Towards 5G", arXiv:1910.01516v1 [cs.NI] [retrieved October, 2019].
- [31] Research Project, "A Massive MIMO Enabled IoT Platform with Networking Slicing for Beyond 5G IoV/V2X and Maritime Services" - SOLID-B5G [31] (<https://solid-b5g.upb.ro/>)
- [32] NGMN Alliance, V 2.5.4, "Verticals URLLC Use Cases and Requirements" February, 2020, <https://www.ngmn.org/publications/verticals-urllc-use-cases-and-requirements.html>, [retrieved October, 2020].
- [33] A. Alalewi, I. Dayoub and S. Cherkaoui, "On 5G-V2X Use Cases and Enabling Technologies: A Comprehensive Survey," in IEEE Access, vol. 9, pp. 107710-107737, 2021, doi: 10.1109/ACCESS.2021.3100472.
- [34] P. Popovski, K. F. Trillingsgaard, O. Simeone, and G. Durisi, "5G wireless network slicing for eMBB, URLLC, and mMTC: A communication theoretic view," IEEE Access, vol. 6, pp. 5576555779, 2018.

# Improving the Design Performance of Field Programmable Gate Array Devices with Efficient Approach to Measure Power Consumption

Esteve Hassan

Electrical and Computer Engineering Technology  
Mohawk College of Applied Arts and Technology  
Hamilton (ON), Canada  
e-mail: esteve.hassan@mohawkcollege.ca

Bilal Al Momani

Electrical and Computer Engineering Technology  
Mohawk College of Applied Arts and Technology  
Hamilton (ON), Canada  
e-mail: bilal.al-momani@mohawkcollege.ca

**Abstract**— The study in this paper is focused on the improvement of a Field Programmable Gate Arrays (FPGA) based design using a hierarchical analysis tool offered by XILINX PlanAhead™. During this work, PlanAhead software is used to address any problems on the physical side of our FPGA design flow to add more modules visibility and control. The design application is a telemetry system intended for health monitoring applications. FPGA is used as the brain control unit at both transmitter and receiver sides. The transmitter side is recording data packets through external interfaced sensors. Verilog Hardware Description Language (Verilog-HDL) has been used to implement the various functionalities required by the FPGA device. The system performance as shown in the results has been optimized using a recent comprehensive tool to reach and maintain the goals of the design. The power performance of the FPGA-based design will be assessed using the XILINX Xpower tool. A Modelsim Code coverage feature has been incorporated to make sure that the test bench will cover all the nets branch statements of the design and create the most accurate Value Change Dump (VCD) file for the power consumption assessment process.

**Keywords**- FPGA; Telemetry system; FPGA design improvement; power assessment.

## I. INTRODUCTION

The challenge is to raise or at least maintain the present level of health care providers without ending up in an uncontrolled cost explosion of services. The increasing number of researchers and manufacturers who are working on a new generation of wireless technology applications for the medical field has led to improved quality and reduced cost of patient care. One of the areas in healthcare that best lend itself to wireless technology is patient monitoring, also known as wireless telemetry. Due to system complexity, the use of FPGA for this vital application has become widely common.

Electronic systems development is becoming more and more complex, fast, powerful, and power-consuming. Indeed, transistor miniaturization dramatically increases the power consumed by a whole chip [1,2]. The main consequences of this trend are the addition of elaborated cooling circuits and the reduction of battery life for the embedded systems. As for timing and die area, power

consumption becomes a critical constraint for electronic system design. A previous study [3] has demonstrated the beneficial effect of power optimization at high-level; it is then necessary to develop high-level estimation tools which use power models for all kinds of components (Application-Specific Application Circuit (ASIC), FPGA) in a system. Playing many important roles in recent applications, FPGAs devices are used in a wide scale of designs ranging from small glue logic replacement to System-on-Chip. The main advantage of FPGA compared to ASIC chips is the flexibility: a design can be reprogrammed partially or totally in-situ. This functionality is realized by a configuration plan and requires a large number of transistors for Static Random Access Memory (SRAM) FPGA; therefore, the drawback is important static power consumption. Moreover, FPGA builders are currently improving this circuit characteristic to facilitate their integration in System on Chip (SoC). The health care field became one of the most recent applications of the FPGA designers [4].

The PlanAhead software provides insight into the data flow of the design by displaying I/O interconnect as well as physical block net bundles [5]. Timing constraints can be then modified within the PlanAhead environment. These analysis results can help to determine what logic should be grouped and floor planned. Paths can be logically sorted, grouped, and selected for floorplanning. TimeAhead environment can also be leveraged with imported timing results from the timing analyzer tool within Xilinx Integrated Synthesis Environment (Vivado™) software [5]. TimeAhead is useful to validate and optimize the constraint set before running any Vivado implementation tools. In addition, it provides visual aids to comprehend the physical implementation results. Design rule checks (DRCs) are provided to catch errors early. It also flags designs that do not properly take advantage of certain device resources, such as the dedicated registers of the XtremeDSP™ slice.

Design solutions can be addressed quickly by visualizing area problems, either in the register transfer logic (RTL) or on the physical implementation side, without having to continue RTL and synthesis iterations. FPGA vendors are facing the difficult task to accurately specify the energy consumption information of their products on the device data sheets because the energy consumption of FPGAs is strongly

dependent on the target circuit including resource utilization, logic partitioning, mapping, placement, and route. While major Computer-Aided Design (CAD) tools have started to report average power consumption under given transition activities, energy optimal FPGA design demands more detailed energy estimation. This work aims to present a useful methodology for estimating the power consumption of an FPGA-based system designed for medical applications. Modelsim code coverage capability will be used to investigate the different styles of test bench coding on the overall power consumption estimation of the FPGA device.

In Section II, a system overview is presented. Sections III-VI are outlining the design methodology for FPGA devices using PlanAhead. ModelSim code coverage is explained in Section VII and Section VIII explains the accurate FPGA power estimation. Section IX is giving the merits of the new method to perform an accurate power consumption assessment. Finally, conclusions are drawn in Section X.

## II. SYSTEM OVERVIEW

The main blocks of the transmitter side FPGA are shown in Fig. 1. The different units of the system were coded with Verilog HDL simulated with ModelSim and implemented with Vivado. The final implementation was targeting the Virtex-7 device since it provides the various features that solve the designer's challenge throughout the entire system. The transmitter FPGA consists mainly of an SPI (Serial Peripheral Interface), RLE (Run Length Encoding) compressor, and framer units. The operation of the system units and the flow of data through the system are controlled by the main FSM (Finite State Machine) controller.

On the receiver side, a data recovery unit is needed to extract the clock from the received bitstream. The de-framer and the RLE decompressor blocks are designed to reconstruct the original data bytes sent by the transmitter.

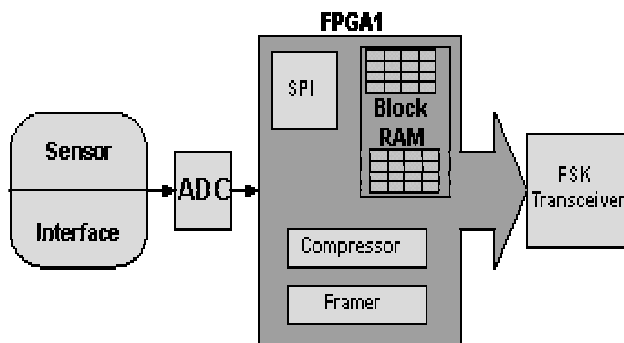


Figure 1. Building blocks of the transmitter FPGA

### A. SPI main units

An efficient SPI unit has been modeled, as shown in Fig. 2. The Master out Slave in (MOSI) signal has been omitted from the design based on the hardware requirements

where data only needed to be transferred from the ADC to the FPGA system. The main units of the SPI are functioning as follows:

1. Clock Divider Unit: Divides the system clock by a certain factor to generate the required SPI clock frequency.
2. Data out clock synchronizer: used to generate both the rising edge (dout7) and the falling edge (dout16) of the ADC clock.
3. ADC Enable unit: triggered on when the start\_conv signal is asserted to generates the following signals:
  - a. Capture signal to capture data transfer from the ADC to the SPI register after each byte transfer.
  - b. Increment signal used to change the address inside the Block RAM unit.
4. Slave Chip Select (CS).
5. SPI Register Unit: contains the SPI serial in/parallel out register, which is enabled when the capture signal is asserted and receives input serial data through ADC\_Din signal. Spiout (output) signal carries the information data bytes to the Block RAM unit.
6. Distributed Block RAM: stores the data bytes in locations determined by the increment signal.

Typically, test benches have become the standard method to verify HDL designs. Test benches invoke the functional design, and then simulate it. Accordingly, an efficient test bench has been written to mimic the behavior of the ADC and verify the operation of the SPI system units.

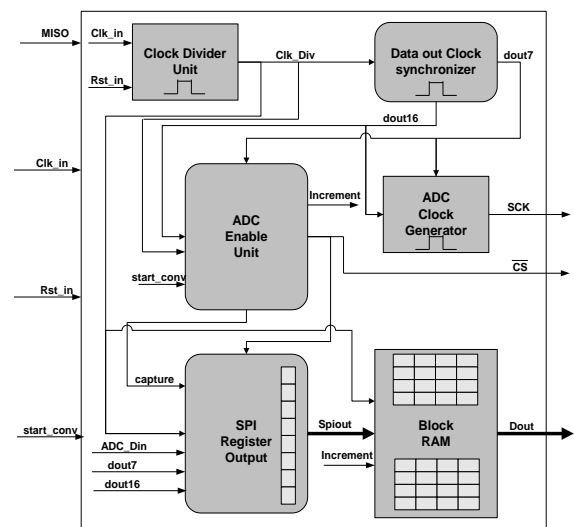


Figure 2. Block units of the developed SPI inside the FPGA

### III. DESIGN FLOW USING PLANAHHEAD (PA)

The PlanAhead tool sits between synthesis and the Vivado place and route (P&R) tools as shown in Fig. 3.

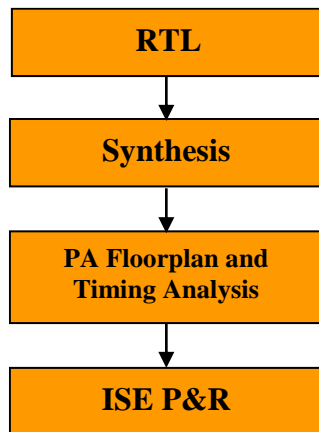


Figure 3. FPGA design flow using Plan Ahead

To increase the design performance, the HDL code has been written taking into consideration the following comments:

The design has been partitioned at the RTL level, such that critical timing paths are confined to individual modules. Critical paths that span large numbers of hierarchical modules can be difficult to floorplan. The outputs of all modules have been registered to help limit the number of modules involved in a critical path.

Dividing large hierarchical blocks into smaller RTL units to avoid the possibility of having long paths, which makes the floorplan a difficult task.

Through analysis and floorplanning, physical constraints are applied to help control the initial implementation of the design. PlanAhead is also used after implementation to analyze the placement and timing results in order to improve the floorplanning and complete the design.

A very optimized Verilog code has been written to describe the different block units of the design since it is based only on the instantiation of the basic units that can be invoked directly from the library. This is essential in the design process to remove any complexity from the model, which makes it easy to understand and debug. In addition, unnecessary resources are not added by the synthesize tool to the code, which leads to a power-efficient model design. An example of such code for the ADC chip selection is shown in Fig. 4.

### IV. PLANAHHEAD IMPLEMENTATION

In this section, the PlanAhead implementation on the transmitter side FPGA will be presented. The on-chip design partitions are referred as physical block (Pblocks).

With PlanAhead software, the utilisation estimates of the device resources viewed below in Fig. 5.

```

//==== Multiplexer of the ADC Chip Select====/
AND2 and2instance3 (.O (and3out),
    .I0 (fdeout5),
    .I1 (Mod_Fjkout)
);

AND2 andinstance4 (.O (and4out),
    .I0 (fdeout4),
    .I1 (inv3out)
);

INV invinstance3 (.O (inv3out),
    .I (Mod_Fjkout));

OR2 OR2_instance1 (.O (En_Adc),
    .I0 (and4out),
    .I1 (and3out));
  
```

Figure 4. Verilog\_HDL sample code form the SPI design

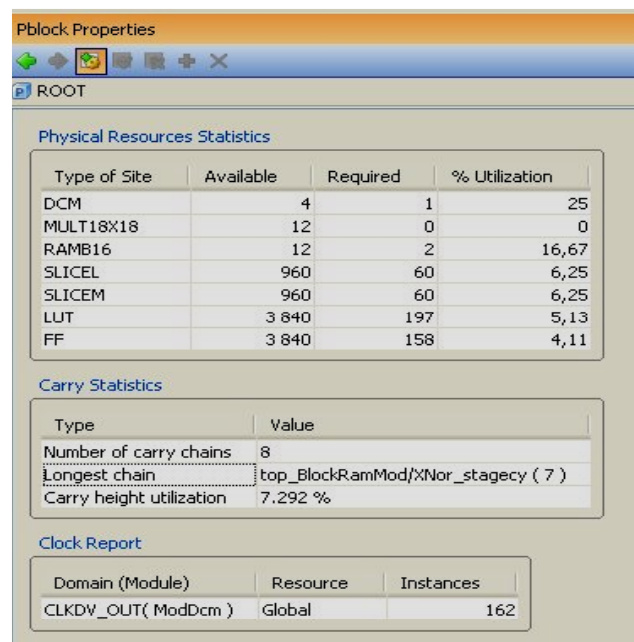


Figure 5. device resources used for the target system design

In order to get a good schematic-level view of the key portions of the design, PlanAhead software has been used for this purpose as well. The schematic of the design top-level is presented in Fig 6. Such views can be a valuable aid in understanding how the modules of the design are connected to each other. It is recommended with PlanAhead to view and analyze the hierarchy of the design. Such a view can be useful to implement the best floorplan and also may indicate

the location of the longest timing path (critical path). In Fig. 7, the hierarchy of the design is displayed.

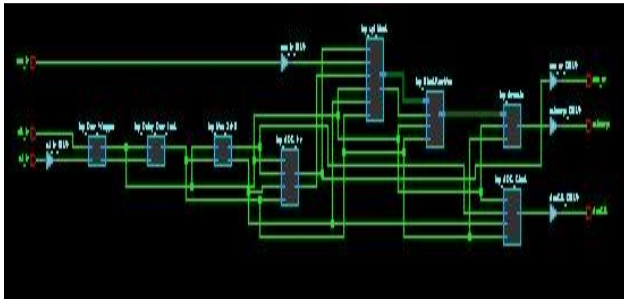


Figure 6. Design top-level schematic

PlanAhead software has an embedded static timing analysis engine and environment called TimeAhead. With this feature, timing estimations can be utilized at various stages of design implementation. The longest path has been explored and highlighted in Fig. 8. This step is necessary for the next coming stages to improve the floorplan for better performance. It is worth mentioning here that in most cases the longest path is associated with the module of the biggest size in a fully synchronous design. In the hierarchy view shown in Fig. 7, the module `top_BlockRamMod` is obviously the one, which has the longest path.

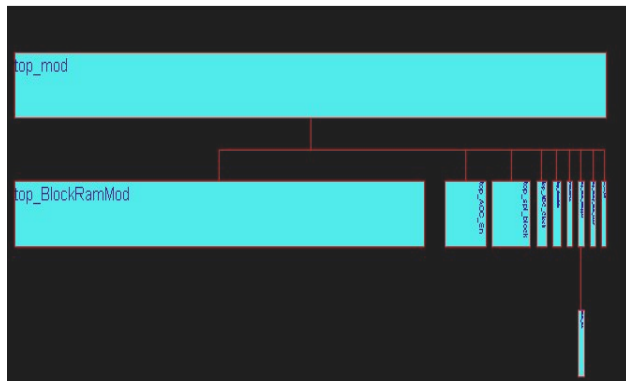


Figure 7. Module hierarchy view from PlanAhead

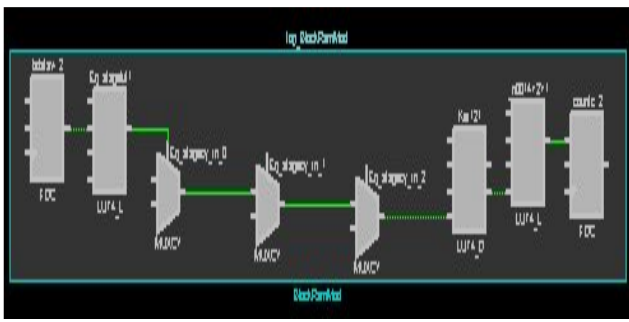


Figure 8. The longest logic delay path

## V. FLOORPLAN STRATEGIES

### A. Problem Description

Assume we are given a set of modules, each of them having an associated resource requirement vector  $\phi = (n1, n2, n3)$ , which means this module requires  $n1$  CLBs,  $n2$  RAMS, and  $n3$  multipliers. The FPGA floorplanning problem is to place modules on the chip so that each rectangular region assigned to a module should satisfy its resource requirements.

For example, we have 6 modules, and their resource requirement vectors are  $\phi_1 = (12, 2, 1)$ ,  $\phi_2 = (30, 4, 4)$ ,  $\phi_3 = (15, 1, 1)$ ,  $\phi_4 = (24, 4, 4)$ ,  $\phi_5 = (18, 2, 2)$ ,  $\phi_6 = (30, 2, 2)$ . Fig. 9 is a feasible floorplan for these modules, which shows a slicing structure.

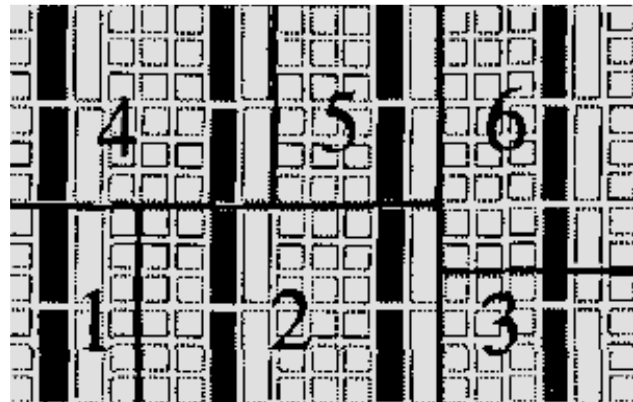


Figure 9. Example of Floorplan slicing structure

In the following sections, the use of PlanAhead tool to implement our floorplan design strategies will be explained.

### B. Logic Placement Before Floorplanning

Fig. 10 shows how the logic modules of the design are distributed by the Vivado tool inside the chip. The FPGA I/O resources displayed as thin rectangles just outside the device are the Input/Output (I/O) pads. I/O banks are displayed as thin rectangles just outside the I/O pads. Digital clock managers (DCMs) are shown graphically as rectangles along the I/O ring. The clock I/O pins are shown as filled rectangles. The interior of the device is broken up into smaller rectangles called tiles. These tiles contain placement sites for the different types of logic primitives pertinent to the architecture being used.

In Table I, a summary of the device utilization before implementing floorplanning is given. The number of slices has been highlighted since it is important figure that indicates the device area covered by the design. Such figure will be used later on for performance comparisons.

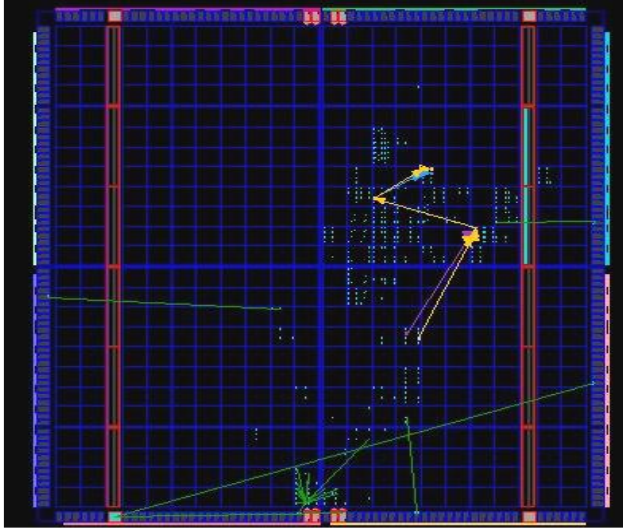


Figure 10. Logic placement before Floorplanning

TABLE I: DEVICE UTILIZATION BEFORE USING PLANAHHEAD TOOL

Device Utilization Summary		
Number of BUFGMUXs	2 out of 8	25%
Number of DCMs	1 out of 4	25%
Number of External IOBs	6 out of 173	3%
Number of LOCed IOBs	2 out of 6	33%
Number of RAMB16s	2 out of 12	16%
Number of Slices	143 out of 1920	7%
Number of SLICEMs	1 out of 960	1%

To get a closer view of the timing properties of the current design, a timing report has been generated as in Fig. 11. The following is the flow used to floorplan our design. The netlist file is generated first inside the Vivado using XST (Xilinx Synthesis Technology). Then the netlist file is used to create a new project in PlanAhead. After floorplanning the design, the netlist and the User Constraint File (UCF) will be exported back into Vivado environment and the timing report can be read from the place and route (P&R) results.

Constraint	Requested	Actual	Logic Levels
TS_clk_in = PERIOD TIMEGRP "clk_in" 20 ns HIGH 50%	N/A	N/A	N/A
TS_top_Dcm_Wrapper_Dcm_Ins_CLKDV_BUF = PE RIOD TIMEGRP "top_Dcm_Wrapper_Dcm_Ins_CLKDV_BUF" TS_clk_in * 32 HIGH 50%	640.000ns	7.834ns	4

Figure 11. Timing report before implementing PlanAhead

From Fig. 11, it can be noticed the large difference between the requested time for running the design (640 nsec) and the actual time given by the P&R report (7.834nsec).

### C. Floorplanning Techniques Implementation

In this section, PlanAhead software will be used to implement two different strategies of floorplanning. The output results of the implementation will be presented and discussed. The main goal is to show how PlanAhead can be employed successfully to optimize the placement area of our design logic.

The first strategy is based on pulling the whole design logic to be focused in one Pblock. This has been done as shown in Fig. 12, where all the modules have been placed in one rectangular at the bottom right corner of the device chip.

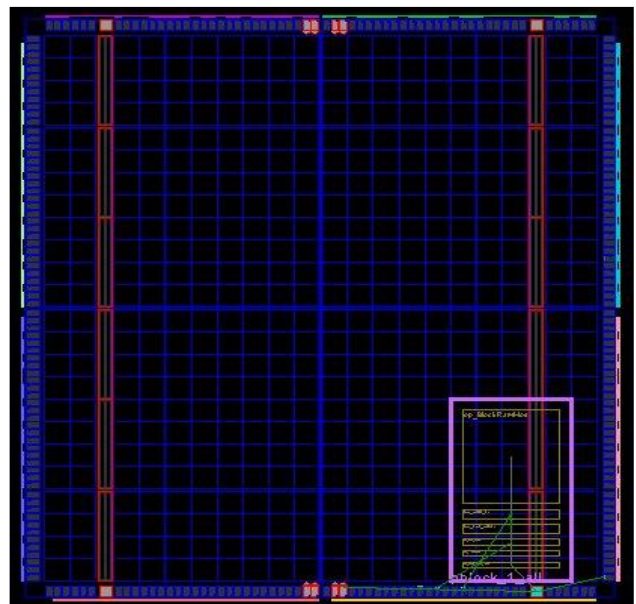


Figure 12. Logic placement after FloorPlanning using 1 Pblock strategy

The summary of the device utilization after implementing this strategy is given in Table II.

TABLE II: DEVICE UTILIZATION USING PLANAHHEAD STRATEGY 1

Device Utilization Summary		
Number of BUFGMUXs	2 out of 8	25%
Number of DCMs	1 out of 4	25%
Number of External IOBs	6 out of 173	3%
Number of LOCed IOBs	6 out of 6	33%
Number of RAMB16s	2 out of 12	16%
Number of Slices	128 out of 1920	7%
Number of SLICEMs	1 out of 960	1%

It is clear from the number of slices that the design area has been compressed by more than 10%. To have a complete

picture, a timing report has been generated using the same procedure mentioned in the previous section and it is shown in Fig. 13.

Constraint	Requested	Actual	Logic Levels
TS_clk_in = PERIOD TIMEGRP "clk_in" 20 ns HIGH 50%	N/A	N/A	N/A
TS_top_Dcm_Wrapper_Dcm_Ins_CLKDV_BUF = PE RIOD TIMEGRP "top_Dcm_Wrapper_Dcm_Ins_CLKDV_BUF" TS_clk_in * 32 HIGH 50%	640.000ns	9.117ns	3

Figure 13. Clock report after implementing the PlanAhead using 1Pblock strategy

One interesting comment that can be drawn from Fig. 13, is the actual time has been increased from the one before implementing this strategy. This can be explained as the design now become more compact in a smaller area, which leads to having data congestion. Despite this increase in time, it will not have any impact on our design performance since we are meeting the required time far below.

In the second strategy, two Pblocks will be used to place the design modules and the necessary connections between these two blocks can be visible in PlanAhead. The placement of the 2Pblock is shown in Fig. 14.

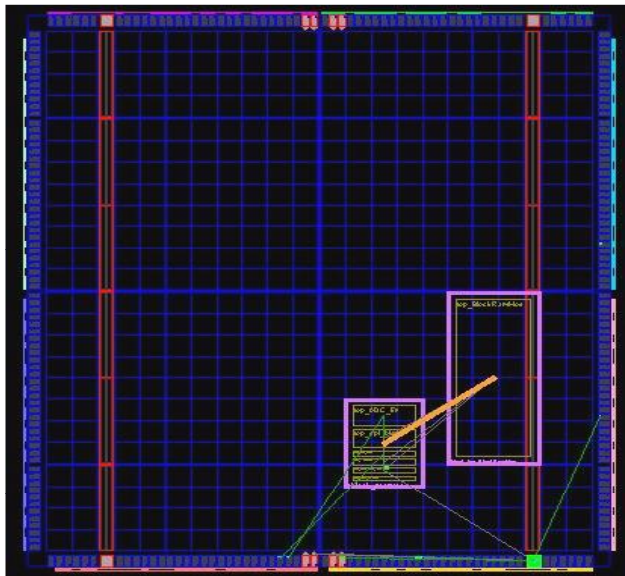


Figure14. Logic placement after FloorPlanning using 2 Pblocks strategy

In the same manner, Table III is showing the device utilization after implementing the second strategy. As

expected the design area has been slightly compressed with this strategy.

TABLE III: DEVICE UTILIZATION USING PLANAhead STRATEGY 2

Device Utilization Summary		
Number of BUFGMUXs	2 out of 8	25%
Number of DCMs	1 out of 4	25%
Number of External IOBs	6 out of 173	3%
Number of LOCed IOBs	6 out of 6	33%
Number of RAMB16s	2 out of 12	16%
Number of Slices	140 out of 1920	7%
Number of SLICEMs	1 out of 960	1%

Finally, the timing report of this implementation is showing less value for the actual time as presented in Fig. 15. With this strategy, a larger area is provided for the design, which reduces the possibility of having a high data congestion rate.

Constraint	Requested	Actual	Logic Levels
TS_clk_in = PERIOD TIMEGRP "clk_in" 20 ns HIGH 50%	N/A	N/A	N/A
TS_top_Dcm_Wrapper_Dcm_Ins_CLKDV_BUF = PE RIOD TIMEGRP "top_Dcm_Wrapper_Dcm_Ins_CLKDV_BUF" TS_clk_in * 32 HIGH 50%	640.000ns	8.134ns	4

Figure 15. Clock report after implementing the PlanAhead using the 2 Pblocks strategy.

Another highlighted field in the utilization summary tables is the one that shows the locked Input/Output Blocks (IOBs). Before implementing floorplanning, only two pins have been given positions in the UCF, these are the clock and reset pins. As the physical locations of these two pins were compulsory, the floorplanning was influenced by this fact. The closest physical location to the design has been chosen to lock the other pins after floorplanning. That is why the number of locked pins is complete in Tables II and III.

By doing a comparative study for the two suggested floorplanning techniques, it is obvious that the first strategy gives the optimum design area solution. On the other hand, the speed of data transfer might be affected due to the data congestion that occurs between the modules but this would not be a serious issue in our case. The second floorplanning strategy slightly reduces the area since more space will be provided for the design modules. The data speed has been improved in compared with the first strategy but still our design meets the requested timing requirements in all the cases.

## VI. FPGA POWER ESTIMATION

Power consumption is mandatory information in modern digital system design.

Chip vendors are naturally in charge of supplying energy consumption information of their products on the device datasheets. However, it is not possible for vendors to specify power consumption information of SRAM-based FPGAs because it is not only dependent on the target device and operating frequency but is highly dependent on the design and operating conditions. Power consumption is strongly dependent on the target circuit including resource utilization, low-level features such as logic partition, mapping, placement, and route. Here a new power estimation methodology is introduced on the FPGA after the design has been optimized with PlanAhead tool as presented by previous sections.

### A. Related Work

For FPGA, some methodologies and models have already been developed to estimate the power consumed specifically by the logic elements. For example, a probabilistic model is proposed by [6]; developed for a CAD tool, this model estimates, at the transistor level, the 0.18  $\mu\text{m}$  Complementary Metal Oxide Semiconductor (CMOS) FPGA power consumption based on place and route. The switching activity used to calculate the dynamic power is determined by the transition density of the signal. The static power is evaluated by a sub-threshold current estimation. The resulting absolute error of this model is 23% compared to measurements. Some techniques are proposed in [7] to reduce both static and dynamic power consumption like drowsy mode, clock gating, guarded evaluation, counter and state machine encoding, but no estimation model is proposed. For a design in Virtex-7, [8] proposes an estimate of the dynamic power consumed by logical elements after routing. Lastly, [9] has presented a Register Transfer level power estimator based on the determination of wire length and switching activity with an average error of 16.2%. The first parameter is calculated by applying Rent's rule during high-level synthesis. The second parameter is evaluated by a fast switching activity calculation algorithm. The model developed by [10] allows estimating the power consumption of distributed memory (using logic elements) in past FPGA families with technical parameters. Another model proposed in [11] uses technical parameters such as effective capacitance of each resource which is hardly obtained. All these methodologies and models use low-level parameters and technical characteristics which are not available before place and route. More precise approaches to estimate FPGA power consumption were described in [12-14].

### B. XPower Xilinx Tool

XPower is a commercial-off-the-shelf tool to estimate the power consumption of Xilinx SRAM-based FPGAs. The design flow of the XPower is shown in Fig. 16. In this part of the work, the implementation of the Xilinx XPower will be investigated. XPower reads in either pre-routed or post-

routed design data, and then makes a power model either for a unit or for the overall design based on the power equation:  $P=CVf$  where  $P$  is average power consumption,  $C$  is equivalent switching capacitance,  $V$  is supply voltage and  $f$  is operating clock frequency or toggle rate. It considers resource usage, toggle rates, input/output power, and many other factors in estimation. Because XPower is an estimation tool, results may not precisely match actual power consumption. The frequency,  $f$ , is determined by users or provided by simulation data from the ModelSim family of HDL simulators.

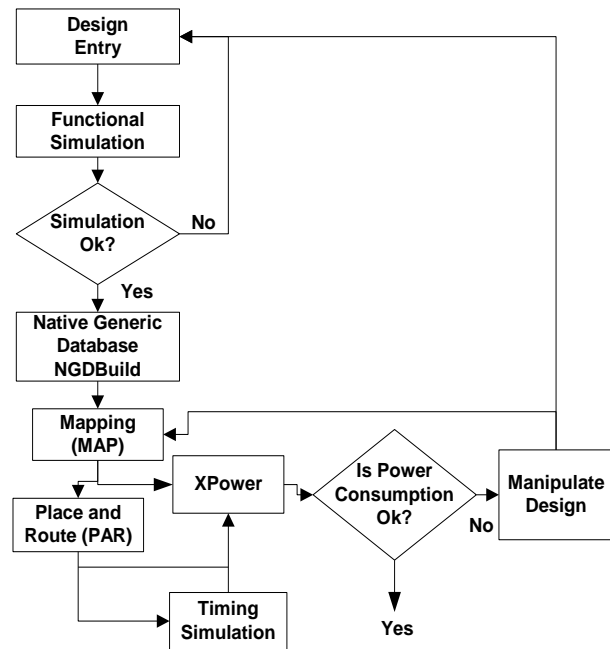


Figure 16. XPower tool design flow

XPower provides two types of information called data view and reports view. The data view shows the power consumption of individual parts of a design such as signals, clocks, logic, and outputs. The report viewer represents the total power consumed by a given design, which is again classified into the power consumption of clocks, logic and outputs, and static (leakage) power. The power consumption of clocks, logic, and outputs are calculated by equivalent switching capacitance models. The static power is based on the constant value quoted in a data book or calculated by an equation associated with temperature, device utilization, and supply voltage.

## VII. MODEL SIM CODE COVERAGE

ModelSim code coverage can display a graph and report file feedback on which statements, branches, conditions, and expressions in the source code have been executed. It also measures bits of logic that have been toggled during the execution. Therefore, it can be considered as a trace tool and probe at the same time that provides a history of the software execution.

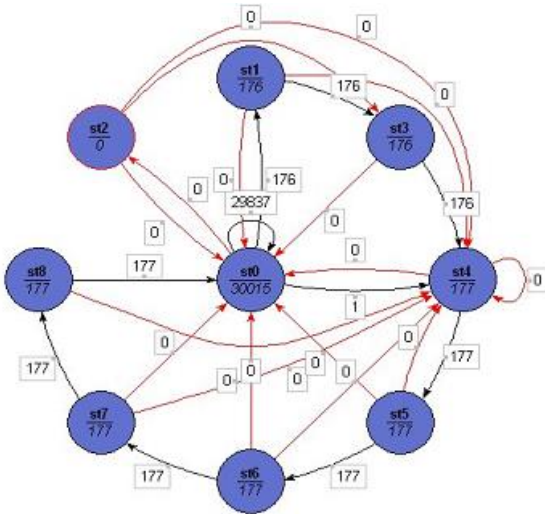


Figure 17. Transmitter FPGA-Compressor unit FSM

As code execution is almost invisible without an accurate trace tool, it is common for the entire blocks or modules of code to go unexecuted during test routines or redundant user-case suites. Coverage metrics showing which functions are not executed are useful for writing new, additional tests or identifying unused “dead” code. In applications where code size is critical, removing dead code reduces both wastes as well as risk in the targeted design. In many cases, code coverage can also be used to analyze errant behavior and the unexpected execution of specific branches or paths. The FSM can be extracted with code coverage as in Fig. 17 for the compressor unit.

The FSM figure clarifies the number of states involved in the design and the interaction between these states. A test bench has been written to examine the behavior of the HDL design. The code coverage is enabled to check the covered and uncovered parts of the design code by the test function which can lead to alter the design and consequently change the power consumption.

Fig. 18 shows some uncovered statements indicated by red X mark. In addition, an example of missed branches is shown in Fig. 19, where the X<sub>T</sub> mark indicates that the true branch of the conditional statement was not covered.

```

BlockRamControl.v
192      equal  <= 1'b1 ;
193      nonequal <= 1'b0 ;
228      n_state = `incrc ;
234      n_state = `tpinc ;
245      default : n_state = `init ;
266      countc1 <= 8'h00 ;
267      bwritec1 <= bwritec1 + 7'h01 ;
270      countc1 <= countc1 + 8'h01 ;
271      bwritec1 <= bwritec1 ;
    
```

Figure 18. Not covered design statements is escaped

```

BlockRamControl.v
191      if (bdataw1 == bdataw)
225      case (c_state)
227          if (equal)
263      case (c_state)
265          if (countc1 == `incrc)
    
```

Figure 19. Not covered design branches

### VIII. ACCURATE FPGA POWER ESTIMATION

The power characterization using XPower tool is done and based on the mapped/placed/routed design. In general, the total power consumption of a CMOS component is given by Equation.1. The dynamic power is due to the component activity while static power represents the power consumed by the leakage current.

$$P_{total} = P_{dynamic} + P_{static} \tag{1}$$

The static power given by the XPower is constant and calculated by the multiplication of maximum leakage current absorbed by the FPGA core and its supply voltage. On the other hand, dynamic power is varying according to the switching activity of the design. Therefore, two factors determine the accuracy of the XPower analyzer estimation: the accuracy of the data within Xpower analyzer and the stimulus provided by the user. It is necessary to mention that XPower relies upon stimulus data to estimate the power consumption for internal components. Valid input frequencies and toggle rates are necessary parameters to generate a proper power estimate. The main four important files that need to be invoked by the tool are the design (\*.ncd), simulation (\*.vcd), physical constraints (\*.pcf), and setting (\*.xml) files.

There are few strategies that can be implemented to reduce the power consumption of the FPGA device; these are:

1. Turn off clocks when they are not in use.
2. Make Block RAMs operate in “no read on write” mode. This reduces toggling of the output of the BRAM.
3. Use a clock enables the reduction of switching activity on the output of Flip Flops (FFs).
4. Partition Logic is driven by global clocks into clock regions and reduces the number to which each global clock is routed.
5. Reduce the total number of columns to which a clock is routed.
6. Reduce the total length of heavily loaded signals.

Mainly, we followed the recommendations in 3 & 4 to reduce the power consumption of our design. Therefore, the global design has been partitioned into a lot of small blocks.

In order to investigate the impact of test bench writing style on the accuracy of the power estimate, two methods have been exercised. In the first one, the ADC\_Din (line

carrying input data coming from the ADC has been stimulated by variable 8-bits data samples, as expected in the practical case. In the second method, only 0 data value is stimulating the ADC\_Din. As an example, the control logic of the compressor BRAM has been considered to see the difference in the code coverage represented by the summary reports given in Figs. 20 and 21.

File: BlockRamControl.v			
Enabled Coverage	Active	Hits	% Covered
Stmts	86	80	93.0
Branches	52	47	90.4
Conditions	6	6	100.0
States	9	8	88.9
Transitions	26	10	38.5

Figure 20. BRAM control coverage report without adc\_in

File: BlockRamControl.v			
Enabled Coverage	Active	Hits	% Covered
Stmts	86	83	96.5
Branches	52	50	96.2
Conditions	6	6	100.0
States	9	9	100.0
Transitions	26	12	46.2

Figure 21. BRAM control coverage report with adc\_in

The hits count shows the number of times the indicated code part has been reached or executed. It is obvious that this count has been increased for all the design parts except the conditions. The states of the design have been fully covered in Fig 21 because the system is dealing with all the possible design options that are required in the verification stage. Sample ModelSim waveforms for the two adc\_in conditions are shown in Figs. 22 and 23.

To investigate the effect of adc\_in on the power consumption of the FPGA device, XPower tool has been used for this purpose. Table IV summarizes the total power and current estimates for both configurations.

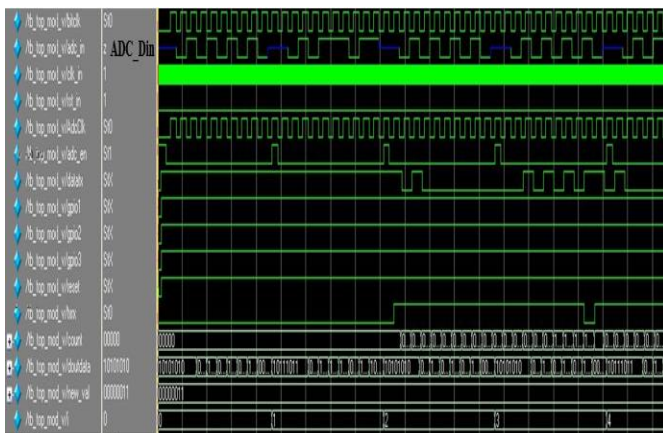


Figure 22. The simulation output waveform of the design with for variable adc\_in

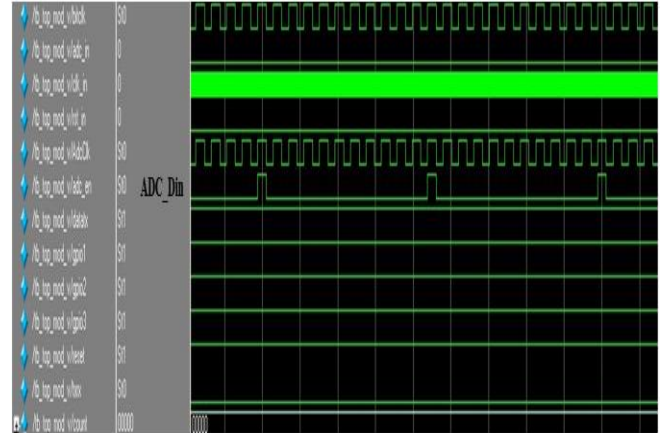


Figure 23. The simulation output waveform of the design with 0 data on adc\_in

TABLE IV: TOTAL CURRENT AND POWER ESTIMATES

Total Power and Current estimates	I(mA) With adc_in	P(mW) With adc_in	I(mA) Without adc_in	P(mW) Without adc_in
Device		59		51
Vccint 1.20V	12	16	11	13
Vccaux 2.50V	16	41	15	38
Vcco25 2.50V	1	2	0	0
Quiescent Vccint 1.20V	10	12	10	12
Quiescent Vccaux 2.50V	15	38	15	38

As given above, more power is needed for the design when ADC\_Din is clocking with different serial data. This leads to the conclusion that the FPGA device will consume higher power if the analog input signal to the ADC is rapidly changing. IN this case, the compressor unit of the design will be fully functioning with all the possible transition states.

The second case is assuming that the analog input has a steady value which is rare in practice, but useful to have power estimates for different working conditions. Thus total dynamic power is more dependent on the states of the input signals. In comparison, the power values in the two cases are different due to the code coverage analysis that has been discussed earlier. As more code has been covered with ADC\_Din is varying, then we can consider that the obtained power estimate with such case has more credibility.

Quiescent power is the same for both configurations since it depends on the device itself using default conditions in moderate environments. To reduce the power consumption of the FPGA without losing accuracy, more work needs to be done outside than inside the device. For example, reduce the ADC resolution or the analog input can be good options. The test bench should be written in a very optimum way to provide a stimulus for all the inputs and read efficiently all the outputs. This is an important issue in the XPower tool since it provides one of the main files for the tool to estimate the power. The code coverage sometimes can help to extract the unnecessary parts from the

design which has a great benefit for the power consumption. As a final comment, obtaining the high code coverage can lead to a higher but more accurate power estimate using XPower.

## IX. CONCLUSIONS

In this paper, PlanAhead tool has been employed as a hierarchical software environment after synthesis to analyze, modify, constrain and implement our design. It has been shown that a significant reduction in both the number and the length of design iterations can be obtained when using this tool.

A wireless system, which has been designed for sensor monitoring, required some optimization. Mainly, PlanAhead has been used to optimize the area occupied by the entire design, giving a better insight into the place and route process. Two strategies have been adopted in this work based on the number of Pblock placed to contain the different modules of the design. From the presented comparative results, using a single Pblock floorplanning design was representing the best scenario in terms of area compressing.

Also part of the work, the power consumption of the FPGA-based system has been investigated after passing through optimization placing with PlanAhead. The use of XPower from XILINX was the main focus of this work as an efficient tool to get good power estimates for the target FPGA device. The relation between the test bench coverage and power estimate accuracy was studied under different design conditions. It has been found that a good test bench with higher design code coverage capability can achieve more accurate power estimates. The presented results reflected clearly the efficiency of this method which can be applied with similar performance on any other Xilinx FPGA device.

## REFERENCES

[1] E. Hassan and B. Al Momani, "New Approach to efficiently Assess the Power Consumption of Field Programmable Gate Array Devices",

The Sixteenth International Conference on Systems ICONS, Portugal, April 2021

[2] N. S. Sung et al., "Leakage Current: Moore's Law Meets Static Power", IEEE Computer Magazine, December 2003, pp 68 – 75.

[3] J. M. Rabaey, M. Pedram, Low Power Design Methodologies, Kluwer Academic Publisher, 1996, ISBN 0-7923-9630-8.

[4] P. Dillinger, J. F. Vogelbruch, J. Leinen, S. Suslov, R. Patzak, H. Winkler, and K. Schwan, "FPGA based real-time image segmentation for medical systems and data processing", IEEE 14<sup>th</sup> NPSS Real Time Conf Proc., June 4-10 Sweden, 2005.

[5] K. Li, L. Lei, Q. Guang, J. Shi, and Y. Hao, "Improving the performance of an SOC design for network processing based on FPGA with PlanAhead", IEEE International Conference on Electronics, Communications and Control (ICECC), Sept 9-11, 2011

[6] K. W. Poon, Power Estimation For Field Programmable Gate Arrays, Ph.D Thesis, department of Electrical and Computer Engineering, University of British Columbia, Vancouver BC, Canada 1999.

[7] X. Guo-Lin, "Power-sensitive design techniques on FPGA devices," Electronics Quality Journal, 2002.

[8] L. Shang, A. S. Kaviani, K. Bathala, "Clock Power Analysis of Low Power Clock Gated Arithmetic Logic Unit on Different FPGA", in IEEE International Conference on Computational Intelligence and Communication Networks, November 14-16, India, 2014.

[9] D. Chen, J. Cong, and Y. Fan, "Low-Power High-Level Synthesis for FPGA Architecture", ISPLED'03, August 25-27 Seoul Korea, 2003.

[10] A. D. Garcia, Estimation et optimisation de la consommation de puissance des circuits logiques programmables du type FPGA [Estimation and Optimization of the Power Consumption logic circuits of the FPGA type], Ph.D Thesis, Ecole nationale supérieure des télécommunications de Paris, 2000.

[11] D. Elleouet, N. Julien, D. Houzet, J. Cousin, and M. Martin, "Power consumption characterization and modeling of embedded memories in XILINX", IEEE Digital System Design Conf Proc., 2004, pp. 394-401.

[12] H. Gyu Lee, S. Nam, and N. Chang, "Cycle-accurate Energy Measurement and High-Level Energy Characterization of FPGAs", IEEE Quality Electronic Design Symp Proc. 2003, pp.267-272.

[13] T. Fryza and M. Waldecker, "Precise Measurement of Power Consumption and Execution Time for Embedded Platforms," 25th International Conference on Systems, Signals and Image Processing (IWSSIP), Maribor, Slovenia, 2018, pp. 1-4.

[14] N. Lawal, F. Lateef, and M. Usman, "Power consumption measurement & configuration time of FPGA," Power Generation System and Renewable Energy Technologies (PGSRET), Islamabad, Pakistan, 2015, pp. 1-5.

# Supervised Machine Learning in Inter-Level, Ultra-Low Frequency Power Line Communications

Kushal Thapa<sup>\*</sup>, Stan McClellan<sup>†</sup>, Damian Valles<sup>§</sup>

Ingram School of Engineering

Texas State University

San Marcos, TX, USA

email: <sup>\*</sup>k\_t260@txstate.edu, <sup>†</sup>stan.mcclellan@txstate.edu, <sup>§</sup>dvalles@txstate.edu

**Abstract** — Power Line Communications (PLC) is a technology that uses power lines to carry communication data alongside electrical signals. This technology has a huge potential and low infrastructure cost due to the pre-existing and ubiquitous power grid. However, the electrical components in the grid and the highly dynamic properties of the grid make power lines a hostile medium for PLC, especially when the PLC signal path extends over multiple levels (current or voltage) of the grid. Subsequently, efficient transmission of the PLC signals from the transmitter end and effective demodulation at the receiver end are both challenging. In our research, we limit PLC transmission frequencies to the ultra-low spectrum and investigate supervised machine learning as a potential signal demodulation technique. Employing inter-level PLC architecture, we transmit and collect baseband-modulated data, then use various machine learning algorithms to recover the data. We also investigate various feature-based and featureless machine learning methods for PLC and conclude that feature-based methods provide better generalization for our dataset.

**Keywords** - ultra-low frequency power line communications; machine learning; smart grid; feature based learning; featureless learning.

## I. INTRODUCTION

The following journal article is an extended version of a previous conference publication [1] and is partially derived from a thesis report [2].

Power Line Communications (PLC) is a technology that enables the transmission of communication signals over power lines. This technology has been in use since the early 1920s for various telemetry and utility applications [3][4]. One major advantage of this technology over other communication media, such as phone lines, optical fibers, etc., is the ubiquity of available infrastructure, i.e., the wires of the power grid itself. However, the grid is also a primary hindrance to the widespread deployment of PLC because of its heterogeneous nature, and dynamic load and noise characteristics [5]. These factors pose difficult challenges in the efficient propagation of PLC signals.

The heterogeneity of the grid comes in the form of varying voltage and current levels, different impedance profiles and circuit architectures, and various grid devices such as power transformers. Transformers cause a particularly difficult problem in signal propagation, especially for higher-frequency PLC signals [6]. This problem can be circumvented by excluding these devices

altogether and bounding the PLC communication path within a single “level” of the power grid. In such an “intra-level” PLC, the system voltage, circuit architecture, and other properties of the power signal are consistent throughout the path of the communication signal, effectively simplifying the problem and allowing for the use of conventional communications techniques. As a result, intra-level PLC has developed into many applications such as powerline Local Area Network (LAN) [7] and baby monitors [8]. Unfortunately, this solution does not address the problem of signal propagation through the different levels of the power grid i.e., “inter-level” PLC.

One existing solution to this propagation problem in inter-level PLC systems is the use of additional equipment like signal repeaters to bypass power transformer interconnection points. These repeaters filter and catch the communication signal in one level and pass it to the next level so that the integrity of the signal is preserved [9]. Broadband over Power Line (BPL) technology, which is a duplex and high data-rate application of the inter-level PLC, is reliant on such devices [9]. However, the cost and complexity associated with developing, deploying, and maintaining these devices have effectively obviated the use of BPL in modern grid communications [10][11]. Another approach, which does not require inter-level bypass devices, is the transmission of Ultra-Low-Frequency (ULF) signals directly over the power line infrastructure. ULF signals do not attenuate as much compared to higher frequency signals, even after passing through distribution (power) transformers, which have a fairly limited passband. Thus, ULF signals, typically in the range of 150 Hz-1350 Hz [12], can be injected into the power lines to effect a low-bandwidth form of PLC. In fact, this approach is the main principle behind a venerable, simplex, low data-rate PLC application called “Audio Frequency Ripple Control” (AFRC) that has been used in many locales worldwide for load peak shaving, street lighting, etc. [12].

A major disadvantage of using ULF bands for communication is the low data rate. However, low-rate communications techniques have been shown to have substantial value in command & control, distributed system management, and other applications, which are distinct from the “bearer-plane” of conventional communications systems [13]–[15]. There is an urgent need for this kind of technology in the power sector. The existing power grids are failing because of the exponential increase in power demand over the last few decades and the resulting issues [16]–[18].

This problem is exacerbated by the disconnect between the power producers and power consumers, which leads to serious supply chain problems. ULF-PLC can help in bridging this disconnect by providing real-time, ubiquitous, low-rate communications facilities, thereby becoming a valuable element in the communication infrastructure of a continuously sensing and self-monitoring power grid called “the smart grid.”

ULF applications like AFRC employ a simplex “downstream” format, i.e., the communication signal propagates from a High Voltage (HV) or Medium Voltage (MV) tier to a Low Voltage (LV) tier. A different approach to communication is an “upstream” method, where the signal originates in the LV tier and is collected at the MV/HV tier, typically a local substation [19][20]. For upstream inter-level PLC, assuming the communication signal effectively transits between the tiers of the distribution grid, then various Digital Signal Processing (DSP) techniques can be utilized to capture, demodulate, and decode the signal at the substation. One complexity of this approach is that DSP-based techniques would have to be unique to that the deployed source-to-destination power grid architecture. In many cases, this complexity would be exaggerated by a requirement to be tailored to individual signals or modulation techniques. This complexity is present because every element in the power grid introduces its own time-varying interference, which is coherent with the fundamental of the power signal. This issue is well-known in terms of distribution grid architecture, but not well-understood in terms of signal processing [21][22]. Thus, an approach driven by DSP alone is not scalable. To make ULF-PLC technology more universally applicable, Machine Learning/Neural Network (ML/NN) algorithms can be employed individually or in concert with conventional DSP-driven approaches [23]. The use of ML/NN algorithms may be particularly beneficial in this environment because they can estimate and dynamically adjust various parameters to correctly reconstruct the transmitted information.

Depending on the application, PLC can benefit from the full spectrum of ML types and techniques (see [23]). In this research into the use of ML/NN in ULF-PLC, supervised learning techniques are examined for two reasons: (1) the availability of labels for the training dataset, which provides an accuracy metric, and (2) the ease of implementation, which provides a path to deployment in a practical setting. The classification task of the ML algorithms was to classify a simple On-Off Keyed (OOK), upstream, inter-level ULF-PLC signal into its on and off states, thereby determining the sequence of information bits transmitted via the power line channel. Although we evaluated some unsupervised or reinforcement learning approaches, the clear benefit of supervised learning in this application provided substantial advantages. As part of the investigation, we examine PLC signal characteristics in the ULF band, explore various ways of processing PLC data to be used in ML/NN, and compare the performance of some common ML/NN algorithms in this domain.

The rest of this paper is organized as follows. Section II provides a brief survey and evaluation of the relevant

literature. Section III describes the methodology used in the collection and processing of our inter-level, upstream ULF-PLC data. Section IV presents the ML/NN framework used in our experimental study. The results of these experiments, alongside their corresponding discussions, are presented in Section V. Finally, the overarching conclusions of the research are presented in Section VI.

## II. LITERATURE SURVEY

This section surveys the existing body of research related to PLC. Although the archival literature covers a wide variety of research in various facets of PLC, we focus on low and ultra-low frequency, narrow-band PLC to survey existing implementation methods.

Korki et al. [24] developed a ULF-PLC model for an LV distribution power grid network involving mathematical analysis of the grid components. To evaluate the proposed model, Bit Error Ratio (BER) versus Signal-to-Noise Ratio (SNR) was investigated through numerical simulation. The simulation results showed that the model had acceptable BER (compared to other communication standards) for communication between neighboring nodes when SNR was above 15dB. As a result, the authors concluded that their analytical approach can satisfactorily model ULF-PLC in the LV region. This research applies a ‘bottom-up’ approach to PLC since it builds a simulation model incorporating the individual parts of the network. Its counterpart, a ‘top-down’ approach, uses measurement and data to estimate the nature of the PLC network. The bottom-up approach is harder to generalize and scale to arbitrary PLC networks because of the highly variable and dynamic nature of the PLC medium. In fact, the model proposed in [24] leverages a highly specific scope (e.g., PLC in a one-phase LV tier between one-hop nodes), which produces very limited results. Therefore, in the present work, a top-down method is used in hopes of producing a generalizable ULF-PLC solution applicable to a wider, less-specific grid domain.

Varadarajan et al. [25] investigated the channel and noise characteristics of the physical layer of PLC systems in the distribution grid. The characterization of channel and noise in the Federal Communications Commission (FCC) regulated PLC frequency band (9kHz to 150kHz) was done with empirical measurements from field tests using a modem, utility meters, and measurement equipment such as spectrum analyzer and oscilloscope. The researchers observed that the presence of distribution transformers causes severe frequency-selective attenuation of the PLC signals, which corroborates our observations. Hence, they concluded that focusing on the less attenuated (lower frequency) sub-bands can increase the quality and the coverage of the transmitted PLC signals. In contrast to [24], this study uses a top-down, empirical approach to characterize the PLC channel, which is simpler than an analytical bottom-up approach. However, the results discussed in [25] are not “constructive” and so do not provide a solution to overcome the challenges of PLC, instead providing observations and suggestions for implementation. In contrast, the present research considers applicable results from [25] (e.g., the effect of transformers

in ULF-PLC) while also exploring several approaches, which can comprise a solution framework to leverage and categorize generally applicable ML-based approaches.

Prasad et al. [26] evaluated the use of Power Line Modems (PLM) for detecting faults in the power grid. To do so, the authors collected raw data containing diagnostic parameters from the PLM, then extracted features from the raw data and used ML algorithms to identify and predict faults. This approach was able to detect faults with high accuracy and predict future faults with a lower, but satisfactory, accuracy. Similar to [24], this study uses mathematical analysis to model PLC architecture. Additionally, similar to [25], this study uses a top-down approach to detect faults through ML. In contrast to [24] and [25] however, [26] also presents a direct application of PLC in terms of useful grid diagnostics. However, [26] is limited in scope and future utility because the associated communication technology (i.e., BPL) has become obsolete [10][11]. Therefore, the present research attempts to evaluate technologies that may be leveraged in a more general implementation of ULF-PLC.

Nassar et al. [27] reviewed the signal processing techniques used to model 3-500 kHz range narrowband PLC (NB-PLC) and presented the local utility applications of NB-PLC using multi-path modeling and transmission-line modeling. In [27], PLC noise is characterized in terms of its periodicity and uncoordinated interference, and a framework for implementing Orthogonal Frequency-Division Multiplexing (OFDM) in NB-PLC is provided. The authors conclude that channel and noise modeling can be used to make robust PLC for two-way communication between the customers and the local utility in the higher frequency bands (e.g., not ULF-PLC). This study uses the channel and noise modeling approach similar to [24] while focusing on NB-PLC above 3kHz for utility applications. Although the approach and outcomes of [27] are comprehensive, no novel techniques or experimentation were introduced. Further, the applicability of spectrum above 3kHz is suspect in the distribution grid due to the large, series inductance presented by power transformers. In contrast, the present work focuses on ULF-PLC and attempts to leverage findings from the various approaches described in the literature.

In summary, two main methods of PLC implementation are prevalent: a ‘bottom-up’ approach, which leverages mathematical modeling and simulation and a ‘top-down’ approach, which leverages empirical measurement to develop useful models and evaluate technology performance. The bottom-up approach is network and application specific, subject to component modeling errors or omissions, cannot be easily scaled, and requires complex simulation. The top-down approach is more easily scalable, simpler to implement, and doesn’t suffer from component modeling errors. Therefore, the objective of the present work is to employ a top-down approach, including a combination of DSP techniques and ML/NN to aid in discriminating inter-level, ULF-PLC communication signals in the distribution grid.

### III. DATA

In this section, the methodology used to collect the raw data and the processes used to convert or transform the raw data to ML-ready datasets are described.

#### A. Transmission and Collection

The data transmission and collection architecture of the inter-level, upstream ULF-PLC is shown in Figure 1. As shown in this figure, baseband modulated ULF-PLC signals were transmitted from a research lab (LV tier) through the distribution grid and collected at a remote substation (MV tier). To create the experimental datasets, an Ametek CS3000 programmable current source [28] was used to generate On-Off Keyed (OOK) current signals with frequencies varying from 690 Hz to 2010 Hz and various amplitudes. These signals were injected into the split-phase, LV (120VRMS) power line via a specially constructed narrowband filter. This filter is a transformer-based bandpass filter or “resonant tank,” which blocks the power signal from entering the output port of the current source while allowing the signal generated by the current source to pass upstream into the power line. The signal injected into the power line first enters a split-phase distribution link typical of conventional “wall outlets,” then into the local distribution grid via three-phase distribution transformers, which “step up” the voltage for longer distance transmission. At each “level change” (tier), the transformer jointly adjusts the voltage (upward) and current (downward), according to the structure of the transformer’s coils (turns ratio). Some signature of the transmitted ULF-PLC signal is introduced into all three phases of the distribution and transmission links during this voltage transition as a result of magnetic cross-coupling within the transformer core [6]. In the substation, current transformers (CT) affixed to MV (13kVRMS) feeders sense the current disturbances introduced by the injected ULF-PLC signal. This current signal was then discretized using a conventional Data Acquisition device (DAQ) [29].

#### B. Raw Time-Series Data

The raw data captured using substation-resident, remote DAQ comprised of a set of three-phase time-series data sequences containing samples of the 60Hz power signal and its harmonics, the injected communication signal (ranging from 690Hz-2010Hz) and its harmonics, and time-variant noise at all frequencies. The acquired signals were sampled at 8kHz using 16-bits of resolution per sample (see more information about the capture parameters in Appendix B). The fundamental of the power signal dominates the raw data because of its extremely high amplitude relative to the injected signal, as shown in Figure 2. The three-phase raw time-series data plotted in this figure contain the PLC signal injected at 1595Hz, but this is not apparent from this plot alone. The vertical scale of the plot is in millivolts (mV) due to the nature of the output signals of the sensing current transformer where the full-scale of 1250mV corresponds to several hundred amperes, whereas the injected signal amplitude was lower than 1A.

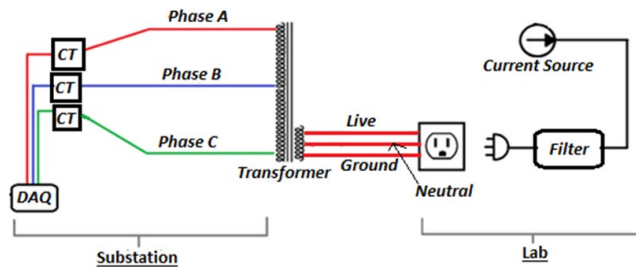


Figure 1. Data transmission and capture architecture for upstream, inter-level ULF-PLC.

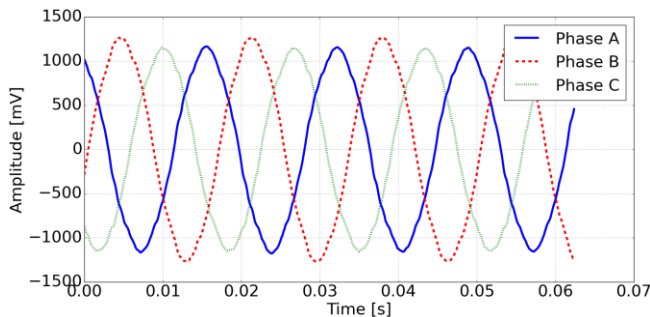


Figure 2. Time-domain plot of three-phase data received at the substation with PLC frequency at 1595Hz. The vertical scale of the plot is in millivolts (mV) due to the nature of the output signals of the sensing current transformer (1250mV corresponds to several hundred amperes).

### C. Processing

Since the raw-time series data were predictably not very useful in our case, the next logical step was to transform the signal into other domains and/or extract useful information (or features) from it.

#### 1) Transformation

Transformation, for our purposes, is defined as the conversion of time-series data to frequency domain or time-frequency domain data. There is very little loss of information in these kinds of transformations as long as care is maintained in the representation and storage of the intermediate or final values. The frequency and time-frequency transformations of our original time-series data are described in subsequent sections.

##### a) Frequency Domain

The time-domain raw data were transformed to the frequency domain using the Fast Fourier transform (FFT) [30]–[32]. Figure 3 shows a representative example of the frequency domain plot of a single-phase sequence containing a ULF-PLC signal transmitted at 1595Hz. As seen in this figure, the power signal and its harmonics dominate the spectral plot. Nonetheless, as indicated by the red arrow in Figure 3, a smaller but prominent peak is present at 1595Hz, which shows the presence of our transmitted PLC signal. However, the spectrum plot cannot show the time-varying nature of the signal, and thus does not provide us information about the OOK encoded data that were transmitted. Hence, a single frequency-domain transformation of the acquired signal may be effective in

detecting the presence or absence of the PLC signal but cannot be used to decode the time-varying information contained within it. Further, errors in framing synchronization in composing the frequency-domain transformation can produce unwanted or misleading side effects.

##### b) Time-frequency Domain

The deficiencies of frequency domain transformation, i.e., the inability to decode OOK information in our case, can be mitigated by appropriate time-frequency analysis such as a spectrogram. The transformation methods used to produce a spectrogram are very similar to the frequency-domain conversion, except the FFT is applied to frames or sub-sequences within the sequence instead of the entire time-series sequence (e.g., Short-Time Fourier Transform, or STFT). This approach provides some indicative information regarding the presence or absence of the PLC signal in those time frames. Therefore, concatenating the spectral analysis of appropriately overlapped and windowed time-domain frames across the length of the data can be used to adequately estimate the spectral configuration of the data.

In practice, there are a few measures that can be taken during this time-frequency transformation to enhance the information contained in the raw data. Windowing the time-domain frames with window functions can minimize the spectral leakage effect [33]–[35]. Similarly, overlapping the time-domain frames prevents information loss caused by the tapered ends of the windowing functions. Parameters related to these techniques, such as window type, frame length, overlap length, as well as other parameters such as frequency resolution affect the quality of the spectrograms, and thus, their values need to be carefully chosen (see Appendix C for these values for present work). Since spectrograms can be produced using Fourier (or similar) transforms, the resulting datasets may have complex-valued representations, with both real and imaginary components. Equation 1 [36] shows the mathematical representation of a complex number ‘z,’ where ‘a’ is the real component, ‘b’ is the imaginary component, and ‘i’ is the indeterminate satisfying  $i^2 = -1$ .

$$z = a + i*b \quad (1)$$

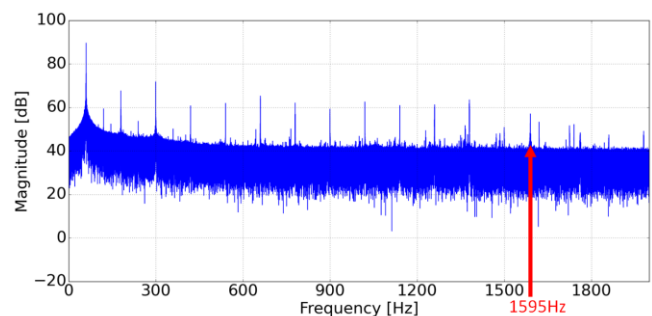


Figure 3. Frequency domain plot of the raw data showing the presence of the ULF-PLC signal at 1595Hz (pointed by the red arrow). The highest peak in this plot shows the dominant power signal at around 60Hz. The odd harmonics of this power signal can be seen as the secondary peaks.

In ML/NN implementation, these complex-valued data pose a critical challenge since the traditional ML/NN algorithms and architecture are typically not structured to operate on complex-valued datasets. One way to overcome this challenge is to devise new ML/NN frameworks, which accommodate complex-valued inputs and have complex-valued weights or coefficients. This is an active area of research [37][38] but out of scope for the present work. An easier, more accessible approach is to use an appropriate, real-valued concatenated or pre-processed representation of the complex-valued data as input to conventional ML/NN structures. In this research, we utilize two different real-valued formats for the complex-valued transform data: the magnitude/phase or polar format, and the rectangular or cartesian format.

#### i) Magnitude/Phase (Polar) Format

The most common method of converting complex-valued data to real-valued data is by combining the rectangular or cartesian real and imaginary components via a polar transformation. In polar form, the magnitude of a complex number is represented by the square root of the sum of squares of the real and imaginary components, and the phase is represented by the arctangent of the ratio of imaginary to real components [36].

For transformed time-series data, taking the magnitude of each complex-valued element of a 2D complex-valued spectrogram produces a magnitude spectrogram. This magnitude spectrogram has the same dimensions as its parent complex-valued spectrogram but does not include phase information. Figure 4(a) shows a magnitude spectrogram of one of our captured ULF-PLC datasets where the PLC frequency is at 1595Hz. This figure shows a dotted band at around 1595Hz, which corresponds to the transmitted OOK PLC signals. The zoomed-in version of this band is shown in the inset black box of Figure 4(a), which clearly shows the ‘On’ and ‘Off’ states of the ULF-PLC signal. The solid bands at various frequencies correspond to the power signal and its odd harmonics (shown by the red arrows in Figure 4(a)), which are spaced 120Hz apart.

The PLC signal also produces its own harmonics, though not as strong as power signal harmonics. Interestingly, the “harmonics” of the ULF-PLC signal are harmonically offset from the ULF-PLC signal based on the fundamental frequency of the power signal, not the ULF-PLC signal. As a result, they are “echoes” or “images” of the ULF-PLC signal with the harmonic structure described by the power signal’s frequency. If the ULF-PLC signal is injected in the frequency bands between the harmonics of the power signal, then a magnitude spectrogram can provide a good estimation of the transmitted information, especially OOK or amplitude-shifted ULF-PLC signal as shown in Figure 4(a). Therefore, the present work uses magnitude spectrograms as one of the ML/NN datasets to evaluate the accuracy of decoding the PLC signals.

As seen from 4(b), the phase spectrogram is very noisy, and the presence of the ULF-PLC signal is not visually apparent. Therefore, phase spectrograms were not used in the present work.

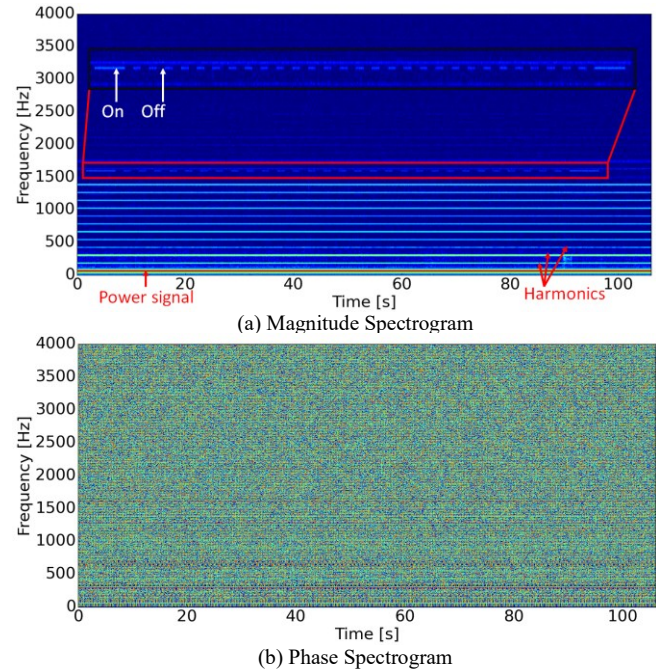


Figure 4. (a) Magnitude spectrogram of the captured data showing the transmitted OOK ULF-PLC signal with the dotted horizontal band at around 1595Hz. The solid bands at lower frequencies correspond to the power signal and its harmonics. (b) Phase spectrogram of the same data.

#### ii) Rectangular (Cartesian) Format

In addition to magnitude and phase spectrograms, other types of spectrograms (e.g., real and imaginary) can be generated as well by manipulating the components of the complex data. Plots in Figure 5 show the real spectrogram and imaginary spectrogram of the same dataset used for magnitude and phase spectrograms in Figure 4.

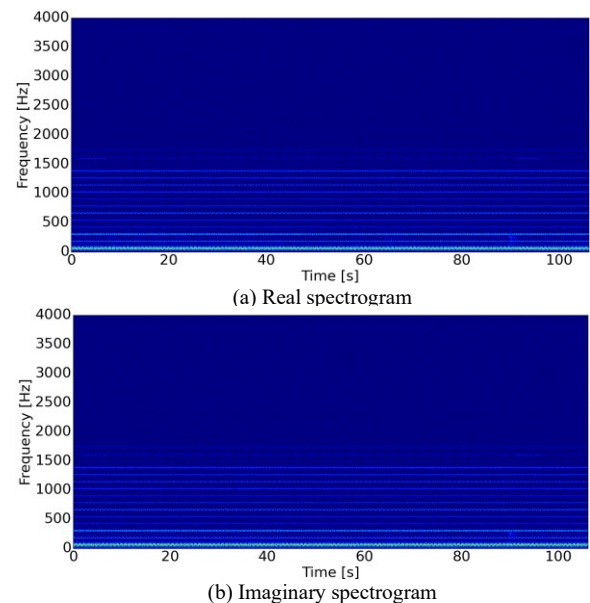


Figure 5. Real spectrogram (a) and imaginary spectrogram (b) of captured data with ULF-PLC signal at 1595 Hz.

The real and imaginary spectrograms show a trace of the PLC signal at 1595Hz; however, this band is not as distinct as the magnitude spectrogram plot in Figure 4. This is expected since the real and imaginary spectrograms completely ignore the other component, resulting in a huge loss of information. However, a combination of these two 2D spectrograms in a 3D space could potentially be better than a magnitude spectrogram since this would be a direct representation of complex-valued data as shown in Equation 1. This 3D spectrogram is hereby referred to as ‘Rectangular spectrogram’ in the present work because of its correspondence to the rectangular form of the complex-valued transform results.

Figure 6 shows in detail how the rectangular spectrogram (and other spectrograms) may be generated from the raw time-series data (as suggested in [39]). First, the 1D raw-time series data are divided into multiple overlapping frames, which are then windowed. Next, these time-series frames are transformed into frequency space using FFT. The 1D complex-valued FFT products for all frames are then combined to get a 2D complex spectrogram. From this complex spectrogram, real, imaginary, magnitude, and phase (not shown) spectrograms are produced. Finally, the real and imaginary spectrograms are stacked to form a 3D rectangular spectrogram.

In previous work [40], the rectangular spectrogram has been shown to produce better accuracy results than the magnitude spectrogram, especially when the signal of interest is dominated by out-of-band interferers such as the power signal fundamental, which is present in PLC transmissions. Therefore, we used 3D rectangular spectrogram datasets for ML/NN analysis in the present work as well.

2) Feature Extraction

Besides the spectrograms, other signal features including amplitude envelope, zero-crossing rate, spectral centroid, etc. can also be used to extract target information from the received ULF-PLC signals. For the present work, three signal features are used: (1) amplitude envelope, (2) root-mean-square energy, and (3) spectral centroid. These features are briefly described in subsequent sections.

a) Amplitude Envelope

The amplitude envelope of a signal describes the variation in the amplitude of the signal over time [41]. It effectively traces the outline of the signal in the time domain and is loosely representative of the instantaneous energy in the signal [42]. In our case, the complete amplitude envelope is not useful since the 60Hz power signal and its harmonics dominate all other superimposed signals, as described previously. As is typical in communications systems, the narrowband amplitude envelope, centered on specific sub-bands, can be more

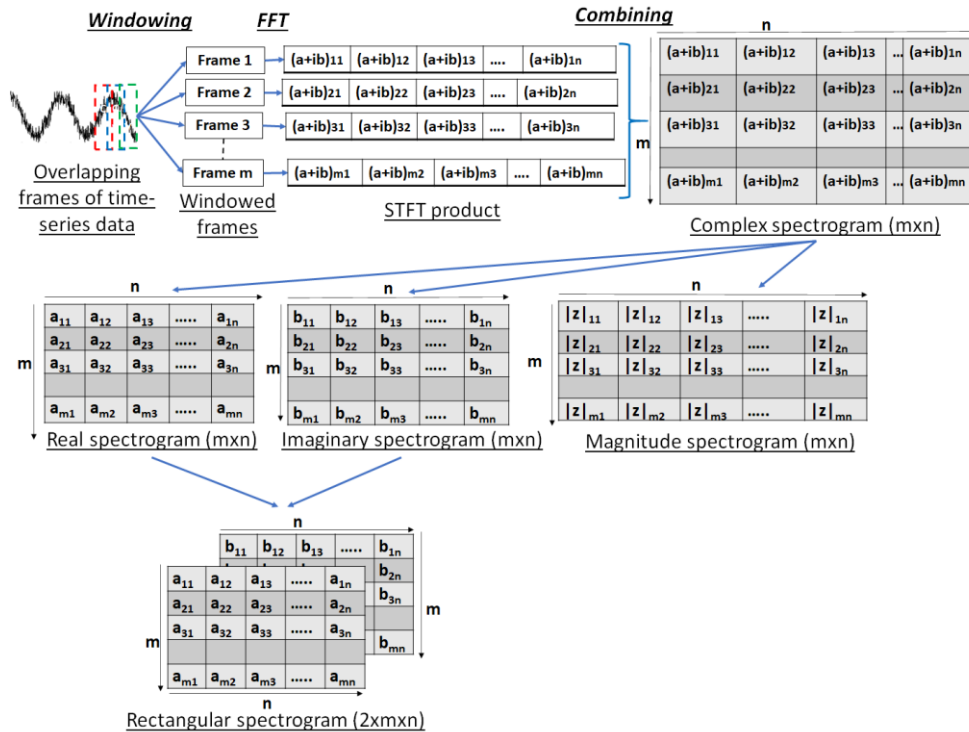


Figure 6. Process of generating rectangular spectrogram from raw time-series data. As shown here, the 1D raw-time series data are first divided into multiple overlapping frames. Then, each of these frames is windowed by a window function. Next, these time-series frames are transformed into frequency space using Fast Fourier Transform (FFT). The 1D complex valued FFT products for all frames are then combined to get a 2D complex spectrogram. From this complex spectrogram, real (denoted by  $a_{xy}$ ), imaginary ( $b_{xy}$ ) and magnitude spectrogram ( $|z|_{xy}$ ) are produced. Finally, the real and imaginary spectrograms are stacked to form a 3D rectangular spectrogram.

useful. To approximate this approach and create a useful training/testing dataset, we filtered the raw frames of the powerline signal with non-overlapping bandpass filters of 100Hz bandwidth (1Hz-100Hz, 101Hz-200Hz,...,2901-3000Hz) to create thirty sub-band representations of the signal. Clearly, the amplitude envelope of certain sub-bands contains the injected PLC signal, so the amplitude envelope can be useful.

#### b) Root-Mean-Square Energy

An energy of a digital signal is defined as the sum of the square of its magnitude [43]. Root-Mean-Square Energy (RMSE) is the square root of the mean energy of a signal, as in Equation 2 [44] where  $x_i$  is the  $i^{\text{th}}$  sample of signal  $x$  and  $N$  is the total number of samples. This is particularly useful for signals that are “balanced” or have zero mean in the time domain.

$$RMSE = \sqrt{\frac{(x_1^2 + x_2^2 + \dots + x_N^2)}{N}} \quad (2)$$

For our raw (full-band) PLC data, the energy (or instantaneous energy in a frame) would again be dominated by the power signal. Hence, we frequency separated the frames as described in Section III.C.2)a) and calculated RMSE for each of the thirty narrowband signals of each frame. Similar to the amplitude envelope, we were expecting variations in the RMSE in the frequency range containing ULF-PLC signals (for example, 1501-1600Hz for the 1595Hz PLC signal) to provide useful information about the PLC signal.

#### c) Spectral Centroid

The spectral centroid is the measure of the center of mass of the signal’s spectrum [45]. Unlike time-domain features such as amplitude envelope and RMSE, the spectral centroid is a frequency-domain feature. The spectrum of our full-band signal contains a primary peak near 60Hz and large secondary harmonic peaks at odd multiples of 60Hz because of the dominant power signal. As shown in Figure 3, whenever the OOK PLC signal is active (‘On’), a peak is

present at that frequency. The presence or absence of the PLC signal shifts the center of mass of the spectral representation, thereby providing a classification measure of the state of the transmitted PLC signal.

#### D. Dataset

The raw data, obtained from DAQ at the substation, were composed of twenty-three individual files in the WAV format. Each of these files contained three-phase, time-domain PLC data (such as shown graphically in Figure 2) with a different baseband PLC transmission frequency for each file ranging from 690Hz to 2010Hz (Appendix B). The remaining processing steps in the present work consider only data from ‘Phase A.’ However, in subsequent research, the comparison between phases after injection of a communication signal on a single phase can also produce some useful insight [16].

The bit duration or baud rate of the injected OOK signal, i.e., the original length of the individual on or off state representing a ‘0’ or ‘1’ bit, in the experimental dataset was about 2 seconds (16,000 samples) when interpreted via conventional “Return-to-Zero (RZ)” line encoding [46]. To enhance the dataset for ML/NN training, we interpreted the transmissions as “Non-Return-to-Zero (NRZ)” with 1,000x repeats per bit, thus providing a substantially larger training set.

Features of the oversampled dataset such as amplitude envelope, RMS energy, and spectral centroid were extracted and compiled into ‘Dataset 1’ (see Figure 7), a 2D dataset with 61 feature columns - 30 each for amplitude envelope and RMS energy, and 1 for spectral centroid - and 18,400 rows (800 per file\*23 files). Similarly, 2D magnitude spectrogram and 3D rectangular spectrograms (Appendix C) were constructed for the signals and combined into ‘Dataset 2’ and ‘Dataset 3’ (see Figure 7). Even though, as seen in Figure 2, the unprocessed, full-band time-series data does not seem to provide any indication of the transmitted PLC signal due to the strong out-of-band interference of the power signal, we compiled this raw data into ‘Dataset 4’ to be certain that the ML/NN evaluation came to the same conclusion.

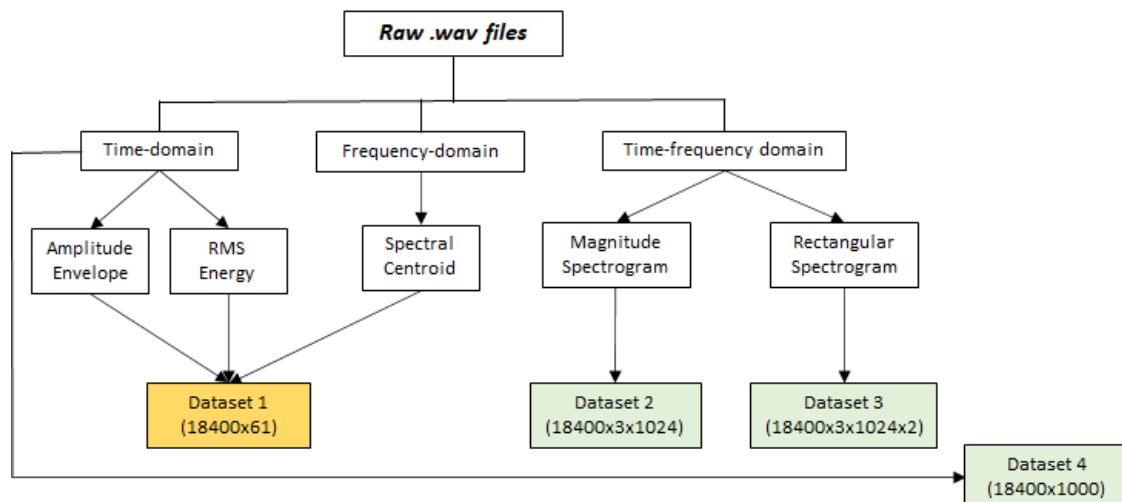


Figure 7. Flow chart showing the summary of steps taken to convert the raw data to ML/NN ready datasets.

The flow chart in Figure 7 shows the summary of these steps (see Appendix E for a more detailed flow chart). In this figure, the orange highlights, i.e., ‘Dataset 1,’ comprises feature-based data while the light green highlights, i.e., ‘Dataset 2,’ ‘Dataset 3’ and ‘Dataset 4,’ comprise featureless data. The summary of these datasets is shown in Table I. The difference between our use of feature-based versus featureless datasets is described in section IV.

TABLE I. DATASETS AND THEIR BRIEF DESCRIPTION

Dataset Name	Type	Description
Dataset 1	Feature-based	Uses amplitude envelope, RMS energy, and spectral centroid
Dataset 2	Featureless	2D magnitude spectrogram
Dataset 3	Featureless	3D rectangular spectrogram
Dataset 4	Featureless	1D time-series data

#### IV. MACHINE LEARNING AND NEURAL NETWORK SETUP

ML/NN can be categorized based on various criteria, such as forms of learning (supervised, unsupervised, reinforcement), types of tasks (classification or prediction), learning techniques (batch or online), etc. [47][48]. Although not a traditional way of classifying ML/NN, a distinction based on data processing requirements can be important because of its implication in realistic applications. Under this criterion, ML/NN can be broadly divided into two categories: feature-based learning and featureless learning. In the current work, we implement both feature-based and featureless ML/NN on our PLC data, comparing and contrasting the performance of these two methods based on various metrics. In this section, the two methods are discussed along with a brief description of their experimental setup, their expected performance, and their relation to our datasets.

##### A. Feature-based ML/NN

In feature-based learning, useful features are extracted from the raw data during pre-processing. These features are then compiled into a dataset before being fed into the ML/NN algorithms. The advantage of this approach is that large datasets with lots of noise and irrelevant features can be transformed and concentrated into smaller datasets, reducing computing time and complexity. However, the ML performance largely depends on the quality and consistency of the extracted features. The study of the data and the knowledge of the domain is vitally important in this type of ML, and thus, substantial effort in ML applications is spent on these data study and feature planning stages.

For the current work, ‘Dataset 1’ was used for feature-based ML/NN, as indicated in Figure 7 and Table 1, with a 70:30 training:testing configuration. To form the models with various supervised algorithms, Python Sci-kit learn [49] was used for Logistic Regression (LR) [50], Support Vector Machines (SVM) [51], and Decision Tree (TREE) [52]. The hyperparameters for these algorithms were optimized using the grid search [53] method. Accuracy, precision [54], recall [55], and f1 scores [56] were computed to evaluate and compare these various models’ training and

testing performance. Learning curves [57] were plotted and evaluated to ensure the models were not overfitting or underfitting. Confusion matrices [58] were also plotted to visualize the accurate label versus the predicted label.

In general, LR does well on linear classification. Our OOK PLC signals are linearly separable. However, the background power line channel, with the power signal and its coherent harmonics, is highly non-linear and introduces coherent distortion. Hence, if the featureless or unprocessed datasets were used on LR, we expected this algorithm to struggle. The feature extraction process we have utilized filters out these background non-linearities to some extent. Therefore, LR should still be able to do reasonably well with feature dataset. SVM, on the other hand, has both linear and non-linear kernels and TREE is a non-linear classifier. Therefore, we expected both of these algorithms to perform well using our feature-based dataset.

Besides these basic “one neuron” ML models, a multi-neuron, multilayer Neural Network (NN) or Artificial Neural Network (ANN) model was also tested using Python’s Tensor Flow [59] and Keras [60]. The various hyperparameters of these NN models were optimized by manual trial and error (see Appendix D). Accuracy scores, loss and validation curves, and confusion matrices were generated to evaluate this model’s performance, which was compared with the other ML models. Since ANN is also a non-linear classifier, we expected this method to provide high classification accuracy. For a low dimensional, low complexity feature dataset such as our PLC data, ANN may be overly complex and could potentially lead to overfitting. However, ANNs are more versatile than LR, SVM, and TREE because of their multi-neuronal, multi-layer structure, and thus, could also be used in ULF-PLC data, which has more complex signal characteristics.

##### B. Featureless ML/NN

In contrast with feature-based learning, featureless learning does not require explicit feature extraction during data pre-processing. Although the ML or NN algorithms still require features, these features are extracted from the raw data by the algorithms themselves thereby removing the burden from the operator. This translates to a more generalizable, repeatable, and uniform ML analysis. This type of ML is more scalable since human intervention is less important when scaling to datasets of different properties. Unfortunately, featureless learning also requires more computational power, and the ML is more prone to noise.

ANN was used for our featureless datasets because of its simple architecture, ease of implementation, scalability, and most importantly, its ability to process multi-dimensional datasets. The multi-neuron nodes and fully connected layers of ANN can process complex information, such as the 2D and 3D spectrogram datasets, where the traditional ML algorithms fail. Therefore, they are an ideal candidate to evaluate our featureless ULF-PLC datasets.

The hyperparameters of the ANN including the number of hidden layers and the number of neurons in each layer were kept the same as for feature-based ANN (Appendix D). Accuracy scores, loss and validation curves, and

confusion matrix were generated for the optimized models for each dataset to evaluate the performance of the models and compare them across datasets.

Within our featureless datasets, we expected the time-series dataset to fail for the reasons presented in Section III.B., and for the magnitude and rectangular spectrogram datasets to produce better outcomes due to the tradeoff between the quality and the quantity of information they contain. For example, the magnitude spectrogram captures the On/Off amplitude information of OOK signals more clearly and compactly. However, as described in Section III.C.1)b)ii), the rectangular spectrogram contains more information about the transmitted PLC signal. Therefore, the accuracy and other performance measures of these two datasets in a NN model depend on how well the NN fits the respective data. With enough optimization, we expected both these datasets to perform similarly.

## V. RESULTS AND DISCUSSIONS

The results of our research are divided into three main sections based on the type of dataset used in ML/NN. Section V.A. covers the results generated from feature-based dataset, Section V.B. covers the results from the use of featureless dataset, and Section V.C. compares the feature-based and featureless datasets.

The experimentation using both feature-based and featureless ML/NN is further divided into three cases, as listed in Table 2, each representing a unique real-life scenario. These scenarios arise because of the nature of the power signals. The frequency of the fundamental power signal in the PLC channel is not constant but oscillates close to 60Hz. This power signal produces strong odd harmonics at 120Hz spacings, which also oscillate corresponding to the fundamental. These dominant signals, therefore, occupy a wide range of variable frequencies in the ULF-PLC spectrum. This problem is exacerbated by additional noise of the channel, which can present time-variant interference to the ULF-PLC signals. Therefore, locating clean frequency bands for transmitting a signal in the ULF spectrum can be challenging.

Case 1, as listed in Table 2, simulates the scenario in which the frequency band to send the PLC signal is known and consistent. This would require a great deal of knowledge of the channel, so that the PLC frequency band does not overlap with the pre-existing harmonics (or the noise), which are also time-varying. Therefore, this is an unlikely scenario; however, if implemented correctly, is the easiest for the receiver to process.

TABLE II. THREE EXPERIMENTAL CASES SIMULATING THREE UNIQUE FREQUENCY SCENARIOS IN ULF-PLC

Case	Description
Case 1	Baseband ULF-PLC signal frequency is always the same, and thus known
Case 2	Baseband ULF-PLC signal frequency changes within a set of known values
Case 3	Baseband ULF-PLC signal frequency changes within a range

Case 2 is similar to Case 1 in the sense that it simulates a scenario where the PLC frequency is known. However, in this case this frequency is not constant, but changes frequently to some known set of values (e.g., frequency hopping [61][62]). This case is built on the assumption that there is a technology present on the transmitter side that facilitates frequency hopping by continuously scanning the power line spectra and identifying an “open” channel from a set of allocated channels. This case is more realistic than Case 1 because it accounts for the variable nature of the channel and the ability to dynamically select open subsections of the low-frequency spectrum. However, this approach still relies on the assumption that the at least some of the frequency bands or sub-channels in the pre-defined set is always optimal for transmission. As a result, effective implementation of a frequency-hopped ULF-PLC system would depend in large part on dynamic spectral analysis of the channel.

Finally, Case 3 simulates a scenario in which the PLC frequency band is unknown as well as dynamic. Like Case 2, this case is built on the assumption that there is system that dynamically identifies an open channel. However, unlike Case 2, the open channel frequency does not need to be from a pre-determined set (but will be within the ULF range). This case also has interesting application in the observation or extraction of unknown events or the presence of anomalous signals in the ULF-PLC bands.

For both types of datasets and all three cases, the performance of the models is evaluated primarily using the metric of training accuracy, which essentially reflects the system’s BER, an important metric in digital communication. BER is the ratio of error bits to the total number of transmitted bits. Thus, BER is the “unit complement” of accuracy, i.e.,  $BER + accuracy = 100\%$ . Therefore, higher accuracy translates to lower BER, which in turn means that communication is more efficient.

### A. Feature-based Dataset

As described in Section III.D. and illustrated in Figure 7, we constructed the feature-based dataset (‘Dataset 1’) by combining the amplitude envelope, RMS energy, and spectral centroid features.

#### 1) Case 1- Known and Static Frequency

For Case 1, the PLC frequency is known. To process, we divided ‘Dataset 1’ into individual frequency subsets, then trained and tested ML/NN within each subset. The data in all these frequency subsets were standardized (separately), the hyperparameters of LR, SVM, and TREE algorithms were optimized, and then fitted with the corresponding models.

The training to test ratio for each experiment was set to 70:30. Since, each frequency subset was trained and tested separately, there were 560 training samples and 240 test samples for each Case 1 experiment. After fitting the models with these training data, the models were tested with test data. The process was repeated ten times (with randomized training test split for each iteration) to explore the variance of the performance of these models. Figure 8 shows the accuracies (mean accuracy curves and the 95%

confidence interval from ten iterations) of the four models from these test data at various frequencies. The inset graph within Figure 8 shows the frequencies, from 930Hz to 1650Hz, where the model test accuracies were consistently over 90%.

As seen in Figure 8, the lower and higher end of the experimental spectrum both have low test accuracies across all models. This is due to the limits of the coupling filter as well as the bandpass filtering nature of the channel for the PLC signals. At lower range of frequencies (below 870Hz in the graph), the harmonics of the fundamental power signal is very strong, and thus, the PLC signal is severely distorted. As frequency increases, these harmonics die off, opening dynamic subchannels into which the PLC signals can be introduced. However, beyond a certain frequency (after 1710Hz in the graph), the PLC signals are heavily attenuated by the transformers and other grid components, including the coupling filter, causing poor PLC output at the receiver. Therefore, there is a frequency window where the PLC signal transmission is optimal. Figure 8 shows that, in our case, this window is between 930Hz to 1650Hz. Within this window, the test accuracies are fairly high (mostly above 95%) and stable for all models, as shown by the inset graph in Figure 8.

In summary, this Case 1 experimentation shows that with sufficient knowledge of the channel and with a set of known PLC frequency, upwards of 95% accuracies can be obtained using feature-based ML/NN. High accuracy of the models means low BER, which translates to high efficiency in communication.

2) Case 2- Known but Dynamic Frequency

For Case 2, we took ‘Dataset 1’ as a whole for training and testing, instead of separating it with respect to frequency as described for Case 1. Hence, ‘Dataset 1’ was randomly split into training and test set, and the ML/NN models were fitted with the training set and evaluated with the test set. The dataset is more complex in this case for ML/NN to generalize because the PLC frequency is not the same throughout, and thus, the weight for the feature column keeps changing during learning process. This results in slower convergence than Case 1, as shown in Figure 9.

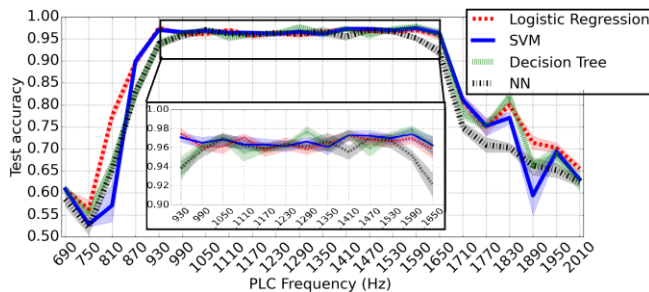
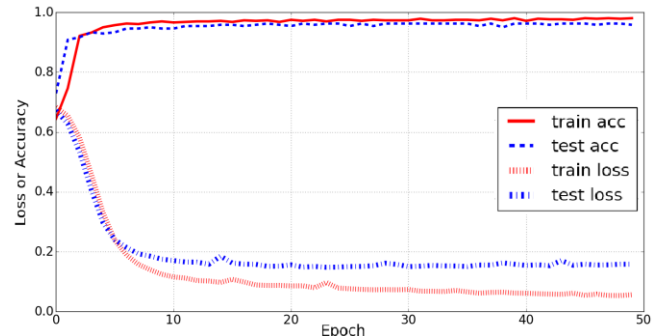
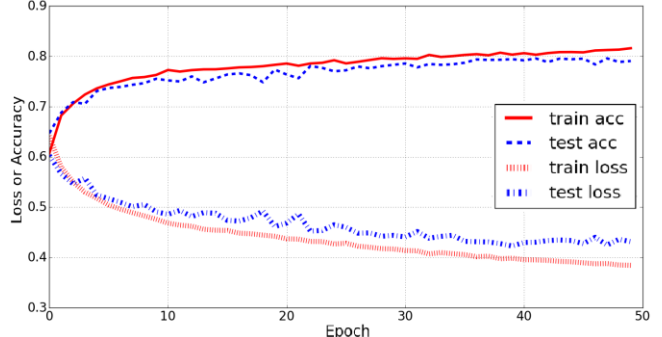


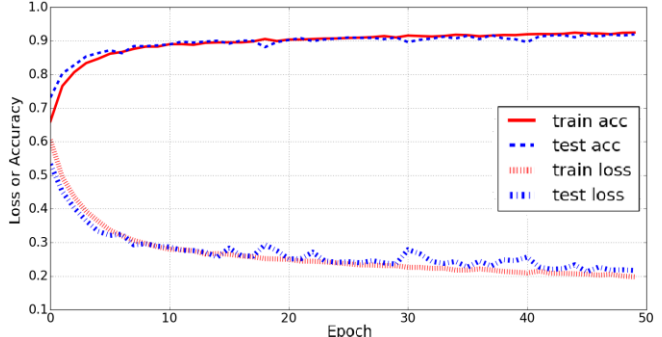
Figure 8. Graph showing test accuracy curves of Logistic Regression, SVM, Decision Tree and Neural Network models fitted with various ULF-PLC signal frequency dataset (subsets of Dataset 1). The shadowed region of the curve represents the 95% confidence interval of the accuracies. The inset graph shows a zoomed-in version of the curves for frequencies from 930Hz to 1650Hz.



(a) Case 1 at frequency of 1290Hz



(b) Case 2 with full ‘Dataset 1’



(c) Case 2 with trimmed ‘Dataset 1’

Figure 9. Graphs showing training and test (or validation) accuracy and loss curves of identical NN for (a) Case 1 with frequency of 1290Hz, (b) Case 2 with full dataset, and (c) Case 2 with trimmed dataset. The trimmed dataset for (c) is from 870Hz to 1710Hz.

As seen in Figure 9(a), the accuracy and loss curves of both training and test sets converge within the first few epochs for Case 1. However, for Case 2, the convergence takes more epochs. Figure 9(b) is for the Case 2 dataset with full range of frequencies, i.e., the complete ‘Dataset 1,’ which shows that the loss and accuracy curves do not stabilize within 50 epochs. In addition, the accuracies are much lower at the end of the training than in Case 1 (approximately 80% compared to around 95% for Case 1). This is because of the presence of 690Hz-810Hz and 1770Hz-2010Hz frequency data within ‘Dataset 1,’ which contains distorted PLC signals as shown in Figure 8. The data corresponding to these frequencies dilute the dataset, thereby causing low accuracies in Case 2. Therefore, for a fairer comparison, we took out these frequency data from the dataset for further Case 2 analysis, resulting in a “trimmed” dataset for Case 2. Figure 9(c) shows the

accuracy and loss curves of this trimmed ‘Dataset 1.’ In addition to the increased accuracies, trimming the dataset resulted in enhanced loss and accuracy curves.

After trimming ‘Dataset 1’ to include only the frequency data from 870Hz-1710Hz (i.e., the passband of our PLC channel), next we fitted the four algorithms with this updated dataset. The training and test accuracies, precision, recall and F1 scores of these models are listed in Table 3.

As seen in Table 3, SVM had the highest scores in all performance metrics for this trimmed ‘Dataset 1’: Case 2. TREE and NN displayed similar performance, while LR outcomes were substantially worse with approximately 10% difference in every metric compared to SVM. Further, observing the recall values, the NN model is competitive with the SVM due to the recall capabilities to classify true labels very well and has a minimal number of samples that were “false negatives.”

To analyze the possible causes of this discrepancy between the various algorithms, we constructed a 2D plot with decision regions for each of these models. The two feature columns for these 2D plots were selected using backwards Sequential Feature Selection (SFS) [63] to give two most influential feature columns for each model. Figure 10 shows these plots for LR, SVM and TREE models. The axis names in these plots are in the format ‘Feature abbreviation’ followed by ‘Frequency sub-band.’ RMSE indicates ‘RMS Energy’ feature while APEV indicates ‘Amplitude Envelope.’

As seen in Figure 10, LR displays a linear and continuous boundary, while the decision boundary of SVM is continuous and curved, and the decision boundaries of TREE are straight but discontinuous. These decision boundaries separate the two OOK signal states (i.e., On and Off or 1 and 0); therefore, the more flexible these boundaries are, the better the accuracy of the models’ classification. The linearity of LR can sometimes prevent it from fitting some training data, whereas the SVM and TREE are more flexible, and thus, can have higher classification accuracy. However, SVM and TREE are more prone to overfitting for the same reason. In our current case, i.e., Case 2, there is no overfitting (or underfitting) on any of our models as shown by the small difference between training and testing accuracies in Table 3.

TABLE III. PERFORMANCE OF LR, SVM, TREE AND NN WITH TRIMMED ‘DATASET 1.’ THE VALUES SHOWN IN THE TABLE ARE THE MEAN +/- STANDARD DEVIATION FROM TEN ITERATIONS

Algorithms	Training accuracy	Testing accuracy	Precision	Recall	F1 score
LR	0.81790 +/- 0.00328	0.81870 +/- 0.00398	0.84334 +/- 0.00522	0.80534 +/- 0.00808	0.82387 +/- 0.00429
SVM	0.92355 +/- 0.00293	0.90826 +/- 0.00388	0.93420 +/- 0.00595	.88838 +/- 0.00473	0.91070 +/- 0.00370
TREE	0.90768 +/- 0.00478	0.86604 +/- 0.00980	0.91220 +/- 0.02532	.82626 +/- 0.02008	0.86661 +/- 0.00889
NN	0.90571 +/- 0.00313	0.90078 +/- 0.00409	0.91201 +/- 0.01740	0.89916 +/- 0.02417	0.90507 +/- 0.00517

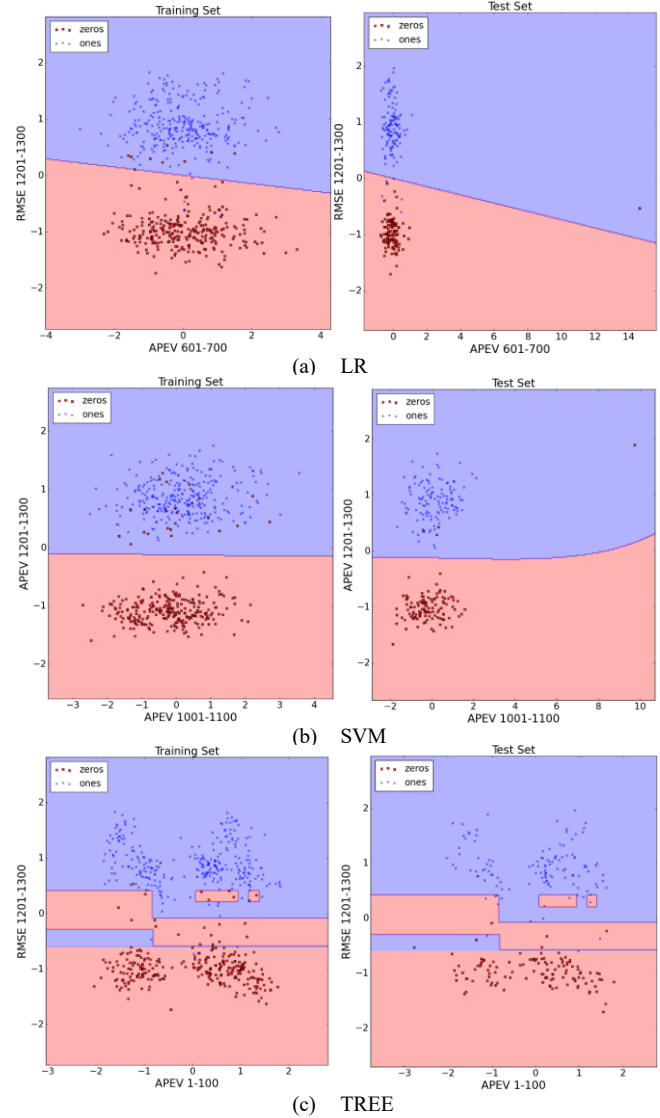


Figure 10. Plots showing training and test data (standardized), plotted over two optimal feature columns, along with the decision boundary and shaded target regions of (a) LR (b) SVM and (c) TREE models. The axis names are in the format ‘Feature abbreviation’ followed by ‘Frequency sub-band.’

### 3) Case 3- Unknown and Dynamic Frequency

In Case 3, the ML/NN is trained with a range of frequencies, and the test is done with some frequency within or close to this range, but not present in the training set. Therefore, the only prior information needed in this scenario for real-life implementation is the general frequency range containing the PLC signal and a training set, which incorporates this same range, or set of potential channels/subchannels. The expectation is that the ML/NN will train within this range and be able to generalize well enough to classify signals, which lie in frequencies or subchannels that were not specifically trained for recognition. To simulate this scenario, we separated ‘Dataset 1’ into individual frequency subsets or subchannels, used all subchannels except one subset for training, and tested on the unused subchannel. Our objective with this case was to test

how well ML/NN models can generalize on data with untrained PLC frequency and to observe what effect the frequency has in the case of ambiguous subchannel isolation. As with Case 2, including the complete ‘Dataset 1’ for this case would dilute the dataset and cause low training accuracy. In practical use cases, the frequency bounds or range of subchannels can be specified. Therefore, for Case 3, we used trimmed ‘Dataset 1’ as in Case 2.

Figure 11 shows the test accuracies of this experiment for the four algorithms (LR, SVM, DT, and NN). In the figure, frequencies shown on the X-axis indicate the subchannel that was not contained in the training set. As a result, the results shown in Figure 11 indicate the accuracy of the ML/NN approach for transmissions where that specific sub-band was used in testing but was not used in training.

As seen in Figure 11, all of the algorithms had some success in generalizing to the test data with untrained PLC sub-bands. However, the performance is not consistent for any algorithms across the whole spectrum. The low accuracies at the extremes, i.e., 870Hz and 1710Hz can be explained by the fact that the models are trained using sub-bands higher or lower from the testing sub-band, but not both higher and lower. Therefore, the model only has the upper or lower set of sub-bands to generalize the test set. This causes low accuracy. Extending this similarity or bounding measure argument, we expect the sub-bands near the middle of the range to have the highest accuracy, decreasing to either side. The curves in Figure 11 promise a similar trend; however, this general trend seems to be contradicted by two big dips around sub-bands centered at 1050Hz and 1350Hz. Upon closer examination of the models at these two sub-bands, we discovered that the inconsistencies are due to the lack of robustness of the models themselves. The architecture and hyperparameters of each model were held constant for all sub-bands and all test scenarios, i.e., the models are not optimized for specific training set. This approach simulates the real-life implementation of this case, where the models are trained across a broad set of subchannels and cannot be optimized for the unknown subchannel. Therefore, our models were not optimized for certain test sets, and they failed at those frequencies. Despite this setback, the models showed high accuracy in the majority of tested sub-bands, and thus showed promising generalization behavior. Further optimization of these models or use of more complex models may be useful in rectifying the inconsistencies.

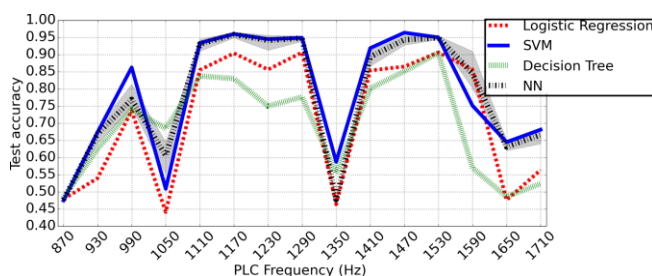


Figure 11. Test accuracies for Logistic Regression, SVM, Decision Tree and Neural Network for Dataset 2: Case 3. The PLC frequency on the x-axis represents the test frequency.

## B. Featureless Dataset

In addition to using a feature-based dataset in ML/NN, we also investigated the use of featureless datasets. We did so by constructing 1D time-series, 2D magnitude spectrogram and 3D rectangular spectrogram datasets, as discussed in Section III.D. NNs were used on each dataset because of their ability to accept multi-dimensional input data. The multi-neuronal architecture of NNs is also more complex than one-neuron structures of LR, SVM or TREE, which could aid in parsing through our noisy featureless datasets. The structure and hyperparameters of the NN for the time-series and magnitude spectrogram dataset were identical to the NN used for the feature-based dataset (Appendix D). For the rectangular spectrogram however, an additional convolution layer and a max pool layer were added (as part of manual optimization) before the fully connected NN layers. The complete architecture of this convolutional neural network (CNN) is shown in Figure 12.

As seen in Figure 12, each sample of the rectangular spectrogram is  $3 \times 1024 \times 2$ , where 2 is the number of channels (i.e., stacked real spectrogram and imaginary spectrograms). The first operation is convolution with  $64 \times 3 \times 3$  filters producing  $1 \times 1022 \times 64$  feature maps that are fed into the max pool layer with pool size  $1 \times 3$  and produces output of  $1 \times 340 \times 64$ . This output is flattened to a 1D array of size of 21,760 samples and fed into the fully connected NN for training and testing. This NN is identical to the ones used in the feature-based dataset (Appendix D). Subsequent sections describe the comparative analysis of these three featureless datasets.

### 1) Case 1- Known and Static Frequency

In Case 1, the NN/CNN is trained and tested within a particular frequency subset or set of subchannels/sub-bands. The test accuracy results of the NN/CNN models are presented in Figure 13.

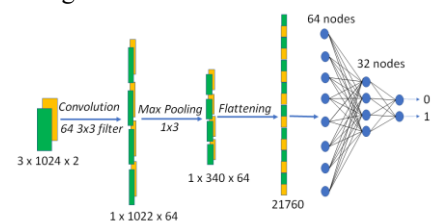


Figure 12. CNN architecture showing the various layers of operation on our rectangular spectrogram dataset.

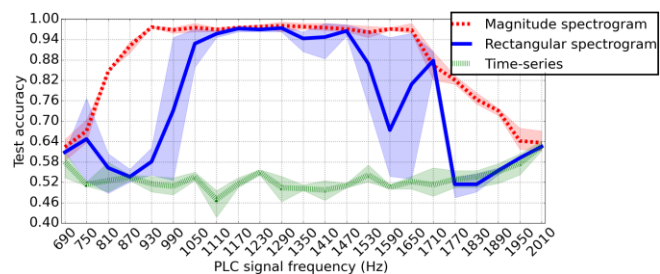


Figure 13. Graph showing test accuracy curves (with 95% confidence interval) of NN models fitted with magnitude spectrogram (Dataset 2), rectangular spectrogram (Dataset 3) and time-series (Dataset 4) datasets containing ULF-PLC signals of various frequencies.

The time-series dataset exhibited poor performance, as expected due to the strong out of band interference (i.e., the power signal). Between the two spectrogram formats, the magnitude spectrogram models exhibited better overall performance, and particularly better accuracy than the rectangular spectrogram models, especially in the lower and the higher end of the spectrum. The magnitude spectrogram models also had a much narrower and more consistent confidence interval than the rectangular spectrogram. The confidence interval result is especially interesting since a larger confidence interval implies larger variance, and hence, the rectangular spectrogram dataset seems to have higher variance in its accuracy results. Higher variance suggests more unpredictability and less repeatability in the performance, which is undesirable.

This discrepancy in performance between magnitude spectrogram and rectangular spectrogram formats can be explained by the type and quantity of information each dataset contains. The magnitude spectrogram, by definition, contains only the magnitude or energy information of the signal, which is directly related to the signal amplitude. So, for OOK signals, the magnitude spectrogram more clearly represents modulation transitions, thus simplifying the task for the NN. In contrast, the rectangular spectrogram holds more information about the signal, including phase data, which could be advantageous in some use cases such as phase-based modulation (e.g., Phase Shift Keying) or a combination of phase and amplitude modulation (e.g., Quadrature Amplitude Modulation). However, in the approaches discussed here, the larger size of the rectangular dataset causes data dilution resulting in lower performance compared to magnitude spectrogram models.

### 2) Case 2- Known but Dynamic Frequency

As in Case 2 of the feature-based ML/NN analysis {Section V.A.2)}, the NN/CNN is trained with the trimmed featureless datasets (without separating frequency subsets). The objective in this approach is to explore which featureless datasets perform the best when trained with samples containing PLC signals of varying frequencies. Table 5 summarizes the result of this experimentation (with ten iterations of each model).

As shown in Table 5, the magnitude spectrogram models outperform other models. The time-series models fail again due to the nature of the unprocessed time-series PLC data and the presence of the strong out-of-band interferer. Interestingly, the recall score of the time-series dataset is very close to 1. This does not necessarily mean that the time-series model performed well. Figure 14 shows the confusion matrix of one of these time-series models, which explains why the recall score was high even though the accuracy was low. As shown in this figure, the time-series model predicted all samples as '1' (On), which explains the low accuracy. The recall is calculated as shown in Equation 3. The true positives are the accurately classified positives (top left quadrant in Figure 14) while the false negatives are misclassified negatives (bottom left quadrant). In our case, both values are zero, giving  $0 \div 0$ , which causes error, but is overwritten as 1 during processing. In this way, the recall was very high.

$$\text{Recall} = \frac{\text{Truepositives}}{\text{Truepositives} + \text{Falsenegatives}} \quad (3)$$

TABLE IV. PERFORMANCE OF MAGNITUDE SPECTROGRAM (DATASET 2), RECTANGULAR SPECTROGRAM (DATASET 3) AND TIME-SERIES (DATASET 4) NN/CNN MODELS. THE VALUES SHOWN IN THE TABLE ARE THE MEAN +/- STANDARD DEVIATION FROM TEN ITERATIONS

Dataset type	Training accuracy	Testing accuracy	Precision	Recall	F1 score
Time-series	0.52595 +/- 0.00000	0.52583 +/- 0.00000	0.52583 +/- 0.00000	1.00000 +/- 0.00000	0.68924 +/- 0.00000
Magnitude spectrogram	1.00000 +/- 0.00000	0.95503 +/- 0.00326	0.96010 +/- 0.00413	0.95415 +/- 0.00512	0.95710 +/- 0.00314
Rectangular spectrogram	0.76138 +/- 0.15679	0.73655 +/- 0.14313	0.74463 +/- 0.14841	0.88257 +/- 0.08874	0.79102 +/- 0.07624

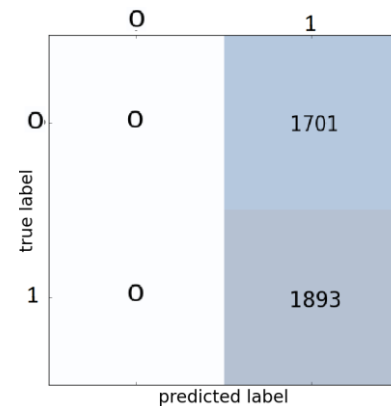


Figure 14. Confusion matrix of a featureless time-series model. This model was fitted with trimmed 'Dataset 4' for Case 2 analysis.

### 3) Case 3- Unknown and Dynamic Frequency

In Case 3, the NN/CNN models are trained using every sub-band within the dataset (Datasets 2, 3 and 4) except one, and tested with the one that was left out of the training process. The objective in this approach was to observe if the NN/CNN featureless models can generalize during the training process to be able to perform well on test data with untrained PLC sub-bands. The result of this experimentation is summarized in Figure 15.

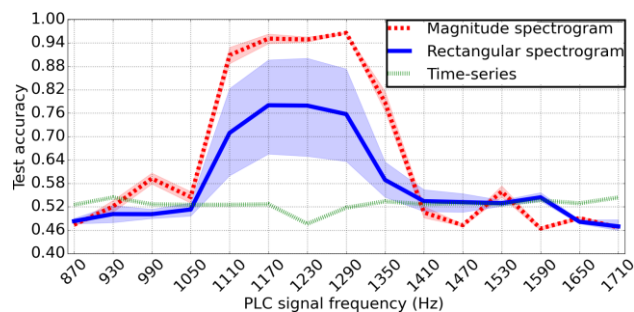


Figure 15. Test accuracy curves of NN/CNN models fitted with magnitude spectrogram, rectangular spectrogram, and time-series dataset for Case 3 analysis.

As seen in Figure 15, the time series data again failed, as expected. The magnitude and rectangular spectrogram formats, however, had some success in generalizing to a new frequency data subset. The bell-shaped accuracy curves of both rectangular and magnitude spectrograms support the “similarity measure” hypothesis formulated previously in Case 3 of feature-based datasets in Section V.A.3). Reiterating, it seems that the ML/NN models are able to generalize the best (and perform well) to a sub-band when trained on the greatest number of similar sub-bands, and in particular sub-bands on “both sides.” The sub-bands near the edge of the passband have the fewest “similar” sub-bands for training whereas the sub-bands in the middle of the passband have the most, and hence, the accuracies for edge cases should be the lowest with increasing accuracy moving towards the middle. The curves for both spectrogram datasets shown in Figure 15 indeed show that the accuracies are low at the edge frequencies and greatest at mid frequencies, supporting our hypothesis. For practical implementation, this means that the training frequency range, for this type of unknown and dynamic PLC frequency scenario, should be wide enough so that the most probable PLC sub-bands or test frequencies lie somewhere in the middle. This structure would ensure good classification accuracy (or low BER), and hence, efficient communication.

### C. Feature-based Vs Featureless Learning

In Sections V.A. and V.B., the results of feature-based and featureless ML/NN/CNN were discussed separately. In the present section, these two methods are compared directly based on the previous results of NN models from each category, as shown in Figure 16. NN is used to compare the two methods because an identical NN (with same hyperparameters) was used with feature-based as well as featureless datasets. For featureless method, the magnitude spectrogram is used as the dataset format of choice (i.e., Datasets 2) because of its overall best performance as shown by results in Section V.B.

Figure 16(a) reveals that the featureless NN model had slightly higher accuracies than the feature-based NN model when testing these models with a trained parameter. In this case, NN models were able to find the relevant features

using extracted features for the feature dataset and feature maps for featureless dataset. However, the information contained within the relevant feature maps is truer to the original raw signal than the lossy extracted features due to a reduction in steps required for data pre-processing. Therefore, the featureless NN models had marginally better performance than feature-based NN.

On the other hand, when the models were asked to generalize to an untrained parameter, as in Case 3 shown in Figure 16 (b), the feature-based NN models perform better overall than featureless NN. This result may be due to the fact that the NN model needed to be more complex for the featureless dataset on account of its greater size (3x1024 per sample for magnitude spectrogram dataset whereas 1x61 for the feature dataset), higher dimensionality (2D for magnitude spectrogram while 1D for feature dataset) or the noise within the dataset (higher noise level in the magnitude spectrogram dataset than the feature dataset). Another probable cause could be that the NN model overfitted the featureless dataset. Overfitting might not have been a problem with the feature-based dataset because of the limited number of features. However, for the featureless dataset, the number of features (in the form of feature maps) is much greater, and thus the weights are spread out during training, causing overfitting of the training data. This overfitting then results in poor generalization for untrained samples.

## VI. CONCLUSION

In this research study, an inter-level, upstream PLC network architecture was created; using this network architecture, OOK ULF baseband PLC signals were transmitted and captured; the captured data was processed to create feature-based and featureless ML/NN datasets. These datasets were used in various ML/NN formats to classify the temporal On/Off states of the transmitted OOK ULF-PLC signal. Using this pipeline, three broad questions related to the use of ML/NN in ULF-PLC data were explored. First, ULF-PLC signal characteristics were evaluated. Second, methods for pre-processing complex-valued communications signals were explored for use in conventional ML algorithms. Finally, the efficacy of a small

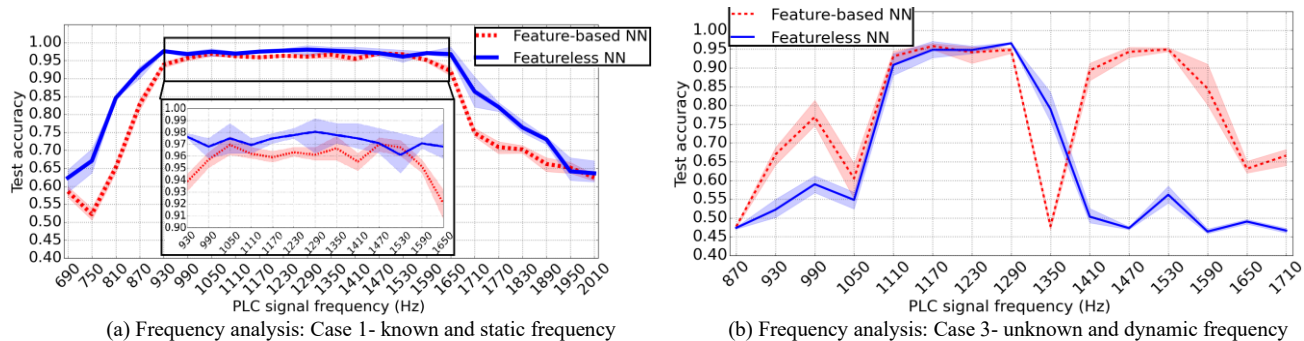


Figure 16. Graphs showing test accuracy curves (with 95% confidence interval) of Neural Network models fitted with feature dataset and magnitude spectrogram-based featureless datasets. (a) Case 1 frequency analysis using feature-based ‘Dataset 1’ and featureless ‘Dataset 2’ and (b) Case 3 frequency analysis using ‘Dataset 1’ and ‘Dataset 2’.

collection of supervised ML techniques in decoding ULF-PLC communication data was evaluated.

#### A. PLC Signal Characteristics

As presented in Section V.A.1) (Figure 8) and Section V.B.1) (Figure 13), the optimal frequency range for inter-level ULF-PLC appears to be confined in a distinct passband around 930Hz-1650Hz. Below this band, the strong odd harmonics of the fundamental power signal interfere directly with the PLC signal, while above this band, grid components such as power transformers attenuate the signals substantially, causing poor signal propagation. This passband frequency range is dependent on various other factors such as the grid architecture (between the PLC signal transmitter and receiver), the coupling filter, etc. Therefore, frequency range as presented in this research may be relatively common but are not universally applicable. However, the bandpass nature of the power line channel is indeed characteristic of ULF-PLC.

#### B. Dataset Characteristics

One of the primary objectives of this study was to explore how the raw ULF-PLC data could be used in ML/NN and what types of data pre-processing might be most desirable or effective. To that end, we investigated two different methods: feature-based and featureless.

Between the three featureless datasets, the time-series format was the least effective because of the dominance of the power signal in this domain as an out-of-band interferer. When the same data was transformed to time/frequency representation, the ML/NN performance improved significantly. The magnitude spectrogram format performed better due to its efficient representation of the OOK ULF-PLC data. If more sophisticated frequency and/or phase shift methods are used for modulating data into the ULF-PLC channel, then the use of rectangular spectrogram formats is likely to outperform magnitude spectrogram formats, as concluded in our previous research [40]. Therefore, there are merits to all of these featureless datasets, in this ULF-PLC application and beyond. In particular the ability of the system to recognize data based on various sub-band configurations is compelling.

The outcomes from feature-based and featureless datasets were compared directly using an identical NN. The results of this comparison are discussed in Section V.C. and shown in Figure 16. Interestingly, the featureless magnitude spectrogram models had higher test accuracy than the feature-based models when the test data had the same PLC signal parameter (frequency) as the training data. However, when the test data had completely different signal parameters, the feature-based models were more consistent in providing high classification accuracies. As a result, we conclude that NN models overfit with the larger featureless dataset, causing it to generalize poorly on the test data with untrained parameters. Therefore, feature-based methods may be more appropriate when generalization is desired.

In addition to testing accuracy, comparison of feature-based and featureless methods using metrics such as the complexity of the ML models, time of processing,

scalability, etc. may be valuable outcomes. In our tests using the ULF-PLC dataset, feature-based models had similar performance to featureless models despite employing simpler algorithms. The use of simpler models along with smaller dataset of the feature-based method resulted in a requirement for substantially less computer processing power and training time. However, the feature-dataset also requires substantial data pre-processing, which requires time and knowledge of the domain, and which can omit unknown, but relevant features. In contrast, although featureless methods require more complex ML/NN models, they are also easier to scale to varying architectures and applications and require less domain-specific knowledge to optimize. Further, they are capable of detecting features and/or outcomes that may have been previously unknown. Therefore, feature-based methods are desirable when training time and computer processing power are a consideration, while featureless methods are attractive when scaling and ease of deployment are the main concerns, and when the dataset environment may not be completely known.

#### C. ML/NN Algorithm Characteristics

To evaluate the ULF-PLC dataset, we utilized three supervised ML algorithms: Logistic Regression (LR), Support Vector Machine (SVM) and Decision Tree (TREE). We also used Neural Network (NN) and Convolutional Neural Network (CNN) models. The comparison between LR, SVM, TREE and NN, presented in Section V.A., indicates that the classification accuracies of these models were very similar, with SVM slightly better in most cases due to its non-linear capability. However, this also meant that SVM models needed much more stringent regularization to avoid overfitting, which increases implementation complexity. In contrast, NN and CNN may be more suitable for featureless datasets because of their relatively more complex architectures and native ability to process multi-dimensional datasets. For the same reason, NN and CNN approaches are also more flexible and scalable.

#### ACKNOWLEDGMENT

We would like to thank Mr. Andres Carvallo, Dr. Semih Aslan and Dr. Vishu Viswanathan for their support and contributions on this research. We also acknowledge Ingram School of Engineering and the Graduate College of Texas State University-San Marcos for providing the opportunity and resources for this research.

APPENDIX

- *Appendix A: Github Page*

The data files and Python scripts used for in this thesis can be found at:

[https://github.com/kushal-thapa/ML\\_for\\_PLC\\_thesis](https://github.com/kushal-thapa/ML_for_PLC_thesis)

- *Appendix B: Features of the raw ULF-PLC data*

Number of raw PLC files: 23

File type: .wav

Length of each file: 100 seconds

PLC signal amplitude: 1A

PLC frequency: 690Hz-2010Hz with 60Hz spacings

Number of channels: 3

Sampling rate: 8000 samples per second

- *Appendix C: Spectrogram Parameters*

Frame size = 500 samples

Frame overlap = 250 samples

FFT size = 1024

Window = Hanning

- *Appendix D: Optimized hyperparameters of the NN for Dataset 1*

No. of hidden layers		2
Hidden layer 1	No. of nodes	64
	Activation function	Relu
Hidden layer 2	No. of nodes	32
	Activation function	Relu
Output layer	No. of nodes	2
	Activation function	Softmax
Learning rate		0.001
Optimizer		Adam
Loss		Sparse categorical crossentropy
Epochs		50
Batch size		16

- *Appendix E: Experimentation steps*

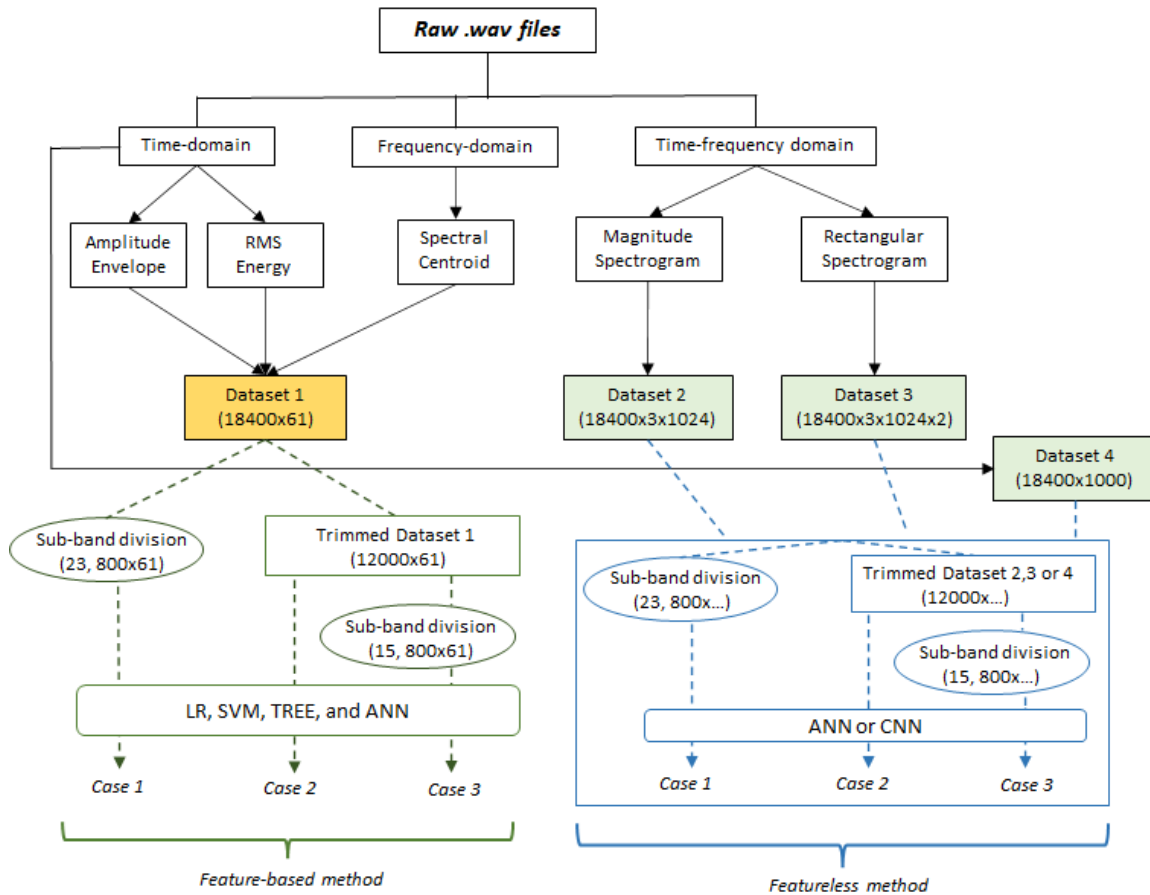


Figure Appendix 1: Extension of Figure 7 showing the creation of datasets and the subsequent use of those datasets in various cases in feature-based and featureless methods.

## REFERENCES

- [1] K. Thapa, S. McClellan, and D. Valles, "Supervised Machine Learning in Digital Power Line Communications," in *The Sixteenth International Conference on Digital Telecommunications*, Porto, Apr. 2021, pp. 16–21. [Online]. Available: [https://www.thinkmind.org/index.php?view=article&articleid=icdt\\_2021\\_1\\_40\\_18004](https://www.thinkmind.org/index.php?view=article&articleid=icdt_2021_1_40_18004) (accessed Nov. 28, 2021).
- [2] K. Thapa, "Digital Signal Processing and Machine Learning Applied to Power Line Communications," Unpublished, Texas State University, San Marcos, Texas, 2021. [Online]. Available: <https://digital.library.txstate.edu/handle/10877/14044> (accessed Nov. 28, 2021).
- [3] K. Dostert, "Telecommunications over the power distribution grid—possibilities and limitations," *IIR-Powerline*, vol. 6, no. 97, 1997.
- [4] M. Schwartz, "Carrier-wave telephony over power lines: Early history [History of Communications]," *IEEE Commun. Mag. Commun. Mag. IEEE IEEE Commun Mag*, vol. 47, no. 1, pp. 14–18, Jan. 2009, doi: 10.1109/MCOM.2009.4752669.
- [5] K. Sharma and L. M. Saini, "Power-line communications for smart grid: Progress, challenges, opportunities and status," *Renew. Sustain. Energy Rev.*, vol. 67, pp. 704–751, Jan. 2017.
- [6] S. U. Ercan, O. Ozgonenel, Y. E. Haj, C. Christopoulos, and D. W. P. Thomas, "Power line communication design and implementation over distribution transformers," in *2017 10th International Conference on Electrical and Electronics Engineering (ELECO)*, Nov. 2017, pp. 190–194.
- [7] A. K. Schurig, "Universal lan power line carrier repeater system and method," US5818821A, Oct. 06, 1998. [Online]. Available: <https://patents.google.com/patent/US5818821A/en> (accessed Nov. 28, 2021).
- [8] R. Du and Q. Xiao, "Baby Monitor," US20090212926A1, Aug. 27, 2009. [Online]. Available: <https://patents.google.com/patent/US20090212926A1/en> (accessed Nov. 28, 2021).
- [9] P. An, X. Chen, J. Wang, S. Zhou, and X. Shan, "Analysis on Application of Repeater Technology in Powerline Communications Networks," in *2007 IEEE International Symposium on Power Line Communications and Its Applications*, Mar. 2007, pp. 273–277. doi: 10.1109/ISPLC.2007.371136.
- [10] K. Bode, "BPL Takes Posthumous Beating With IBEC Closure - ISP Blames Tornadoes, Though BPL Failures Played a Role," *DSL Reports*. <http://www.dslreports.com/shownews/BPL-Takes-Posthumous-Beating-With-IBEC-Closure-117677> (accessed Nov. 28, 2021).
- [11] J. Tanner, "You can't kill BPL if it's already dead | Telecom Ramblings," Jan. 13, 2012. <https://www.telecomramblings.com/2012/01/you-cant-kill-bpl-if-its-already-dead/> (accessed Nov. 28, 2021).
- [12] D. Dzung, I. Berganza, and A. Sendin, "Evolution of powerline communications for smart distribution: From ripple control to OFDM," in *2011 IEEE International Symposium on Power Line Communications and Its Applications*, Apr. 2011, pp. 474–478. doi: 10.1109/ISPLC.2011.5764444.
- [13] "Intelligent Platform Management Interface Specification Second Generation." Intel Corporation, Hewlett-Packard Company, NEC Corporation, Dell Inc., Oct. 01, 2013. [Online]. Available: <https://www.intel.com/content/www/us/en/products/docs/servers/ipmi/ipmi-second-gen-interface-spec-v2-rev1-1.html> (accessed Nov. 28, 2021).
- [14] "Spacecraft Onboard Interface Systems—Low Data-Rate Wireless Communications for Spacecraft Monitoring and Control." Council of the Consultative Committee for Space Data Systems (CCSDS), May 2013. [Online]. Available: <https://public.ccsds.org/Pubs/882x0m1.pdf> (accessed Nov. 28, 2021).
- [15] D. Cooper and T. Jeans, "Narrowband, low data rate communications on the low-voltage mains in the CENELEC frequencies. I. Noise and attenuation," *IEEE Trans. Power Deliv. Power Deliv. IEEE Trans. IEEE Trans Power Deliv.*, vol. 17, no. 3, pp. 718–723, Jul. 2002, doi: 10.1109/TPWRD.2002.1022794.
- [16] S. McClellan, D. Valles, and G. Koutitas, "Dynamic Voltage Optimization Based on In-Band Sensors and Machine Learning," *Appl. Sci.-BASEL*, vol. 9, no. 14, Jul. 2019, doi: 10.3390/app9142902.
- [17] A. Narayan, "California's electric grid needs an overhaul," *Bus. J. Serv. Fresno Cent. San Joaquin Val.*, no. 325799, pp. 18–18, 1/1/2021 2021.
- [18] S. Littlechild and L. Kiesling, "Hayek and the Texas blackout," *Electr. J.*, vol. 34, no. 6, p. 106969, Jul. 2021, doi: 10.1016/j.tej.2021.106969.
- [19] S. McClellan, "Suppression of interference in power and communications signals," US9876516B2, Jan. 23, 2018. [Online]. Available: <https://patents.google.com/patent/US9876516B2/en> (accessed Nov. 28, 2021).
- [20] J. J. LoPorto and S. McClellan, "Intelligent power system and methods for its application," US8519832B2, Aug. 27, 2013. [Online]. Available: <https://patents.google.com/patent/US8519832B2/en> (accessed Nov. 28, 2021).
- [21] J. Arrillaga and N. R. Watson, *Power system harmonics*. John Wiley & Sons, 2004.
- [22] J. Niitsoo, I. Palu, J. Kilter, P. Taklaja, and T. Vaimann, "Residential load harmonics in distribution grid," in *2013 3rd International Conference on Electric Power and Energy Conversion Systems*, Oct. 2013, pp. 1–6. doi: 10.1109/EPECS.2013.6713054.
- [23] A. M. Tonello, N. A. Letizia, D. Righini, and F. Marcuzzi, "Machine Learning Tips and Tricks for Power Line Communications," *IEEE Access*, vol. 7, pp. 82434–82452, 2019, doi: 10.1109/ACCESS.2019.2923321.
- [24] M. Korki, N. Hosseinzadeh, H. L. Vu, T. Moazzeni, and C. H. Foh, "A channel model for power line communication in the smart grid," in *2011 IEEE/PES Power Systems Conference and Exposition*, Mar. 2011, pp. 1–7. doi: 10.1109/PSCE.2011.5772561.
- [25] B. Varadarajan, Il Han Kim, A. Dabak, D. Rieken, and G. Gregg, "Empirical measurements of the low-frequency power-line communications channel in rural North

- America,” in *2011 IEEE International Symposium on Power Line Communications and Its Applications*, Apr. 2011, pp. 463–467. doi: 10.1109/ISPLC.2011.5764442.
- [26] G. Prasad, Y. Huo, L. Lampe, A. Mengi, and V. C. M. Leung, “Fault Diagnostics with Legacy Power Line Modems,” in *2019 IEEE International Symposium on Power Line Communications and its Applications (ISPLC)*, Apr. 2019, pp. 1–6. doi: 10.1109/ISPLC.2019.8693385.
- [27] M. Nassar, J. Lin, Y. Mortazavi, A. Dabak, I. H. Kim, and B. L. Evans, “Local Utility Power Line Communications in the 3–500 kHz Band: Channel Impairments, Noise, and Standards,” *IEEE Signal Process. Mag.*, vol. 29, no. 5, pp. 116–127, Sep. 2012, doi: 10.1109/MSP.2012.2187038.
- [28] “California Instruments CS Series - AC Current Source,” *Ametek Programmable Power*. [www.powerandtest.com/power/ac-power-sources/cs-series](http://www.powerandtest.com/power/ac-power-sources/cs-series) (accessed Nov. 28, 2021).
- [29] “DI-1100 4-channel USB Data Acquisition Starter Kit,” *DATAQ Instruments*. <https://www.dataq.com/products/di-1100/> (accessed Nov. 28, 2021).
- [30] S. Bochner, K. Chandrasekharan, and K. Chandrasekharan, *Fourier transforms*, no. 19. Princeton University Press, 1949.
- [31] E. O. Brigham and R. Morrow, “The fast Fourier transform,” *IEEE Spectr.*, vol. 4, no. 12, pp. 63–70, 1967.
- [32] K. R. Rao, D. N. Kim, and J. J. Hwang, *Fast Fourier transform : algorithms and applications*. Springer, 2010.
- [33] D. A. Lyon, “The discrete fourier transform, part 4: spectral leakage,” *J. Object Technol.*, vol. 8, no. 7, 2009.
- [34] A. Breitenbach, “Against spectral leakage,” *Measurement*, vol. 25, no. 2, pp. 135–142, 1999.
- [35] V. Mathews and D. Youn, “Spectral leakage suppression properties of linear and quadratic windowing,” *IEEE Trans. Acoust. Speech Signal Process.*, vol. 32, no. 5, pp. 1092–1095, 1984.
- [36] T. M. Apostol, *Mathematical analysis.*, Second edition. Addison-Wesley Pub. Co., 1974.
- [37] J. S. Dramsch, M. Lüthje, and A. N. Christensen, “Complex-valued neural networks for machine learning on non-stationary physical data,” *Comput. Geosci.*, vol. 146, p. 104643, Jan. 2021, doi: 10.1016/j.cageo.2020.104643.
- [38] H. G. Zimmermann, A. Minin, and V. Kuserbaeva, “Comparison of the complex valued and real valued neural networks trained with gradient descent and random search algorithms,” 2010, pp. 213–218.
- [39] J. Shima, “Weak signal processing systems and methods,” 10879946, Dec. 29, 2020. [Online]. Available: <http://patft1.uspto.gov/netacgi/nph-Parser?Sect1=PTO1&Sect2=HITOFF&d=PALL&p=1&u=%2Fnethtml%2FPTO%2Fsrchnum.htm&r=1&f=G&l=50&s1=10879,946.PN.&OS=PN/10879,946&RS=PN/10879,946> (accessed Nov. 28, 2021).
- [40] K. Thapa, S. McClellan, and D. Valles, “An Evaluation of Neural Network Performance Using Complex-Valued Input Data,” in *ICDT 2021 : The Sixteenth International Conference on Digital Telecommunications*, Porto, Apr. 2021, pp. 27–31. [Online]. Available: [https://www.thinkmind.org/index.php?view=article&articleid=icdt\\_2021\\_1\\_60\\_18006](https://www.thinkmind.org/index.php?view=article&articleid=icdt_2021_1_60_18006) (accessed Nov. 28, 2021).
- [41] T. Smyth, “Amplitude Envelopes,” *Amplitude Envelopes*. [http://musicweb.ucsd.edu/~trmsmyth/sinusoids171/Amplitude\\_Envelopes.html](http://musicweb.ucsd.edu/~trmsmyth/sinusoids171/Amplitude_Envelopes.html) (accessed Nov. 28, 2021).
- [42] R. G. Lyons and D. L. Fugal, *The essential guide to digital signal processing*. Prentice Hall, 2014.
- [43] B. Boashash, Ed., “Chapter 4 - Advanced Time-Frequency Signal and System Analysis,” in *Time-Frequency Signal Analysis and Processing (Second Edition)*, Oxford: Academic Press, 2016, pp. 141–236. doi: 10.1016/B978-0-12-398499-9.00004-2.
- [44] S. Tjoa, “Energy and RMSE,” *musicinfoetrieval.com*. <https://musicinformationretrieval.com/energy.html> (accessed Nov. 28, 2021).
- [45] J. M. Grey and J. W. Gordon, “Perceptual effects of spectral modifications on musical timbres,” *J. Acoust. Soc. Am.*, vol. 63, pp. 1493–1500, May 1978.
- [46] K. W. Cattermole, “Principles of digital line coding,” *Int. J. Electron.*, vol. 55, no. 1, p. 3, Jul. 1983.
- [47] S. C. H. Hoi, D. Sahoo, J. Lu, and P. Zhao, “Online learning: A comprehensive survey,” *Neurocomputing*, vol. 459, pp. 249–289, Oct. 2021.
- [48] J. Brownlee, “14 Different Types of Learning in Machine Learning,” *Machine Learning Mastery*, Nov. 10, 2019. <https://machinelearningmastery.com/types-of-learning-in-machine-learning/> (accessed Nov. 28, 2021).
- [49] F. Pedregosa *et al.*, “Scikit-learn: Machine Learning in Python,” *J. Mach. Learn. Res.*, vol. 12, no. 85, pp. 2825–2830, 2011.
- [50] “sklearn.linear\_model.LogisticRegression,” *scikit learn*. [https://scikit-learn.org/stable/modules/generated/sklearn.linear\\_model.LogisticRegression.html](https://scikit-learn.org/stable/modules/generated/sklearn.linear_model.LogisticRegression.html) (accessed Nov. 28, 2021).
- [51] “sklearn.svm.SVC.” <https://scikit-learn.org/stable/modules/generated/sklearn.svm.SVC.html> (accessed Nov. 28, 2021).
- [52] “sklearn.tree.DecisionTreeClassifier.” <https://scikit-learn.org/stable/modules/generated/sklearn.tree.DecisionTreeClassifier.html> (accessed Nov. 28, 2021).
- [53] “sklearn.model\_selection.GridSearchCV.” [https://scikit-learn.org/stable/modules/generated/sklearn.model\\_selection.GridSearchCV.html](https://scikit-learn.org/stable/modules/generated/sklearn.model_selection.GridSearchCV.html) (accessed Nov. 28, 2021).
- [54] “sklearn.metrics.precision\_score.” [https://scikit-learn.org/stable/modules/generated/sklearn.metrics.precision\\_score.html](https://scikit-learn.org/stable/modules/generated/sklearn.metrics.precision_score.html) (accessed Nov. 28, 2021).
- [55] “sklearn.metrics.recall\_score.” [https://scikit-learn.org/stable/modules/generated/sklearn.metrics.recall\\_score.html](https://scikit-learn.org/stable/modules/generated/sklearn.metrics.recall_score.html) (accessed Nov. 28, 2021).
- [56] “sklearn.metrics.f1\_score.” [https://scikit-learn.org/stable/modules/generated/sklearn.metrics.f1\\_score.html](https://scikit-learn.org/stable/modules/generated/sklearn.metrics.f1_score.html) (accessed Nov. 28, 2021).
- [57] “Plotting Learning Curves — scikit-learn 0.24.2 documentation.” [https://scikit-learn.org/stable/auto\\_examples/model\\_selection/plot\\_learning\\_curve.html](https://scikit-learn.org/stable/auto_examples/model_selection/plot_learning_curve.html) (accessed Nov. 28, 2021).
- [58] “sklearn.metrics.confusion\_matrix.” [https://scikit-learn.org/stable/modules/generated/sklearn.metrics.confusion\\_matrix.html](https://scikit-learn.org/stable/modules/generated/sklearn.metrics.confusion_matrix.html) (accessed Nov. 28, 2021).
- [59] M. Abadi *et al.*, “Tensorflow: Large-scale machine learning on heterogeneous distributed systems,” *ArXiv Prepr. ArXiv160304467*, 2016.
- [60] A. Gulli and S. Pal, *Deep learning with Keras*. Packt Publishing Ltd, 2017.

- [61] K. M. Dostert, "Frequency-hopping spread-spectrum modulation for digital communications over electrical power lines," *IEEE J. Sel. Areas Commun. Sel. Areas Commun. IEEE J. IEEE J Sel. Areas Commun.*, vol. 8, no. 4, pp. 700–710, May 1990, doi: 10.1109/49.54466.
- [62] D. J. Torrieri, *Principles of spread-spectrum communication systems.*, Fourth edition. Springer, 2018.
- [63] "sklearn.feature\_selection.SequentialFeatureSelector — scikit-learn 0.24.2 documentation." [https://scikit-learn.org/0.24/modules/generated/sklearn.feature\\_selection.SequentialFeatureSelector.html](https://scikit-learn.org/0.24/modules/generated/sklearn.feature_selection.SequentialFeatureSelector.html) (accessed Nov. 28, 2021).

## Cloud Cost Optimization Based on Shifted N-policy M/M/M/K Queue Model

Zsolt Saffer

*Institute of Statistics and Mathematical Methods in Economics*  
*Vienna University of Technology*  
 Vienna, Austria  
 Email: zsolt.saffer@tuwien.ac.at

**Abstract**—Cloud cost optimization is an important issue having also impact on the economy of the Cloud service, since it enables the Cloud service provider the service provisioning at minimum cost. This paper provides the performance analysis and cost optimization of an Infrastructure-as-a-Service Cloud model with a capacity control policy. The Virtual Machines are modelled as parallel resources, which can be either in active or in standby state. The capacity of the cloud is controlled by changing the number of active Virtual Machines. The cost model, which the cloud provider encounters, takes into account both energy consumption and performance measures. The major objective of the work is to provide a tractable analytic model, which is suitable for practical use. For this purpose, we model the Cloud services by an  $M/M/M/K$  queue. We propose a simple control policy, in which a predefined portion of Virtual Machines are always active. The remaining ones are activated simultaneously when the number of requests reaches a threshold and deactivated when the number of requests falls below the predefined portion of active Virtual Machines. We call this policy as shifted  $N$ -policy. We provide the stationary analysis of the model and derive closed form results for the distribution of the number of requests as well as for several performance measures. The cost model leads to a discrete optimization task, which we approximate by a nonlinear continuous optimization task. After applying numerous approximations, we provide, in form of solution formulas, approximate solutions of the optimization task in the two most relevant traffic ranges. We give illustrating examples for the most important approximations and properties of the model as well as validate the approximate solution formulas by numeric optimization. The major results of the work are the closed form approximate solution formulas, which give the optimal threshold under the most relevant ranges of parameters and provide insight into the dependency of the optimum on the model and cost parameters.

**Keywords**—*optimization; cloud model; queueing model; N-policy.*

### I. INTRODUCTION

Cloud cost optimization is an important issue having also impact on the economy of the Cloud service, since it enables the Cloud service provider the service provisioning at minimum cost. This paper is an extension of our previous work [1], in which we provided a performance evaluation and optimization of an Infrastructure-as-a-Service (IaaS) Cloud model with a proposed simple threshold based resource control. The major objective of this research is to establish a tractable analytic model, which is also suitable for practical use.

The growing demand for computational resources lead to a concept of Cloud computing. With a wide spreaded use of computer networks, new applications emerged in the '90-s in many areas, e.g., business, science or web-applications.

They created a growing demand for computational resources, which does not necessarily locate locally. This lead to a new distributed computing paradigm called Cloud computing [2] [3] [4] [5]. In this work, we focus on IaaS type Cloud service, in which computing resources are delivered to customers. Besides of the physically distributed character of Cloud services, another key attribute of clouds is the virtualization, which enables to decouple the computing resources from the physical hardware and deliver them to customers as Virtual Machines (VM).

The users want guaranteed performance and the Cloud service provider want to ensure it and supervise the operation. These require proper performance modelling and evaluation enabling to get insights into the relationships among the used resources and the performance.

However, the performance evaluation of Cloud services is a complex issue, since it depends on many factors. Analytic models are either too simplified to obtain meaningful relationships or lead to rather complex numeric solution, which does not provide an explicit relationships among the used resources and the performance. There are many research works on performance modelling of clouds. An advanced work on performance analysis is [6], which provides a numeric solution. An outstanding work is [7], in which a multi-level interacting stochastic sub-models approach is proposed, leading to a numeric method to compute the performance measures. For an overview on research works on performance evaluation of clouds the reader is referred to the survey [8] and the references herein.

Cloud cost optimization requires a resource management technique. The work [9] provides an approach to predict resource usage in Cloud computing, which can be seen as a simplest way to enable the managing of the system. Resource scheduling techniques are proposed in [10], [11] and [12]. Energy-aware resource allocation mechanism for management of clouds is proposed in [13]. Energy efficient resource management and allocation policies for clouds are summarized in [14] [15]. One recent efficient resource control mechanism for clouds is the threshold based activation and deactivation of VMs, proposed e.g., in [16]. This mechanism can be modelled by hysteresis queue and in [16] computational algorithms are provided for computing the optimal thresholds. For another numerical approaches to cloud cost optimization we refer to [17] and [18]. As expected, optimization of clouds is even more complex issue than its performance evaluation. Therefore, the vast majority of works on Cloud cost optimization

proposes a computational solution.

In this paper, we present a performance evaluation and optimization of an IaaS Cloud model with a proposed simple threshold based resource control, but in contrast to the vast majority of relevant works, we provide approximate explicit formulas for determining the only threshold of the control mechanism. The formulas hold in most relevant range of parameters. The resource control mechanism, introduced in [1], is called as shifted  $N$ -policy. According to this policy, a predefined portion of VMs are always active. The remaining ones are activated simultaneously when the number of requests reaches a threshold  $N$  (like in  $N$ -policy) and deactivated when the number of requests falls below the predefined portion of active VMs. This explains the name of the policy. The cloud is modeled by multi-server  $M/M/M/K$  queue. Note that, as pointed out in [19], the  $M/M/m$  queue can be an acceptable approximation of the  $GI/GI/m$  queue until the coefficient of variations of both the interarrival and the service times are not far from 1.

In [1], we presented closed form results for the stationary distribution of the number of requests and several performance measures in the shifted  $N$ -policy  $M/M/M/K$  model. The cost model lead to a discrete optimization task, which we approximated by a nonlinear continuous optimization task. We provided a closed form approximate solution formula for the high traffic range, in which the utilization is higher than a model parameter dependent threshold.

In this work, we recall the results of [1] and extend the solution of the optimization task to the low traffic range, i.e., in which the utilization is lower than the above model parameter dependent threshold. Additionally, we generalize the former approximate solution formula for the high traffic range by relaxing its restrictions by omitting the condition on cost parameters. Moreover, we also provide the details of the stationary analysis and the derivations both in the former and new optimization parts.

The major contributions of this research are the closed form approximate solution formulas for the optimal value of the threshold  $N$  under the most relevant ranges of parameters. The secondary contribution of this research is the proposal of the shifted  $N$ -policy control mechanism and its stationary analysis in the context of  $M/M/M/K$  model. The advantage of using the proposed shifted  $N$ -policy control is that it makes the cloud resource management very simple due to the approximate analytic formulas for the optimal threshold, i.e., no need for computational algorithm. On the other hand, it leads to somewhat higher optimal cost than other more complex computational solutions, e.g., the hysteresis policy with multi-thresholds. The proposed optimization can be used for example for the use case "Enabling add-on services on top of the infrastructure", e.g., computing-as-a-service, analytics or Business Intelligence(BI)-as-a-service.

We also provide illustrating examples for the approximations and the most important properties of the model as well as validate the approximate solution formulas by numeric optimization in the relevant range of parameters.

The rest of this paper is organized as follows. Section II is devoted to the description of the model. The stationary analysis of the queueing model is given in Section III. In Section IV, we construct the cost function to be optimized. The dependency of the probability of the empty system on threshold  $N$ , as fundamental building block of the optimization, is investigated in Section V. The approximate minimization for high traffic range is presented in Section VI. This is followed by establishing the approximate minimization for low traffic range in Section VII. In Section VIII, we illustrate the approximate solution formulas as well as provide their numeric validation. The work is concluded in Section IX.

## II. CLOUD MODEL DESCRIPTION

In this section, we give the description of the IaaS Cloud model and the shifted  $N$ -policy queueing model.

### A. IaaS Cloud model

The IaaS Cloud delivers low-level computational resources to the users. The Physical Machines (PMs) are grouped into two pools: active (running) and standby machines. The PMs in standby can represent either turned-on (but not ready) or turned-off machines. The computational resources are provided to users in the form of VMs. Total number of available VMs is  $M > 100$ , from which  $0.1M \leq L \leq 0.5M$  VMs are always active. The resource control is realized by threshold based activation and deactivation of the remaining  $M - L$  VMs. The model has buffer with capacity for  $K - M \gg 1$  users. When all active VMs are busy upon arrival of a new request then it is directed into the buffer, where it waits until getting an access to a VM becoming free. When the buffer is full upon arrival of a new request, then the request is lost.

### B. Shifted $N$ -policy queueing model

The queueing system modelling the IaaS Cloud is an  $M/M/M/K$  queue with shifted  $N$ -policy. In the queueing context the VMs are called as servers. The request arrive according to Poisson process with rate  $\lambda > 0$  and the service times are exponentially distributed with parameter  $\mu > 0$ . The arrival process and the service process are assumed to be mutually independent. The system has  $M \geq 1$  servers and buffer capacity for  $K - M \gg 1$  requests. When the servers and the buffer are full upon arrival of a new request, then the request is lost.

The control of the VMs is realized by the newly proposed shifted  $N$ -policy. According to this policy  $L < M$  servers are always active. When the queueing system is empty then the remaining  $M - L$  servers are in standby. They will be activated simultaneously when the number of requests in the system reaches the threshold  $L + 1 \leq N \leq M$ . After having all the  $M$  servers active,  $M - L$  servers will be deactivated simultaneously, when the number of requests in the system reaches again  $L$ . This policy has hysteresis-like characteristic (in number of requests), which makes it suitable to use as energy efficient resource control. However, it is much simpler

than the hysteresis queue, which could facilitate the developing of analytically tractable approximation.

The queue is always stable due to the finiteness of the underlying Continuous-Time Markov chain (CTMC) model (see in Section III). The (approximate) utilization of the system, denoted by  $\rho$  is given by

$$\rho = \frac{\lambda}{M\mu}. \quad (1)$$

Although this expression would be exact only in case of  $K - M = \infty$ , otherwise the blocking probability should be also taken into account to get an exact expression, under the model assumption  $K - M \gg 1$  the expression (1) can be considered as a good approximation of the utilization.

### III. ANALYSIS OF THE QUEUING MODEL

Let  $n \geq 0$  be the number of requests in the system. The process  $\{n(t), t \geq 0\}$  is a finite state CTMC.

#### A. State diagram

The state diagram of the  $M/M/M/K$  queue with shifted  $N$ -policy can be seen in Figure 1.

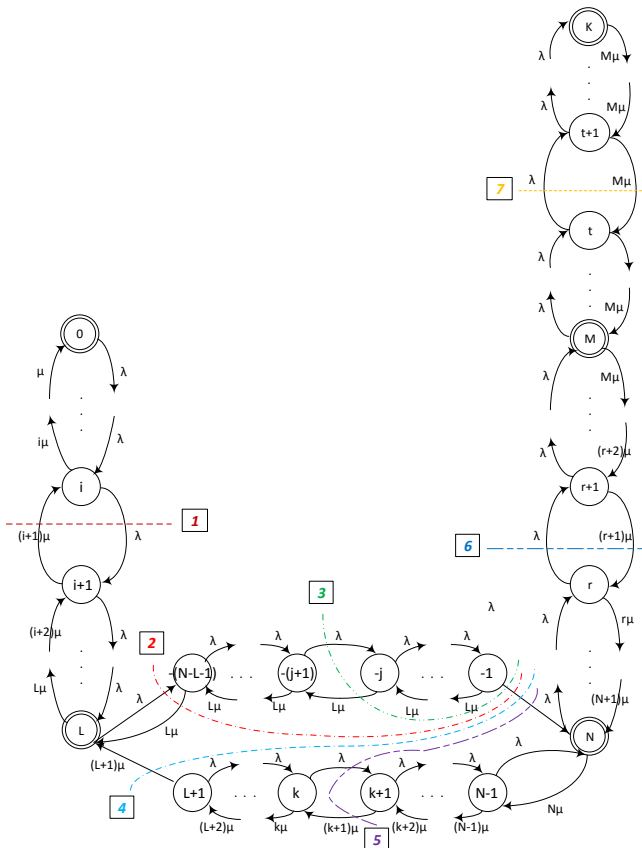


Figure 1. State diagram.

Basically the states are denoted according to the number of requests in the system. However, the notation of the states, in which the  $L < n < N$ , depends on the number of active

servers. If there are  $L$  active servers then the states are denoted by the number  $-(N - n)$ . Otherwise (i.e., there are  $M$  active servers) the default numbering,  $n$  is used. On this way the states can be described as a contiguous range  $[-(N - L - 1), \dots, -1, 0, 1, \dots, K]$ .

#### B. Stationary analysis

We perform the stationary analysis rather by utilizing the principle of global balance equations instead of applying the standard way by means of equilibrium equations. This results in shorter derivations for the stationary distribution of the number of requests in the system. We define the stationary probability,  $p_i$  as the probability that the system is in state  $i$ , for  $-(N - L - 1) \leq i \leq K$ .

1) *Global balance equations:* We marked the selected set of states used for the balance equations on the state diagram. Each case is marked by a separator line and an associated number in small square, which is used to identify the case.

- 1)  $(i + 1)\mu p_{i+1} = \lambda p_i, i = 0, \dots, L - 1,$
- 2)  $L\mu p_{-(N-L-1)} + \lambda p_{-1} = \lambda p_L,$
- 3)  $L\mu p_j + \lambda p_{-1} = \lambda p_{j-1}, j = -(N - L - 2), \dots, -1,$
- 4)  $(L + 1)\mu p_{L+1} = \lambda p_{-1},$
- 5)  $(k + 1)\mu p_{k+1} = \lambda p_k + \lambda p_{-1}, k = L + 1, \dots, N - 1,$
- 6)  $(r + 1)\mu p_{r+1} = \lambda p_r, r = N, \dots, M - 1,$
- 7)  $M\mu p_{t+1} = \lambda p_t, t = M, \dots, K - 1.$

2) *Stationary distribution of the number of requests:* By solving the balance equations by applying standard techniques (see in Appendix (I)), we get the stationary distribution of the number of requests as

$$\begin{aligned}
 p_k &= \frac{\left(\frac{\lambda}{\mu}\right)^k}{k!} p_0, \text{ for } k = 1, \dots, L, \\
 p_k &= \left(\frac{\lambda}{L\mu}\right)^{N-L} \frac{\left(\frac{\lambda}{L\mu}\right)^k - 1}{1 - \left(\frac{\lambda}{L\mu}\right)^{N-L}} p_L, \\
 &\text{for } k = -(N - L - 1), \dots, -1, \\
 p_k &= \sum_{i=L}^{k-1} \frac{i!}{k!} \left(\frac{\lambda}{\mu}\right)^{k-i} p_{-1}, \text{ for } k = L + 1, \dots, N, \\
 p_k &= \frac{N!}{k!} \left(\frac{\lambda}{\mu}\right)^{k-N} p_N, \text{ for } k = N + 1, \dots, M, \\
 p_k &= \left(\frac{\lambda}{M\mu}\right)^{k-M} p_M, \text{ for } k = M + 1, \dots, K \quad (2)
 \end{aligned}$$

and  $p_0$  can be determined from the normalization condition  $\sum_{k=-(N-L-1)}^K p_k = 1$ .

The probabilities  $p_L, p_{-1}, p_N$  and  $p_M$  are probabilities of events representing some boundary in the operation of the considered queueing model. They are given by

$$\begin{aligned}
P_L &= \frac{\left(\frac{\lambda}{\mu}\right)^L}{L!} p_0, \\
p_{-1} &= \alpha p_L, \text{ where } \alpha = \left(\frac{\lambda}{L\mu}\right)^{N-L-1} \frac{1 - \frac{\lambda}{L\mu}}{1 - \left(\frac{\lambda}{L\mu}\right)^{N-L}}, \\
p_N &= \sum_{i=L}^{N-1} \frac{i!}{N!} \left(\frac{\lambda}{\mu}\right)^{N-i} p_{-1} = \frac{\left(\frac{\lambda}{\mu}\right)^N}{N!} s_{L,N} \alpha p_L, \\
\text{where } s_{L,N} &= \sum_{i=L}^{N-1} \frac{i!}{\left(\frac{\lambda}{\mu}\right)^i}, \\
p_M &= \frac{N!}{M!} \left(\frac{\lambda}{\mu}\right)^{M-N} p_N. \tag{3}
\end{aligned}$$

#### IV. COST FUNCTION

In this section, we establish the cost model of the cloud provider and apply it to the shifted N-policy queue. This results in the cost function.

##### A. Cost model

The cloud provider encounters different type of costs with different weights. These are taken into account by the help of cost parameters, which are defined by

- $C_{on}$  - cost of an active VM/time unit,
- $C_{off}$  - cost of a standby VM/time unit,
- $C_W$  - cost of waiting of a request/time unit (= holding a request in the buffer/time unit),
- $C_R$  - cost of loss of an arriving request,
- $C_A$  - activation cost of a VM (changing from standby to active state),
- $C_D$  - deactivation cost of a VM (changing from active to standby state).

Using these parameters the cloud cost can be specified by the following function

$$\begin{aligned}
C_{cloud} &= E[\text{number of active servers}] C_{on} \tag{4} \\
&+ E[\text{number of standby servers}] C_{off} \\
&+ E[W] C_W + p_{loss} \lambda C_R, \\
&+ (\text{activation rate of standby VMs}) (M-L) C_A \\
&+ (\text{deactivation rate of active VMs}) (M-L) C_D,
\end{aligned}$$

where  $E[\ ]$  stands for the expected value of a random variable,  $W$  is the waiting time of the requests in the buffer and  $p_{loss}$  is the probability of loss.

Note that the operation of N-policy implies that one of the major trade-off of the model is the relation  $C_{on} - C_{off}$  versus  $C_W$ , which in fact appears also in the approximate solution formulas for computing the threshold  $N$  (via parameter  $A$  see in subsections VI-F and VII-D, where parameters  $b$  and  $c$  depend on  $A$ ).

##### B. Constructing the cost function

The cost function, to be optimized, can be constructed by applying the cost model (4) to the shifted N-policy queue.

1) *Adapting the cost model to the shifted N-policy queue:*  
The so far unknown terms arising in (4) can be expressed with the help of parameters, stationary probabilities and performance measures of the shifted N-policy queue as follows.

$$\begin{aligned}
E[\text{number of active servers}] &= L + (1 - p_{s1})(M - L), \tag{5} \\
E[\text{number of standby servers}] &= p_{s1}(M - L), \\
(\text{activation rate of standby VMs}) &= \lambda p_{-1}, \\
(\text{deactivation rate of active VMs}) &= (L + 1)\mu p_{L+1},
\end{aligned}$$

where  $p_{s1} = P\{\text{the number of active VMs} = L\}$ .

Substituting the expressions (5) into (4) we get the cost function,  $F_1$  as

$$\begin{aligned}
F_1 &= \left(L + (1 - p_{s1})(M - L)\right) C_{on} + p_{s1}(M - L) C_{off} \\
&+ E[W] C_W + p_{loss} \lambda C_R \\
&+ \lambda p_{-1} (M - L) C_A + (L + 1)\mu p_{L+1}(M - L) C_D. \tag{6}
\end{aligned}$$

2) *Performance measures:* The performance measures  $p_{s1}$ ,  $p_{loss}$  and  $E[W]$  influence the cloud cost. They are given by

$$\begin{aligned}
p_{s1} &= \sum_{k=0}^L p_k + \sum_{k=-(N-L-1)}^{-1} p_k \tag{7} \\
&= \sum_{k=0}^L \frac{\left(\frac{\lambda}{\mu}\right)^k}{k!} p_0 + \sum_{k=-(N-L-1)}^{-1} \left(\frac{\lambda}{L\mu}\right)^{N-L} \frac{\left(\frac{\lambda}{L\mu}\right)^k - 1}{1 - \left(\frac{\lambda}{L\mu}\right)^{N-L}} p_L \\
&= \sum_{k=0}^L \frac{\left(\frac{\lambda}{\mu}\right)^k}{k!} p_0 + \sum_{k=1}^{N-L-1} \frac{\left(\frac{\lambda}{L\mu}\right)^k - \left(\frac{\lambda}{L\mu}\right)^{N-L}}{1 - \left(\frac{\lambda}{L\mu}\right)^{N-L}} p_L \\
&= \sum_{k=0}^L \frac{\left(\frac{\lambda}{\mu}\right)^k}{k!} p_0 + \frac{\frac{\lambda}{L\mu} - \left(\frac{\lambda}{L\mu}\right)^{N-L}}{1 - \frac{\lambda}{L\mu}} - (N - L - 1) \left(\frac{\lambda}{L\mu}\right)^{N-L}}{1 - \left(\frac{\lambda}{L\mu}\right)^{N-L}} p_L.
\end{aligned}$$

$$p_{loss} = p_K = \left(\frac{\lambda}{M\mu}\right)^{K-M} p_M = \left(\frac{\lambda}{M\mu}\right)^K \frac{M^M}{M!} \frac{N!}{\left(\frac{\lambda}{\mu}\right)^N} p_N. \tag{8}$$

$$\begin{aligned}
E[W] &= \sum_{k=-(N-L-1)}^{-1} (k + N - L) p_k + \sum_{k=M+1}^K (k - M) p_k \\
&= \sum_{k=1}^{N-L-1} k p_{-(N-L)+k} + \sum_{k=M+1}^K (k - M) p_k \\
&= \tau p_L + \sigma p_M, \tag{9}
\end{aligned}$$

where

$$\begin{aligned} \tau &= \frac{\frac{\lambda}{L\mu}}{\left(1 - \frac{\lambda}{L\mu}\right)^2} \\ &- (N-L) \frac{\left(\frac{\lambda}{L\mu}\right)^{N-L}}{1 - \left(\frac{\lambda}{L\mu}\right)^{N-L}} \left( \frac{1}{1 - \frac{\lambda}{L\mu}} + \frac{N-L-1}{2} \right), \\ \sigma &= \frac{\lambda}{M\mu} \frac{1 - \left(\frac{\lambda}{M\mu}\right)^{K-M+1}}{\left(1 - \frac{\lambda}{M\mu}\right)^2} - (K-M+1) \frac{\left(\frac{\lambda}{M\mu}\right)^{K-M+1}}{1 - \frac{\lambda}{M\mu}}. \end{aligned} \quad (10)$$

The derivation of the above expression of  $E[W]$  can be found in Appendix (II).

3) *Final form of the cost function  $F_1$* : Applying the balance equation  $(L+1)\mu p_{L+1} = \lambda p_{-1}$ , the expression of  $p_{-1}$  from (3), (9) and (8) in (6) as well as performing rearrangements yields

$$\begin{aligned} F_1 &= \lambda \alpha p_L (M-L) C_A + \lambda \alpha p_L (M-L) C_D \\ &+ (\tau p_L + \sigma p_M) C_W + \left[ \left( \frac{\lambda}{M\mu} \right)^K \frac{M^M N!}{M! \left( \frac{\lambda}{\mu} \right)^N} p_N \right] \lambda C_R \\ &- (C_{on} - C_{off})(M-L)p_{s1} + M C_{on} \\ &= \left( \lambda(C_A + C_D)(M-L)\alpha + C_W \tau \right) p_L \\ &+ C_W \sigma p_M + C_R \lambda \left[ \left( \frac{\lambda}{M\mu} \right)^K \frac{M^M N!}{M! \left( \frac{\lambda}{\mu} \right)^N} \right] p_N \\ &- (C_{on} - C_{off})(M-L)p_{s1} + M C_{on}. \end{aligned} \quad (11)$$

The last but one line of (11) can be rearranged by using the expressions of  $p_M$  and  $p_N$  from (3) leading to

$$\begin{aligned} &C_W \sigma p_M + C_R \lambda \left[ \left( \frac{\lambda}{M\mu} \right)^K \frac{M^M N!}{M! \left( \frac{\lambda}{\mu} \right)^N} \right] p_N \\ &= \left[ C_W \sigma \frac{\left( \frac{\lambda}{\mu} \right)^M}{M!} + C_R \lambda \left( \frac{\lambda}{M\mu} \right)^K \frac{M^M}{M!} \right] \frac{N!}{\left( \frac{\lambda}{\mu} \right)^N} p_N \\ &= \left[ C_R \lambda \left( \frac{\lambda}{M\mu} \right)^K \frac{M^M}{M!} + C_W \sigma \frac{\left( \frac{\lambda}{\mu} \right)^M}{M!} \right] s_{L,N} \alpha p_L. \end{aligned} \quad (12)$$

Substituting (12) back into (11) we get the final form of the cost function in terms of  $p_L$  and  $p_{s1}$  as

$$\begin{aligned} F_1 &= \left[ \left( \lambda(C_A + C_D)(M-L) + \eta s_{L,N} \right) \alpha + C_W \tau \right] p_L \\ &- (C_{on} - C_{off})(M-L)p_{s1} + M C_{on}, \text{ where} \\ \eta &= \left[ C_R \lambda \left( \frac{\lambda}{M\mu} \right)^K \frac{M^M}{M!} + C_W \sigma \frac{\left( \frac{\lambda}{\mu} \right)^M}{M!} \right]. \end{aligned} \quad (13)$$

## V. CHARACTERIZING $p_0$ AS A DEPENDENCY OF N

Unfortunately  $p_0$ , which is involved in almost every term of (13) via the expression of  $p_L$ , depends on  $N$ . Now we characterize  $p_0$  as a dependency of  $N$  in order to identify parameter regions, in which  $p_0$  is approximately independent

of  $N$ . This leads to further restriction on the parameter range. We define the probability coefficients

$$\begin{aligned} p_{s1w} &= \frac{1}{p_0} p_{s1} \\ p_{s2w} &= \frac{1}{p_0} \sum_{k=L+1}^N p_k = \sum_{k=L+1}^N \frac{\left( \frac{\lambda}{\mu} \right)^k}{k!} \sum_{i=L}^{k-1} \frac{i!}{\left( \frac{\lambda}{\mu} \right)^i} \alpha \frac{p_L}{p_0}, \\ p_{s3w} &= \frac{1}{p_0} \sum_{k=N+1}^M p_k = \frac{N!}{\left( \frac{\lambda}{\mu} \right)^N} \sum_{k=N+1}^M \frac{\left( \frac{\lambda}{\mu} \right)^k}{k!} \frac{p_N}{p_0} \\ &= \frac{N!}{\left( \frac{\lambda}{\mu} \right)^N} \sum_{k=N+1}^M \frac{\left( \frac{\lambda}{\mu} \right)^k}{k!} \frac{\left( \frac{\lambda}{\mu} \right)^N}{N!} s_{L,N} \alpha \frac{p_L}{p_0} \\ &= \sum_{k=N+1}^M \frac{\left( \frac{\lambda}{\mu} \right)^k}{k!} \sum_{i=L}^{N-1} \frac{i!}{\left( \frac{\lambda}{\mu} \right)^i} \alpha \frac{p_L}{p_0}, \\ p_{s4w} &= \frac{1}{p_0} \sum_{k=M+1}^K p_k = \sum_{k=M+1}^K \rho^{k-M} \frac{p_M}{p_0} \\ &= \frac{\rho - \rho^{K-M+1}}{1 - \rho} \frac{N!}{M!} \left( \frac{\lambda}{\mu} \right)^{M-N} \frac{p_N}{p_0}, \end{aligned} \quad (14)$$

which are the terms of the coefficient of  $p_0$  in the normalization equation, i.e.,  $p_{sw} p_0 = 1$ , where  $p_{sw} = p_{s1w} + p_{s2w} + p_{s3w} + p_{s4w}$  and it is referred as psum. Moreover, the values  $p_{s1w}$ ,  $p_{s2w}$ ,  $p_{s3w}$  and  $p_{s4w}$  are referred as psum1, psum2, psum3 and psum4, respectively, or simple psum parts.

We assume  $K-M \gg 1$ . Under this assumption  $\rho^{K-M} \ll 1$  holds for the whole traffic range  $\rho < 1$  and thus the term  $\rho^{K-M}$  can be neglected comparing to 1. Using it, the approximation of  $p_{s4w}$ , denoted by  $p_{s4w}^*$ , for the whole traffic range  $\rho < 1$  can be given by

$$\begin{aligned} p_{s4w}^* &= \frac{\rho}{1 - \rho} \frac{N!}{M!} \left( \frac{\lambda}{\mu} \right)^{M-N} \frac{p_N}{p_0} \\ &= \frac{\rho}{1 - \rho} \frac{N!}{M!} \left( \frac{\lambda}{\mu} \right)^{M-N} \frac{\left( \frac{\lambda}{\mu} \right)^N}{N!} s_{L,N} \alpha \frac{p_L}{p_0} \\ &= \frac{\rho}{1 - \rho} \frac{\left( \frac{\lambda}{\mu} \right)^M}{M!} \sum_{i=L}^{N-1} \frac{i!}{\left( \frac{\lambda}{\mu} \right)^i} \alpha \frac{p_L}{p_0}. \end{aligned} \quad (15)$$

The evaluation of the  $N$  dependency of the psum parts requires further approximations. However, these approximations themselves depend on the traffic range. Therefore, in the following we split the investigation of the  $N$  dependency of  $p_0$  according to the traffic ranges determining the appropriate approximations.

### A. Traffic range $\frac{\lambda}{L\mu} > 1$

We assume  $N-L \gg 1$ . Under this assumption  $\left( \frac{\lambda}{L\mu} \right)^{N-L} \gg 1$  holds for the traffic range  $\frac{\lambda}{L\mu} > 1$  and thus the term  $\left( \frac{\lambda}{L\mu} \right)^{N-L}$  dominates over 1. We make use of this in the approximations.

1) Approximation for  $p_{s1}$  and  $\alpha$ : Using  $(\frac{\lambda}{L\mu})^{N-L} \gg 1$  the second term of  $p_{s1}$  in (7) can be approximated as

$$\begin{aligned} & \frac{\frac{\lambda}{L\mu} - (\frac{\lambda}{L\mu})^{N-L}}{1 - \frac{\lambda}{L\mu}} - (N-L-1) \left(\frac{\lambda}{L\mu}\right)^{N-L} \\ & \frac{1 - (\frac{\lambda}{L\mu})^{N-L}}{1 - \frac{\lambda}{L\mu}} p_L \\ & \approx \frac{(\frac{\lambda}{L\mu})^{N-L} - (N-L-1) \left(\frac{\lambda}{L\mu}\right)^{N-L}}{-\left(\frac{\lambda}{L\mu}\right)^{N-L}} p_L \\ & = \left( (N-L-1) - \frac{L\mu}{1 - \frac{L\mu}{\lambda}} \right) p_L. \end{aligned}$$

This together with the upper limit  $\sum_{k=0}^L \frac{(\frac{\lambda}{\mu})^k}{k!} \leq \frac{1}{1 - \frac{L\mu}{\lambda}} \frac{(\frac{\lambda}{\mu})^L}{L!}$  for  $\frac{\lambda}{\mu} > L$  (see in Appendix III-A applied to  $q = \frac{\lambda}{\mu}$ ) gives the estimation for  $p_{s1}$  as

$$\begin{aligned} p_{s1} & \approx \frac{1}{1 - \frac{L\mu}{\lambda}} \frac{(\frac{\lambda}{\mu})^L}{L!} p_0 + \left( (N-L-1) - \frac{L\mu}{1 - \frac{L\mu}{\lambda}} \right) p_L \\ & = \left( (N-L-1) + \frac{1}{1 - \frac{L\mu}{\lambda}} - \frac{L\mu}{1 - \frac{L\mu}{\lambda}} \right) p_L \\ & = (N-L) p_L. \end{aligned}$$

Note that  $\frac{1}{1 - \frac{L\mu}{\lambda}}$ , for  $\frac{\lambda}{L\mu} > \xi$  with  $\xi = 1.2$ , is small compared to  $(N-L)$  due to  $N-L \gg 1$  and hence the effect of the overestimation by the upper limit can be neglected. Similarly, by using  $(\frac{\lambda}{L\mu})^{N-L} \gg 1$ ,  $\alpha$  can be approximated in this traffic range as

$$\alpha \approx \left( \frac{\lambda}{L\mu} \right)^{N-L-1} \frac{\frac{\lambda}{L\mu} - 1}{\left( \frac{\lambda}{L\mu} \right)^{N-L}} = \left( 1 - \frac{L\mu}{\lambda} \right).$$

By using the above approximations of  $p_{s1}$  and  $\alpha$ , the approximations of the terms  $p_{s1w}$ ,  $p_{s2w}$  and  $p_{s3w}$ , denoted by  $p_{s1w}^*$ ,  $p_{s2w}^*$  and  $p_{s3w}^*$ , respectively, can be given as

$$\begin{aligned} p_{s1w}^* & = (N-L) \frac{p_L}{p_0} \\ p_{s2w}^* & = \sum_{k=L+1}^N \frac{(\frac{\lambda}{\mu})^k}{k!} \sum_{i=L}^{k-1} \frac{i!}{(\frac{\lambda}{\mu})^i} \left( 1 - \frac{L\mu}{\lambda} \right) \frac{p_L}{p_0}, \\ p_{s3w}^* & = \sum_{k=N+1}^M \frac{(\frac{\lambda}{\mu})^k}{k!} \sum_{i=L}^{N-1} \frac{i!}{(\frac{\lambda}{\mu})^i} \left( 1 - \frac{L\mu}{\lambda} \right) \frac{p_L}{p_0}. \end{aligned}$$

2) Behavior of  $p_{s2w} + p_{s3w}$  in dependency of  $N$ : Hereinafter it will be shown that the sum  $p_{s2w}^* + p_{s3w}^*$  is approximately independent of  $N$  when  $\rho$  is above some threshold, which depends on  $\frac{M}{L}$ .

Taking the difference of  $p_{s2w}^*$  and  $p_{s3w}^*$  with respect to  $N$  gives

$$\begin{aligned} \Delta_N p_{s2w}^* & = p_{s2w}^*(N) - p_{s2w}^*(N-1) \\ & = \frac{(\frac{\lambda}{\mu})^N}{N!} \sum_{i=L}^{N-1} \frac{i!}{(\frac{\lambda}{\mu})^i} \left( 1 - \frac{L\mu}{\lambda} \right) \frac{p_L}{p_0}. \\ \Delta_N p_{s3w}^* & = p_{s3w}^*(N) - p_{s3w}^*(N-1) \\ & = \sum_{k=N+1}^M \frac{(\frac{\lambda}{\mu})^k}{k!} \sum_{i=L}^{N-1} \frac{i!}{(\frac{\lambda}{\mu})^i} \left( 1 - \frac{L\mu}{\lambda} \right) \frac{p_L}{p_0} \\ & \quad - \sum_{k=N}^M \frac{(\frac{\lambda}{\mu})^k}{k!} \sum_{i=L}^{N-2} \frac{i!}{(\frac{\lambda}{\mu})^i} \left( 1 - \frac{L\mu}{\lambda} \right) \frac{p_L}{p_0} \\ & = \sum_{k=N+1}^M \frac{(\frac{\lambda}{\mu})^k}{k!} \sum_{i=L}^{N-1} \frac{i!}{(\frac{\lambda}{\mu})^i} \left( 1 - \frac{L\mu}{\lambda} \right) \frac{p_L}{p_0} \\ & \quad - \sum_{k=N}^M \frac{(\frac{\lambda}{\mu})^k}{k!} \sum_{i=L}^{N-1} \frac{i!}{(\frac{\lambda}{\mu})^i} \left( 1 - \frac{L\mu}{\lambda} \right) \frac{p_L}{p_0} \\ & \quad + \sum_{k=N}^M \frac{(\frac{\lambda}{\mu})^k}{k!} \frac{(N-1)!}{(\frac{\lambda}{\mu})^{N-1}} \left( 1 - \frac{L\mu}{\lambda} \right) \frac{p_L}{p_0} \\ & = -\frac{(\frac{\lambda}{\mu})^N}{N!} \sum_{i=L}^{N-1} \frac{i!}{(\frac{\lambda}{\mu})^i} \left( 1 - \frac{L\mu}{\lambda} \right) \frac{p_L}{p_0} \\ & \quad + \sum_{k=N}^M \frac{(\frac{\lambda}{\mu})^k}{k!} \frac{(N-1)!}{(\frac{\lambda}{\mu})^{N-1}} \left( 1 - \frac{L\mu}{\lambda} \right) \frac{p_L}{p_0}. \end{aligned}$$

Thus for  $\Delta_N(p_{s2w}^* + p_{s3w}^*)$  we get

$$\Delta_N(p_{s2w}^* + p_{s3w}^*) = \sum_{k=N}^M \frac{(\frac{\lambda}{\mu})^k}{k!} \frac{(N-1)!}{(\frac{\lambda}{\mu})^{N-1}} \left( 1 - \frac{L\mu}{\lambda} \right) \frac{p_L}{p_0}.$$

The sum  $p_{s2w}^* + p_{s3w}^*$  at  $N = L+1$ , i.e., at the smallest possible value of  $N$  can be expressed as

$$\begin{aligned} p_{s2w}^*(L+1) + p_{s3w}^*(L+1) & = \frac{(\frac{\lambda}{\mu})^{L+1}}{(L+1)!} \frac{L!}{(\frac{\lambda}{\mu})^L} \left( 1 - \frac{L\mu}{\lambda} \right) \frac{p_L}{p_0} \\ & \quad + \sum_{k=L+2}^M \frac{(\frac{\lambda}{\mu})^k}{k!} \frac{L!}{(\frac{\lambda}{\mu})^L} \left( 1 - \frac{L\mu}{\lambda} \right) \frac{p_L}{p_0} \\ & = \sum_{k=L+1}^M \frac{(\frac{\lambda}{\mu})^k}{k!} \frac{L!}{(\frac{\lambda}{\mu})^L} \left( 1 - \frac{L\mu}{\lambda} \right) \frac{p_L}{p_0} \\ & = \sum_{k=L+1}^M \frac{(\frac{\lambda}{\mu})^k}{k!} \left( 1 - \frac{L\mu}{\lambda} \right), \end{aligned}$$

where we used  $\frac{p_L}{p_0} = \frac{(\frac{\lambda}{\mu})^L}{L!}$ .

Now we compare  $\Delta_N(p_{s2w}^* + p_{s3w}^*)$  to  $p_{s2w}^*(L+1) + p_{s3w}^*(L+1)$ . The expression of  $\Delta_N(p_{s2w}^* + p_{s3w}^*)$  and  $p_{s2w}^*(L+1) + p_{s3w}^*(L+1)$  can be rewritten by applying the formula for  $\sum_{k=A+1}^B \frac{q^k}{k!} \frac{A!}{q^A}$  (see in Appendix III-B) with  $q = \frac{\lambda}{\mu}$  to  $A = N-1$ ,  $B = M$  and  $A = L$ ,  $B = M$ , respectively as

$$\begin{aligned} \Delta_N(p_{s2w}^* + p_{s3w}^*) &= \sum_{k=N}^M \frac{(\frac{\lambda}{\mu})^k}{k!} \frac{N-1!}{(\frac{\lambda}{\mu})^{N-1}} \frac{p_L}{p_0} \left(1 - \frac{L\mu}{\lambda}\right) \\ &= f_1^* \frac{1 - (f_1^*)^{M-N+1}}{1 - f_1^*} \left(1 - \frac{L\mu}{\lambda}\right) \frac{p_L}{p_0}, \end{aligned}$$

where  $f_1^* = \frac{\mu}{f_0^*}$  and  $N \leq f_0^* \leq M$ ,

$$\begin{aligned} p_{s2w}^*(L+1) + p_{s3w}^*(L+1) &= \sum_{k=L+1}^M \frac{(\frac{\lambda}{\mu})^k}{k!} \left(1 - \frac{L\mu}{\lambda}\right) \\ &= \frac{(\frac{\lambda}{\mu})^L}{L!} \sum_{k=L+1}^M \frac{(\frac{\lambda}{\mu})^k}{k!} \frac{L!}{(\frac{\lambda}{\mu})^L} \left(1 - \frac{L\mu}{\lambda}\right) \\ &= f_1 \frac{1 - (f_1)^{M-L}}{1 - f_1} \left(1 - \frac{L\mu}{\lambda}\right) \frac{p_L}{p_0}, \end{aligned}$$

where  $f_1 = \frac{\mu}{f_0}$  and  $L+1 \leq f_0 \leq M$ ,

as well as  $f_1^* < f_1$  due to  $L < N - 1$  for  $N \geq L + 2$ , where  $\Delta_N(p_{s2w}^* + p_{s3w}^*)$  can be interpreted. We investigate the case when  $f_1^* > 1$  holds. In this case  $p_{s2w}^*(L+1) + p_{s3w}^*(L+1) \approx \frac{f_1^{M-L+1}}{f_1-1} (1 - \frac{L\mu}{\lambda}) \frac{p_L}{p_0}$  due to  $M - L \gg 1$ . If  $f_1^* < 1$  then

$$\frac{p_{s2w}^*(L+1) + p_{s3w}^*(L+1)}{\Delta_N(p_{s2w}^* + p_{s3w}^*)} \approx \frac{f_1^{M-L+1}}{f_1-1} \frac{1-f_1^*}{f_1^*} \gg 1,$$

since the dominating term  $f_1^{M-L+1} \gg 1$ . If  $f_1^* > 1$  then the quotient  $\frac{p_{s2w}^*(L+1) + p_{s3w}^*(L+1)}{\Delta_N(p_{s2w}^* + p_{s3w}^*)}$  can be approximated as

$$\begin{aligned} \frac{p_{s2w}^*(L+1) + p_{s3w}^*(L+1)}{\Delta_N(p_{s2w}^* + p_{s3w}^*)} &\approx \frac{f_1^{M-L+1}}{(f_1^*)^{M-N+2}} \frac{f_1^* - 1}{f_1 - 1} \\ &= \left(\frac{f_1}{f_1^*}\right)^{M-N+2} f_1^{N-L-1} \frac{f_1^* - 1}{f_1 - 1} \gg 1, \end{aligned}$$

since for the major term of the expression  $\left(\frac{f_1}{f_1^*}\right)^{M-N+2} f_1^{N-L-1} \gg 1$  holds, because either  $M - N + 2 \gg 1$  (recall that  $f_1^* < f_1$ ) or  $N - L - 1 \gg 1$  depending on the value of  $N$ . Thus for the traffic range, for which  $f_1 > 1$  holds,  $\Delta_N(p_{s2w}^* + p_{s3w}^*)$  can be neglected comparing to  $p_{s2w}^*(L+1) + p_{s3w}^*(L+1)$ . Applying it recursively to  $p_{s2w}^*(N) + p_{s3w}^*(N)$  for  $N = L+1, \dots, M-1$  we get

$$p_{s2w}^*(N) + p_{s3w}^*(N) \approx \sum_{k=L+1}^M \frac{(\frac{\lambda}{\mu})^k}{k!} \left(1 - \frac{L\mu}{\lambda}\right)$$

for  $N = L+1, \dots, M$ , for  $f_1 > 1$ .

This means that the sum  $p_{s2w} + p_{s3w}$  approximately independent of  $N$  in the traffic range, for which  $f_1 > 1$  holds.

However, in traffic range, for which  $f_1 < 1$  holds,  $p_{s2w}^*(L+1) + p_{s3w}^*(L+1) \approx \frac{f_1}{1-f_1} (1 - \frac{L\mu}{\lambda}) \frac{p_L}{p_0}$  due to  $M - L \gg 1$  and hence the quotient  $\frac{p_{s2w}^*(L+1) + p_{s3w}^*(L+1)}{\Delta_N(p_{s2w}^* + p_{s3w}^*)}$  can be approximated as

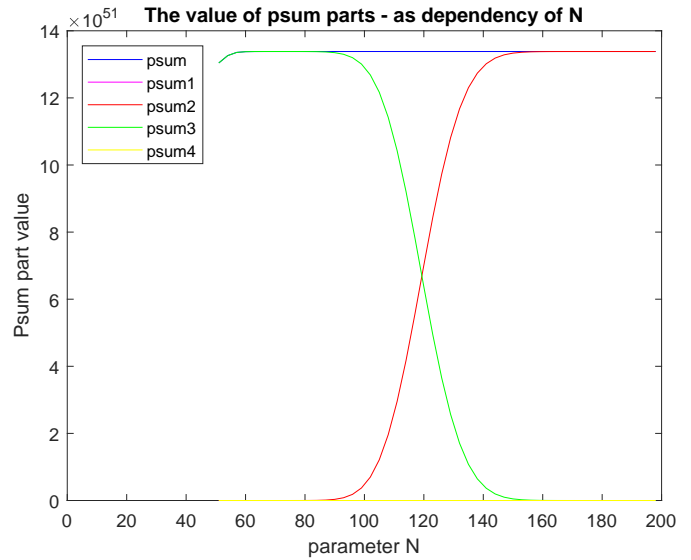


Figure 2. The magnitudes of  $p_{s1w}, p_{s2w}, p_{s3w}, p_{s4w}$  and their sum,  $M = 200, L = 50, \rho = 0.6$ .

$$\frac{p_{s2w}^*(L+1) + p_{s3w}^*(L+1)}{\Delta_N(p_{s2w}^* + p_{s3w}^*)} \approx \frac{f_1}{f_1^* - (f_1^*)^{M-N+2}} \frac{1 - f_1^*}{1 - f_1}.$$

This formula shows that, depending on the values of  $f_1^* < f_1$  and  $f_1 < 1$ , the above quotient can fall in the magnitude of 1, and therefore  $\Delta_N(p_{s2w}^* + p_{s3w}^*)$  can not be neglected compared to  $p_{s2w}^*(L+1) + p_{s3w}^*(L+1)$ . This implies that the value  $p_{s2w} + p_{s3w}$  depends on  $N$  in the traffic range, for which  $f_1 < 1$  holds.

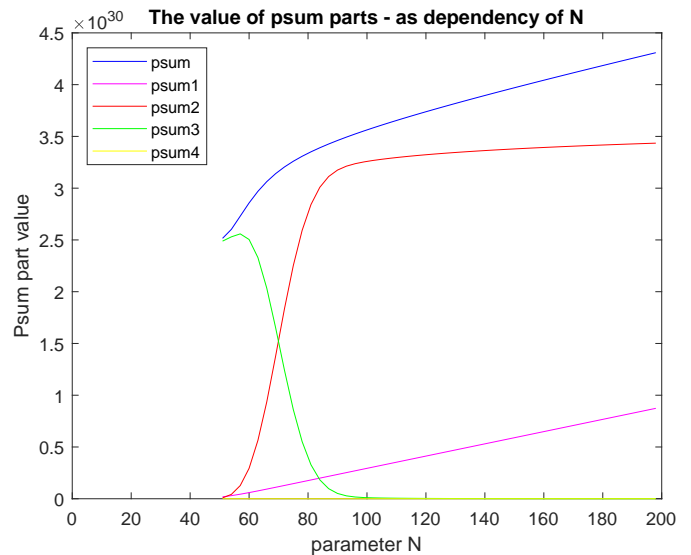


Figure 3. The magnitudes of  $p_{s1w}, p_{s2w}, p_{s3w}, p_{s4w}$  and their sum,  $M = 200, L = 50, \rho = 0.35$ .

For the completeness, the traffic range boundary, for which  $f_1$  is close to 1, still have to be estimated. An upper limit can be obtained for  $\rho M = \frac{\lambda}{\mu}$  by applying the upper limit

for  $q$  at  $f_1$  close to 1 (see in Appendix III-C) to  $q = \frac{\lambda}{\mu}$  and  $A = L$  leading to  $\frac{\lambda}{\mu} < L e^{\frac{5.5}{L}}$ . In order to ensure the validity of the above approximations the value of  $f_1$  must be somewhat above 1, thus we set  $f_1 = 1.1$ . Taking into account that, by neglecting the dependency of  $f_0$  on  $\frac{\lambda}{\mu}$ ,  $f_1$  is approximately proportional to  $\frac{\lambda}{\mu}$  we get an upper limit at the traffic range boundary, denoted by  $\rho_c$ , as

$$\rho_c = \frac{\lambda}{M\mu} < \frac{L}{M} 1.1 e^{\frac{5.5}{L}} \approx \frac{L}{M} 1.2 \text{ for } L \geq 60.$$

Although the above factor  $1.1 e^{\frac{5.5}{L}} \approx 1.2$  increases for  $L < 60$ , the quotient  $\frac{M}{L}$  also increases and thus it causes a counter-effect due to higher overestimation of  $\frac{\lambda}{\mu}$  by the upper limit, which together justify the keeping of the approximate factor 1.2.

3) *The sum  $p_{s2w} + p_{s3w}$  versus  $p_{s1w}$ :* If  $f_1 > 1$  then  $p_{s2w}^* + p_{s3w}^* \approx \frac{f_1^{M-L+1}}{f_1-1} (1 - \frac{L\mu}{\lambda}) \frac{p_L}{p_0}$  due to  $M - L \gg 1$ . In this case the major term  $f_1^{M-L+1} \gg (N-L)$  and hence  $p_{s2w}^* + p_{s3w}^* \gg (N-L) \frac{p_L}{p_0} = p_{s1w}^*$ , which implies that  $p_{s1w}^*$  can be neglected comparing to  $p_{s2w}^* + p_{s3w}^*$ .

On the other hand, if  $f_1 < 1$  then  $p_{s2w}^* + p_{s3w}^* \approx \frac{f_1}{1-f_1} (1 - \frac{L\mu}{\lambda}) \frac{p_L}{p_0}$  and the coefficient  $\frac{f_1}{1-f_1} (1 - \frac{L\mu}{\lambda})$  becomes less than  $N - L$ . It follows that  $p_{s1w}^*$  dominates over  $p_{s2w}^* + p_{s3w}^*$  and hence  $p_{s1w}^* + p_{s2w}^* + p_{s3w}^*$  depends linearly on  $N$  in the corresponding traffic range.

4) *Effect of  $p_{s4w}$ :* Observe that the expression of  $p_{s4w}^*$  in (15) without the first multiplication factor  $\frac{\rho}{1-\rho}$  is the same as the value of the expression of  $p_{s3w}$  in (14) for  $k = M$ . The item  $\frac{(\frac{\lambda}{\mu})^k}{k!}$  in the sum  $\sum_{k=L+1}^M \frac{(\frac{\lambda}{\mu})^k}{k!}$  takes its maximum at  $k \approx \frac{\lambda}{\mu}$ , since  $\frac{\lambda}{\mu} > 1$  for  $k < \frac{\lambda}{\mu}$  and  $\frac{\lambda}{\mu} < 1$  for  $k > \frac{\lambda}{\mu}$ . It follows that the major part of  $p_{s3w}^*$  is determined by the items  $(\frac{\lambda}{\mu} - \Delta) \leq k \leq \frac{\lambda}{\mu} + \Delta$  for some  $\Delta$ . The last item with  $k = M$  can contribute to the sum practically only if  $\frac{\lambda}{\mu} > M - \Delta$ . For such a case  $\rho = \frac{\lambda}{M\mu}$  is close to 1 for which also the multiplication factor in (15),  $\frac{\rho}{1-\rho}$ , has a value  $\gg 1$ .

It follows that  $p_{s4w}$  can emerge to the magnitude of the value of  $p_{s3w}$ , and thus that of the sum  $p_{s2w} + p_{s3w}$ , only for  $\rho$  close to 1, otherwise it is negligible compared to that sum.

On the other hand, we show that  $p_{s4w}$  is independent of  $N$  for values of  $\rho$  close to 1. Applying the formula for  $\sum_{k=A+1}^B \frac{k! q^A}{q^k A!}$  (see in Appendix III-D) to  $A = L - 1$ ,  $B = N - 1$ , the expression of  $p_{s4w}^*$ , (15), can be rearranged as

$$\begin{aligned} p_{s4w}^* &= \frac{\rho}{1-\rho} \frac{(\frac{\lambda}{\mu})^M}{M!} \sum_{i=L}^{N-1} \frac{i!}{(\frac{\lambda}{\mu})^i} \alpha \frac{p_L}{p_0} \\ &= \frac{\rho}{1-\rho} \frac{(\frac{\lambda}{\mu})^M}{M!} \sum_{i=L}^{N-1} \frac{i!}{(\frac{\lambda}{\mu})^i} \frac{(\frac{\lambda}{\mu})^L}{L!} \alpha \\ &= \frac{\rho}{1-\rho} g_1 \frac{1 - (g_1)^{N-L}}{1 - g_1} \frac{\lambda}{L} \frac{(\frac{\lambda}{\mu})^M}{M!} \alpha, \\ &\text{where } g_1 = \frac{g_0}{\frac{\lambda}{\mu}} \text{ and } L \leq g_0 \leq N - 1. \end{aligned}$$

It can be seen from the above formula that, for values of  $\rho$  close to 1, for which  $\rho > \frac{N}{M} > \frac{g_0}{M} \Leftrightarrow \frac{\lambda}{\mu} > g_0$  holds,  $p_{s4w}^*$  can be approximated as  $\frac{\rho}{1-\rho} \frac{g_1}{1-g_1} \frac{\lambda}{L} \frac{(\frac{\lambda}{\mu})^M}{M!} (1 - \frac{L\mu}{\lambda})$ , which is independent of  $N$ .

5) *Illustrating the relations of the magnitudes of  $p_{s1w}, p_{s2w}, p_{s3w}, p_{s4w}$  and their sum:* The magnitudes of  $p_{s1w}, p_{s2w}, p_{s3w}, p_{s4w}$  and their sum compared to each other are illustrated on Figures 2, 3 and 4. The figures were created by varying  $\rho$  under the parameter setting  $M = 200, L = 50, K = 300, \mu = 1$ . It can be seen on Figure 2 that the sum  $p_{s3w} + p_{s4w}$  is approximately independent of  $N$  and dominates over the other terms as expected due to  $\rho = 0.6 > 1.2 \frac{L}{M} = 0.3$ . These relations start to change as  $\rho$  gets closer to  $1.2 \frac{L}{M}$ , where the sum  $p_{s3w} + p_{s4w}$  starts to depend on  $N$  and  $p_{s1w}$  starts to emerge comparing to  $p_{s3w} + p_{s4w}$  as well as starts to affect the overall sum  $p_{sw}$  to become linear with  $N$ .

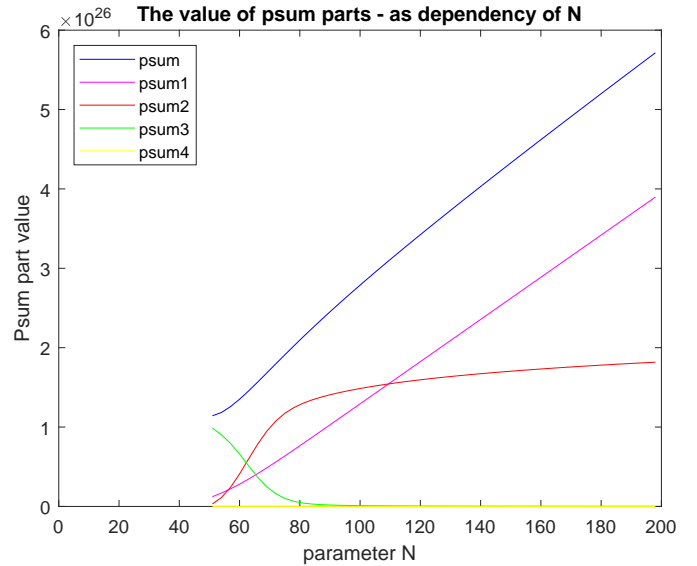


Figure 4. The magnitudes of  $p_{s1w}, p_{s2w}, p_{s3w}, p_{s4w}$  and their sum,  $M = 200, L = 50, \rho = 0.3$ .

This can be seen on Figure 3 with  $\rho = 0.35$  and even more on Figure 4 with  $\rho = 0.3$ , where the dependency of the overall sum  $p_{sw}$  on  $N$  becomes clearly linear.

#### B. Traffic range $\frac{\lambda}{L\mu} < 1$

We assume again  $N - L \gg 1$ . Under this assumption  $(\frac{\lambda}{L\mu})^{N-L} \ll 1$  holds for the traffic range  $\frac{\lambda}{L\mu} < 1$  and thus the term  $(\frac{\lambda}{L\mu})^{N-L}$  can be neglected compared to 1.

1) *Approximation for  $p_{s1}$  and  $\alpha$ :* Using  $(\frac{\lambda}{L\mu})^{N-L} \ll 1$  the expression of  $p_{s1}$  in (7) can be approximated as

$$\begin{aligned} p_{s1} &\approx \sum_{k=0}^L \frac{(\frac{\lambda}{\mu})^k}{k!} p_0 \\ &+ \left( \frac{\frac{\lambda}{L\mu}}{1 - \frac{\lambda}{L\mu}} - (N - L - 1) \left( \frac{\lambda}{L\mu} \right)^{N-L} \right) p_L. \end{aligned} \quad (16)$$

Using the notations  $h = \frac{\lambda}{L\mu}$  and  $z = N - L$  the derivative of the major part of the last term in (16) with respect to  $z$  is given by  $(zh^z)' = h^z(z \ln(h) + 1)$ . Thus, a condition for  $z \ln(h) + 1 < 0$  is  $z > \frac{-1}{\ln(h)}$ , since  $\ln(h) < 0$ . The inequalities  $\ln(h) < -0.22$  and  $\frac{-1}{\ln(h)} < 4.5$  hold for  $h < 0.8$ , and hence  $z > 10$  is sufficient for  $(zh^z)' < 0$ . It follows that for  $N - L \gg 1$ , e.g., for  $N - L > 10$ , the nonnegative term  $(N - L)(\frac{\lambda}{L\mu})^{N-L}$  is monotone decreasing with increasing  $N - L$ . Then it is enough to compute the values of the middle and the last terms of (16) for several values of  $\frac{\lambda}{L\mu}$  with  $N - L = 10$  to see the magnitude of the last term comparing to the middle one. It turns out that except for high  $\frac{\lambda}{L\mu}$  (above 0.8) and low  $(N - L) (\lesssim 40)$  the last term of (16) can be neglected compared to the middle one. Taking it into account, we get another approximation for  $p_{s1}$  as

$$p_{s1} \approx \sum_{k=0}^L \frac{(\frac{\lambda}{L\mu})^k}{k!} p_0 + \left( \frac{\frac{\lambda}{L\mu}}{1 - \frac{\lambda}{L\mu}} \right) p_L. \quad (17)$$

Using  $(\frac{\lambda}{L\mu})^{N-L} \ll 1$  in the expression of  $\alpha$  in (3) we get the approximation of  $\alpha$  in this traffic range as

$$\alpha \approx \left( 1 - \frac{\lambda}{L\mu} \right) \left( \frac{\lambda}{L\mu} \right)^{N-L-1}. \quad (18)$$

2) *The properties of  $p_{s1w}$* : Using (17), the sum  $p_{s1w}$  can be approximated as

$$p_{s1w} \approx \sum_{k=0}^L \frac{(\frac{\lambda}{L\mu})^k}{k!} + \left( \frac{\frac{\lambda}{L\mu}}{1 - \frac{\lambda}{L\mu}} \right) \frac{p_L}{p_0}. \quad (19)$$

The formula (19) also shows that  $p_{s1w}$  is approximately independent of  $N$  in the traffic range of  $\frac{\lambda}{L\mu} < 1$ , except for the rather small sub-range mentioned at the derivation of (17).

In the following we establish a lower limit for the first term of  $p_{s1w}$  for  $\frac{\lambda}{\mu} = tL$  and  $1 \leq L_0 \leq L$ .

$$\begin{aligned} \sum_{k=0}^L \frac{(\frac{\lambda}{L\mu})^k}{k!} &= \sum_{k=0}^L \frac{(\frac{\lambda}{L\mu})^{k-L}}{k!/L!} \frac{(\frac{\lambda}{L\mu})^L}{L!} = \sum_{k=0}^L \frac{L!/k!}{(\frac{\lambda}{L\mu})^{L-k} p_0} \frac{p_L}{p_0} \\ &= \left( 1 + \frac{L}{\frac{\lambda}{L\mu}} + \frac{L(L-1)}{(\frac{\lambda}{L\mu})^2} + \dots + \frac{L!}{(\frac{\lambda}{L\mu})^L} \right) \frac{p_L}{p_0} \\ &= \left( 1 + \frac{1}{t} + \frac{(1 - \frac{1}{L})}{t^2} + \dots + \frac{(1 - \frac{1}{L}) \dots (1 - \frac{L-1}{L})}{t^L} \right) \frac{p_L}{p_0} \\ &\geq \left( 1 + \frac{1}{t} + \frac{(1 - \frac{1}{L})}{t^2} + \dots + \frac{(1 - \frac{1}{L}) \dots (1 - \frac{L_0-1}{L})}{t^{L_0}} \right) \frac{p_L}{p_0} \\ &\geq \left( 1 + \frac{1}{t} + \frac{(1 - \frac{1}{L_0})}{t^2} + \dots + \frac{(1 - \frac{1}{L_0}) \dots (1 - \frac{L_0-1}{L_0})}{t^{L_0}} \right) \frac{p_L}{p_0}. \end{aligned}$$

This limit can be computed for a given values of  $t$  and  $L_0$ . For a realistic range it yields

$$\sum_{k=0}^L \frac{(\frac{\lambda}{L\mu})^k}{k!} > 8.22 \frac{p_L}{p_0}, \quad \frac{\lambda}{\mu} \leq 0.8L, \quad L \geq 10. \quad (20)$$

Therefore, the magnitude of the multiplication factor of  $\frac{p_L}{p_0}$  in the first term of  $p_{s1w}$  falls in the magnitude of ten and above.

3) *The sum  $p_{s2w} + p_{s3w}$  compared to  $p_{s1w}$* : The approximate expression  $p_{s2w}^*$  and  $p_{s3w}^*$  can be obtained by applying (18) in the expression of  $p_{s2w}$  and  $p_{s3w}$  in (14), respectively.

We investigate the sum  $p_{s2w}^* + p_{s3w}^*$  at  $N = L + 1$ , i.e., at the smallest possible value of  $N$ .

$$\begin{aligned} p_{s2w}^*(L+1) + p_{s3w}^*(L+1) &= \frac{(\frac{\lambda}{L\mu})^{L+1}}{(L+1)!} \frac{L!}{(\frac{\lambda}{L\mu})^L} \left( 1 - \frac{\lambda}{L\mu} \right) \frac{p_L}{p_0} \\ &+ \sum_{k=L+2}^M \frac{(\frac{\lambda}{L\mu})^k}{k!} \frac{L!}{(\frac{\lambda}{L\mu})^L} \left( 1 - \frac{\lambda}{L\mu} \right) \frac{p_L}{p_0} \\ &= \sum_{k=L+1}^M \frac{(\frac{\lambda}{L\mu})^k}{k!} \frac{L!}{(\frac{\lambda}{L\mu})^L} \left( 1 - \frac{\lambda}{L\mu} \right) \frac{p_L}{p_0}. \end{aligned}$$

Applying the formula for  $\sum_{k=A+1}^B \frac{q^k}{k!} \frac{A!}{q^A}$  (see in Appendix III-B) with  $q = \frac{\lambda}{L\mu}$  to  $A = L$ ,  $B = M$  we get an upper limit for the sum  $p_{s2w}^*(L+1) + p_{s3w}^*(L+1)$  as

$$\begin{aligned} p_{s2w}^*(L+1) + p_{s3w}^*(L+1) &= \frac{\lambda}{f_0\mu} \frac{1 - (\frac{\lambda}{f_0\mu})^{M-L}}{1 - \frac{\lambda}{f_0\mu}} \\ &* \left( 1 - \frac{\lambda}{L\mu} \right) \frac{p_L}{p_0} < \frac{\frac{\lambda}{L\mu} - (\frac{\lambda}{L\mu})^{M-L+1}}{1 - \frac{\lambda}{L\mu}} \left( 1 - \frac{\lambda}{L\mu} \right) \frac{p_L}{p_0} \\ &= \left[ \frac{\lambda}{L\mu} - \left( \frac{\lambda}{L\mu} \right)^{M-L+1} \right] \frac{p_L}{p_0} < \frac{\lambda}{L\mu} \frac{p_L}{p_0} < \frac{p_L}{p_0}, \quad (21) \end{aligned}$$

where we utilized that  $L < f_0$  and  $M - L \gg 1$ .

Now we investigate the effect of increasing  $N$  by 1 on  $p_{s2w}(N) + p_{s3w}(N)$ .

$$\begin{aligned} p_{s2w}(N+1) + p_{s3w}(N+1) &= \frac{\alpha(N+1, L)}{\alpha(N, L)} p_{s2w}(N) \\ &+ \frac{(\frac{\lambda}{L\mu})^{N+1}}{(N+1)!} \sum_{i=L}^N \frac{i!}{(\frac{\lambda}{L\mu})^i} \alpha(N+1, L) \frac{p_L}{p_0} + \frac{\alpha(N+1, L)}{\alpha(N, L)} p_{s3w}(N) \\ &+ \sum_{k=N+1}^M \frac{(\frac{\lambda}{L\mu})^k}{k!} \frac{N!}{(\frac{\lambda}{L\mu})^N} \alpha(N+1, L) \frac{p_L}{p_0} \\ &- \frac{(\frac{\lambda}{L\mu})^{N+1}}{(N+1)!} \sum_{i=L}^N \frac{i!}{(\frac{\lambda}{L\mu})^i} \alpha(N+1, L) \frac{p_L}{p_0} \\ &= \frac{\lambda}{L\mu} \left( p_{s2w}(N) + p_{s3w}(N) \right) \\ &+ \sum_{k=N+1}^M \frac{(\frac{\lambda}{L\mu})^k}{k!} \frac{N!}{(\frac{\lambda}{L\mu})^N} \alpha(N+1, L) \frac{p_L}{p_0}. \end{aligned}$$

Applying again the formula for  $\sum_{k=A+1}^B \frac{q^k}{k!} \frac{A!}{q^A}$  (see in Appendix III-B) with  $q = \frac{\lambda}{L\mu}$  to  $A = N$ ,  $B = M$  and assuming  $p_{s2w}(N) + p_{s3w}(N) < \frac{p_L}{p_0}$  we get an upper limit for  $p_{s2w}^*(N+1) + p_{s3w}^*(N+1)$  as

$$\begin{aligned}
 & p_{s2w}^*(N+1) + p_{s3w}^*(N+1) < \frac{\lambda}{L\mu} \left( p_{s2w}^*(N) + p_{s3w}^*(N) \right) \\
 & + \frac{\lambda}{N\mu} \frac{1 - \left(\frac{\lambda}{N\mu}\right)^{M-N}}{1 - \frac{\lambda}{N\mu}} \left(1 - \frac{\lambda}{L\mu}\right) \left(\frac{\lambda}{L\mu}\right)^{N-L} \frac{p_L}{p_0} \\
 & < \left( p_{s2w}^*(N) + p_{s3w}^*(N) \right) + \frac{\lambda}{1 - \frac{\lambda}{N\mu}} \left(1 - \frac{\lambda}{L\mu}\right) \left(\frac{\lambda}{L\mu}\right)^{N-L} \\
 & \times \frac{p_L}{p_0} < \frac{\lambda}{L\mu} \frac{p_L}{p_0} + \frac{\lambda}{1 - \frac{\lambda}{N\mu}} \left(1 - \frac{\lambda}{N\mu}\right) \left(\frac{\lambda}{L\mu}\right)^{N-L} \frac{p_L}{p_0} \\
 & = \left[ \frac{\lambda}{L\mu} + \frac{\lambda}{N\mu} \left(\frac{\lambda}{L\mu}\right)^{N-L} \right] \frac{p_L}{p_0} < \frac{\lambda}{L\mu} \left[ 1 + \left(\frac{\lambda}{L\mu}\right)^{N-L} \right] \frac{p_L}{p_0},
 \end{aligned}$$

where we used  $0 < \frac{\lambda}{N\mu} < \frac{\lambda}{L\mu} < 1$  and  $M - N \geq 0$ .

The factor  $\frac{\lambda}{L\mu} \left(1 + \left(\frac{\lambda}{L\mu}\right)^{N-L}\right)$  is monotone increasing with  $\frac{\lambda}{\mu}$  and less than 1 for the range of  $\frac{\lambda}{\mu} < 0.8L$  and  $N - L \gg 1$ , e.g.,  $N - L > 10$ . Thus, starting with (21) and applying mathematical induction we get

$$p_{s2w}(N) + p_{s3w}(N) < \frac{p_L}{p_0} \quad \text{for } N = L + 1, \dots, M. \quad (22)$$

Comparing (22) to (20) shows that  $p_{s2w} + p_{s3w}$  is negligible comparing to  $p_{s1w}$  in the major part of the range  $\frac{\lambda}{L\mu} < 1$ .

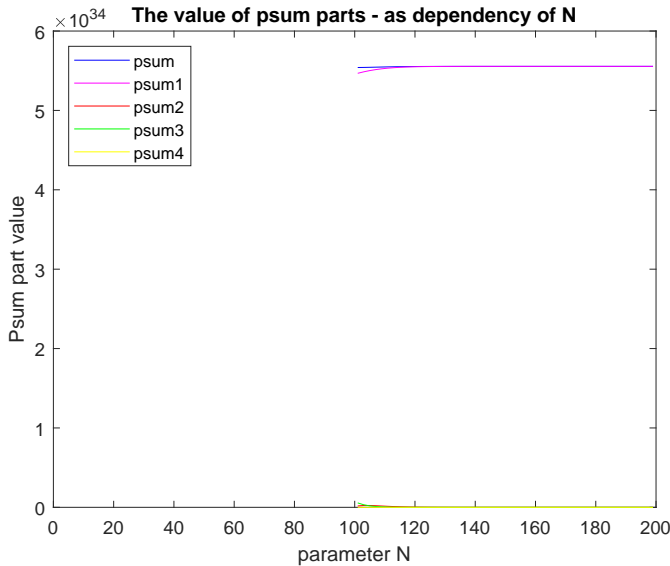


Figure 5. The magnitudes of  $p_{s1w}, p_{s2w}, p_{s3w}, p_{s4w}$  and their sum,  $M = 200, L = 100, \rho = 0.4$ .

4) *The sum  $p_{s4w}$  compared to  $p_{s1w}$ :* We assume  $\frac{M}{L} \geq 2$ . This implies  $\rho \leq 0,5$  in the traffic range of  $\frac{\lambda}{L\mu} < 1$ . Hence, the relation  $\frac{\rho}{1-\rho} \leq 1$  holds. Using it in (15) leads to an upper limit for  $p_{s4w}$  as

$$p_{s4w}^* = \frac{\rho}{1 - \rho} \frac{N!}{M!} \left(\frac{\lambda}{\mu}\right)^{M-N} \frac{p_N}{p_0} \leq \frac{N!}{M!} \left(\frac{\lambda}{\mu}\right)^{M-N} \frac{p_N}{p_0}.$$

Observe that it equals to the value of the expression of  $p_{s3w}$  in (14) for  $k = M$ . It follows that  $p_{s4w}^* < p_{s3w}$  and therefore

$p_{s4w}$  can be neglected compared to  $p_{s1w}$  due to  $p_{s2w} + p_{s3w} \ll p_{s1w}$ .

5) *Illustrating the relations of the magnitudes of  $p_{s1w}, p_{s2w}, p_{s3w}, p_{s4w}$  and their sum:* The magnitudes of  $p_{s1w}, p_{s2w}, p_{s3w}, p_{s4w}$  and their sum compared to each other are illustrated on Figures 5, 6 and 7. The figures were created by varying  $\rho$  under the parameter setting  $M = 200, L = 100, K = 250, \mu = 1$ . It can be seen on Figure 5 that the probability coefficient  $p_{s1w}$  is approximately independent of  $N$  and dominates over the other terms as expected due to  $\frac{\lambda}{L\mu} \leq 0.8 \Leftrightarrow \rho \leq 0.8 \frac{L}{M} = 0.4$ . This independence start to change as  $\rho$  becomes higher than  $0.8 \frac{L}{M}$ , where the probability coefficient  $p_{s1w}$  and thus also the overall sum  $p_{sw}$  start to depend on  $N$  for low  $N - L$ .

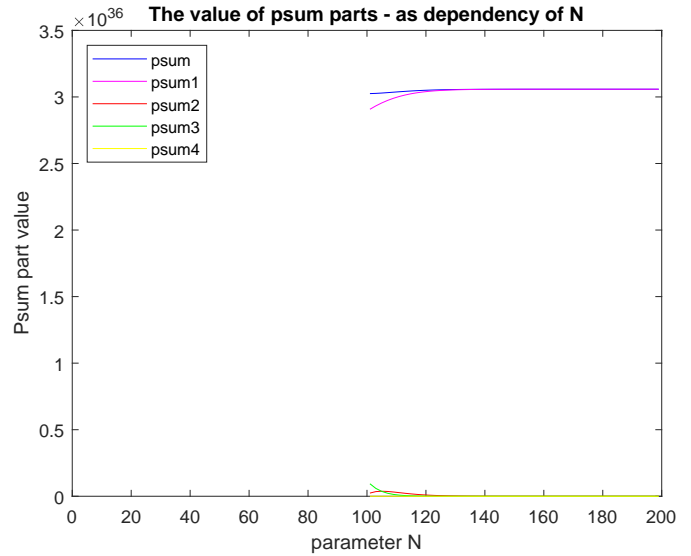


Figure 6. The magnitudes of  $p_{s1w}, p_{s2w}, p_{s3w}, p_{s4w}$  and their sum,  $M = 200, L = 100, \rho = 0.42$ .

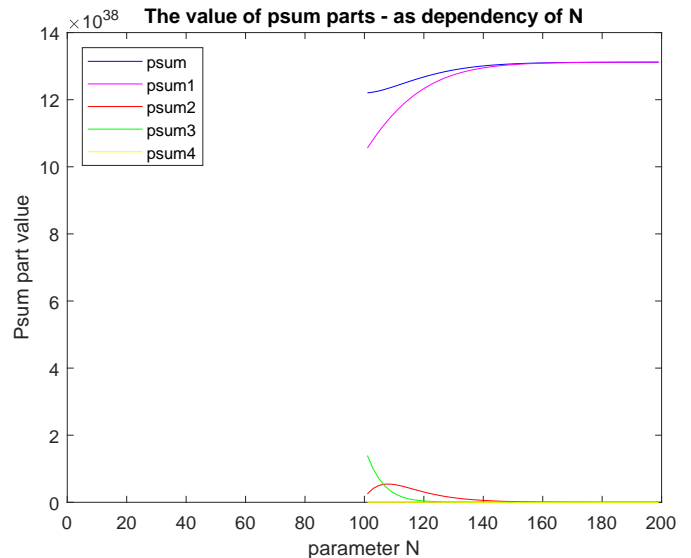


Figure 7. The magnitudes of  $p_{s1w}, p_{s2w}, p_{s3w}, p_{s4w}$  and their sum,  $M = 200, L = 100, \rho = 0.45$ .

This can be seen on Figure 6 with  $\rho = 0.42$  and even more on Figure 7 with  $\rho = 0.45$ , where also the starting increase of the magnitude of sum  $p_{s2w} + p_{s3w}$  can be observed.

### C. Approximately $N$ independent regions of $p_0$

Figure 8 illustrates the dependency of  $p_0$  in the traffic range of  $\frac{\lambda}{L\mu} > 1$  for the parameter setting  $M = 400$ ,  $L = 100$ ,  $K = 450$ ,  $\mu = 1$  and  $\rho = 0.6$ . It can be seen on the figure that  $p_0$  is independent of  $N$  for  $N \gtrsim 110$ , which corresponds to  $N - L \approx 10 \gg 1$ .

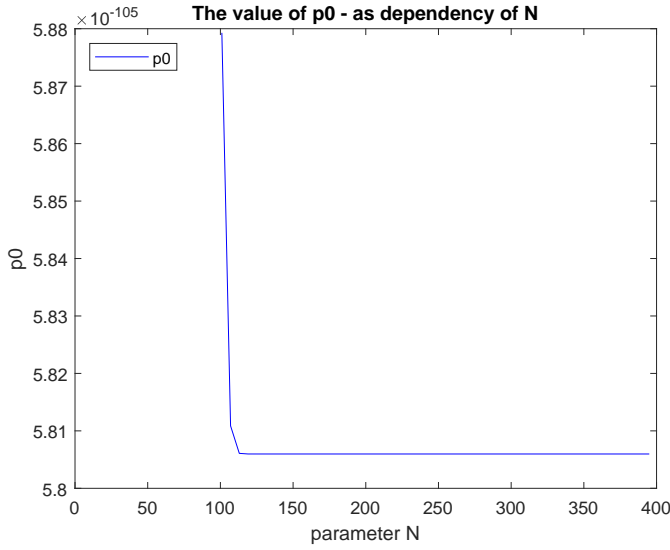


Figure 8. Probability  $p_0$  in dependency of threshold  $N$ , high traffic range.

Similarly, the dependency of  $p_0$  in the traffic range of  $\frac{\lambda}{L\mu} < 1$  is illustrated on Figure 9 for the parameter setting  $M = 200$ ,  $L = 100$ ,  $K = 250$ ,  $\mu = 1$  and  $\rho = 0.4$ .

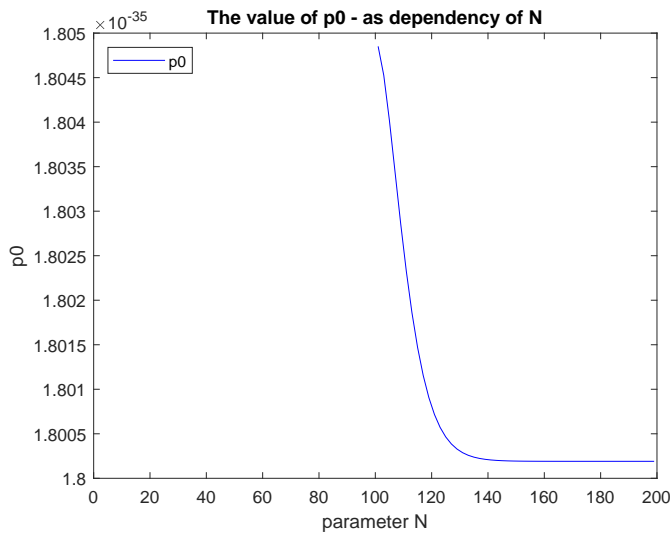


Figure 9. Probability  $p_0$  in dependency of threshold  $N$ , low traffic range.

For the first sight it seems that there is a dependency on  $N$  in the range of  $100 \leq N \lesssim 130$ . However, the value of  $p_0$  changes in relative less than 0.3%. Therefore, the figure shows that  $p_0$  is independent of  $N$  practically in the whole range of  $N > 100$ .

### VI. APPROXIMATE MINIMIZATION - IN TRAFFIC RANGE

$$\frac{\lambda}{L\mu} > 1$$

In the  $N$  independent regions of  $p_0$  also  $p_L$  is independent of  $N$ . Hence, the function to be minimized, (13), can be reduced by omitting the  $N$  independent term  $MC_{on}$  and dividing it by  $p_L$ . This results in a function  $F_2$ , to be minimized, as

$$F_2 = \left[ \left( \lambda(C_A + C_D)(M - L) + \eta s_{L,N} \right) \alpha + C_W \tau \right] - (C_{on} - C_{off})(M - L) \frac{p_{s1}}{p_L}. \quad (23)$$

The optimization of (23) with respect to  $N$  still seems not to be tractable on analytic way due to the complex dependency of several of its terms on  $N$ , like  $s_{L,N}$  or  $\tau$ . Therefore, we simplify the optimization task by applying approximations, like the ones for  $\alpha$  and  $p_{s1}$ . On the other hand, these approximations will restrict the parameter range, for which they hold.

#### A. Approximating the function to be minimized

Besides of the approximations for  $\alpha$  and  $p_{s1}$ , we need approximation also for  $\tau$ .

1) Approximation for  $\tau$ : When  $N - L \gg 1$  then  $(\frac{\lambda}{L\mu})^{N-L} \gg 1$  holds for the traffic range  $\frac{\lambda}{L\mu} > 1$  and thus the term  $1 - (\frac{\lambda}{L\mu})^{N-L}$  can be approximated by  $-(\frac{\lambda}{L\mu})^{N-L}$ . Utilizing it in the expression of  $\tau$  in (10) gives the approximation for  $\tau$  as

$$\begin{aligned} \tau^* &\approx \frac{\frac{\lambda}{L\mu}}{(1 - \frac{\lambda}{L\mu})^2} - (N - L) \frac{1}{\frac{\lambda}{L\mu} - 1} + \frac{(N - L)(N - L - 1)}{2} \\ &= \frac{1}{\frac{\lambda}{L\mu} - 1} \left( \frac{\frac{\lambda}{L\mu}}{\frac{\lambda}{L\mu} - 1} - (N - L) \right) + \frac{(N - L)(N - L - 1)}{2}. \end{aligned}$$

2) Applying the approximations for  $p_0$ ,  $\alpha$ ,  $\tau$  and  $p_{s1}$ : The minimizing task can be significantly reduced by applying the approximations of  $\alpha$ ,  $\tau$  and  $p_{s1}$  in (23). This leads to the approximate objective function  $F_{2app}$  as

$$\begin{aligned} F_{2app} &= \left( \lambda(C_A + C_D)(M - L) + \eta s_{L,N} \right) \left( 1 - \frac{L\mu}{\lambda} \right) \\ &\quad + C_W \frac{1}{\frac{\lambda}{L\mu} - 1} \left( \frac{\frac{\lambda}{L\mu}}{\frac{\lambda}{L\mu} - 1} - (N - L) \right) \\ &\quad + C_W \frac{(N - L)(N - L - 1)}{2} \\ &\quad - (C_{on} - C_{off})(M - L)(N - L). \end{aligned} \quad (24)$$

Figure 10 illustrates the approximation of the cost function  $F_2$  by  $F_{2app}$  in dependency of threshold  $N$  for the parameter

setting  $M = 200, L = 50, K = 300, \mu = 1, C_W = 50, C_{off} = 15, C_{on} = 50, C_a = 30, C_d = 20, C_R = 20$ , and  $\rho = 0.6$ . The figure shows a very good match. The mismatch on the left side of the curve is caused by violating the condition  $N - L \gg 1$  as  $N$  becomes close to  $L$ .

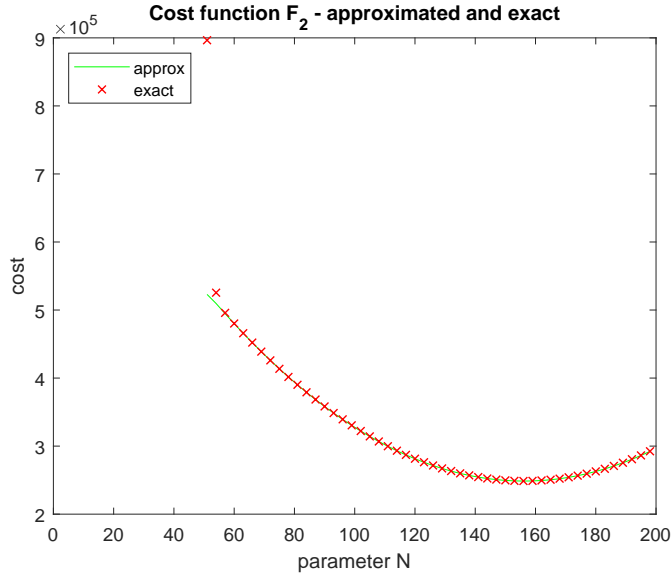


Figure 10. Exact and approximate values of the cost function  $F_2$  in dependency of threshold  $N$ .

### B. Approximate equation for determining the local minimum

We obtain an approximate equation for determining the local minimum of (24) by taking its difference with respect to  $N$  and setting  $\Delta_N F_{2app} \approx 0$ . Evaluating  $\Delta \left( (N-L)(N-L) \right)$  gives

$$\begin{aligned} \Delta \left( (N-L)(N-L) \right) &= (N-L)^2 - (N-1-L)^2 \\ &= 2(N-L-1) + 1 = 2(N-L) - 1. \end{aligned}$$

Using  $\Delta_N s_{L,N} = \frac{(N-1)!}{(\frac{\lambda}{M\mu})^{N-1}}$  and the above expression for  $\Delta(N-L)(N-L)$  leads to the equation

$$\begin{aligned} \eta \left( 1 - \frac{L\mu}{\lambda} \right) \frac{(N-1)!}{(\frac{\lambda}{M\mu})^{N-1}} &= (C_{on} - C_{off})(M-L) \quad (25) \\ &+ C_W \frac{1}{\frac{\lambda}{L\mu} - 1} - C_W(N-L-1). \end{aligned}$$

In order to get closer to the solution of equation (25) first we investigate its structure.

### C. Structure of the equation

To identify the structure of equation (25), we simplify its form by applying further approximations. The relation  $K - M - 1 \gg 1$  holds usually under practical settings. Hence, the term  $(\frac{\lambda}{M\mu})^{K-M+1}$  can be neglected due to  $\rho = \frac{\lambda}{M\mu} < 1$ , which gives an approximation for  $\sigma$  as

$$\begin{aligned} \sigma &= \frac{\lambda}{M\mu} \frac{1 - (\frac{\lambda}{M\mu})^{K-M+1}}{(1 - \frac{\lambda}{M\mu})^2} - (K-M+1) \frac{(\frac{\lambda}{M\mu})^{K-M+1}}{1 - \frac{\lambda}{M\mu}} \\ &\approx \frac{\lambda}{M\mu} \frac{1}{(1 - \frac{\lambda}{M\mu})^2} = \frac{\rho}{(1-\rho)^2}. \end{aligned}$$

Applying rearrangement on the expression of  $\eta$  and applying again the negligibility of the term  $(\frac{\lambda}{M\mu})^{K-M}$  in it, leads to an approximation for  $\eta$  as

$$\begin{aligned} \eta &= \left[ C_R \lambda \left( \frac{\lambda}{M\mu} \right)^{K-M} \frac{(\frac{\lambda}{\mu})^M}{M!} + C_W \sigma \frac{(\frac{\lambda}{\mu})^M}{M!} \right] \\ &\approx C_W \frac{\rho}{(1-\rho)^2} \frac{(\frac{\lambda}{\mu})^M}{M!}. \end{aligned} \quad (26)$$

Using (26) in the equation (25) and further rearrangement gives the simplified form of the equation as

$$\frac{(\frac{\lambda}{\mu})^M}{M!} \frac{(N-1)!}{(\frac{\lambda}{\mu})^{N-1}} u_0(\rho) = r(\rho, N), \quad \text{where} \quad (27)$$

$$u_0(\rho) = C_W \frac{\rho}{(1-\rho)^2} \left( 1 - \frac{1}{\rho \frac{M}{L}} \right) \quad \text{and}$$

$$r(\rho, N) = C_W \left( A(M-L) + \frac{1}{\rho \frac{M}{L} - 1} - (N-L-1) \right)$$

$$\text{with } A = \frac{C_{on} - C_{off}}{C_W}.$$

The term  $\frac{(\frac{\lambda}{\mu})^M}{M!} \frac{(N-1)!}{(\frac{\lambda}{\mu})^{N-1}}$  on the left hand side (lhs) of (27) constitutes the structure of the equation. Its magnitude varies in a huge range for larger  $M$  and  $N$  depending on the value of the parameters. Therefore, we also use its natural logarithm in the course of the analysis. By introducing the notation

$$p(\rho, N) = \frac{(\frac{\lambda}{\mu})^M}{M!} \frac{(N-1)!}{(\frac{\lambda}{\mu})^{N-1}},$$

the equation (27) can be given in a short form as

$$p(\rho, N) u_0(\rho) = r(\rho, N). \quad (28)$$

### D. Properties of function $p(\rho, N)$

The approximate global solution of the considered minimization task requires the knowledge of several properties of function  $p(\rho, N)$ .

1) *Dependency on  $\rho$* : Applying the Stirling formula  $n! \approx \sqrt{2\pi n} n^{(n+1/2)} e^{-n}$  to both  $M$  and  $N-1$  in the expression of  $p(\rho, N)$  gives an approximation as

$$\begin{aligned} p(\rho, N) &= \frac{(\frac{\lambda}{\mu})^M}{M!} \frac{(N-1)!}{(\frac{\lambda}{\mu})^{N-1}} = \left( \frac{\lambda}{\mu M} \right)^{(M-N+1)} \frac{M^M (N-1)!}{M! M^{N-1}} \\ &\approx \rho^{(M-N+1)} e^{(M-N+1)} \sqrt{\frac{N-1}{M}} \left( \frac{N-1}{M} \right)^{N-1}. \end{aligned} \quad (29)$$

It can be seen from (29) that the dependency of  $p(\rho, N)$  on  $\rho$  follows power law. This leads to rapid changes under the typical model parameter settings, e.g., increasing  $\rho$  by 2.5% at  $M - N + 1 = 95$  leads to 10 times multiplication due to  $1.025^{95} \approx 10$ .

2) *Dependency of  $p(\rho, N)$  on  $N$* : Taking the natural logarithm of (29) we get

$$\ln [p(\rho, N)] = (M - N + 1) \left( \ln(\rho) + 1 \right) + \left( (N - 1) + \frac{1}{2} \right) \ln \left( \frac{N - 1}{M} \right).$$

By introducing the notation

$$\beta = \frac{N - 1}{M} \quad (30)$$

this can be rewritten as

$$\ln [p(\rho, \beta)] = M \left[ (1 - \beta) \left( \ln(\rho) + 1 \right) + \left( \beta + \frac{1}{2M} \right) \ln(\beta) \right].$$

Taking its first derivative with respect to  $\beta$  gives

$$\frac{\partial \ln [p(\rho, \beta)]}{\partial \beta} = M \left[ \ln \left( \frac{\beta}{\rho} \right) + \frac{1}{2M\beta} \right] \approx M \ln \left( \frac{\beta}{\rho} \right),$$

since in the typical model parameter ranges  $\beta \geq \frac{L}{M} \geq 0.1$  and  $M > 100$  and thus, except in the small sub-range  $\beta \approx \rho$ , the term  $\frac{1}{2M\beta}$  can be neglected. The first derivative of  $p(\rho, N)$

with respect to  $N$  comes by using  $\frac{\partial p(\rho, N)}{\partial N} = \frac{\partial (e^{\ln [p(\rho, N)]})}{\partial N} = p(\rho, N) \frac{\partial \ln [p(\rho, \beta)]}{\partial \beta} \frac{d\beta}{dN} = p(\rho, N) \frac{1}{M} * \frac{\partial \ln [p(\rho, \beta)]}{\partial \beta}$ , which yields

$$\frac{\partial p(\rho, N)}{\partial N} \approx p(\rho, N) \ln \left( \frac{\beta}{\rho} \right). \quad (31)$$

The sign of  $\ln \left( \frac{\beta}{\rho} \right)$  divides the  $\beta - \rho$  plane into two disjunct sub-areas regarding the characteristic of  $p(\rho, N)$  with respect to  $N$  as

$$p(\rho, N) \text{ is } \left\{ \begin{array}{l} \text{monotone decreasing, if } \beta < \rho \\ \text{monotone increasing, if } \beta \geq \rho \end{array} \right\}. \quad (32)$$

Moreover the dependency of  $p(\rho, N)$  on  $N$  is faster than exponential, since  $|\ln \left( \frac{\beta}{\rho} \right)|$  is increasing with decreasing  $N$  (increasing  $N$ ) in the range  $\beta < \rho$  ( $\beta \geq \rho$ ).

3) *The "low magnitude range"*: We investigate the case when  $p(\rho, N) = e^{const}$  holds, where  $const$  is a given real constant. With the notation of  $\beta$  this equation can be given by

$$M \left[ (1 - \beta) \left( \ln(\rho) + 1 \right) + \left( \beta + \frac{1}{2M} \right) \ln(\beta) \right] = const. \quad (33)$$

Observe that this equation implicitly defines a boundary function  $\beta(\rho)$  (or equivalently  $\rho(\beta)$ ), which separates the "low magnitude range"  $p(\rho, N) \leq e^{const}$  from the complementer range, in which  $p(\rho, N) > e^{const}$ . In the range  $p(\rho, N) \leq e^{const}$  the magnitude of  $\ln(p(\rho, N))$  is less than  $const$ , which explains the name "low magnitude range". We say that a  $\beta - \rho$

point is inside and outside of the "low magnitude range" if  $p(\rho, \beta) \leq e^{const}$  holds and does not hold for that point, respectively. By rearranging (33) we get the expression of  $\ln(\rho)$  along the boundary function as

$$\ln(\rho) = \frac{const}{(1 - \beta) M} - \frac{\beta}{1 - \beta} \ln(\beta) - 1 - \frac{1}{(1 - \beta) 2 M} \ln(\beta).$$

Therefore, the sensitivity of  $\ln(\rho)$  with respect to the  $const$ ,  $\zeta$  is given by

$$\zeta = \frac{1}{(1 - \beta) M}. \quad (34)$$

An upper limit for the factor  $\ln \left( \frac{\beta}{\rho} \right)$  determining the relation between  $p(\rho, N)$  and its first derivative with respect to  $N$  (see (31)) along the boundary function can be obtained as

$$\begin{aligned} \ln \left( \frac{\beta}{\rho} \right) &= \ln(\beta) - \ln(\rho) = \ln(\beta) + \frac{\beta}{1 - \beta} \ln(\beta) + 1 \\ &\quad - \left( \frac{const}{(1 - \beta) M} - \frac{1}{(1 - \beta) 2 M} \ln(\beta) \right) \\ &\leq \frac{1}{1 - \beta} \ln(\beta) + 1 \leq -\frac{1}{2} (1 - \beta) < 0. \end{aligned} \quad (35)$$

where we used the non-negativity of the term in the brackets and the inequality  $\ln(\beta) \leq -(1 - \beta) - \frac{1}{2}(1 - \beta)^2$ . Hence,

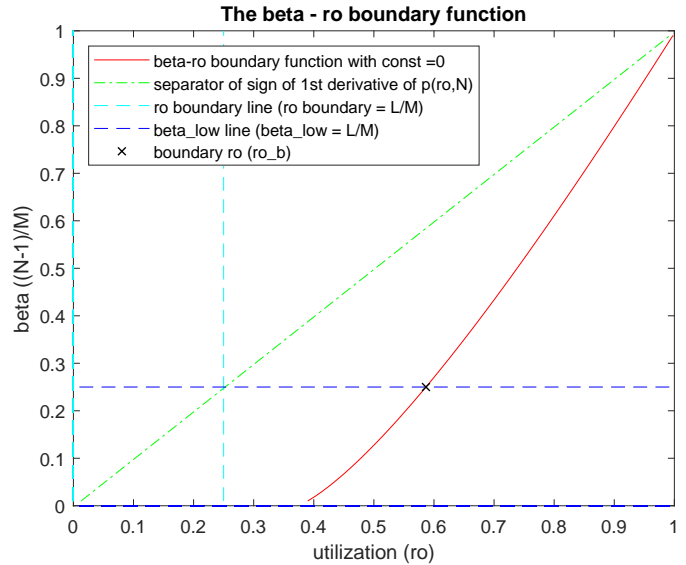


Figure 11. The  $\beta - \rho$  boundary function,  $const = 0$ ,  $M=200$ ,  $L=50$ .

the boundary curve lies under the line separating the  $\beta - \rho$  plane into parts with monotone decreasing and increasing  $p(\rho, N)$  with respect to  $N$ . The permitted region of the  $\beta - \rho$  plane is restricted by  $\beta \geq \beta_{low} = \frac{L}{M}$  and  $\rho > \beta_{low}$  due to the limitations  $N - 1 \geq L \Leftrightarrow \frac{N-1}{M} \geq \frac{L}{M}$  and  $\frac{L}{\mu} > L \Leftrightarrow \rho > \frac{L}{M}$ , respectively. The  $\rho$  at cross point of the horizontal line  $\beta = \beta_{low}$  and the boundary curve is called boundary  $\rho$  and denoted by  $\rho_b$ . All these are shown on the illustrating example Figure 11. Since  $\frac{\partial p(\rho, N)}{\partial N} < 0$  on the

boundary curve, the "low magnitude range" is located above the red marked boundary curve. Note that for  $const \geq 0$ , the whole range above the boundary curve belongs to the "low magnitude range", since  $p(\rho, \beta)$  is monotone increasing with  $\beta$  above  $\beta = \rho$  and  $\ln(p(\rho, 1)) = 0 \leq const$ .

4) *Monotonicity of  $\rho(\beta)$* : The first derivative of the boundary function  $\rho(\beta)$  with respect to  $\beta$  can be determined from (33) by applying the implicit function's derivative rule. This leads to

$$\begin{aligned} \frac{d\rho(\beta)}{d\beta} &= -\frac{\frac{\partial \ln[p(\rho, \beta)]}{\partial \beta}}{\frac{\partial \ln[p(\rho, \beta)]}{\partial \rho}} = -\frac{M \left[ \ln\left(\frac{\beta}{\rho}\right) + \frac{1}{2M\beta} \right]}{M(1-\beta)\frac{1}{\rho}} \\ &= \frac{\ln\left(\frac{\rho}{\beta}\right) - \frac{1}{2M\beta}}{1-\beta} \rho > 0, \end{aligned} \quad (36)$$

since  $\ln\left(\frac{\rho}{\beta}\right) > \frac{1}{2}(1-\beta)$  due to (35) and  $(1-\beta) > \frac{1}{M\beta}$  for  $0.5 - \sqrt{0.5 - \frac{1}{M}} < 0.1 \leq \beta < 0.5 + \sqrt{0.5 - \frac{1}{M}} \approx 0.99$ . The relation (36) implies that  $\rho$  is monotone increasing with respect to  $\beta$  on the boundary curve up to  $\beta \approx 0.99$ .

#### E. Constructing the approximate minimization

1) *Solution regimes*: For the sake of better understanding of the idea of the solution, first we consider a modified form of the equation (28) as

$$p(\rho, N) = r(\rho, N). \quad (37)$$

The idea of the approximate solution is based on the concept of "low magnitude range". Let  $N_s$  stand for the solution of  $r(\rho, N) = 0$ . Since  $\frac{d}{dN} r(\rho, N) = -C_W$ , the value of  $r(\rho, N)$  changes from 0 up to  $C_W$  while decreasing  $N$  from  $N_s$  to  $N_s - 1$ . On the other hand, the value of  $p(\rho, N)$  falls between 0 and  $C_W$  everywhere in the "low magnitude range" with  $const = \ln(C_W)$ . Hence, if  $N_s - 1$  falls inside of the "low magnitude range" then it follows that  $r(\rho, N)$  must cross  $p(\rho, N)$  somewhere between  $N_s$  and  $N_s - 1$  due to the continuity of  $r(\rho, N)$ . Therefore,  $N_s$  can be considered as approximate solution of (37).

We denote the value of  $N$  on the boundary curve by  $N_b$ , which depends on  $\rho$ . Due to (35),  $\left| \ln\left(\frac{\rho}{\beta}\right) \right| \lesssim 0.5$  and hence, along the boundary curve, the first derivative of  $p(\rho, N)$  is in the magnitude of  $-C_W$  and the dependency of  $p(\rho, N)$  on  $N$  is faster than exponential. Let us investigate a case, for which  $N_s - 1$  falls inside the "low magnitude range", i.e., it locates above the boundary curve for some value of  $\rho$ . By decreasing  $N$ , at  $N = N_b$ , we have  $r(\rho, N_b) > C_W = p(\rho, N_b)$ . By further decreasing  $N$ , the first derivative of  $p(\rho, N)$  becomes in absolute value greater than that one of  $r(\rho, N)$ , and hence, afterwards an other cross point of the functions  $p(\rho, N)$  and  $r(\rho, N)$  must exist, let us say at  $N = N_1$ . This is a maximum point of the cost function, since at this point (in  $N$ ), with decreasing  $N$ , the sign of  $p(\rho, N) - r(\rho, N)$  changes from negative to positive. After further decreasing  $N$  it reaches the point,  $N = N_2$ , where the value of the cost function falls under  $N_s$ . The situation is illustrated on Figure 12.

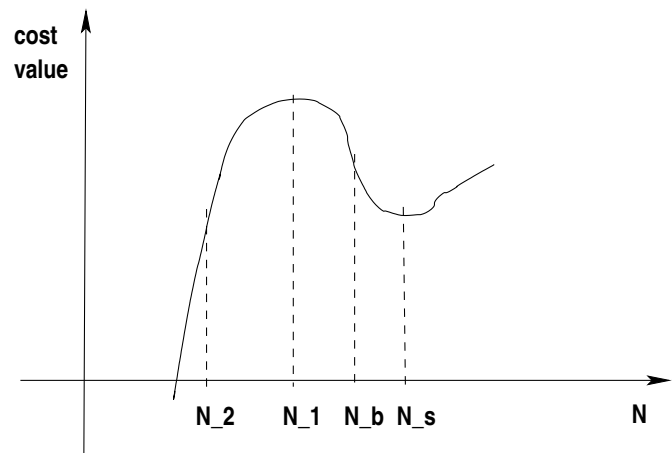


Figure 12. Example cost function.

The above discussed decrease from  $N_b$  to  $N_2$  in any range of  $N$ , in which  $p(\rho, N)$  is monotone decreasing with respect to  $N$ , causes an increase in the value of  $p(\rho, N)$ , which equivalently can be also considered as an increase in  $const$  of (33). This change in  $const$  corresponds to a shift of the boundary curve to right (see (34)). Hence, the points with  $N_2$  in a dependency of  $\rho$  lie on another boundary curve with an increased  $const$ , where  $\Delta const$  (= the increase in  $const$ ) is determined by the change  $p(\rho, N_b) \rightarrow p(\rho, N_2)$ .

If  $\rho > \rho_b$  then the point in  $\beta$  corresponding to  $N_1$  (locating under the boundary curve) can fall over the  $\beta_{low}$  line. Until  $N_2$  falls still below the  $\beta_{low}$  line, the value of the cost function at  $\beta_{low}$  is still higher than at  $\beta_s$  (corresponding to  $N_s$ ), and therefore the global minimum of the cost function is still at  $N_s$ . However, if  $N_2$  also falls above  $\beta_{low}$  line then the global minimum of the cost function is just above  $\beta_{low}$  (corresponding to  $N = L + 1$ ). If  $\rho > \rho_b$ , it can also happen that  $\beta_s$  falls outside of the "low magnitude range" (= under the boundary curve and above the  $\beta_{low}$  line). In this case  $\left| \frac{d}{dN} p(\rho, N) \right|$  is either still  $\leq C_W$  or it is also possible, with  $\beta_s$  far under the boundary curve, that it is  $> C_W$ . In the later case there is no cross point at all, as well as the cost function is monotone increasing with respect to  $N$  and hence the global minimum is just above  $\beta_{low}$ . Note that in the range  $N > N_s$  there can not be any cross point of the functions  $p(\rho, N)$  and  $r(\rho, N)$ , since  $p(\rho, N) > 0$  and  $r(\rho, N) < 0$  in that range.

It follows from the above argumentation that the global minimum of the cost function is approximately at  $N_s$  in the range of  $\rho < \rho_b$  and  $\beta_{low} \leq \beta_s < 1$ , since in this case the boundary curve locates under the horizontal  $\beta_{low}$  line and hence  $\beta_s$  always falls in the "low magnitude range". Above  $\rho_b$  there is a gap in  $\rho$  until a specific point,  $\rho_s$ , at which  $N_2$  reaches the  $\beta_{low}$  line and hence in this gap  $\beta_s$  can fall also below the boundary curve. However, the derivative of  $p(\rho, N)$  with respect to  $N$  is in absolute still less than  $C_W$  while  $N_s$  not much less than  $N_b$  (see (35)) and therefore we assume that the global minimum of the cost function still close to  $N_s$ . Finally above  $\rho_s$  the position of the global minimum of the

cost function changes to  $N = L + 1$ .

The position of  $\rho_s$  depends on  $\Delta const$ , which, as change in  $const$ , causes a shift of the boundary  $\rho$ , from  $\rho_b$  to  $\rho_s$ .

2) *The magnitude of  $\Delta const$* : The change in  $const$  is a sum of the changes due to  $p(\rho, N_b) \rightarrow p(\rho, N_1)$  and  $p(\rho, N_1) \rightarrow p(\rho, N_2)$  on  $\ln$  level.

The first part of the sum counts for the increase  $p(\rho, N_b) \rightarrow p(\rho, N_1)$  on  $\ln$  level. During  $N_b \rightarrow N_1$  the value of  $p(\rho, N)$  increases from  $C_w$  up to  $(N_s - N_1)C_w$ . Hence, the first part of change in  $const$  is given by

$$\ln \left( \frac{p(\rho, N_1)}{p(\rho, N_b)} \right) = \ln \left( \frac{(N_s - N_1)C_w}{C_w} \right) = \ln(N_s - N_1). \quad (38)$$

The second part of the sum stands for increase  $p(\rho, N_1) \rightarrow p(\rho, N_2)$ , on  $\ln$  level. During  $N_1 \rightarrow N_2$  the cost function  $F_{2app}$  decreases so much as its increases during  $N_s \rightarrow N_1$ . The major term of  $\Delta F_{2app}$  during the transition  $N_s \rightarrow N_1$  is  $r(\rho, N)$ , which is linear with  $N$ , and its value changes from 0 to  $(N_s - N_1)C_w$ . Therefore, the increase of the cost function  $F_{2app}$  during  $N_s \rightarrow N_1$  is overestimated as

$$F_{2app}(N_1) - F_{2app}(N_s) \lesssim \frac{(N_s - N_1)^2 C_w}{2}. \quad (39)$$

In the range  $N \leq N_1$ , the change of  $F_{2app}$  is dominated by  $p(\rho, N)$  due to its over-exponential character against the linear character of  $r(\rho, N)$ . Therefore, we model the change of  $F_{2app}$  during the transition  $N_2 \rightarrow N_1$  by  $p(\rho, N) \gtrsim e^{\chi N}$  with  $\chi$  equal to the derivative factor at  $N = N_1$ , i.e.,  $\chi = \ln \left( \frac{\beta_{N_1}}{\rho} \right) < 0$ , where  $\beta_{N_1}$  is the value of  $\beta$  at  $N = N_1$ . This yields

$$\begin{aligned} F_{2app}(N_1) - F_{2app}(N_2) &\gtrsim \int_{N=N_2}^{N_1} e^{\chi N} \\ &= \frac{1}{\chi} \left( p(\rho, N_1) - p(\rho, N_2) \right) = \frac{1}{|\chi|} \left( p(\rho, N_2) - p(\rho, N_1) \right) \\ &= \ln \left( \frac{\rho}{\beta_{N_1}} \right) \left( p(\rho, N_2) - p(\rho, N_1) \right). \end{aligned} \quad (40)$$

Combining (39) and (40) we have

$$p(\rho, N_2) - p(\rho, N_1) \lesssim \frac{1}{\ln \left( \frac{\rho}{\beta_{N_1}} \right)} \frac{(N_s - N_1)^2 C_w}{2},$$

and therefore

$$\begin{aligned} \ln \left( \frac{p(\rho, N_2)}{p(\rho, N_1)} \right) &= \ln \left( \frac{p(\rho, N_2) - p(\rho, N_1)}{p(\rho, N_1)} + 1 \right) \\ &\lesssim \ln \left[ \frac{(N_s - N_1)^2 C_w}{2 \ln \left( \frac{\rho}{\beta_{N_1}} \right) (N_s - N_1) C_w} + 1 \right] \\ &\approx \ln \left[ \frac{(N_s - N_1)}{2 \ln \left( \frac{\rho}{\beta_{N_1}} \right)} \right] \\ &= \ln(N_s - N_1) - \ln \left[ 2 \ln \left( \frac{\rho}{\beta_{N_1}} \right) \right]. \end{aligned} \quad (41)$$

Putting (38) and (41) together we get an estimation for  $\Delta const$  as

$$\Delta const \approx 2 \ln(N_s - N_1) - \ln \left[ 2 \ln \left( \frac{\rho}{\beta_{N_1}} \right) \right]. \quad (42)$$

Due to the over-exponential character of  $p(\rho, N)$  the value of  $N_1$  is close to  $N_2$  in general. We will use the estimation of  $\Delta const$  to determine the value of  $\rho_s$  at which the boundary curve (with  $const$  including also  $\Delta const$  as additive term) crosses the  $\beta_{low}$  line. Thus around that specific value of  $\rho_s$  we have  $N_2 \approx L$ . Therefore,  $N_1$  can be approximated by  $L$  in (42), which results in the estimate for the magnitude of  $\Delta const$  as

$$\Delta const \approx 2 \ln(N_s - L) - \ln \left[ 2 \ln \left( \frac{\rho}{\beta_{low}} \right) \right]. \quad (43)$$

Based on (35) (and that  $const \ll M$  holds in the final relation for  $\rho_s$  (51)), an approximation can be given for  $\ln \left( \frac{\rho_s}{\beta_L} \right)$  as

$$\ln \left( \frac{\rho_s}{\beta_{low}} \right) \gtrsim \frac{1}{2} (1 - \beta_{low}). \quad (44)$$

Applying (44) to (43) we get the final form of the estimation for the magnitude of  $\Delta const$  as

$$\begin{aligned} \Delta const &\approx 2 \ln(\Delta N) - \ln(1 - \beta_{low}), \\ &\text{where } \Delta N = N_s - L. \end{aligned} \quad (45)$$

3) *Estimation of  $\Delta const$* : The value of  $N_s$ , the solution of  $r(\rho, N_s) = 0$ , can be given from (27) as

$$N_s = A(M - L) + \frac{1}{\rho \frac{M}{L} - 1} + L + 1. \quad (46)$$

Hence,  $\Delta N$  can be expressed as

$$\Delta N = N_s - L = A(M - L) + \frac{1}{\rho \frac{M}{L} - 1} + 1,$$

which can be rearranged as

$$\Delta N = AM \left[ (1 - \beta_{low}) + \frac{1}{A M} \left( \frac{1}{\rho \frac{M}{L} - 1} + 1 \right) \right].$$

The term  $\frac{1}{\rho \frac{M}{L} - 1} + 1$  can be limited as  $1 < \frac{1}{\frac{\rho}{\beta_{low}} - 1} + 1 \leq 6$  assuming  $\rho \geq \beta_{low} \xi$  with  $\xi = 1.2$ . This term counts in  $\ln(\Delta N)$  only if  $\frac{1}{A M} \left( \frac{1}{\rho \frac{M}{L} - 1} + 1 \right)$  dominates over  $(1 - \beta_{low})$ , in which case it causes an uncertainty around  $\ln(6) \approx 1.79$  on  $\Delta const$  level. In order to minimize this uncertainty, we approximate this term by  $\sqrt{6} \approx 2.45$  causing an uncertainty not higher than  $\ln(\sqrt{6}) \approx \frac{1.79}{2} \approx 0.9$  on  $\Delta const$  level. Based on this,  $\ln(\Delta N)$  can be estimated as

$$\ln(\Delta N) = \ln(A) + \ln(M) + \ln \left( 1 - \beta_{low} + \frac{2.45}{AM} \right). \quad (47)$$

Now using (47) in (45) we can estimate  $\Delta const$  as

$$\Delta const \approx 2 \left[ \ln(A) + \ln(M) + \ln \left( 1 - \beta_{low} + \frac{2.45}{AM} \right) \right] - \ln(1 - \beta_{low}). \quad (48)$$

4) *Relation for  $\rho_s$* : So far we discussed the way of solution without considering the term  $u_0(\rho)$  on the lhs of equation (28). Now we take into account also the term  $u_0(\rho)$ . In this case  $\ln[p(\rho, 1)] \ln[u_0(\rho)]$  can be greater than  $\ln(C_W)$  for  $\beta$  close to 1, but  $N_s$  can be considered as approximate solution also in this case, since the derivatives of  $r(\rho, N)$  and  $p(\rho, N)u_0(\rho)$  have different signs in that range. By including the term  $u_0(\rho)$ , the relation for the boundary curve crossing the  $\beta_{low}$  line at  $\rho_s$  can be given by

$$M \left[ (1 - \beta_{low}) \left( \ln(\rho_s) + 1 \right) + \left( \beta_{low} + \frac{1}{2M} \right) \ln(\beta_{low}) \right] + \ln[u_0(\rho_s)] = \ln(C_W) + \Delta const.$$

By substituting the expression of  $u_0(\rho)$  from (27) and using  $\left( 1 - \frac{1}{\rho_s \frac{M}{L}} \right) = \left( 1 - \frac{\beta_{low}}{\rho_s} \right) = \frac{\beta_{low}}{\rho_s} \left( \frac{\rho_s}{\beta_{low}} - 1 \right)$  we get

$$M \left[ (1 - \beta_{low}) \left( \ln(\rho_s) + 1 \right) + \left( \beta_{low} + \frac{1}{2M} \right) \ln(\beta_{low}) \right] + \ln(C_W) + \ln(\rho_s) + \ln \left( \frac{1}{(1 - \rho_s)^2} \right) + \ln(\beta_{low}) - \ln(\rho_s) + \ln \left( \frac{\rho_s}{\beta_{low}} - 1 \right) = \ln(C_W) + \Delta const.$$

Rearranging yields

$$M \left[ (1 - \beta_{low}) \left( \ln(\rho_s) + 1 \right) + \left( \beta_{low} + \frac{1}{2M} \right) \ln(\beta_{low}) \right] = -\ln(\beta_{low}) - \ln \left( \frac{1}{(1 - \rho_s)^2} \right) - \ln \left( \frac{\rho_s}{\beta_{low}} - 1 \right) + \Delta const. \quad (49)$$

By using (44) the term  $\ln \left( \frac{\rho_s}{\beta_{low}} - 1 \right)$  can be rearranged as

$$\ln \left( \frac{\rho_s}{\beta_{low}} - 1 \right) \approx \ln \left( e^{\frac{1}{2}(1 - \beta_{low})} - 1 \right) \approx \ln \left( \frac{1}{2}(1 - \beta_{low}) \right), \quad (50)$$

where we utilized that  $\frac{1}{2}(1 - \beta_{low}) \leq 0.45$  for  $\beta_{low} \geq 0.1$ . The term  $-\ln \left( \frac{1}{(1 - \rho_s)^2} \right)$  gives an uncertainty of  $\approx -4.6$  on rhs of (49) ( $1 \leq \frac{1}{(1 - \rho_s)^2} \leq 100$  for  $\rho_s \leq 0.9$  and thus  $\ln(100) = 4.6$ ) corresponding to difference of  $\frac{4.6}{(1 - 0.5)^{100}} \approx 0.09$  on  $\ln(\rho)$  level (according to the first term on the rhs of (34)) when assuming  $M \geq 100$  and again  $\beta_{low} \leq 0.5$ . The relation  $\rho_s \leq 0.9$  can be justified by the approximate solution of (49) for  $\rho_s$  by assuming that its rhs  $\leq 0.1M$ . Utilizing that  $\rho_s$  is monotone increasing with respect to  $\beta_{low}$  (see (36)), and setting  $\max(\beta_{low}) = 0.5$ , according to (34) we get  $\ln(\rho_s) \approx \frac{0.1}{0.5} - \ln(0.5) - 1 \approx -0.1 \Leftrightarrow \rho_s \approx 0.9$ . In order to minimize the above uncertainty of the term  $-\ln \left( \frac{1}{(1 - \rho_s)^2} \right)$ , we

approximate it by  $-2.3$ . Using this approximation and (50) as well as (48), we get the final form of the relation for  $\rho_s$  as

$$M \left[ (1 - \beta_{low}) \left( \ln(\rho_s) + 1 \right) + \left( \beta_{low} + \frac{1}{2M} \right) \ln(\beta_{low}) \right] = 2 \left[ \ln(A) + \ln(M) + \ln \left( 1 - \beta_{low} + \frac{2.45}{AM} \right) \right] - \ln \left( \frac{1}{2} \right) - 2 \ln(1 - \beta_{low}) - \ln(\beta_{low}) - 2.3. \quad (51)$$

#### F. Approximate solution formula

Now putting all together we get the approximate solution formula.

##### Conditions

- 1)  $100 \leq M$ ,
- 2)  $0.1 \leq \beta_{low} \leq 0.5$  with  $\beta_{low} = \frac{L}{M}$ ,
- 3)  $\rho \geq \beta_{low} \xi$  with  $\xi = 1.2$ ,
- 4)  $N - L \gg 1$ , practically  $N > L + 10$ ,
- 5)  $K - M \gg 1$ , practically  $K > M + 10$ .

##### Solution formula

If Conditions 1-5 hold, then

$$N_{opt} = \begin{cases} \min(\lfloor A(M-L) + \frac{1}{\rho \frac{M}{L} - 1} + L + 1 \rfloor, M) & \text{if } \rho \leq \rho_s, \\ L + 1 & \text{if } \rho_s < \rho < 1, \end{cases}$$

where

$$\ln(\rho_s) = \frac{const}{(1 - \beta_{low}) * M} - \frac{\beta_{low}}{1 - \beta_{low}} \ln(\beta_{low}) - 1 - \frac{1}{(1 - \beta_{low}) * 2 * M} \ln(\beta_{low}) \text{ and}$$

$$const = 2 \left[ \ln(A) + \ln(M) + \ln \left( 1 - \beta_{low} + \frac{2.45}{AM} \right) \right] - \ln \left( \frac{1}{2} \right) - 2 \ln(1 - \beta_{low}) - \ln(\beta_{low}) - 2.3. \quad (52)$$

Note that the condition  $N - L \gg 1$  refers to  $N_s$  and hence  $N_{opt} = L + 1 < L + 10$  in the solution formula does not violate this condition.

Observe that the approximate optimal  $N$  does not depend on  $C_A$ ,  $C_D$  and  $C_R$ . This is because they have no impact on  $N$  in the considered range of parameters. The cost parameters  $C_A$ ,  $C_D$  influence  $N$  only via  $p_0$  and hence they effect the optimal  $N$  in the range, in which  $p_0$  depends on  $N$ . The cost parameter  $C_R$  has impact on the optimal  $N$  via  $\eta$  and hence it is effective only for small values of  $K - M$  (see in (26)).

#### VII. APPROXIMATE MINIMIZATION - IN TRAFFIC RANGE

$$\frac{\lambda}{L\mu} < 1$$

For the  $N$  independent regions of  $p_0$  the function to be minimized, (13), can be reduced to the minimization of (23) like we did it for the traffic range  $\frac{\lambda}{L\mu} > 1$ . In order to further simplify the optimization task, we establish an approximate equation for determining the local minimum for (23). Of course this approximation restricts the parameter range, for which it holds.

A. Necessary approximations

In this subsection, we establish the approximations, which are needed to establish the approximate equation for determining the local minimum. Again, we make use that under the assumption  $N - L \gg 1$  the relation  $(\frac{\lambda}{L\mu})^{N-L} \ll 1$  holds for the traffic range  $\frac{\lambda}{L\mu} < 1$  and thus the term  $(\frac{\lambda}{L\mu})^{N-L}$  can be neglected compared to 1.

1) Approximation for  $\tau$ : Using  $(\frac{\lambda}{L\mu})^{N-L} \ll 1$  the expression of  $\tau$  in (10) can be approximated as

$$\tau = \frac{\frac{\lambda}{L\mu}}{(1 - \frac{\lambda}{L\mu})^2} - \left(\frac{\lambda}{L\mu}\right)^{N-L} (N-L) \left(\frac{1}{1 - \frac{\lambda}{L\mu}} + \frac{N-L-1}{2}\right). \tag{53}$$

2) Approximate  $\Delta_N \alpha$ ,  $\Delta_N \frac{p_{s1}}{p_L}$  and  $\Delta_N \tau$ : Taking  $\Delta_N$  on (18) we get

$$\begin{aligned} \Delta_N \alpha &\approx \left(1 - \frac{\lambda}{L\mu}\right) \left(\frac{\lambda}{L\mu}\right)^{N-L-1} - \left(1 - \frac{\lambda}{L\mu}\right) \left(\frac{\lambda}{L\mu}\right)^{N-L-2} \\ &= \left(1 - \frac{\lambda}{L\mu}\right) \left(\frac{\lambda}{L\mu} - 1\right) \left(\frac{\lambda}{L\mu}\right)^{N-L-2} \\ &= -\left(1 - \frac{\lambda}{L\mu}\right)^2 \left(\frac{\lambda}{L\mu}\right)^{N-L-2}. \end{aligned} \tag{54}$$

It can be seen from (16) that the first two terms of  $\frac{p_{s1}}{p_L}$  are independent of  $N$ . Thus, using the expression based on the second approximation form (17) for taking  $\Delta_N$  would neglect the major term of  $\Delta_N \frac{p_{s1}}{p_L}$ , which would lead to incorrect approximation. Therefore,  $\Delta_N$  must be taken on the expression based on the first approximation of  $p_{s1}$  in (16), which yields

$$\begin{aligned} \Delta_N \frac{p_{s1}}{p_L} &\approx (N-L-2) \left(\frac{\lambda}{L\mu}\right)^{N-L-1} - (N-L-1) \left(\frac{\lambda}{L\mu}\right)^{N-L} \\ &= \left(\frac{\lambda}{L\mu}\right)^{N-L-1} \left((N-L-2) - \frac{\lambda}{L\mu}(N-L-1)\right) \\ &= \left(\frac{\lambda}{L\mu}\right)^{N-L-1} \left((N-L-1)\left(1 - \frac{\lambda}{L\mu}\right) - 1\right). \end{aligned} \tag{55}$$

Taking  $\Delta_N$  on (53) leads to

$$\begin{aligned} \Delta_N \tau &= -\left(\frac{\lambda}{L\mu}\right)^{N-L} (N-L) \left[\frac{1}{1 - \frac{\lambda}{L\mu}} + \frac{N-L-1}{2}\right] \\ &\quad + \left(\frac{\lambda}{L\mu}\right)^{N-L-1} (N-L-1) \left[\frac{1}{1 - \frac{\lambda}{L\mu}} + \frac{N-L-2}{2}\right] \\ &= \left(\frac{\lambda}{L\mu}\right)^{N-L-1} (N-L-1) \\ &\quad \times \left[\left(\frac{1}{1 - \frac{\lambda}{L\mu}} + \frac{N-L-1}{2}\right) \left(1 - \frac{\lambda}{L\mu}\right) - \frac{1}{2}\right] \\ &\quad - \left(\frac{\lambda}{L\mu}\right)^{N-L} \left(\frac{1}{1 - \frac{\lambda}{L\mu}} + \frac{N-L-1}{2}\right) \\ &= \left(\frac{\lambda}{L\mu}\right)^{N-L-1} \left[(N-L-1) \left(1 - \frac{\lambda}{L\mu}\right) - \frac{\lambda}{L\mu}\right] \\ &\quad \times \left[\frac{N-L-1}{2} + \frac{1}{1 - \frac{\lambda}{L\mu}}\right] - \left(\frac{\lambda}{L\mu}\right)^{N-L-1} \frac{N-L-1}{2}. \end{aligned} \tag{56}$$

3) Limits on  $s_{L,N}$ : Applying a lower limit on every term of the sum in the expression of  $s_{L,N}$  we get a lower limit on it as

$$\begin{aligned} s_{L,N} &= \sum_{i=L}^{N-1} \frac{i!}{\left(\frac{\lambda}{\mu}\right)^i} \\ &= \frac{(N-1)!}{\left(\frac{\lambda}{\mu}\right)^{N-1}} \left(1 + \frac{\lambda}{N-1} + \dots + \frac{\left(\frac{\lambda}{\mu}\right)^{N-1-L}}{(N-1)\dots(L+1)}\right) \\ &\geq \frac{(N-1)!}{\left(\frac{\lambda}{\mu}\right)^{N-1}} \sum_{i=0}^{N-1-L} \left(\frac{\lambda}{(N-1)\mu}\right)^i \\ &= \frac{(N-1)!}{\left(\frac{\lambda}{\mu}\right)^{N-1}} \frac{1 - \left(\frac{\lambda}{(N-1)\mu}\right)^{N-L}}{1 - \frac{\lambda}{(N-1)\mu}} \approx \frac{(N-1)!}{\left(\frac{\lambda}{\mu}\right)^{N-1}} \frac{1}{1 - \frac{\lambda}{(N-1)\mu}}, \end{aligned} \tag{57}$$

where in the last step we utilized that  $\left(\frac{\lambda}{(N-1)\mu}\right)^{N-L} \ll 1$  for  $N-L \gg 1$  due to  $\frac{\lambda}{(N-1)\mu} \leq \frac{\lambda}{L\mu} < 1$ .

Similarly, applying an upper limit on every term of the sum in the expression of  $s_{L,N}$ , we get an upper limit on it as

$$\begin{aligned} s_{L,N} &= \sum_{i=L}^{N-1} \frac{i!}{\left(\frac{\lambda}{\mu}\right)^i} \\ &= \frac{(N-1)!}{\left(\frac{\lambda}{\mu}\right)^{N-1}} \left(1 + \frac{\lambda}{N-1} + \dots + \frac{\left(\frac{\lambda}{\mu}\right)^{N-1-L}}{(N-1)\dots(L+1)}\right) \\ &< \frac{(N-1)!}{\left(\frac{\lambda}{\mu}\right)^{N-1}} \sum_{i=0}^{N-1-L} \left(\frac{\lambda}{L\mu}\right)^i = \frac{(N-1)!}{\left(\frac{\lambda}{\mu}\right)^{N-1}} \frac{1 - \left(\frac{\lambda}{L\mu}\right)^{N-L}}{1 - \frac{\lambda}{L\mu}}. \end{aligned} \tag{58}$$

B. Establishing an approximation for  $\Delta_N F_2$

1) Basic form of  $\Delta_N F_2$ : Taking  $\Delta_N$  on the function (23) to be minimized and using  $\Delta_n a(n)b(n) = a(n)\Delta_n b(n) + \Delta_n a(n)b(n-1)$  we get

$$\begin{aligned} \Delta_N F_2 &= \lambda(C_A + C_D)(M - L)\Delta_N \alpha \\ &+ \eta \left( \Delta_N s_{L,N} \alpha(N - 1, L) + s_{L,N} \Delta_N \alpha(N, L) \right) \\ &+ C_W \Delta_N \tau - (C_{on} - C_{off})(M - L)\Delta_N \frac{p_{s1}}{PL}. \end{aligned}$$

2) Applying the approximations: Using  $\Delta_N s_{L,N} = \frac{(N-1)!}{(\frac{\lambda}{\mu})^{N-1}}$  and applying the approximations for  $\alpha$ ,  $\Delta_N \alpha$ ,  $\Delta_N \frac{p_{s1}}{PL}$  and  $\Delta_N \tau$ , i.e., (18), (54), (55), (56) yields

$$\begin{aligned} \Delta_N F_2 &\approx \eta \left[ \frac{(N-1)!}{\left(\frac{\lambda}{\mu}\right)^{N-1}} \left(1 - \frac{\lambda}{L\mu}\right) \left(\frac{\lambda}{L\mu}\right)^{N-L-2} \right. \\ &- \left. s_{L,N} \left(1 - \frac{\lambda}{L\mu}\right)^2 \left(\frac{\lambda}{L\mu}\right)^{N-L-2} \right] \\ &- (C_{on} - C_{off})(M - L) \\ &\times \left(\frac{\lambda}{L\mu}\right)^{N-L-1} \left[ (N - L - 1) \left(1 - \frac{\lambda}{L\mu}\right) - 1 \right] \\ &+ C_W \left(\frac{\lambda}{L\mu}\right)^{N-L-1} \left[ (N - L - 1) \left(1 - \frac{\lambda}{L\mu}\right) - \frac{\lambda}{L\mu} \right] \\ &\times \left( \frac{N - L - 1}{2} + \frac{1}{1 - \frac{\lambda}{L\mu}} \right) - C_W \left(\frac{\lambda}{L\mu}\right)^{N-L-1} \frac{N - L - 1}{2} \\ &- \lambda(C_A + C_D)(M - L) \left(1 - \frac{\lambda}{L\mu}\right)^2 \left(\frac{\lambda}{L\mu}\right)^{N-L-2}. \end{aligned} \tag{59}$$

The exact and approximated values of the function  $\Delta_N F_2$  by  $F_{2app}$  are shown on Figure 13 in dependency of threshold  $N$  for the parameter setting  $M = 200, L = 100, K = 250, \mu = 1, C_W = 10, C_{off} = 0.01, C_{on} = 0.02, C_a = 0.03, C_d = 0.02, C_R = 200$ , and  $\rho = 0.6$ .

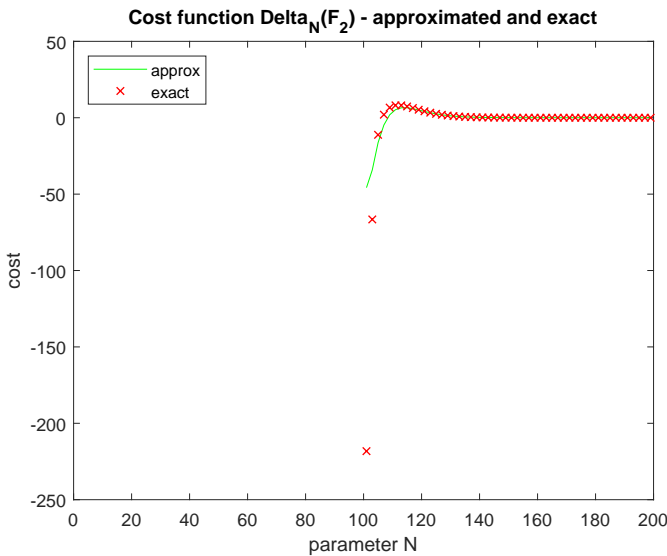


Figure 13. Exact and approximate values of the function  $\Delta_N F_2$  in dependency of threshold  $N$ .

The figure shows a very good match. The mismatch on the left side of the curve is caused by violating the condition  $N - L \gg 1$ , which was utilized by the approximations, as  $N$  becomes close to  $L$ .

Due to  $K - M \gg 1$  the approximation for  $\eta$  in (26) holds also in traffic range  $\frac{\lambda}{L\mu} < 1$ . Using it in (59) results in

$$\begin{aligned} \Delta_N F_2 &\approx C_W \frac{\rho}{(1 - \rho)^2} \frac{\left(\frac{\lambda}{\mu}\right)^M}{M!} \left[ \frac{(N-1)!}{\left(\frac{\lambda}{\mu}\right)^{N-1}} - s_{L,N} \left(1 - \frac{\lambda}{L\mu}\right) \right] \\ &\times \left(1 - \frac{\lambda}{L\mu}\right) \left(\frac{\lambda}{L\mu}\right)^{N-L-2} \\ &- C_W \left(\frac{\lambda}{L\mu}\right)^{N-L-1} \\ &\times \left\{ \frac{C_{on} - C_{off}}{C_W} (M - L) \left[ (N - L - 1) \left(1 - \frac{\lambda}{L\mu}\right) - 1 \right] \right. \\ &- \left. \left[ (N - L - 1) \left(1 - \frac{\lambda}{L\mu}\right) - \frac{\lambda}{L\mu} \right] \left( \frac{N - L - 1}{2} + \frac{1}{1 - \frac{\lambda}{L\mu}} \right) \right. \\ &\left. + \frac{N - L - 1}{2} + \frac{\lambda(C_A + C_D)}{C_W} (M - L) \frac{L\mu}{\lambda} \left(1 - \frac{\lambda}{L\mu}\right)^2 \right\}. \end{aligned} \tag{60}$$

3) Limits on the term  $\left[ \frac{(N-1)!}{\left(\frac{\lambda}{\mu}\right)^{N-1}} - s_{L,N} \left(1 - \frac{\lambda}{L\mu}\right) \right]$ : The term  $\left[ \frac{(N-1)!}{\left(\frac{\lambda}{\mu}\right)^{N-1}} - s_{L,N} \left(1 - \frac{\lambda}{L\mu}\right) \right]$  on the lhs of (59) is positive. This can be shown by the help of the upper limit on  $s_{L,N}$ , (58) as

$$\begin{aligned} &\frac{(N-1)!}{\left(\frac{\lambda}{\mu}\right)^{N-1}} - s_{L,N} \left(1 - \frac{\lambda}{L\mu}\right) \\ &\geq \frac{(N-1)!}{\left(\frac{\lambda}{\mu}\right)^{N-1}} - \frac{(N-1)!}{\left(\frac{\lambda}{\mu}\right)^{N-1}} \frac{1 - \left(\frac{\lambda}{L\mu}\right)^{N-L}}{1 - \frac{\lambda}{L\mu}} \left(1 - \frac{\lambda}{L\mu}\right) \\ &= \frac{(N-1)!}{\left(\frac{\lambda}{\mu}\right)^{N-1}} \left\{ 1 - \left[ 1 - \left(\frac{\lambda}{L\mu}\right)^{N-L} \right] \right\} \\ &= \frac{(N-1)!}{\left(\frac{\lambda}{\mu}\right)^{N-1}} \left(\frac{\lambda}{L\mu}\right)^{N-L} > 0. \end{aligned} \tag{57}$$

On the other hand, by using the lower limit on  $s_{L,N}$ , (57) we get an upper limit on  $\left[ \frac{(N-1)!}{\left(\frac{\lambda}{\mu}\right)^{N-1}} - s_{L,N} \left(1 - \frac{\lambda}{L\mu}\right) \right]$  as

$$\begin{aligned} &\frac{(N-1)!}{\left(\frac{\lambda}{\mu}\right)^{N-1}} - s_{L,N} \left(1 - \frac{\lambda}{L\mu}\right) \\ &\approx \frac{(N-1)!}{\left(\frac{\lambda}{\mu}\right)^{N-1}} - \frac{(N-1)!}{\left(\frac{\lambda}{\mu}\right)^{N-1}} \frac{1}{1 - \frac{\lambda}{(N-1)\mu}} \left(1 - \frac{\lambda}{L\mu}\right) \\ &= \frac{(N-1)!}{\left(\frac{\lambda}{\mu}\right)^{N-1}} \left[ 1 - \left(1 - \frac{\lambda}{L\mu}\right) \frac{1}{1 - \frac{\lambda}{(N-1)\mu}} \right] \\ &\leq \frac{(N-1)!}{\left(\frac{\lambda}{\mu}\right)^{N-1}} \left[ 1 - \left(1 - \frac{\lambda}{L\mu}\right) \right] = \frac{(N-1)!}{\left(\frac{\lambda}{\mu}\right)^{N-1}} \frac{\lambda}{L\mu}, \end{aligned} \tag{61}$$

where in the last but one step we utilized  $\frac{1}{1 - \frac{\lambda}{(N-1)\mu}} > 1$  due to  $\frac{\lambda}{(N-1)\mu} \leq \frac{\lambda}{L\mu} < 1$ .

4) *Final form of the approximation for  $\Delta_N F_2$* : We introduce the notation

$$B = \frac{\lambda(C_A + C_D)}{C_W}$$

Replacing the term  $\left[ \frac{(N-1)!}{(\frac{\lambda}{\mu})^{N-1}} - s_{L,N} \left( 1 - \frac{\lambda}{L\mu} \right) \right]$  by its upper limit (61) in (60), using the notations  $A$  (introduced in (27)) and  $B$  and performing rearrangements leads to an upper limit on  $\Delta_N F_2$  as

$$\begin{aligned} \Delta_N F_2 &\lesssim \left( \frac{\lambda}{L\mu} \right)^{N-L-1} \frac{(\frac{\lambda}{\mu})^M (N-1)!}{M! (\frac{\lambda}{\mu})^{N-1}} \\ &\times C_W \frac{\rho}{(1-\rho)^2} \left( 1 - \frac{\lambda}{L\mu} \right) - \left( \frac{\lambda}{L\mu} \right)^{N-L-1} C_W \\ &\times \left\{ A(M-L) \left[ (N-L-1) \left( 1 - \frac{\lambda}{L\mu} \right) - 1 \right] \right. \\ &- \left. \left[ (N-L-1) \left( 1 - \frac{\lambda}{L\mu} \right) - \frac{\lambda}{L\mu} \right] \left( \frac{N-L-1}{2} + \frac{1}{1 - \frac{\lambda}{L\mu}} \right) \right. \\ &\left. + \frac{N-L-1}{2} + B(M-L) \frac{L\mu}{\lambda} \left( 1 - \frac{\lambda}{L\mu} \right)^2 \right\}. \end{aligned}$$

We define  $x$  as

$$x = N - L - 1.$$

Using this notation and performing further rearrangements we get the final form of the approximation for  $\Delta_N F_2$  as

$$\begin{aligned} \Delta_N F_2 &< \left( \frac{\lambda}{L\mu} \right)^{N-L-1} C_W \\ &\times \left( \frac{(\frac{\lambda}{\mu})^M (N-1)!}{M! (\frac{\lambda}{\mu})^{N-1}} u_1(\rho) + q(\rho, N) \right), \end{aligned}$$

where

$$\begin{aligned} u_1(\rho) &= \frac{\rho}{(1-\rho)^2} \left( 1 - \frac{\rho}{L} \right) \quad \text{and} \\ q(\rho, N) &= ax^2 - bx + c, \quad \text{and } x = N - L - 1, \\ a &= \frac{1}{2} \left( 1 - \frac{\lambda}{L\mu} \right), \quad b = \left[ \left( A(M-L) - \frac{1}{2} \right) \left( 1 - \frac{\lambda}{L\mu} \right) \right], \\ c &= \left\{ \left[ A - B \frac{L\mu}{\lambda} \left( 1 - \frac{\lambda}{L\mu} \right)^2 \right] (M-L) - \frac{\frac{\lambda}{L\mu}}{1 - \frac{\lambda}{L\mu}} \right\}. \end{aligned} \tag{62}$$

**C. Constructing the approximate minimization**

As we will see, the construction of the approximate minimization is based on the existence of range of  $N$ , in which the cost function is almost constant, and the properties of the quadratic equation  $q(\rho, N) = 0$ .

1) *Existence of almost constant cost ranges*: The term  $\left( \frac{\lambda}{L\mu} \right)^{N-L-1}$  decreases rapidly with increasing  $N$  in the range of  $\frac{\lambda}{L\mu} < 1$ . Hence, after enough large values of  $N$ , at the latest when  $N - L - 1$  reaches several tens, it suppresses the rhs of (62). Thus in that range  $\Delta F_2 \approx 0$  and therefore the cost

function is almost constant. The range of  $N$ , in which the cost function is almost constant will be called as "almost constant cost range".

In general the value of the factorial terms in (62) can vary in a huge magnitude range. However  $p(\rho, N) = \frac{(\frac{\lambda}{\mu})^M (N-1)!}{M! (\frac{\lambda}{\mu})^{N-1}}$  is monotone increasing in the range of  $\beta > \rho$  (see (32), which is the case due to  $\beta \geq \beta_{low} \Leftrightarrow N - 1 \geq L$  and  $1 > \frac{\lambda}{L\mu} \Leftrightarrow \beta_{low} > \rho$ , and thus  $p(\rho, N) \leq p(\rho, M) = 1$ . Also the term  $u_1(\rho)$  is upper limited by  $u_1(\rho) < \frac{\rho}{(1-\rho)^2} < \frac{0.5}{(1-0.5)^2} = 2$  for  $\rho < \beta_{low} \leq 0.5$ . It follows that the term  $\frac{(\frac{\lambda}{\mu})^M (N-1)!}{M! (\frac{\lambda}{\mu})^{N-1}} u_1(\rho)$  can not grow any large in the allowed traffic range and hence it will be also suppressed by term  $\left( \frac{\lambda}{L\mu} \right)^{N-L-1}$  when  $N - L - 1$  reaches several tens depending on the value of  $\rho$ .

Figures 14 and 15 illustrate the existence of "almost constant cost range" for two typical form cost function curves.

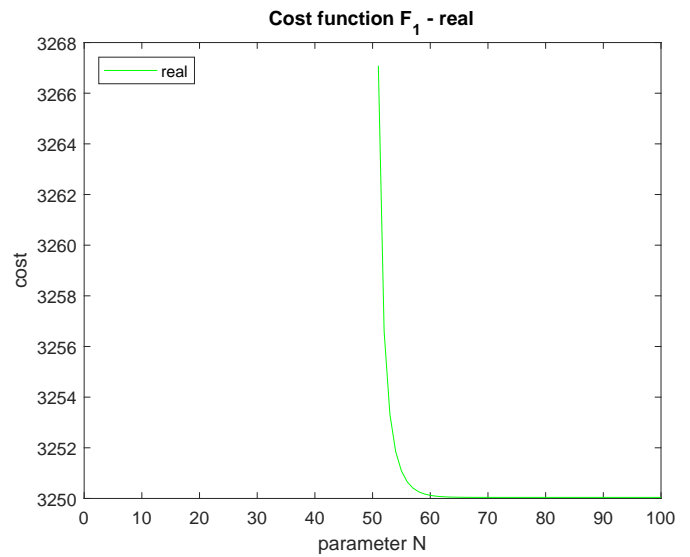


Figure 14. Typical cost function curve - Type 1.

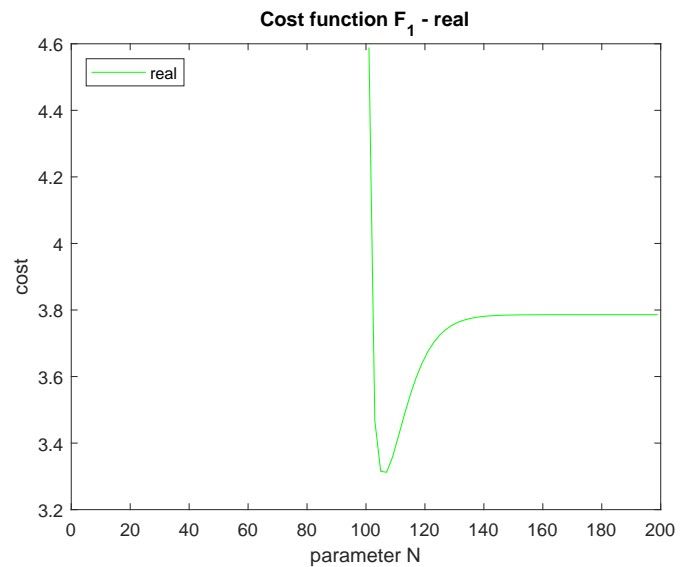


Figure 15. Typical cost function curve - Type 2.

Figure 14 and 15 were created by using the parameter settings  $M = 100, L = 50, K = 150, \mu = 1, C_W = 50, C_{off} = 15, C_{on} = 50, C_a = 30, C_d = 20, C_R = 200, \rho = 0.3$  and  $M = 200, L = 100, K = 250, \mu = 1, C_W = 10, C_{off} = 0.01, C_{on} = 0.02, C_a = 0.03, C_d = 0.02, C_R = 200, \rho = 0.4$ , respectively.

In the range of  $N - L - 1 \gg 1$ , e.g.,  $N - L - 1 > 10$ , the term  $\frac{(\frac{\lambda}{L\mu})^M}{M!} \frac{(N-1)!}{(\frac{\lambda}{L\mu})^{N-1}} u_1(\rho)$  falls in a very low magnitude range and thus it can be neglected comparing to  $q(\rho, N)$ . Hence, in that range the maximum value of  $\Delta F_2$  is determined by  $q(\rho, N)$ . Due to the parabolic character of  $q(\rho, N)$  the maximum of its absolute value in the range of  $x = 0, \dots, M - L - 1$ , denoted by  $q_{ul}$ , is upper limited by the maximum of its absolute value at  $x = 0$ , at  $x = M - L - 1$  and at its local extremum, which is at  $x = \frac{b}{2a}$  due to  $\frac{\partial q(\rho, N)}{\partial x} = 0 \Leftrightarrow 2ax - b = 0$ . Therefore,  $q_{ul}$  can be given by

$$q_{ul} = \max \left[ |c|, |a(M - L - 1)^2 - b(M - L - 1) + c|, \left| c - \frac{b^2}{4a} \right| \right]. \quad (63)$$

Let  $N_{uccl}$  stand for an upper limit on the lower boundary of the "almost constant cost range". This upper limit is determined by the equation

$$q_{ul} \left( \frac{\lambda}{L\mu} \right)^{N_{uccl} - L - 1} = \epsilon,$$

where  $\epsilon$  is the required precision, e.g.,  $\epsilon = 0.01$ . Solving the above equation results in  $N_{uccl}$  as

$$N_{uccl} = \lfloor \frac{\ln(\frac{\epsilon}{q_{ul}})}{\ln(\frac{\lambda}{L\mu})} + L + 1 \rfloor \text{ with } \epsilon < q_{ul}.$$

2) *The concept of the approximate solution:* The existence of almost constant cost ranges implies that either there is a cost minimum at  $N_{opt}$  below the lower boundary of the "almost constant cost range" or the cost at any  $N$  in the whole "almost constant cost range" can be considered as minimal.

The situation is determined by the properties of  $\Delta_N F_2$  in the range of  $N$  below the lower boundary of the "almost constant cost range". In the majority of that range the term  $\frac{(\frac{\lambda}{L\mu})^M}{M!} \frac{(N-1)!}{(\frac{\lambda}{L\mu})^{N-1}} u_1(\rho)$  can be neglected comparing to  $q(\rho, N)$  and therefore the properties (sign and position of roots) of the parabola  $q(\rho, N)$  determines the situation as follows:

Let  $x_l$  and  $x_h$  stand for the real roots of the quadratic equation  $q(\rho, N) = 0$  with  $x_l < x_h$ , if they exists. Similarly, let  $N_l$  and  $N_h$  stand for the corresponding values in  $N$ , i.e.,  $N_l = x_l + L + 1$  and  $N_h = x_h + L + 1$ . The coefficient of  $x^2$  in the above quadratic equation is positive, since  $a$  is positive due to  $\frac{\lambda}{L\mu} < 1$ . Therefore, in the range  $x < x_l$  and  $x > x_h$  the value of  $q(\rho, N)$  is positive. Similarly, in the range  $x_l < x < x_h$  the value of  $q(\rho, N)$  is negative.

It follows from the above argumentation that the approximate solution can be constructed as follows.

- 1) The quadratic equation  $q(\rho, N)$  has two real roots and  $x_h \geq 0 \Leftrightarrow N_h \geq L + 1$ .
  - If  $N_h < N_{uccl}$  then the cost function  $F_2$  has local minimum at  $N_h$ ,
  - otherwise any  $N$  in the "almost constant cost range" is a local minimum.

Moreover if  $x_l < 0$  or  $x_l \geq 0$ , but it lies close enough to 0 then the above local minimum places are also global. Otherwise it is also possible that the value of  $F_2$  at  $x = 0$  is less then at the above local minimum places.

- 2) In any other case (two real roots and  $x_h < 0$ , one real root or no real root)  $q(\rho, N) > 0$  and thus  $F_2$  is monotone increasing in the range of  $x > 0 \Leftrightarrow N \geq L + 1$ , and hence it has global minimum at  $N = L + 1$ ,

3) *Condition for discriminant of the quadratic equation to be positive:* The coefficients of the quadratic equation  $q(\rho, N) = (ax^2 - bx + c) = 0$  can be rearranged as

$$\begin{aligned} a &= \frac{1}{2} \left( 1 - \frac{\lambda}{L\mu} \right), \\ b &= \left[ \left( A(M - L) - \frac{1}{2} \right) \left( 1 - \frac{\lambda}{L\mu} \right) \right] = \left[ 2A(M - L) - 1 \right] a, \\ c &= \left\{ \left[ A - B \frac{L\mu}{\lambda} \left( 1 - \frac{\lambda}{L\mu} \right)^2 \right] (M - L) - \frac{\frac{\lambda}{L\mu}}{1 - \frac{\lambda}{L\mu}} \right\} \\ &= \left( A(M - L) - \frac{\frac{\lambda}{L\mu}}{1 - \frac{\lambda}{L\mu}} \right) - 4B(M - L) \frac{\beta_{low}}{\rho} a^2 \\ &= \left( A(M - L) + 1 - \frac{1}{2a} \right) - 4B(M - L) \frac{\beta_{low}}{\rho} a^2. \end{aligned} \quad (64)$$

We rearrange the discriminant of the equation  $D = b^2 - 4ac$  as

$$\begin{aligned} D &= \left[ \left( A(M - L) - \frac{1}{2} \right) \left( 1 - \frac{\lambda}{L\mu} \right) \right]^2 \\ &+ 16B(M - L) \frac{\beta_{low}}{\rho} a^3 \\ &- 2 \left( 1 - \frac{\lambda}{L\mu} \right) \left[ \left( A(M - L) - \frac{1}{2} \right) + \left( \frac{1}{2} - \frac{\frac{\lambda}{L\mu}}{1 - \frac{\lambda}{L\mu}} \right) \right] \\ &= \left[ \left( A(M - L) - \frac{1}{2} \right) \left( 1 - \frac{\lambda}{L\mu} \right) - 1 \right]^2 - 1 \\ &- 2 \left( 1 - \frac{\lambda}{L\mu} \right) \left( \frac{1}{2} - \frac{\frac{\lambda}{L\mu}}{1 - \frac{\lambda}{L\mu}} \right) + 16B(M - L) \frac{\beta_{low}}{\rho} a^3 \\ &= \left[ \left( A(M - L) - \frac{1}{2} \right) \left( 1 - \frac{\lambda}{L\mu} \right) - 1 \right]^2 \\ &- \left[ 3 \left( 1 - \frac{\lambda}{L\mu} \right) - 1 \right] + 16B(M - L) \frac{\beta_{low}}{\rho} a^3 \\ &= (b - 1)^2 - \left( -16B(M - L) \frac{\beta_{low}}{\rho} a^3 + 6a - 1 \right). \end{aligned}$$

We introduce the notation

$$E = \left( -16B(M - L) \frac{\beta_{low}}{\rho} a^3 + 6a - 1 \right). \quad (65)$$

With this notation we have

$$D = (b - 1)^2 - E. \tag{66}$$

If  $E < 0$  then  $D > 0$ .

Otherwise, i.e., for  $E \geq 0$ , ensuring  $D > 0$  gives

$$(b - 1)^2 > E.$$

If  $(b - 1) \geq 0$  then it leads to

$$\begin{aligned} b - 1 &> \sqrt{E} \Leftrightarrow \\ \left(2A(M - L) - 1\right)a &> 1 + \sqrt{E} \Leftrightarrow \\ A(M - L) &> \frac{1}{2} + \frac{1 + \sqrt{E}}{2a}. \end{aligned}$$

In the other case of  $(b - 1) < 0$  we get

$$\begin{aligned} 1 - b &> \sqrt{E} \Leftrightarrow \\ \left(2A(M - L) - 1\right)a &< 1 - \sqrt{E} \Leftrightarrow \\ A(M - L) &< \frac{1}{2} + \frac{1 - \sqrt{E}}{2a}. \end{aligned}$$

Summarizing the necessary and sufficient condition for  $D > 0$  can be given by

$$\left\{ \begin{array}{l} - \text{ if } E < 0, \\ \left[ A(M - L) > \frac{1}{2} + \frac{1 + \sqrt{E}}{2a} \text{ or } \right. \\ \left. A(M - L) < \frac{1}{2} + \frac{1 - \sqrt{E}}{2a} \right] \text{ if } E \geq 0 \end{array} \right\}, \tag{67}$$

where  $E$  is defined in (65).

4) *Conditions for nonnegative upper root:* The roots of the quadratic equation  $q(\rho, N) = (ax^2 - bx + c) = 0$  are given by

$$x_{1,2} = \frac{b \pm \sqrt{b^2 - 4ac}}{2a}.$$

Assuming  $D > 0$  the quadratic equation has two roots. The upper root  $x_h$  can be nonnegative in two cases.

*Case 1.* The condition  $b < 0$  holds.

In this case a second condition  $D \geq b^2$  is also required to have nonnegative upper root. It also ensures  $D \geq 0$ .

Due to  $(1 - \frac{\lambda}{L\mu}) > 0$  the condition  $b < 0$  yields

$$A(M - L) < \frac{1}{2}.$$

The second condition is equivalent to  $4ac \leq 0$ , and due to  $a > 0$  leads to  $c \leq 0$ , which results in the condition

$$\begin{aligned} \left(A(M - L) + 1 - \frac{1}{2a}\right) &\leq 4B(M - L) \frac{\beta_{low}}{\rho} a^2 \Leftrightarrow \\ B(M - L) &\geq \frac{\rho}{\beta_{low}} \frac{1}{4a^2} \left(A(M - L) + 1 - \frac{1}{2a}\right). \end{aligned}$$

Hence, the condition for ensuring both  $b < 0$  and  $D \geq b^2$  can be summarized as

$$\left\{ \begin{array}{l} A(M - L) < \frac{1}{2} \text{ and} \\ B(M - L) \geq \frac{\rho}{\beta_{low}} \frac{1}{4a^2} \left(A(M - L) + 1 - \frac{1}{2a}\right) \end{array} \right\}. \tag{68}$$

Note that in this case the lower root is always negative and hence the local minimum at  $N_h$  or in the "almost constant cost range" is also a global one.

*Case 2.* The condition  $b \geq 0$  holds.

In this case  $x_h = b + \sqrt{D} > 0$  holds always due to  $D > 0$ . Thus no additional condition is necessary. The condition  $b \geq 0$  leads to

$$A(M - L) \geq \frac{1}{2}.$$

The conditions both for  $b \geq 0$  and  $D > 0$  for this case can be summarized as

$$\left\{ \begin{array}{l} A(M - L) \geq \frac{1}{2} \text{ if } E < 0, \\ \left[ A(M - L) > \frac{1}{2} + \frac{1 + \sqrt{E}}{2a} \text{ or } \right. \\ \left. \left( A(M - L) \geq \frac{1}{2} \text{ and } A(M - L) < \frac{1}{2} + \frac{1 - \sqrt{E}}{2a} \right) \right] \text{ if } E \geq 0 \end{array} \right\}, \tag{69}$$

where  $E$  is defined in (65).

5) *The effect of the lower root on the global minimum:*

Herein we investigate the magnitude of the lower root for the case  $b \geq 0$  and  $D > 0$ . First, we provide a lower limit for  $D$  by applying  $D > 0$  in (66). If  $E < 0$  then  $D = (b - 1)^2 - E > (b - 1)^2$ . Otherwise  $E \geq 0$  and we can establish a lower limit

$$\begin{aligned} D &= (b - 1)^2 - E = (b - 1)^2 - (\sqrt{E})^2 \\ &= (b - 1 - \sqrt{E})(b - 1 + \sqrt{E}) \\ &\geq \left( \min(|(b - 1 - \sqrt{E})|, |(b - 1 + \sqrt{E})|) \right)^2. \end{aligned}$$

Hence, the lower limit for  $D > 0$  can be summarized as

$$D \geq \left\{ \begin{array}{l} (b - 1)^2, \text{ if } E < 0, \\ (b - 1 - \sqrt{E})^2, \text{ if } b \geq 1 \text{ and } E \geq 0, \\ (b - 1 + \sqrt{E})^2, \text{ if } 0 < b < 1 \text{ and } E \geq 0 \end{array} \right\}.$$

Based on it, we can give an upper limit for  $x_l$  for the case  $b \geq 0$  and  $D > 0$  as

$$\begin{aligned} x_l &= \frac{b - \sqrt{D}}{2a} \\ &\leq \left\{ \begin{array}{l} \frac{b - |b - 1|}{2a} = \frac{1}{2a}, \text{ if } E < 0 \text{ and } b \geq 1, \\ \frac{b - |b - 1|}{2a} = \frac{2b - 1}{2a}, \text{ if } E < 0 \text{ and } 0 < b < 1, \\ \frac{b - (b - 1 - \sqrt{E})}{2a} = \frac{1 + \sqrt{E}}{2a}, \text{ if } E \geq 0 \text{ and } b \geq 1, \\ \frac{b - (1 - b - \sqrt{E})}{2a} = \frac{2b - 1 + \sqrt{E}}{2a}, \text{ if } E \geq 0 \text{ and } 0 < b < 1 \end{array} \right\}. \end{aligned}$$

Assuming  $\frac{\lambda}{L\mu} \leq \psi$  with  $\psi = 0.8$ , we have  $\frac{1}{2a} < \frac{1}{(1 - 0.8)} = 5$ . Moreover  $E \leq 6a - 1 \leq 2$  and thus  $\sqrt{E} < \sqrt{2} < 1.5$ . Thus

for the first and third cases we have  $x_l \leq \frac{1}{2a} \leq \frac{1+\sqrt{E}}{2a} < 5 * 2.5 = 12.5$ . In the second and fourth cases  $x_l \leq \frac{2b-1+\sqrt{E}}{2a} \leq \frac{1+\sqrt{E}}{2a} < 12.5$ , since  $b < 1$ . Therefore,  $x_l$  is low in all the four cases comparing to the range of  $N$ , and thus the chance of having lower cost at  $N = L + 1$  than the local minimum at  $N_h$  or in the "almost constant cost range" can be neglected. It follows that the local minimum can be considered as a global one.

#### D. Approximate solution formula

Now taking into account the necessary limitations and arguments we get the approximate solution formula.

##### Conditions

- 1)  $100 \leq M$ ,
- 2)  $0.1 \leq \beta_{low} \leq 0.5$  with  $\beta_{low} = \frac{L}{M}$ ,
- 3)  $\rho \leq \beta_{low}\psi$  with  $\psi = 0.8$ ,
- 4)  $N - L \gg 1$ , practically  $N > L + 10$ ,
- 5)  $K - M \gg 1$ , practically  $K > M + 10$ ,

##### Solution formula

If Conditions 1-5 hold, then

- If

$$\begin{aligned} & \text{either} \\ & \left[ A(M-L) < \frac{1}{2} \text{ and} \right. \\ & \left. B(M-L) \geq \frac{\rho}{\beta_{low}} \frac{1}{4a^2} \left( A(M-L) + 1 - \frac{1}{2a} \right) \right] \\ & \text{or} \\ & \left\{ \begin{array}{l} A(M-L) \geq \frac{1}{2} \\ A(M-L) > \frac{1}{2} + \frac{1+\sqrt{E}}{2a} \\ \left( A(M-L) \geq \frac{1}{2} \text{ and } A(M-L) < \frac{1}{2} + \frac{1+\sqrt{E}}{2a} \right) \end{array} \right. \begin{array}{l} \text{if } E < 0, \\ \\ \text{if } E \geq 0 \end{array} \end{aligned}$$

holds then

$$N_{opt} = \left\{ \begin{array}{ll} N_h & \text{if } N_h < N_{uccl} \\ \text{any } N \in [N_{uccl}, M] & \text{if } N_{uccl} \leq N_h \end{array} \right\},$$

where

$$N_{uccl} = \lfloor \frac{\ln(\frac{\epsilon}{q_{ul}})}{\ln(\frac{\lambda}{L\mu})} + L + 1 \rfloor \text{ with } \epsilon < q_{ul},$$

$$N_h = \lfloor \frac{b + \sqrt{b^2 - 4ac}}{2a} + L + 1 \rfloor, \quad (70)$$

and  $q_{ul}$ ,  $a$ ,  $b$ ,  $c$  and  $E$  is given in (63), (64) and (65), respectively.

- Otherwise

$$N_{opt} = L + 1.$$

The approximate optimal  $N$  does not depend on  $C_R$  also in this traffic range. The cost parameter  $C_R$  has impact on the optimal  $N$  via  $\eta$  and hence it is effective only for small values of  $K - M$ .

## VIII. NUMERICAL COMPARISONS

In this section, we illustrate the approximations and validate the approximate solution formula by numeric optimization.

#### A. High traffic range - $\frac{\lambda}{L\mu} > 1$

The setting  $C_{on} = 50$ ,  $C_{off} = 15$ ,  $C_a = 30$ ,  $C_d = 20$  and  $C_R = 20$  was used for all experiments. The parameters  $C_a$ ,  $C_d$  and  $C_R$  have no impact on the approximate solution formula in the considered range of parameters.

#### B. Illustration of the approximate solution formula

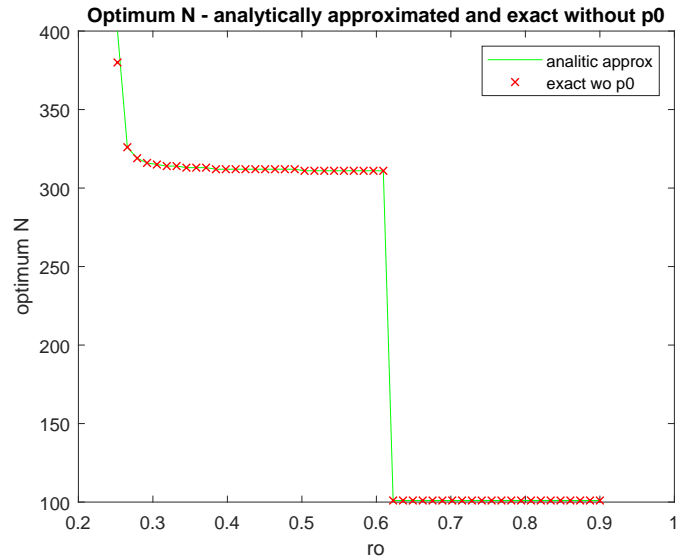


Figure 16. Exact and approximate optimal  $N$  ( $F_2$ ) in dependency of  $\rho$ .

The comparison of the exact and approximate optimal  $N$  of  $F_2$  can be seen in Figure 16 in dependency of  $\rho$  for the parameter setting  $M = 400$ ,  $L = 100$ ,  $K = 450$ ,  $C_W = 50$ ,  $\mu = 1$  and  $\rho > 0.25 = \frac{L}{M}$ .

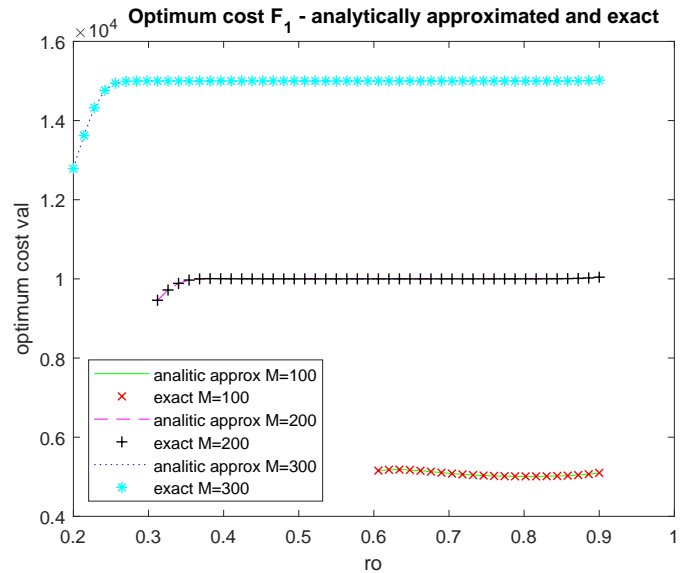


Figure 17. Exact and approximate optimal value ( $F_1$ ) in dependency of  $\rho$  for different values of  $M$ .

Figure 17 shows the exact and approximate optimal value of  $F_1$  in dependency of  $\rho$  for different values of  $M$  with the parameter setting  $L = 50, K = M + 100, C_W = 50, \mu = 1$  and  $\rho > 0.25 = \frac{L}{M}$ .

Both figures show a very good match.

C. Validation of the approximate formula

We validated the approximate solution formula by numeric optimization in the considered range of parameters. Figure 18 shows the ratio of the approximated and the exact optimal value of  $F_1$  for the range of parameters  $100 \leq M \leq 700$  and  $\rho > \frac{L}{M}$  with the parameter setting  $L = 50, K = M + 100, C_W = 50, \mu = 1$ .

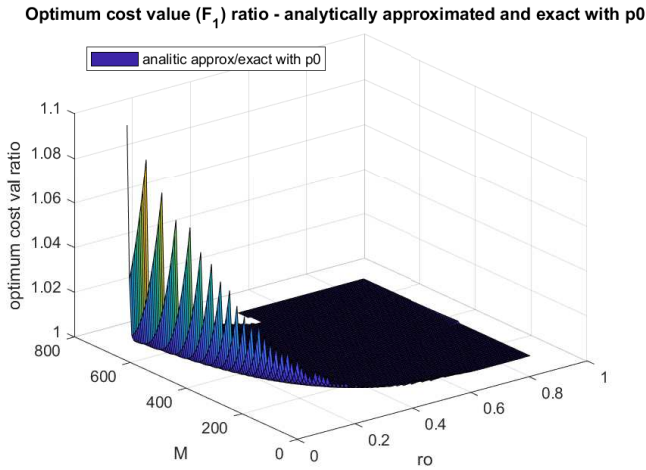


Figure 18. Ratio of the approximated and exact optimal value ( $F_1$ ) for  $100 \leq M \leq 700$  and  $\frac{L}{M} < \rho$ .

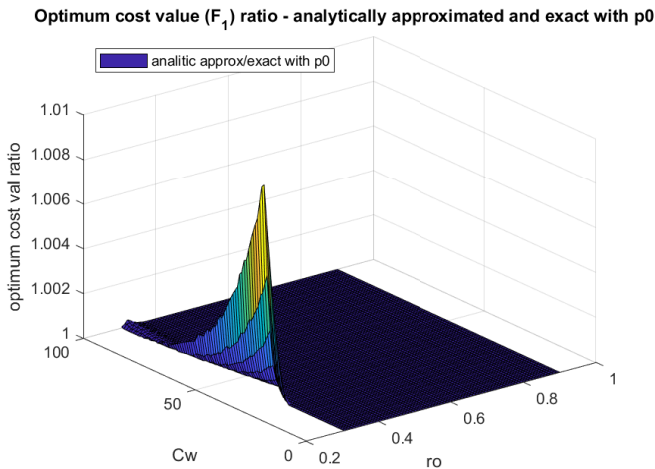


Figure 19. Ratio of the approximated and exact optimal value ( $F_1$ ) for  $0.1 \leq C_W \leq 100$  and  $\frac{L}{M} = 0.25 < \rho$ .

Similarly, Figure 19 shows the ratio of the approximated and the exact optimal value of  $F_1$  for the range of parameters

$0.1 \leq C_W \leq 100$  and  $\rho > 0.25 = \frac{L}{M}$  with the parameter setting  $L = 50, M = 200, K = 300, \mu = 1$ .

Both figures show a very good match until approaching the  $\rho$  boundary  $\frac{L}{M}$ , where the condition 3, does not hold any more.

D. Low traffic range -  $\frac{\lambda}{L\mu} < 1$

We used two basic parameter settings and their variations for all experiments. One of them is  $M = 100, L = 50, K = M + 50, \mu = 1, C_W = 50, C_{off} = 15, C_{on} = 50, C_a = 30, C_d = 20$ , which represents a typical cost function curve of Type 1. The other one is  $M = 200, L = 100, K = M + 50, \mu = 1, C_W = 10, C_{off} = 0.01, C_{on} = 0.02, C_a = 0.03, C_d = 0.02$  and it belongs to cost function curves of Type 2. Although the parameter  $C_R$  was set to 200 in both cases, it has no impact on the approximate solution formula in the considered range of parameters due to condition 5.

E. Illustration of the approximate solution formula

First, we illustrate the approximate solution formula for typical cost function curve of Type 2 (see Figure 15) under the parameter setting  $M = 200, L = 100, K = M + 50, \mu = 1, C_W = 10, C_{off} = 0.01, C_{on} = 0.02, C_a = 0.03, C_d = 0.02, C_R = 200$ , while  $\rho$  is varied in the low traffic range. Figure 20 shows the approximate optimal  $N$  and the upper limit on the lower boundary of the "almost constant cost range",  $N_{uccl}$ , both as a function of  $\rho$ .

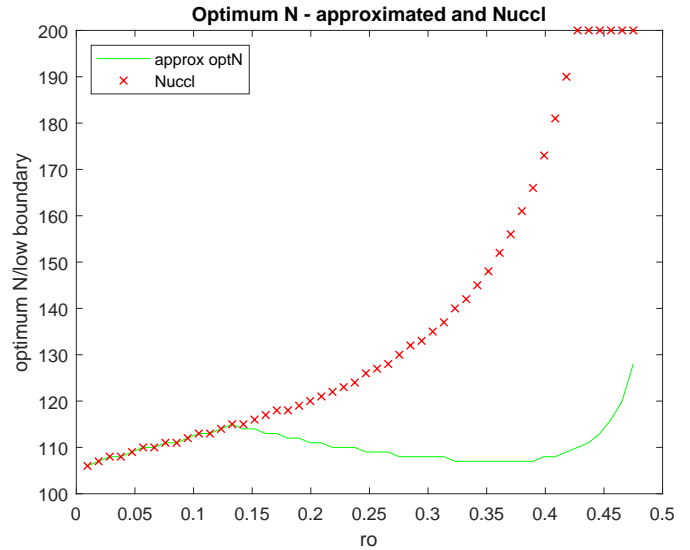


Figure 20. Approximate optimal  $N$  and  $N_{uccl}$  in dependency of  $\rho$  - Type 2 cost function.

It can be seen on the figure that higher the  $\rho$ , higher the upper limit on the lower boundary of the "almost constant cost range". Additionally it can be also observed on the figure that there exists a global optimum point above some  $\rho$ , for cost function curves of Type 2, which is also expected from the form of the cost curve.

Figure 21 shows the exact and approximate optimal  $N$  in dependency of  $\rho$ , while keeping the above parameter setting for the cost function curve of Type 2.

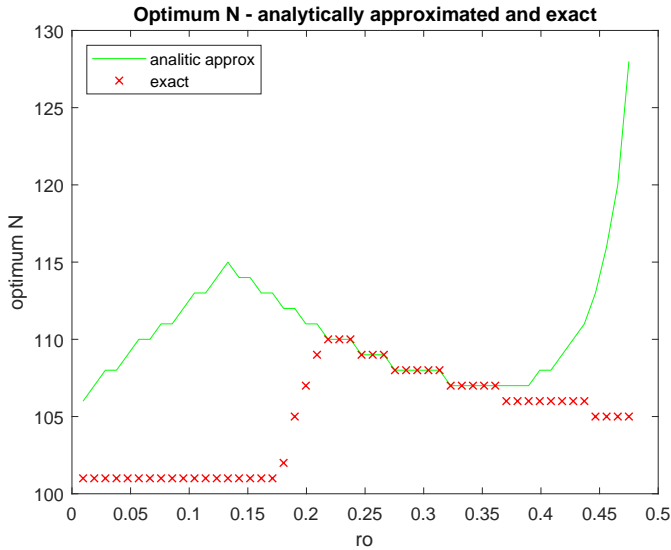


Figure 21. Exact and approximate optimal  $N$  in dependency of  $\rho$  - Type 2 cost function.

If the approximate optimal  $N$  equals to  $N_{uccl}$  then the whole "almost constant cost range" is a range of optimal  $N$ -s, for which the value of the cost function is approximately the same, i.e., it changes only in a negligible magnitude. Note that this range can fall also below  $N_{uccl}$ , since  $N_{uccl}$  is only an upper limit on the lower boundary of the "almost constant cost range". This explains the mismatch between the exact optimal  $N$  and the approximate one, which is set simple to  $N_{uccl}$ , in the traffic range  $\rho \lesssim 0.15$ . In fact the lower boundary of the "almost constant cost range" can be below its upper limit,  $N_{uccl}$ , also for the values of  $\rho$  somewhat above 0.15, which explains that the mismatch continues up to  $\approx 0.21$ .

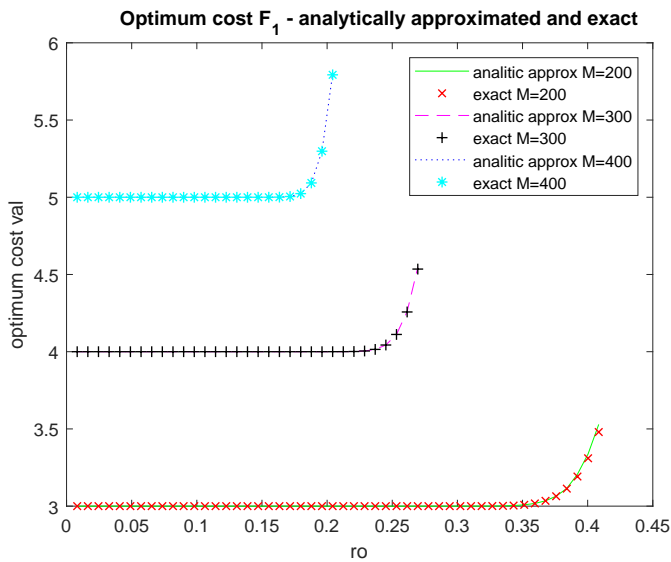


Figure 22. Exact and approximate optimal value ( $F_1$ ) in dependency of  $\rho$  for different values of  $M$ .

However this mismatch does not have any significance,

since the value of the cost function is approximately the same in the whole range of optimal  $N$ -s. It follows that the approximate optimal  $N$  for the traffic range  $\rho \lesssim 0.21$  is irrelevant and the exact and approximate optimal value of  $F_1$  show a good match, as it can be seen on the lowest curve (with  $M = 200$ ) in Figure 22. In the next traffic range  $\rho > 0.21$  the exact and approximate optimal  $N$  show a good match until approaching  $\rho = 0.4$ . Above that point the condition 3. does not hold any more, which causes a mismatch between the exact and approximate values not only in optimal  $N$  but also in optimal value. Therefore, we focus on the traffic range  $\rho \leq \frac{L}{M}\psi$  with  $\psi = 0.8$ .

Figure 22 compares the exact and approximate optimal value of the cost function in dependency of  $\rho$  for different values of  $M$  with the above parameter setting and  $\rho \leq \frac{L}{M}\psi$ . The figure shows a good match for all three values of  $M$ .

Next we illustrate the approximate solution formula for typical cost function curves of Type 1 (see Figure 14) under the parameter setting  $M = 100, L = 50, K = M + 50, \mu = 1, C_W = 50, C_{off} = 15, C_{on} = 50, C_a = 30, C_d = 20, C_R = 200$ , while  $\rho$  is varied in the low traffic range.

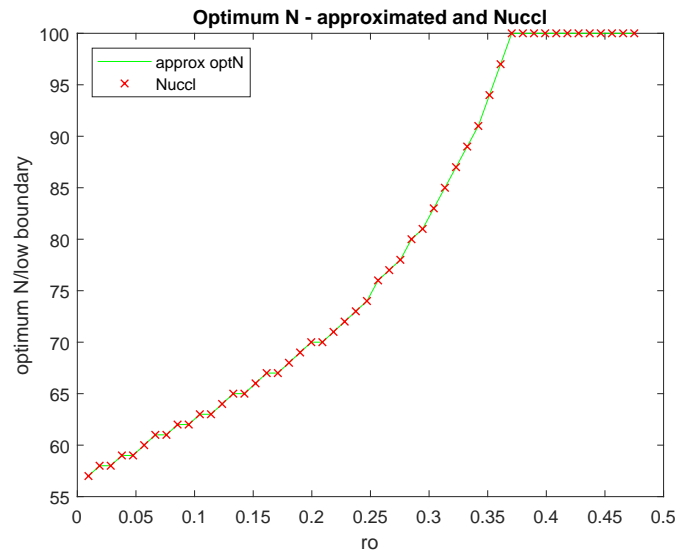


Figure 23. Approximate optimal  $N$  and  $N_{uccl}$  in dependency of  $\rho$  - Type 1 cost function.

Figure 23 plots the approximate optimal  $N$  and  $N_{uccl}$  as a dependency of  $\rho$ . The figure shows that there exists a range of optimal  $N$ -s for cost function curves of Type 1 with any value of  $\rho$ , which is expected again from the form of the cost curve. In this case the approximate optimal  $N$  is irrelevant since any value in the range of optimal  $N$ -s can be considered as optimal  $N$ . Therefore, we focus on the approximate optimal value.

The exact and approximate optimal value of the cost function in dependency of  $\rho$  are plotted on Figure 24 for different values of  $C_w$ , with the above parameter setting and  $\rho \leq \frac{L}{M}\psi$ . The figure shows again a good match.

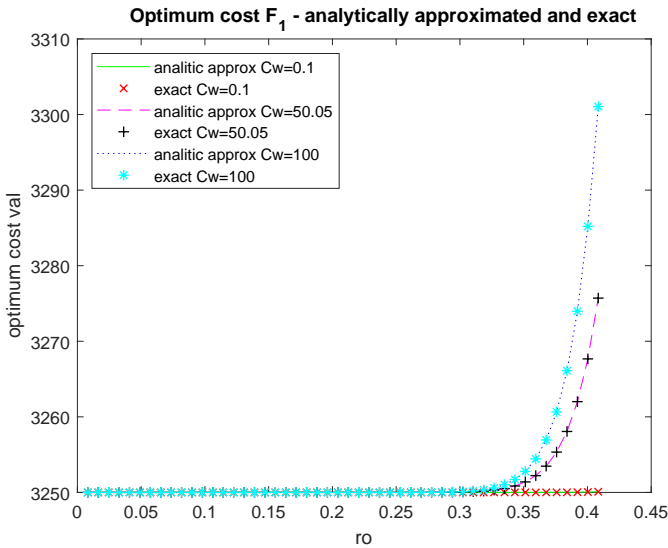


Figure 24. Exact and approximate optimal value ( $F_1$ ) in dependency of  $\rho$  for different values of  $C_W$ .

**F. Validation of the approximate formula**

We validated the approximate solution formula for the traffic range  $\frac{\lambda}{L\mu} < 1$  again by numeric optimization in the considered range of parameters.

First, we validate it by the help of the parameter set for cost function curve of Type 2,  $M = 200, L = 100, K = M + 50, \mu = 1, C_W = 10, C_{off} = 0.01, C_{on} = 0.02, C_a = 0.03, C_d = 0.02, C_R = 200$ .

Figure 25 and 26 show the ratio of the approximated and the exact optimal  $N$  and the ratio of the approximated and the exact optimal value of  $F_1$ , respectively, for the range of parameters  $200 \leq M \leq 800$  and  $\rho \leq \frac{L}{M}\psi$ .

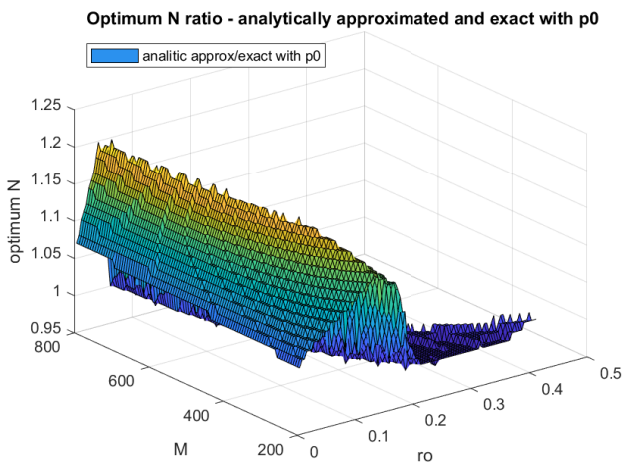


Figure 25. Ratio of the approximated and exact optimal  $N$  for  $200 \leq M \leq 800$  and  $\rho \leq \frac{L}{M}\psi$ .

It can be seen on Figure 25 that the approximated optimal  $N$  deviates from its exact value by a factor 0.95 – 1.2 for low values of  $\rho$ . This is due to the existence of range of optimal

$N$  making the approximate optimal  $N$  irrelevant as explained at Figure 21. For higher values of  $\rho$  (up to  $\rho \leq \frac{L}{M}\psi$ ) the exact and approximated optimal  $N$  show a good match.

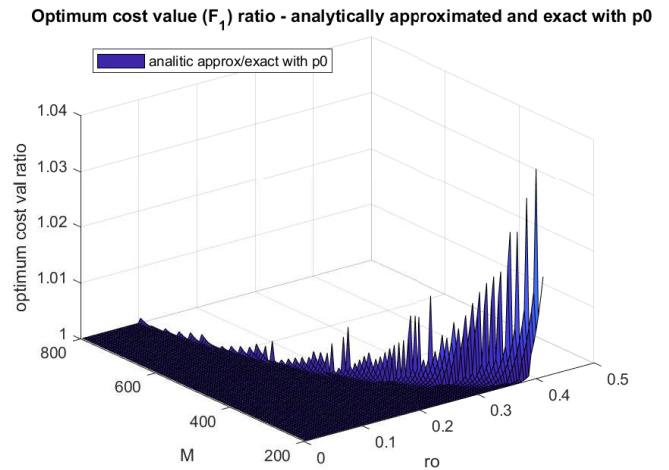


Figure 26. Ratio of the approximated and exact optimal value ( $F_1$ ) for  $200 \leq M \leq 800$  and  $\rho \leq \frac{L}{M}\psi$ .

The approximated and exact optimal value of  $F_1$  show a very good match, as it can be seen on Figure 26.

Now we validate the approximate solution formula also by the help of the parameter setting for cost function curve of Type 1,  $M = 100, L = 50, K = M + 50, \mu = 1, C_W = 50, C_{off} = 15, C_{on} = 50, C_a = 30, C_d = 20, C_R = 200$ . In this case the approximate optimal  $N$  is irrelevant for the whole range of  $\rho$  due to the existence of a range of optimal  $N$ -s and therefore we validate only the optimal value of the cost function.

Figure 27 shows the ratio of the approximated and the exact optimal value of  $F_1$  for the range of parameters  $100 \leq M \leq 700$  and  $\rho \leq \frac{L}{M}\psi$ .

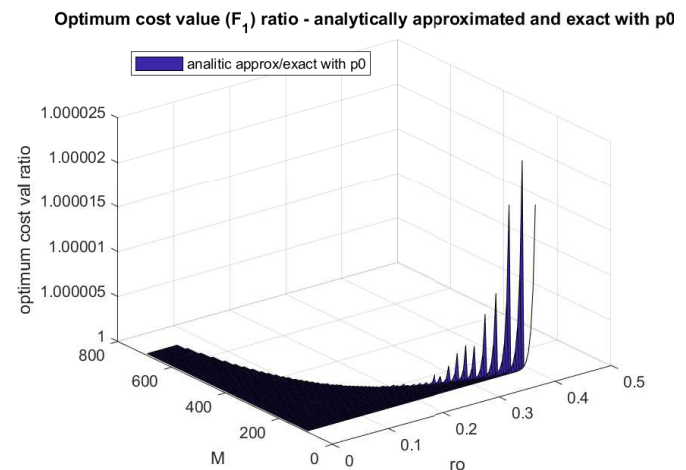


Figure 27. Ratio of the approximated and exact optimal value ( $F_1$ ) for  $100 \leq M \leq 700$  and  $\rho < \frac{L}{M}\psi$ .

The approximated and exact optimal value of the cost function  $F_1$  show a very good match. A small mismatch (like

also in Figure 26) can be observed in the parameter area of approaching the traffic boundary  $\frac{L}{M}\psi$ , above which the condition 3, does not hold any more.

Keeping the parameter setting for the cost function curve of Type 1, Figure 28 shows the ratio of the approximated and the exact optimal value of the cost function  $F_1$  for the range of parameters  $0.1 \leq C_W \leq 100$  and  $\rho \leq \frac{L}{M}\psi$ .

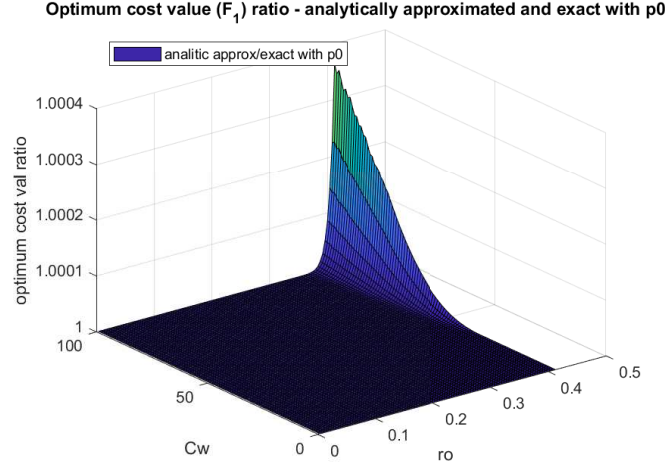


Figure 28. Ratio of the approximated and exact optimal value ( $F_1$ ) for  $0.1 \leq C_W \leq 100$  and  $\rho \leq \frac{L}{M}\psi$ .

The figure shows a very good match of the approximated and exact optimal values of cost function  $F_1$ .

## IX. CONCLUSION AND FUTURE WORK

In this paper, we continued our previous work [1]. We extended the solution to the low traffic range and generalized the approximate solution formula for the high traffic range by omitting the condition on the cost parameters. Moreover, we also provided the details of the stationary analysis and the derivations both in the former and new optimization parts. The first contribution of this research is the proposal of the shifted N-policy for a simple, but energy efficient control of number of active VMs in the IaaS Cloud. A secondary contribution is the stationary analysis of the underlying queueing model. However, the major contributions are the approximate formulas for computing the optimal threshold  $N$ , which minimizes the cloud provider's cost, in the most relevant parameter ranges. The validation of the approximate solution formulas by means of numeric optimization show good match. The closed form approximate solution formulas enable a simple management of the cloud and give an insight into the dependency of the optimal threshold  $N$  on the model and cost parameters.

A future research work is to investigate the validity of the solution formulas outside of the parameter ranges defined by the conditions of the solution formulas. A second potential research topic is to establish an approximate solution also for the traffic range around  $\frac{\lambda}{\mu} = L \Leftrightarrow \rho = \frac{L}{M}$ . Further future research topics are the optimization of  $L$  besides fixed  $N$  and the rather more difficult joint optimization of parameters  $L$  and  $N$ .

## APPENDIX I

### DERIVATION OF STATIONARY DISTRIBUTION OF THE NUMBER OF REQUESTS

1)  $p_k$  for  $k = 1, \dots, L$ : From the balance equation (1) we have

$$p_{i+1} = \frac{\lambda}{(i+1)\mu} p_i, \quad i = 0, \dots, L-1 \Leftrightarrow$$

$$p_i = \frac{\lambda}{i\mu} p_{i-1}, \quad i = 1, \dots, L.$$

Solving it recursively for  $i = 1, \dots, L$  gives

$$p_k = \frac{\left(\frac{\lambda}{\mu}\right)^k}{k!} p_0, \quad \text{for } k = 1, \dots, L.$$

2)  $p_k$  for  $k = -(N-L-1), \dots, -1$ : The balance equation (3) can be rearranged as

$$p_j = \frac{\lambda}{L\mu} (p_{j-1} - p_{-1}) \quad \text{for } j = -(N-L-2), \dots, -1.$$

Solving it recursively for  $j = -(N-L-2), \dots, -1$  we get

$$p_{-(N-L)+k} = \left(\frac{\lambda}{L\mu}\right)^{k-1} p_{-(N-L-1)} - \sum_{j=1}^{k-1} \left(\frac{\lambda}{L\mu}\right)^j p_{-1}$$

$$= \left(\frac{\lambda}{L\mu}\right)^{k-1} p_{-(N-L-1)} - \frac{\lambda}{L\mu} \frac{1 - \left(\frac{\lambda}{L\mu}\right)^{k-1}}{1 - \frac{\lambda}{L\mu}} p_{-1}$$

for  $k = 2, \dots, (N-L-1)$ .

Setting  $k = N-L-1$  gives

$$p_{-1} = \left(\frac{\lambda}{L\mu}\right)^{N-L-2} p_{-(N-L-1)} - \frac{\frac{\lambda}{L\mu} - \left(\frac{\lambda}{L\mu}\right)^{N-L-1}}{1 - \frac{\lambda}{L\mu}} p_{-1},$$

from which  $p_{-1}$  can be expressed in terms of  $p_{-(N-L-1)}$  as

$$p_{-1} = \frac{1 - \frac{\lambda}{L\mu}}{1 - \left(\frac{\lambda}{L\mu}\right)^{N-L-1}} \left(\frac{\lambda}{L\mu}\right)^{N-L-2} p_{-(N-L-1)},$$

$$= \frac{1}{\sum_{j=0}^{N-L-2} \left(\frac{\lambda}{L\mu}\right)^j} \left(\frac{\lambda}{L\mu}\right)^{N-L-2} p_{-(N-L-1)}.$$

Applying the expression of  $p_{-(N-L-1)}$  from the balance equation (2) in the above relation and rearrangement leads to

$$p_{-1} \sum_{j=0}^{N-L-2} \left(\frac{\lambda}{L\mu}\right)^j = \left(\frac{\lambda}{L\mu}\right)^{N-L-2} \frac{\lambda}{L\mu} (p_L - p_{-1}) \Leftrightarrow$$

$$p_{-1} \sum_{j=0}^{N-L-1} \left(\frac{\lambda}{L\mu}\right)^j = \left(\frac{\lambda}{L\mu}\right)^{N-L-1} p_L,$$

which results in the expression of  $p_{-1}$  as

$$\begin{aligned}
 p_{-1} &= \left(\frac{\lambda}{L\mu}\right)^{N-L-1} \frac{1 - \frac{\lambda}{L\mu}}{1 - \left(\frac{\lambda}{L\mu}\right)^{N-L}} p_L \\
 &= \left(\frac{\lambda}{L\mu}\right)^{N-L-1} \frac{1}{\sum_{j=0}^{N-L-1} \left(\frac{\lambda}{L\mu}\right)^j} p_L.
 \end{aligned}$$

Substituting it back into the expression of  $p_{-(N-L-1)}$  from the balance equation (2) leads to the expression of  $p_{-(N-L-1)}$  as

$$\begin{aligned}
 p_{-(N-L-1)} &= \frac{\lambda}{L\mu} \left(1 - \frac{\left(\frac{\lambda}{L\mu}\right)^{N-L-1}}{\sum_{j=0}^{N-L-1} \left(\frac{\lambda}{L\mu}\right)^j}\right) p_L \\
 &= \frac{\lambda}{L\mu} \frac{\sum_{j=0}^{N-L-2} \left(\frac{\lambda}{L\mu}\right)^j}{\sum_{j=0}^{N-L-1} \left(\frac{\lambda}{L\mu}\right)^j} p_L \\
 &= \frac{\lambda}{L\mu} \frac{1 - \left(\frac{\lambda}{L\mu}\right)^{N-L-1}}{1 - \left(\frac{\lambda}{L\mu}\right)^{N-L}} p_L.
 \end{aligned}$$

Now substituting the expressions of  $p_{-1}$  and  $p_{-(N-L-1)}$  back into the expression of  $p_{-(N-L)+k}$  and rearranging it leads to

$$\begin{aligned}
 p_{-(N-L)+k} &= \left(\frac{\lambda}{L\mu}\right)^{k-1} \frac{\lambda}{L\mu} \frac{1 - \left(\frac{\lambda}{L\mu}\right)^{N-L-1}}{1 - \left(\frac{\lambda}{L\mu}\right)^{N-L}} p_L \\
 &\quad - \frac{\lambda}{L\mu} \frac{1 - \left(\frac{\lambda}{L\mu}\right)^{k-1}}{1 - \frac{\lambda}{L\mu}} \left(\frac{\lambda}{L\mu}\right)^{N-L-1} \frac{1 - \frac{\lambda}{L\mu}}{1 - \left(\frac{\lambda}{L\mu}\right)^{N-L}} p_L \\
 &= \frac{\left(\frac{\lambda}{L\mu}\right)^k \left[1 - \left(\frac{\lambda}{L\mu}\right)^{N-L-1}\right] - \left(\frac{\lambda}{L\mu}\right)^{N-L} \left[1 - \left(\frac{\lambda}{L\mu}\right)^{k-1}\right]}{1 - \left(\frac{\lambda}{L\mu}\right)^{N-L}} p_L \\
 &= \frac{\left(\frac{\lambda}{L\mu}\right)^k - \left(\frac{\lambda}{L\mu}\right)^{N-L}}{1 - \left(\frac{\lambda}{L\mu}\right)^{N-L}} p_L \text{ for } k = 1, \dots, (N-L-1),
 \end{aligned}$$

where we utilized that this formula holds also for  $k = 1$ . Applying the reindexing  $-(N-L)+k \Rightarrow k$ , we get

$$\begin{aligned}
 p_k &= \left(\frac{\lambda}{L\mu}\right)^{N-L} \frac{\left(\frac{\lambda}{L\mu}\right)^k - 1}{1 - \left(\frac{\lambda}{L\mu}\right)^{N-L}} p_L \\
 &\text{for } k = -(N-L-1), \dots, -1.
 \end{aligned}$$

3)  $p_k$  for  $k = L+1, \dots, N$ : The balance equation (5) can be rearranged as

$$\begin{aligned}
 p_{k+1} &= \frac{\lambda}{(k+1)\mu} p_k + \frac{\lambda}{(k+1)\mu} p_{-1}, k = L+1, \dots, N-1 \Leftrightarrow \\
 p_k &= \frac{\lambda}{k\mu} p_{k-1} + \frac{\lambda}{k\mu} p_{-1}, k = L+2, \dots, N.
 \end{aligned}$$

Solving it recursively for  $k = L+2, \dots, N$  we get

$$\begin{aligned}
 p_k &= \prod_{i=L+2}^k \frac{\lambda}{i\mu} p_{L+1} + \sum_{i=L+2}^k \prod_{\ell=i}^k \frac{\lambda}{\ell\mu} p_{-1} \\
 &= \frac{(L+1)!}{k!} \left(\frac{\lambda}{\mu}\right)^{k-(L+1)} p_{L+1} + \sum_{i=L+2}^k \frac{(i-1)!}{k!} \left(\frac{\lambda}{\mu}\right)^{k-i+1} p_{-1}, \\
 &\quad k = L+2, \dots, N.
 \end{aligned}$$

Using the expression of  $p_{L+1}$  from balance equation (4) and rearrangement gives

$$\begin{aligned}
 p_k &= \frac{(L+1)!}{k!} \left(\frac{\lambda}{\mu}\right)^{k-(L+1)} \frac{\lambda}{(L+1)\mu} p_{-1} \\
 &\quad + \sum_{i=L+2}^k \frac{(i-1)!}{k!} \left(\frac{\lambda}{\mu}\right)^{k-i+1} p_{-1} \\
 &= \left[ \frac{L!}{k!} \left(\frac{\lambda}{\mu}\right)^{k-L} + \sum_{i=L+2}^k \frac{(i-1)!}{k!} \left(\frac{\lambda}{\mu}\right)^{k-i+1} \right] p_{-1} \\
 &= \sum_{i=L+1}^k \frac{(i-1)!}{k!} \left(\frac{\lambda}{\mu}\right)^{k-(i-1)} p_{-1} \\
 &= \sum_{i=L}^{k-1} \frac{i!}{k!} \left(\frac{\lambda}{\mu}\right)^{k-i} p_{-1}, k = L+1, \dots, N,
 \end{aligned}$$

where we utilized that this formula holds also for  $k = L+1$  due to balance equation (4).

4)  $p_k$  for  $k = N+1, \dots, M$ : From the balance equation (6) we have

$$\begin{aligned}
 p_{r+1} &= \frac{\lambda}{(r+1)\mu} p_r, r = N, \dots, M-1 \Leftrightarrow \\
 p_r &= \frac{\lambda}{r\mu} p_{r-1}, r = N+1, \dots, M.
 \end{aligned}$$

Solving it recursively for  $r = N+1, \dots, M$  gives

$$p_k = \frac{N!}{k!} \left(\frac{\lambda}{\mu}\right)^{k-N} p_N, \text{ for } k = N+1, \dots, M.$$

5)  $p_k$  for  $k = M+1, \dots, K$ : From the balance equation (7) we have

$$\begin{aligned}
 p_{t+1} &= \frac{\lambda}{M\mu} p_t, t = M, \dots, K-1 \Leftrightarrow \\
 p_t &= \frac{\lambda}{M\mu} p_{t-1}, t = M+1, \dots, K.
 \end{aligned}$$

Solving it recursively for  $t = M+1, \dots, K$  gives

$$p_k = \left(\frac{\lambda}{M\mu}\right)^{k-M} p_M, \text{ for } k = M+1, \dots, K.$$

APPENDIX II  
DERIVATION OF  $E[W]$

The expected waiting time of the requests is defined by

$$E[W] = \sum_{k=1}^{N-L-1} k p_{-(N-L)+k} + \sum_{k=M+1}^K (k-M)p_k.$$

The first term of  $E[W]$  can be rearranged as

$$\begin{aligned} \sum_{k=1}^{N-L-1} k p_{-(N-L)+k} &= \sum_{k=1}^{N-L-1} k \frac{\left(\frac{\lambda}{L\mu}\right)^k - \left(\frac{\lambda}{L\mu}\right)^{N-L}}{1 - \left(\frac{\lambda}{L\mu}\right)^{N-L}} p_L \\ &= \frac{1}{1 - \left(\frac{\lambda}{L\mu}\right)^{N-L}} \left[ \frac{\lambda}{L\mu} \frac{1 - \left(\frac{\lambda}{L\mu}\right)^{N-L}}{\left(1 - \frac{\lambda}{L\mu}\right)^2} - (N-L) \frac{\left(\frac{\lambda}{L\mu}\right)^{N-L}}{1 - \frac{\lambda}{L\mu}} \right. \\ &\quad \left. - \frac{(N-L)(N-L-1)}{2} \left(\frac{\lambda}{L\mu}\right)^{N-L} \right] p_L = \left\{ \frac{\frac{\lambda}{L\mu}}{\left(1 - \frac{\lambda}{L\mu}\right)^2} \right. \\ &\quad \left. - (N-L) \frac{\left(\frac{\lambda}{L\mu}\right)^{N-L}}{1 - \left(\frac{\lambda}{L\mu}\right)^{N-L}} \left[ \frac{1}{1 - \frac{\lambda}{L\mu}} + \frac{N-L-1}{2} \right] \right\} p_L, \end{aligned}$$

where we used the formula

$$\sum_{k=1}^n k q^k = q \frac{1 - q^{n+1}}{(1 - q)^2} - (n+1) \frac{q^{n+1}}{1 - q}.$$

The second term of  $E[W]$  can be rearranged as

$$\begin{aligned} \sum_{k=M+1}^K (k-M)p_k &= \sum_{k=M+1}^{K-M} (k-M) \left(\frac{\lambda}{M\mu}\right)^{k-M} p_M \\ &= \sum_{i=0}^{K-M} ((i+1) - 1) \left(\frac{\lambda}{M\mu}\right)^i p_M \\ &= \left[ \frac{d \left( \sum_{i=0}^{K-M} \left(\frac{\lambda}{M\mu}\right)^{i+1} \right)}{d \left( \frac{\lambda}{M\mu} \right)} - \sum_{i=0}^{K-M} \left(\frac{\lambda}{M\mu}\right)^i \right] p_M \\ &= \left[ \frac{d \left( \frac{\frac{\lambda}{M\mu} - \left(\frac{\lambda}{M\mu}\right)^{K-M+2}}{1 - \frac{\lambda}{M\mu}} \right)}{d \left( \frac{\lambda}{M\mu} \right)} - \frac{1 - \left(\frac{\lambda}{M\mu}\right)^{K-M+1}}{1 - \frac{\lambda}{M\mu}} \right] p_M \\ &= \left[ \frac{\left(1 - (K-M+2)\left(\frac{\lambda}{M\mu}\right)^{K-M+1}\right) \left(1 - \frac{\lambda}{M\mu}\right)}{\left(1 - \frac{\lambda}{M\mu}\right)^2} \right. \\ &\quad \left. + \frac{\lambda}{M\mu} \frac{\left(1 - \left(\frac{\lambda}{M\mu}\right)^{K-M+1}\right)}{\left(1 - \frac{\lambda}{M\mu}\right)^2} \right. \\ &\quad \left. - \frac{1 - \frac{\lambda}{M\mu} - \left(1 - \frac{\lambda}{M\mu}\right) \left(\frac{\lambda}{M\mu}\right)^{K-M+1}}{\left(1 - \frac{\lambda}{M\mu}\right)^2} \right] p_M \\ &= \left[ \frac{\lambda}{M\mu} \frac{\left(1 - \left(\frac{\lambda}{M\mu}\right)^{K-M+1}\right)}{\left(1 - \frac{\lambda}{M\mu}\right)^2} - (K-M+1) \frac{\left(\frac{\lambda}{M\mu}\right)^{K-M+1}}{1 - \frac{\lambda}{M\mu}} \right] p_M. \end{aligned}$$

Putting all these together as well as using  $\tau$  and  $\sigma$  defined in (10), we get the final expression of  $E[W]$  as

$$E[W] = \tau p_L + \sigma p_M.$$

APPENDIX III  
AUXILIARY RELATIONS

A. Upper limit for  $\sum_{k=0}^L \frac{q^k}{k!}$

Statement:

$$\sum_{k=0}^L \frac{q^k}{k!} \leq \frac{1}{1 - \frac{L}{q}} \frac{q^L}{L!} \text{ for } L \in \mathbb{N}, 0 < q \text{ and } L < q.$$

The statement can be shown as

$$\begin{aligned} \sum_{k=0}^L \frac{q^k}{k!} &= \frac{q^L}{L!} \sum_{k=0}^L \frac{q^k L!}{k! q^L} \\ &= \frac{q^L}{L!} \left( 1 + \frac{L}{q} + \frac{L(L-1)}{q^2} + \dots + \frac{L \dots 1}{q^L} \right) \\ &\leq \frac{q^L}{L!} \left( 1 + \frac{L}{q} + \frac{L L}{q^2} + \dots + \frac{L \dots L}{q^L} \right) \\ &= \frac{q^L}{L!} \sum_{k=0}^L \left(\frac{L}{q}\right)^k = \frac{q^L}{L!} \frac{1 - \left(\frac{L}{q}\right)^{L+1}}{1 - \frac{L}{q}} \leq \frac{1}{1 - \frac{L}{q}} \frac{q^L}{L!}, \end{aligned}$$

where in the last step we utilized  $0 \leq \frac{L}{q} < 1$  and  $0 < L + 1$ .

B. Formula for  $\sum_{k=A+1}^B \frac{q^k A!}{k! q^A}$

Statement: The following formula holds for  $\sum_{k=A+1}^B \frac{q^k A!}{k! q^A}$  for  $A, B \in \mathbb{N}, A < B, 0 < q$  as well as  $q \neq A + 1$  and  $q \neq B$

$$\sum_{k=A+1}^B \frac{q^k A!}{k! q^A} = f_1 \frac{1 - f_1^{B-A}}{1 - f_1},$$

where  $f_1 = \frac{q}{f_0}$  and  $A + 1 \leq f_0 \leq B$ .

The sum in the statement can be rearranged as

$$\begin{aligned} \sum_{k=A+1}^B \frac{q^k A!}{k! q^A} &= \left( \frac{q}{A+1} + \frac{q^2}{(A+1)(A+2)} + \dots + \frac{q^{B-A}}{(A+1) \dots B} \right). \end{aligned}$$

If all terms in the denominators are replaced by  $A + 1$  then we get an upper limit as

$$\begin{aligned} \sum_{k=A+1}^B \frac{q^k A!}{k! q^A} &\leq \left( \frac{q}{A+1} + \frac{q^2}{(A+1)(A+1)} + \dots + \frac{q^{B-A}}{(A+1) \dots (A+1)} \right) \\ &= \sum_{i=1}^{B-A} \left(\frac{q}{A+1}\right)^i = \frac{q}{A+1} \frac{1 - \left(\frac{q}{A+1}\right)^{B-A}}{1 - \frac{q}{A+1}}. \end{aligned}$$

Similarly, replacing all terms in the denominator by  $B$ , we get a lower limit as

$$\begin{aligned} \sum_{k=A+1}^B \frac{q^k A!}{k! q^A} &\geq \left( \frac{q}{B} + \frac{q^2}{B B} + \dots + \frac{q^{B-A}}{B \dots B} \right) \\ &= \sum_{i=1}^{B-A} \left(\frac{q}{B}\right)^i = \frac{q}{B} \frac{1 - \left(\frac{q}{B}\right)^{B-A}}{1 - \frac{q}{B}}. \end{aligned}$$

It follows from the development of the function  $x^{\frac{1-(x)^{B-A}}{1-x}}$  in the range  $\frac{q}{B} \leq x \leq \frac{q}{A+1}$  that there exists an  $f_1 = \frac{q}{f_0}$  with  $A + 1 \leq f_0 \leq B$ , for which

$$\sum_{k=A+1}^B \frac{q^k A!}{k! q^A} = f_1 \frac{1 - f_1^{B-A}}{1 - f_1}$$

holds.

Note that keeping  $B$  (or  $A$ ) constant a higher  $A$  (or  $B$ ) implies higher  $f_0$  and thus lower  $f_1$ .

C. Upper limit for  $q$  at  $f_1$ , in the formula for  $\sum_{k=A+1}^B \frac{q^k A!}{k! q^A}$ , close to 1

Statement: An upper limit for  $q$ , for which  $f_1$  in the formula in III-B has a value close to 1, can be given as

$$q < Ae^{\frac{5.5}{A}}$$

where  $A \in \mathbb{N}$ ,  $0 < A$ ,  $0 < q$  as well as  $q \neq A + 1$ .

The sum  $\sum_{k=A+1}^B \frac{q^k A!}{k! q^A}$  can be rearranged as

$$\sum_{k=A+1}^B \frac{q^k A!}{k! q^A} = \frac{q}{A(1 + \frac{1}{A})} + \frac{q^2}{A^2(1 + \frac{1}{A})(1 + \frac{2}{A})} + \dots + \frac{q^{B-A}}{A^{B-A}(1 + \frac{1}{A}) \dots (1 + \frac{B-A}{A})}$$

Using  $1 + x \approx e^x$  and  $\sum_{k=1}^n k = \frac{n(n+1)}{2}$  in the above expression we get

$$\begin{aligned} \sum_{k=A+1}^B \frac{q^k A!}{k! q^A} &\approx \frac{q}{A e^{\frac{1}{A}}} + \frac{q^2}{A^2 e^{\frac{1}{A}} e^{\frac{2}{2A}}} + \dots + \frac{q^{B-A}}{A^{B-A} e^{\frac{1}{A}} \dots e^{\frac{B-A}{A}}} \\ &= \frac{q}{A e^{\frac{1}{A}}} + \frac{q^2}{A^2 e^{\frac{2 \times 3}{2A}}} + \dots + \frac{q^{B-A}}{A^{B-A} e^{\frac{(B-A)(B-A+1)}{2A}}} \\ &= \frac{q/A}{e^{\frac{1}{A}}} + \frac{(q/A)^2}{(e^{\frac{1}{A}} e^{\frac{1}{2A}})^2} + \dots + \frac{(q/A)^{B-A}}{(e^{\frac{1}{A}} e^{\frac{B-A-1}{2A}})^{(B-A)}} \end{aligned}$$

The  $k$ -th term of the sum has the form  $(\frac{q/A}{e^{\frac{1}{A}} e^{\frac{k-1}{2A}}})^k$  and thus it decreases with increasing  $k$  due to  $e^{\frac{1}{2A}} > 1$ . Let us determine the value of  $k$ , as a function of  $q$  and  $A$ , at which the  $k$ -th term equals to 1.

$$\frac{q/A}{e^{\frac{1}{A}} e^{\frac{k-1}{2A}}} = 1 \Leftrightarrow \frac{q/A}{e^{\frac{1}{A}}} = e^{\frac{k-1}{2A}} \Leftrightarrow \frac{k-1}{2A} = \ln(q/A) - \frac{1}{A} \Leftrightarrow k = 2A \ln(q/A) - 1$$

Around  $f_1 \approx 1$  the magnitude of the sum  $\sum_{k=A+1}^B \frac{q^k A!}{k! q^A}$  changes from  $\ll 1$  to  $\gg 1$  with increasing  $f_1$  (and  $q$ ). This can be taken into account by setting  $k \gg 1$ , since in this case the first  $k$  terms are  $\geq 1$  implying  $\sum_{k=A+1}^B \frac{q^k A!}{k! q^A} > k \gg 1$ . In fact the  $k$ -th term will be even higher than 1 due to the overestimations of the terms with the form  $1 + x$  by  $e^x$ .

Therefore, setting a value lower than  $k \gg 1$  is enough to have  $\sum_{k=A+1}^B \frac{q^k A!}{k! q^A} > k \gg 1$  and thus  $2A \ln(q/A) - 1$  is a lower limit for  $k$ . We count for  $k \gg 1$  by setting  $k = 10$ . This leads to the upper limit of  $q$  as

$$10 > 2A \ln(q/A) - 1 \Leftrightarrow \ln(q/A) < \frac{5.5}{A} \Leftrightarrow q < Ae^{\frac{5.5}{A}}$$

Note that with increasing  $\frac{B-A}{A} = \frac{B}{A} - 1$  increases also the overestimation of  $q$  by the above limit.

D. Formula for  $\sum_{k=A+1}^B \frac{k! q^A}{q^k A!}$

Statement: The following formula holds for  $\sum_{k=A+1}^B \frac{k! q^A}{q^k A!}$  for  $A, B \in \mathbb{N}$ ,  $A < B$  and  $0 < q$  as well as  $q \neq A + 1$  and  $q \neq B$

$$\sum_{k=A+1}^B \frac{k! q^A}{q^k A!} = g_1 \frac{1 - g_1^{B-A}}{1 - g_1}$$

where  $g_1 = \frac{q_0}{q}$  and  $A + 1 \leq g_0 \leq B$ .

The sum in the statement can be rearranged as

$$\begin{aligned} \sum_{k=A+1}^B \frac{k! q^A}{q^k A!} &= \left( \frac{A+1}{q} + \frac{(A+1)(A+2)}{q^2} + \dots + \frac{(A+1) \dots B}{q^{B-A}} \right) \cdot \end{aligned}$$

If all terms in the nominators are replaced by  $A + 1$  then we get a lower limit as

$$\begin{aligned} \sum_{k=A+1}^B \frac{k! q^A}{q^k A!} &\geq \left( \frac{A+1}{q} + \frac{(A+1)(A+1)}{q^2} + \dots + \frac{(A+1) \dots (A+1)}{q^{B-A}} \right) \\ &= \sum_{i=1}^{B-A} \left( \frac{A+1}{q} \right)^i = \frac{A+1}{q} \frac{1 - (\frac{A+1}{q})^{B-A}}{1 - \frac{A+1}{q}} \end{aligned}$$

Similarly, replacing all terms in the nominator by  $B$ , we get an upper limit as

$$\begin{aligned} \sum_{k=A+1}^B \frac{k! q^A}{q^k A!} &\leq \left( \frac{B}{q} + \frac{B B}{q^2} + \dots + \frac{B \dots B}{q^{B-A}} \right) \\ &= \sum_{i=1}^{B-A} \left( \frac{B}{q} \right)^i = \frac{B}{q} \frac{1 - (\frac{B}{q})^{B-A}}{1 - \frac{B}{q}} \end{aligned}$$

It follows from the development of the function  $x^{\frac{1-(x)^{B-A}}{1-x}}$  in the range  $\frac{A+1}{q} \leq x \leq \frac{B}{q}$  that there exists an  $g_1 = \frac{q_0}{q}$  with  $A + 1 \leq g_0 \leq B$ , for which

$$\sum_{k=A+1}^B \frac{k! q^A}{q^k A!} = g_1 \frac{1 - g_1^{B-A}}{1 - g_1}$$

holds.

Note that keeping  $B$  (or  $A$ ) constant a higher  $A$  (or  $B$ ) implies higher  $g_0$  and thus higher  $g_1$ .

## REFERENCES

- [1] Z. Saffer, "Optimization of Cloud Model Based on Shifted N-policy  $M/M/m/K$  Queue," in E. Borcoci, editor, IARIA, AICT2021: 17th Advanced International Conference on Telecommunications, Valencia, Spain, pp. 11-20, 2021.
- [2] F. Durao, J. Fernando, S. Carvalho, A. Fonseka and V. C. Garcia, "A systematic review on cloud computing," *J. Supercomput.*, vol. 68, no. 3, pp. 1321–1346, 2014.
- [3] C. Chapman, W. Emmerich, F. G. Mrquez, S. Clayman and A. Galis, "Software architecture definition for on-demand cloud provisioning," *Cluster Comput.*, vol. 15, no. 2, pp. 79–100, 2011.
- [4] N. A. Sultan, "Reaching for the cloud: How SMEs can manage," *Int. J. Inf. Manage.*, vol. 31, pp. 272-278, 2011.
- [5] W. Christof et al., "Cloud computing - A classification business models and research directions," *J. Bus. Inf. Syst. Eng.*, vol. 1, no. 5, pp. 391-399, 2009.
- [6] H. Khazaei, J. Mistic and v.B. Mistic, "Performance analysis of Cloud computing centers using  $M/G/m/m+r$  queuing systems," *IEEE Trans. Parallel Distrib. Syst.*, vol. 23, no. 5, pp. 936-943, 2012.
- [7] R. Ghosh, F. Longo, V.K. Naik and K.S. Trivedi, "Modeling and performance analysis of large scale IaaS clouds Future Generation Computer Systems," *Future Generation Computer Systems*, vol. 29, pp. 1216–1234, 2013.
- [8] Q. Duan, "Cloud service performance evaluation: status, challenges, and opportunities a survey from the system modeling perspective," *Digital Communications and Networks*, vol. 3, no. 2, pp. 101–111, 2017.
- [9] G. Kaur, A. Bala and I. Chana, "An intelligent regressive ensemble approach for predicting resource usage in cloud computing," *Journal of Parallel and Distributed Computing*, vol. 123, pp. 1–12, 2019.
- [10] R. Yang, X. Ouyang, Y. Chen, P. Townend and J. Xu, "Intelligent resource scheduling at scale: A machine learning perspective," in 2018 IEEE Symposium on Service-Oriented System Engineering (SOSE), 3, pp. 132141, 2018.
- [11] M. Ghobaei-Arani, S. Jabbehdari and M. A. Pourmina, "An autonomic resource provisioning approach for service-based cloud applications: A hybrid approach," *Future Generation Computer Systems*, vol. 78, pp. 191–210, 2018.
- [12] J. N. Witanto, H. Lim and M. Atiquzzaman, "Adaptive selection of dynamic vm consolidation algorithm using neural network for cloud resource management," *Future Generation Computer Systems*, vol. 87, pp. 35–42, 2018.
- [13] A. Beloglazov, J. Abawajy and R. Buyya, "Energy-aware resource allocation heuristics for efficient management of data centers for Cloud computing," *Future Generation Comput. Syst.*, Vol. 28, no. 5, pp. 755-68, 2012.
- [14] F. Nzanywayingoma and Y. Yang, "Efficient resource management techniques in cloud computing environment: a review and discussion," *International Journal of Computers and Applications*, vol. 41, no. 3, pp. 165–182, 2019.
- [15] T. Ma, Y. Chu, L. Zhao and O. Ankhbayar, "Resource Allocation and Scheduling in Cloud Computing: Policy and Algorithm," *IETE Technical Review*, vol. 31, no. 1, pp. 4–16, 2014.
- [16] T. Tournaire, H. Castel-Taleb, E. Hyon and T. Hoche, "Generating optimal thresholds in a hysteresis queue: application to a cloud model," *MASCOTS 2019: 27th International Symposium on Modeling, Analysis, and Simulation of Computer and Telecommunication Systems*, Rennes, France, Oct 2019, pp.283–294.
- [17] B. Wan, J. Dang, Z. Li, H. Gong, F. Zhang and S. Oh, "Modeling Analysis and Cost-Performance Ratio Optimization of Virtual Machine Scheduling in Cloud Computing," *IEEE Transactions on Parallel and Distributed Systems*, vol. 31, no. 7, pp. 1518–1532, 2020.
- [18] Y. Mansouri, A. N. Toosi and R. Buyya, "Cost Optimization for Dynamic Replication and Migration of Data in Cloud Data Centers," in *IEEE Transactions on Cloud Computing*, vol. 7, no. 3, pp. 705-718, 2019.
- [19] W. Whitt, "Approximations for the  $GI/G/m$  queue," *Production Oper. Management*, vol. 2, pp. 114–161, 1993.